DEVELOPMENT OF BORON SUBOXIDE COMPOSITES WITH IMPROVED TOUGHNESS

Anthony Andrews

A thesis submitted to the Faculty of Engineering and the Built Environment, University of the Witwatersrand, in fulfilment of the requirements for the degree of Doctor of Philosophy in Engineering.

June 2008

DECLARATION

I declare that this thesis is my own, unaided work. It is being submitted for the degree of Doctor of Philosophy in Engineering at the University of the Witwatersrand, Johannesburg. It has not been submitted before for any degree or examination in any other University.

Anthony Andrews

---------- day of ----------, 2008

ABSTRACT

The research efforts by material scientists in the area of boron suboxide materials have been directed towards improving the fracture toughness by microstructural tailoring and adopting various effective toughening mechanisms. In this perspective, the current work reports the development of boron suboxide composites with improved toughness.

The relationships between densification and microstructure and microstructure and mechanical properties of boron suboxide (B_6O) composites have been studied in detail using hot pressing technique. Various suitable sintering additives were selected based on thermodynamic calculations. Laboratory prepared B_6O powders were initially milled using steel balls in an attrition mill to drive the particle sizes down to submicron range. Contaminations from steel balls were acid washed in HCl. The amounts of impurities remaining in the powders were characterised using Inductively Couple Plasma (ICP) technique. Submicron B_6O powders were then admixed with Al_2O_3-Y_2O_3, Al_2O_3-Y_2O_3-SiO_2, Al_2O_3-SiO_2, Al_2O_3, TiC, TiB_2 and Pd additive systems in a planetary ball mill. Al_2O_3-Y_2O_3 systems, with various molar ratios were used to study the influence of grain boundary composition on densification, microstructure and mechanical properties.

Hot pressing experiments were conducted in a temperature range of 1600 – 1900^oC under a pressure of 50 MPa for 20 minutes in argon atmosphere. The microstructure and phase composition of the hot pressed composites were characterised using scanning electron microscopy (SEM), transmission electron microscopy (TEM) and X-ray diffractometry (XRD). Densities of the samples were measured to determine the extent of densification. Vickers hardness and indentation toughness were used to characterise the mechanical properties of the hot pressed materials. Careful analysis of the indentation data has been made and such analysis has provided an estimate of the toughness properties of the B_6O composites.

'Pure' B_6O hot pressed at 1900°C had Vickers hardness of 35 GPa (500g load) but was found to be brittle. The experimental results revealed that B_6O composites containing Al_2O_3-Y_2O_3 and Al_2O_3-Y_2O_3-SiO_2 systems processed at 1800°C exhibit excellent combination of hardness (27 - 34 GPa using 500g load) and fracture toughness (3 - 6 $MPam^{1/2}$). Densities higher than 97% of theoretical densities were achieved. Hot pressing these composites at higher temperature (1850°C) is observed to slightly lower the hardness values. Amorphous grain boundary phases were formed.

Composites containing Al_2O_3, TiB_2, and TiC, respectively were hot pressed at 1900°C. Vickers hardness in the range of 27 – 31 GPa were obtained using 500g load whilst fracture toughness values were in the range of 4 – 7 $MPam^{1/2}$. B_6O composite produced by addition of Pd had a hardness of 22 GPa using 5kg load but a high fracture toughness of 13 $MPam^{1/2}$. Fracture toughness values obtained in this work are the highest recorded so far for B_6O composites.

The mechanisms leading to the achievement of superior toughness and the possible reasons for toughness variation with the different additives as well as with hot pressing temperature are critically analysed. It has been shown that B_6O can be sintered using a wide range of oxide additives which could result in improvement of mechanical properties, especially fracture toughness. Microstructural tailoring of these composites could potentially see widespread application of B_6O composites as structural material.

DEDICATION

To the most important people in my life: my parents, brothers and sisters, and most especially, my dear wife, Akos and son, Somiah.

ACKNOWLEDGEMENTS

I would like to acknowledge the following people for the valuable contributions which facilitated the completion of this research work.

(i). Prof. I. Sigalas for suggestions and supervising this work.

(ii). Dr. M. Herrmann for his advice, useful comments, time and constructive criticism.

(iii). K. Katuku for his assistance in getting good SEM images.

(iv). Prof. Kleebe for his help in TEM work.

(v). Support staff of the School of Chemical and Metallurgical Engineering (University of the Witwatersrand) namely, Aubrey, Graham, Gift, Johnson, Bruce and Theo for their assistance with specimen preparation.

(vi). Element Six (Pty) Ltd – Diamond Research Laboratory for their financial support.

(vii). NRF for financial assistance.

(viii). Keke, Thembinkosi, Aron, Nana, and David for their special friendship and all staff and postgraduate students in the School of Chemical and Metallurgical Engineering for their friendship.

(ix). My family, especially mum and dad, for the support and sacrifices throughout this period.

(x). Finally, to my wife, Akos. Thank you for your continued love, support and above all patience.

TABLE OF CONTENTS

LIST OF FIGURES

LIST OF TABLES

LIST OF SYMBOLS

SEM	=	Scanning Electron Microscopy
EDX	=	Energy Dispersive X-ray Spectroscopy
TEM	=	Transition Electron Microscopy
XRD	=	X-ray diffraction
ICSD	=	International Centre for Diffraction Data
ICP-OES	=	Inductively coupled plasma optical emission spectroscopy
Hv	=	Vickers hardness
K_{IC}	=	Fracture toughness
GPa	=	GigaPascal
MPa	=	MegaPascal
hr(s)	=	hour(s)
min(s)	=	minute(s)
μm	=	micron
wt%	=	Weight percent
^{o}C	=	degrees Celsius
K	=	degrees Kelvin

1 Introduction

The development of synthetic ultrahard materials with hardness values approaching or even exceeding that of diamond has been of great interest to material scientists. With Vickers hardness (Hv) of composite materials ranging between 50 to 70 GPa, diamond is the hardest material known, followed by cubic boron nitride, cBN (35 to 40 GPa). Diamond, cBN and their sintered composites are widely used in industry as wear parts (bearings, nozzles, milling media, and pump impellers) and sawing, grinding and cutting tools. However, diamond has a major drawback due to its reaction with iron and cannot be used for machining ferrous alloys [(1)]. This prompted the synthesis of cBN. The structure of cBN is derived from that of diamond with half the carbon atoms being replaced by boron and the other half by nitrogen atoms. cBN is half as hard as diamond, but does not react as strongly with iron and can be used for machining ferrous alloys. However, as temperature increases cBN weakens due to diffusion wear and transformation to hexagonal structure (hBN) [(1)]. The synthesis of diamond and cubic boron nitride materials also requires high pressures and temperatures, which makes production expensive and limits the sizes and geometric forms possible for their polycrystalline ceramics and their composites.

Boron suboxide is third in hardness after diamond and cBN (31 to 38 GPa) [(2-8)]. The hardness of a single crystal boron suboxide (B_6O) is about 45 GPa which is comparable to that of cBN (45-50 GPa) [(9)]. Additionally, the fracture toughness of B_6O single crystal was found to be 4.5 $MPam^{1/2}$, which is higher than that of cBN (2.8 $MPam^{1/2}$), and also approaches that of single crystal diamond (5 $MPam^{1/2}$). Boron suboxide has a better thermal stability compared to diamond [(9)] and can be synthesised without the need for high pressure. Boron suboxide therefore becomes a potentially good candidate for cutting tools and other industrial applications where abrasive wear resistance is essential. For these reasons and because of the need to replace expensive diamond in many other applications, boron suboxide has been of

technological interest. The strong covalent bonds and short interatomic bond length contribute to the exceptional physical and chemical properties such as great hardness, low mass density, high chemical inertness and excellent wear resistance [3][6][10-13].

Novel boron suboxide (nominally B_6O) has been synthesised and sintered and their properties have been widely discussed. Sintering is usually carried out in a specially designed cell at high-pressures or low-pressure conditions and at high-temperatures [2][3][5][7][11][14-16]. Boron suboxide (B_6O) formed at or near ambient pressure is generally oxygen deficient, has poor crystallinity, and very small grain size. High pressure applied during the synthesis of B_6O can significantly increase the crystallinity, oxygen stoichiometry, and crystal size of the products [12][17]. Boron suboxide powders of nominal composition B_2O, B_3O, B_4O, B_6O_{1-x} ($0.72 \leq x \leq 0.96$), B_8O, $B_{12}O$, $B_{15}O$, $B_{18}O$, $B_{20}O$ and $B_{22}O$ have been reported [18-22]. Although boron suboxide is reported as having nominal compositions, it is widely accepted to be non-stoichiometric and the reported compositions range from $B_6O_{0.72}$ to $B_6O_{0.96}$. Thus, the formula is best reported as B_6O_x where $x < 1$ [20]. The boron suboxide investigated in this work is of nominal composition B_6O.

In spite of the high fracture toughness (4.5 $MPam^{1/2}$) of a single crystal B_6O, the fracture toughness for polycrystalline B_6O is less than 1.5 $MPam^{1/2}$ which limits industrial applications. The Vickers microhardness values obtained for polycrystalline B_6O through high-pressure high-temperature processes range from 31 to 38 GPa. The reason for the low fracture toughness obtained in the sintered compacts is not understood. Efforts have been made to increase the fracture toughness by forming B_6O composites with other ultrahard materials such as diamond, boron carbide (B_4C), and cBN [4][7][14]. High hardness values were recorded for the composites (Hv ~ 46 GPa under 200g load) but fracture toughness values did not exceed 1.8 $MPam^{1/2}$. Recently, Shabalala [16] produced B_6O composites with aluminium borates as the second phase via hot pressing and obtained high fracture toughness (3.1 $MPam^{1/2}$) with respectable hardness (Hv ~ 31 GPa under 500g load). These suggest that a

careful selection of additives and/or binders in combination with controlled sintering conditions could result in a production of B_6O composites having a unique combination of mechanical properties suitable for industrial applications.

In light of the literature review, the objectives which were identified in order to improve the overall mechanical properties, especially fracture toughness, of boron suboxide composites for industrial applications were to synthesize submicron boron suboxide (B_6O) powder and to hot press the synthesised powder. The overall mechanical properties of the sintered B_6O compact were to be improved by addition of carefully selected binders and to relate the microstructure to mechanical properties.

In achieving the above objectives a detailed literature review of boron suboxide-based ultrahard materials together with their properties, and the possible avenues of improving the mechanical properties are given in Chapter 2. Chapter 3 constitutes the modelling of B_6O thermodynamic data at high temperatures (800 – 2300K) which assisted in selecting suitable additives for this work and for future investigations. The methodology and equipments used for the investigation are outlined in Chapter 4. Chapters 5 and 6 present the results and discussion of the synthesis, milling, and hot pressing B_6O composite materials, respectively. Conclusions and recommendations from this project are dealt with in Chapter 7.

2 Literature Review

2.1 Introduction

This chapter summarises the available knowledge on boron-based superhard materials with particular emphasis on boron suboxide materials.

2.2 Hard materials

Hardness is defined as the resistance of a material to plastic deformation [(1)]. Hardness can also be defined as the resistance of a material to indentation by another material [(23)]. Hardness can be measured in several ways and includes scratching, grinding and indenting methods. In addition, there are a number of factors to consider when determining the hardness of any material. For instance, the indenter geometry, testing load, and time taken for the indentation have to be considered. The hardness of a single crystal depends on the slip systems that can be affected by the stresses generated by the indentation. The hardness of polycrystalline material on the other hand depends on the single crystal hardness of the majority phase, as well as the residual stresses, secondary phases, microstructural textures, grain size, applied load, porosity, structure and composition of the grain boundaries [(1)].

Hard materials on the other hand are solids with high hardness in the range of 8 to 10 on the Mohs' scale of hardness [(1)]. This scale of hardness was developed for minerals. However, in material science, Vickers, Rockwell or Knoop hardness are used. Ultrahard materials have hardness values comparable to that of diamond. Ultrahard materials are materials with Vickers hardness (Hv) higher than 40 GPa [(8)]. Generally, the hardest materials which are also those of highest bulk moduli, are to be found among certain of the light elements (e.g. boron and carbon) or compounds between them, for instance cubic boron nitride, boron suboxide and boron carbide [(24)]. Ultrahard materials are widely used as wear parts, grinding, and cutting tools.

Currently, only diamond and cubic boron nitride (cBN) are used in industry as ultrahard materials. Table 2.1 shows the properties of some selected hard materials.

Table 2.1: Density, hardness, bulk and shear modulus of some selected hard materials.

Material	Density (g/cm^3)	Hv_1 (GPa)	Bulk modulus (GPa)	Shear modulus (GPa)	Reference
Diamond	3.52	70	443	535	(25)
c-BN	3.48	45-50	400	409	(25)
B_4C	2.52	30-50	250	-	(25)
TiB_2	4.50	30-33	244	263	(25)
AlB_{12}	2.58	26	-	-	(25)
$AlMgB_{14}$	2.66	32-35*	212	231	(25) (26)

*Load not specified

2.3 Crystal structure of boron-based hard materials

The disadvantage of carbon-based materials such as low oxidation resistance of diamond can be improved by boron-based hard materials of the binary or ternary systems B-C, B-N, B-O, B-C-N [(1)(27)]. Diamond oxidises in air above 600°C whereas cubic boron nitride (cBN) is resistant to oxidation up to 1100°C in air [(28)]. Boron is one of the two elements (along with nitrogen) that forms compounds with all its neighbouring elements (BeB_x, MgB_x, AlB_x, B_xSi, B_xC). Additionally, boron is the only element whose compounds with adjacent (and not only adjacent) elements in the periodic table are not simply thermally stable, but furthermore have the highest hardness values known [(22)]. Boron-rich solids form a class of light element-containing 'super-hard' materials, with high tensile strength and large values of the bulk modulus and cohesive energy [(15)(29)]. cBN, $B_{22}O$, B_2O, B_6O, and B_4C are known as boron-containing superhard materials, with a Vickers microhardness (Hv) of 30-55 GPa [(3)(12)(18)(30)]. The crystal structure of boron, boron suboxides and boron carbides are discussed below.

2.3.1 Crystal structure of boron

Elemental boron is a hard material with microhardness of 30 GPa. The high hardness is related to the low molar volume of 5 cm^3 and a covalent bonding of the rhombohedral crystal structure. Boron compounds have exceptional properties in respect to their chemical bonding, crystal structure, and phonon and electron conduction [22][31]. Boron (valence of 3) exhibits a number of different compositions and structures arising from the specific electronic nature of its atom. The properties of α-rhombohedral boron, for example, can be significantly changed by the addition of other atomic constituents [32]. $B_{12}O_2$ and $AlMgB_{14}$ are examples whose hardness values were claimed to approximate that of cubic boron nitride (cBN). Boron atoms form very stable clusters such as an octahedron, an icosahedron, and other polyhedrons. Such structure characteristics resulting from the covalent nature of the bonding and forming a rigid three-dimensional framework, determine their bulk properties of high hardness and refractory nature.

Boron exists in several phases including the crystalline forms of α and β rhombohedral boron, α and β tetragonal boron, and an amorphous form. The different phases depend on the temperature, pressure, and reactants present during formation [20]. The phase diagram of boron is given in figure 2.1 showing the stability region of the different phases. Each phase exhibits different chemical and physical characteristics. It has been found (by *ab initio calculations*) that at low temperatures, α-boron is the most stable phase, while at high temperatures β is the most favourable phase [33]. Tetragonal phases are generally formed at intermediate temperatures when impurities are present. Amorphous boron deposited at low temperatures, tends to be fine-grained and most reactive [20][34].

Table 2.2 compares the structural parameters of α- and β-boron, along with some of their physical properties and table 2.3 compares the lattice parameters for α-boron, boron carbide and some selected boron suboxides. In case of the atomic density ρ, α phase is denser than the β phase by 7%. It is also seen (Table 2.2) that the α-boron is

stiffer than β-boron, with respect to the bulk modulus and Debye temperature. This is consistent with the fact that α-boron is denser than β-boron. Therefore α-boron is a stronger material.

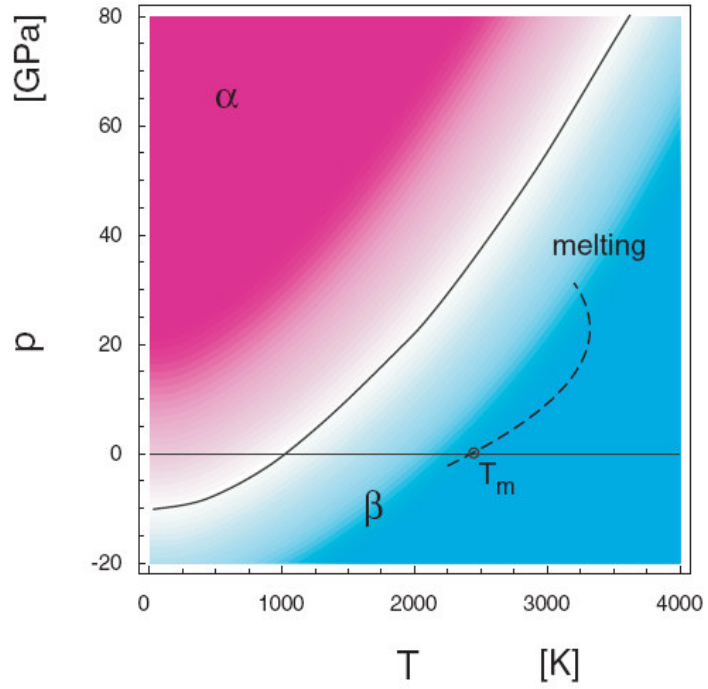

Figure 2.1: Phase diagram of boron. Red indicates the region where α-boron is stable, while blue indicates β-boron. The melting curve is indicated by a dashed line, which is started from an experimental point T_m = 2340 K [33].

Table 2.2: Structural parameters of α- and β-boron in experiment: Lattice parameters a_0 and α, number of atoms N_{atom}, atom density ρ, coordination number N_c, Debye temperature θ_D, and bulk modulus B_0. The bond length is presented as the minimum d_{min} and average d_{avg} for all the bonds [35].

	α-boron	β-boron
a_0 (Å)	5.057	10.145
α (°)	58.06	65.17
N_{atom}	12	105
ρ (/Å^3)	0.1373	0.1278
N_c	5.50	6.40
d_{min} (Å)	1.71	1.62
d_{avg} (Å)	1.77	1.80
θ_D (K)	1430	1200-1300
B_0 (GPa)	213-224	185-210

Table 2.3: Cell parameters for boron, boron carbide and selected samples of B_6O (Space group $R\bar{3}m$, hexagonal axes).

Compound	Cell parameters (nm)			Reference
	a_h	c_h	c_h/a_h	
α-rh B	4.927(3)	12.564(7)	2.55	(24)
$B_6O_{0.787}$	5.3824(4)	12.322(1)	2.289	(24)
$B_6O_{0.839}$	5.3761(7)	12.326(3)	2.293	(24)
$B_6O_{0.95}$	5.3902(2)	12.3125(4)	2.284	(12)
B_6O	5.395	12.342	2.282	(36)
B_4C	5.5991(5)	12.074(2)	2.156	(24)

The crystal structures of α- and β-boron are shown in figure 2.2. Both have a rhombohedral Bravais lattice with a space group of $R\bar{3}m$ in its perfect form. The icosahedral unit B_{12} is a common building block [(18)(35)]. The structure of β-boron is complex with a unit cell consisting of 105 atoms, which can be classified into 15 nonequivalent atomic sites on the assumption of $R\bar{3}m$ symmetry [(37)]. Site B(13) in figure 2.2 is only partially occupied with an occupancy of 73.4%. The missing boron atoms appear at extra site B(16) with an occupancy of 26.6%.

The most easily available modification of boron that is found commercially or made within the laboratory is the β phase [(35)]. Hence, this phase is considered to be the thermodynamically stable phase [(18)(35)].

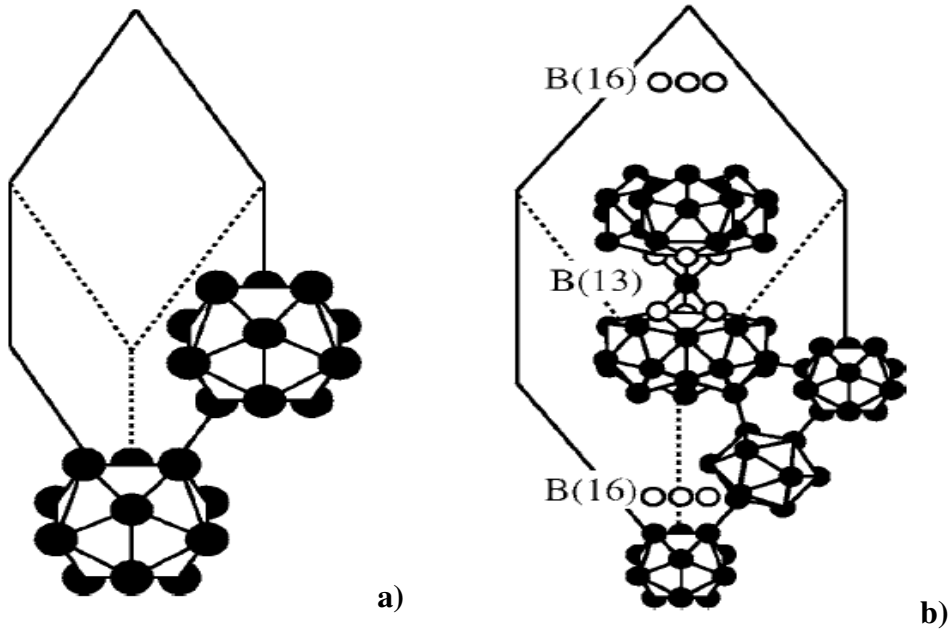

Figure 2.2: Crystal structure of α- (a) and β-boron (b). α-boron has a rhombohedral structure (space group $R\bar{3}m$) with 12 atoms in a cell. β-boron has the same space group, but it contains 105 atoms in a cell. The closed (open) circles represent atomic sites with full (partial) occupancy. Atomic sites with partial occupancy are indicated [(35)].

2.3.2 Crystal structure of boron suboxides

Oxygen atoms dissolving into electron deficient α-rhombohedral boron structure results in the formation of boron suboxide. This decreases the c/a ratio of the boron structure [12][24]. Structure models of boron suboxides suggest oxygen occupancy of the 6*c* positions with the coefficients depending on the composition. The axial ratio decreases with increasing oxygen content (Table 2.3). For instance, the unit cell parameters for sample produced by Hubert *et al*. [12] were refined from powder X-ray diffraction data to a = 5.3902(1) Å, c = 12.3125(2) Å, which gives a c/a ratio of 2.284.

The structure of boron suboxide (nominally B_6O) is built of eight B_{12} icosahedra units situated at the apices of the rhombohedral unit cell (space group $R\bar{3}m$). The structure can be viewed as a distorted cubic close packing (ccp) of B_{12} icosahedra. Figure 2.3 shows the structure of B_6O. The unit lattice of B_6O has α-rhombohedral boron type of structure consisting of B_{12} cluster as the fundamental frame. Two oxygen atoms are located in the interstices along the [111] rhombohedral direction, replacing the 3-center, 2-electron bond that links the icosahedra in this direction [3][11][17][24]. The O-O bonding distance is 0.307 nm, which prevent direct O-O bonding [17][24]. Consequently, each oxygen atom is only bonded to three equatorial boron atoms belonging to three different boron icosahedra. Due to its short interatomic bond lengths and strong covalent character between boron- boron, B_6O displays a range of outstanding physical and chemical properties such as high hardness, low mass density, semiconductivity, high chemical inertness, high melting point, and excellent wear resistance [3]. There have even been reports that samples of material with nominal composition near '$B_{22}O$' scratch the softer {100} faces of diamond [18]. However, boron suboxide is nonstoichiometric [9][18]. Reported compositions ranges from $B_6O_{0.72}$ to $B_6O_{0.86}$ at near ambient pressures [15][29][38].

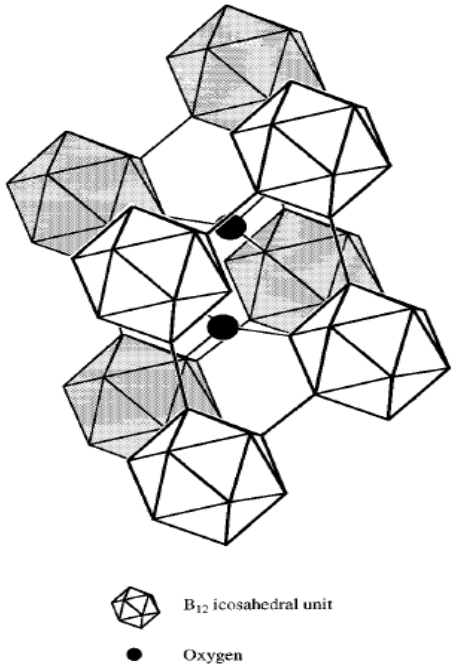

Figure 2.3: (a) Structure of B_6O built of eight icosahedral units situated at the vertices of the rhombohedral unit cell. Gray icosahedra are in the background. The icosahedra are composed of 12 B atoms situated at the corners of a slightly distorted icosahedron. Oxygen atoms are three-coordinated to boron atoms in separate icosahedra in the (001) plane [(17)(15)].

Compared to room-temperature synthesis, high-pressure high-temperature (HPHT) techniques produce B_6O much closer to the ideal composition (highest O occupancy, $B_6O_{0.96}$) with improved crystallinity [(12)(15)(17)]. Pressures up to 10 GPa have been used. Structural investigations have shown that there is only partial occupancy of the oxygen position [(6)(39)]. An investigation by Lundström and Andreev [(24)] showed that the oxygen occupancy varies from 0.787(5) at 1450°C to 0.831(5) and 0.839(4) at 1350°C and 1250°C respectively. High pressure synthesis of boron suboxide in the presence of an oxidizing agent results in an increase in the oxygen chemical potential, as should be expected, and that drives the composition of the B_6O phase closer to the nominal stoichiometry [(6)(12)(15)(17)]. Table 2.4 shows published data on the occupancy of the 6*c* positions in the known boron suboxides. The formula of the suboxide is therefore more conveniently written as B_6O_{1-x} [(6)].

Table 2.4: Site Occupancies and the number of atoms per hexagonal unit cell for boron suboxides.

Compound	Occupancy of the 6*c* position, oxygen	Total number of atoms per unit cell	Reference
$B_6O_{0.72}$	0.72	40.32	(40)
$B_6O_{0.76}$	0.76	40.56	(39)
$B_6O_{0.77}$	0.77	40.62	(17)
$B_6O_{0.787}$	0.79	40.72	(24)
$B_6O_{0.839}$	0.84	41.03	(24)
$B_6O_{0.89}$	0.89	41.34	(17)
$B_6O_{0.93}$	0.93	41.58	(39)
$B_6O_{0.95}$	0.95	41.70	(17)

B_2O was reported to crystallise in the space group P3 with the hexagonal unit cell a = 2.879 Å and c = 7.052 Å, containing four boron and two oxygen atoms [30]. The structure was suggested to consist of buckled atomic layers (consisting either of boron atoms or of boron and oxygen atoms), stacked in the c direction (corresponding to [111] direction of the sphalerite cell) in the sequence BB layer and double OB-BO layer. Lundström [29] calculated the interatomic distances using space group $P\bar{3}m1$ with boron at the atomic positions 2*c* (z = 0.375) and 2*d* (z = 0.042), respectively, and oxygen at 2*d* (z = 0.292). It was assumed that $d_{BB} = d_{BO}$. The calculations show that the B-B distances within and between the buckled boron layer are normal, namely 1.765 Å. The B-O distances are, however, larger within the two halves of the B-O double layer, namely 1.765 Å, a consequence of the assumption made. If the half layers of the double layer are assumed to be plane, the B-O distance is 1.66 Å, which is more reasonable considering the interatomic distances in other B-O solids. In B_6O for instance, the distance is slightly less than 1.50 Å. The shortest B-O distance between a boron atom in the buckled boron layer and an oxygen atom in the buckled layer is, however as large as 2.35 Å, which indicates a very weak bonding between these two types of layers. This distance will be even larger if the B-O half layers are assumed to be plane. This means that the structure suggested by Endo *et al.* [30] for B_2O has mainly properties characteristic of layer structures, including no great

hardness. Based on the calculations conducted by Lundström, it was concluded that the proposed structure of B_2O is unstable. This means that the crystal structure of B_2O needs to be investigated more closely. In addition to the most studied form of boron suboxide (B_6O_{x-1} and B_2O), other boron suboxides (B_xO) of nominal composition B_3O, B_4O, B_7O, $B_{15}O$, $B_{20}O$, and $B_{22}O$ have been reported [18-22]. However, there is practically no common opinion either on their composition or structure.

2.3.3 Crystal structure of boron carbides

Boron carbides are among a number of materials with crystal structure derived from that of α-rhombohedral boron. The crystal structure of boron carbide (B_4C), which is better represented as $B_{13}C_2$, is built of B_{12} icosahedra linked together by C-B-C chains (figure 2.4). Using IR absorption, Becher and Thévenot [41] have confirmed the existence of the C-B-C chains in compounds such as B_4C and $B_{5.52}C$. The space group is $R\bar{3}m$ (No. 166) similar to boron suboxide. The incorporation of carbon in boron carbide was understood to supply the extra two electrons to the crystal of α-boron, replacing the weak three-centre bond with strong covalent bonds. These relatively weak three-centre bonds are mainly responsible for the cohesion in the *ab* plane. The arrangement is such that an elongated hole is formed between two three-centre bonded triangles along the trigonal axis [24][29].

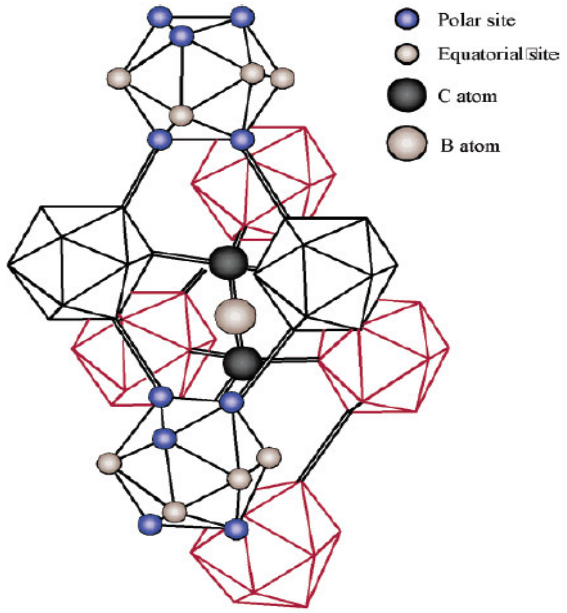

Figure 2.4: Crystal structure of $B_{13}C_2$ [42].

Compounds crystallizing in the B_4C-like structure are formed between boron and nine elements of the periodic table, namely Be, C, N, O, Si, P, S, As, and Se [40]. The structures belonging to the structural family of B_4C differ mainly in the number and type of atoms accommodated in the elongated holes occurring along the hexagonal *c* axis (rhombohedral space diagonal) of the unit cell. Icosahedral borides of P ($B_{12}P_2$) and As ($B_{12}As_2$) pnictides, for example, are materials based on 12-atom boron clusters in which boron atoms occupy the 12 vertices of the icosahedra and two atom chains (P_2 or As_2) that reside between icosahedra [42].

Even though boron carbide and boron suboxide are related to the same rhombohedral structure, boron suboxide is harder than boron carbide. The difference is somewhat connected to the inter-icosahedral atoms [43]. In boron suboxide and boron carbide, O and C atoms are placed between icosahedra, linking them with strong covalent bonds. These intracluster bonds are stronger in boron suboxide than in boron carbide due to the higher electronegativity of oxygen relative to carbon. With the development of the

first-principles approach, Gao *et al*. [42] had predicted the hardness of a number of boron-rich phases. It is believed that boron-rich materials formed by adding some element to boron icosahedra have great potential as new superhard materials for industrial use.

2.4 Synthesis and structure of nonstiochiometric boron suboxide (B_6O) powders

The synthesis of boron suboxide powders and description of its properties have been extensively reported in literature. Wartik and Apple produced amorphous BO(s) by dehydration of $B_2(OH)$ in *vacuum* [44]. Kanda *et al*. also prepared BO(s) by reacting B_2O_3 with B at 1050°C also in *vacuum* [45]. The other suboxide of boron frequently mentioned in literature is B_7O which was first reported by Weinstraub [46]. B_7O was then prepared by reduction of B_2O_3 with Mg. Pasternak [47] confirmed this B_7O by chemical analysis. Additionally, powders of nominal composition B_2O, B_3O, B_4O, B_6O_{x-1} (where $0.72 \leq x \leq 0.96$), $B_{12}O$, $B_{15}O$, $B_{18}O$, $B_{20}O$ and $B_{22}O$ have been reported of being formed [18][19-22][31]. One of the difficulties in establishing the correct composition for this oxide is that only boron was determined with the difference assumed to be oxygen [36]. The different methods of producing boron suboxide powders are summarised below.

Boron suboxide powders can be produced by reacting stoichiometric amounts of elemental boron and boron oxide under controlled conditions ($1000^oC \leq T \leq 2200^oC$; 1hr ≤ time ≤ 12hr; argon atmosphere) [3][4][11][12][15][17][20]. Alternatively, boron suboxide powders can be produced by reacting boron with *M*O where *M* is Mg or Zn [5][20][48][49] or by reducing other oxides such as SnO, Ga_2O_3, In_2O_3, Bi_2O_3, $Li_2B_4O_7$, $KClO_3$ and CdO [19][21][24]. It was reported that the boro-thermic reduction of B_2O_3, ZnO and $Li_3B_4O_7$ resulted in the highest yields and purest reaction products. The specific form of B_xO produced depends on the process conditions and the ratio of

elemental boron to boron oxide loaded into the reaction cell [(2)]. The reaction of boron and boron oxide can generally be represented as [(2)];

$$(3x-2)B(s)+B_2O_3(l)\rightarrow 3B_xO(s) \qquad [\mathbf{2.1}]$$

In the case of reacting boron with zinc oxide, the following reaction [**2.2**] was used [(5)].

$$8B+ZnO\rightarrow B_6O+2B+Zn(g)\uparrow \qquad [\mathbf{2.2}]$$

The high temperature solid-liquid reaction [**2.1**] is achieved by wet mixing powdered boron and powdered B_2O_3 using a molar ratio of B:B_2O_3 = 16:1.03 in a mixer (e.g. agate mortar). Ethanol/hexane or other non-oxygenated dispersion liquid is normally used as solvent. The excess B_2O_3 takes into consideration that a small amount of B_2O_3 does not react with B, but rather volatilises during the heat treatment [(3)]. Nevertheless, this excess B_2O_3 can be removed after synthesis when washed in warm ethanol and/or water [(9)]. The preparation of boron suboxide (B_6O) in small quantities can also be carried out by oxidation of boron (directly or platinum catalysed) with oxygen gas at ambient pressure and at 1100-1800^oC [(36)].

Stoichiometric high-pressure high-temperature phases of B_2O have been prepared by Hall and Compton [(21)] and Endo *et al.* [(30)]. In the former study, a graphite-like B_2O was synthesised by the reduction of B_2O_3 with B or Li and by oxidation of B with $KClO_3$. The preparation was carried out within the pressure and temperature ranges of 5-7.5 GPa and 1200-1800^oC. The B_2O synthesised by Endo *et al*. was carried out by reacting boron powder with oxygen derived from the thermal decomposition of CrO_3 to CrO_2 at pressures of 3.5-5.5 GPa in the temperature range 1000-1200^oC. The recovered B_2O appeared to have a diamond-like structure and was characterised by Vickers microhardness (100g load) of 40.5 GPa.

The boron used can either be in the form of amorphous boron or crystalline boron. The B_2O_3 used is assumed to be pure (i.e. 99.9% pure). However, it is reported [(2)] that if the elemental boron used is less than 95% pure (with about 6% Mg), a harder B_6O material is formed. It is believed that the Mg aid in sintering of boron suboxide resulting in improved form of B_6O which is greater in hardness.

The synthesis of boron suboxide (B_6O) by reactive sintering can be carried out either at ambient/near ambient pressure or high pressure conditions. Boron suboxide powders produced at or near ambient pressure is generally nonstiochiometric with the reported compositions ranging from $B_6O_{0.72}$ to $B_6O_{0.86}$ [(11)(24)(38)(50)]. Additionally, the synthesis typically produces fine-grained powders mixed with amorphous boron material [(15)].

The synthesis of boron suboxide at high pressures (4–5.5 GPa) resulted in near perfect icosahedra particles, euhedral (trigonal) grains (up to 40 µm), and multiply-twinned particles (MPTs) [(11)(15)(17)]. These results were unexpected because the X-ray powder diffraction pattern remained fully consistent with the $R\bar{3}m$ space group, which does not allow the presence of five-fold symmetry [(12)(15)(51)]. The presence of re-entrant faces on some particles allowed the identification of these icosahedra as multiply-twinned particles rather than quasi-crystalline materials. Figure 2.5 shows morphology of B_6O MTPs. Icosahedral MTPs of B_6O serve as the nucleus for the icosahedral packing of B_{12} units. Growth occurs by addition of successive layers of B_{12} icosahedra to each triangular face. The icosahedral morphology of the grains makes them potentially useful for high-wear-resistance applications. Other morphologies that have been reported include intergrown subhedral to anhedral icosahedral grains, and rounded anhedral sintered masses [(11)(17)].

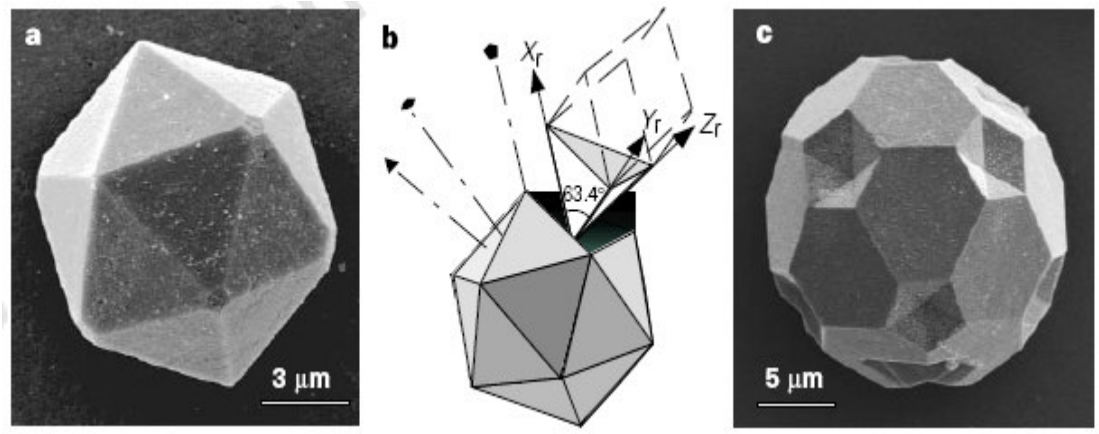

Figure 2.5: Morphology of B_6O MTPs. (a) SEM image of an isolated icosahedron. (b) Descriptive model of a regular icosahedron consisting of 20 tetrahedral individuals, illustrating the relationship between a tetrahedral individual and a rhombohedral cell. (c) SEM image of B_6O MTPs with well developed faces forming re-entrant angles at the apices, indicative of twinning [(15)(17)].

2.5 Sintering of boron suboxide (B_6O) materials

Boron suboxide (B_6O) is typically unsinterable under ambient pressure conditions. Fully densified compacts of B_6O are difficult to achieve even by pressure sintering techniques such as hot pressing or hot isostatic pressing [(19)]. No appropriate sintering aid has been found because B_6O is easily oxidized to form B_2O_3 causing degradation of the mechanical strength of the resultant sintered compact [(7)]. Sintering of boron suboxides, like other sintering processes, is believed to occur in stages. The sintering mechanism of boron suboxide in the B-B_2O_3 system is summarised in section 2.5.1. Additionally, work carried out on B_6O powder sintered via low-pressure high-temperature (LPHT) and high-pressure high-temperature (HPHT) conditions and their properties are summarised in sections 2.5.2 and 2.5.3, respectively.

2.5.1 Sintering mechanism

The sintering mechanism of boron suboxide at low-pressure (20 to 29 MPa) and high-temperature (up to 2000°C) has been studied by Brodhag and Thévenot [(19)]. 'Sound' pellets were reaction hot pressed from a mixture of boron and boron anhydride.

Additionally, $B_{12}O_2$ powder was prepared by boron reduction of zinc oxide. Boron nitride lining was used to avoid carbon diffusion in the sample during hot pressing in graphite dies. No densification effect was observed for $B_{12}O_2$ powder below the sintering temperature of 1600°C. Nevertheless, three important densification stages for reactive hot pressing were observed (figure 2.6).

The first stage at about 290°C is believed to be due to the fusion of B_2O_3 and the resulting liquid penetrating between the solid particles. The reaction at about 1200°C leads to further densification, and proper sintering starts at 1800°C [(19)]. The absolute and relative volume compositions showed that a higher pressure provides better penetration by the liquid phase and therefore a better reaction. From figure 2.6a, the highest pressure (29 MPa) resulted in a highest final density. Table 2.5 shows the absolute densities of the hot pressed materials. Figure 2.6b gives details of the densification kinetics during the reaction which seems to have three steps in the range 1000 - 1400°C. From their investigations, it was concluded that the boron suboxide powder sinters better than the reactive one (about 200°C lower). The reason was attributed to traces of zinc remaining in the powder as well as other microstructure-related reasons. For the reactive hot pressing experiments, the de-agglomeration (* on figure 2.6) leads to a lower green density, but the sintering rate is higher and the sintering temperature is lower. Homogeneity of the mixture improves the reaction and causes the disappearance of large pores due to initial B_2O_3 agglomerates [(19)].

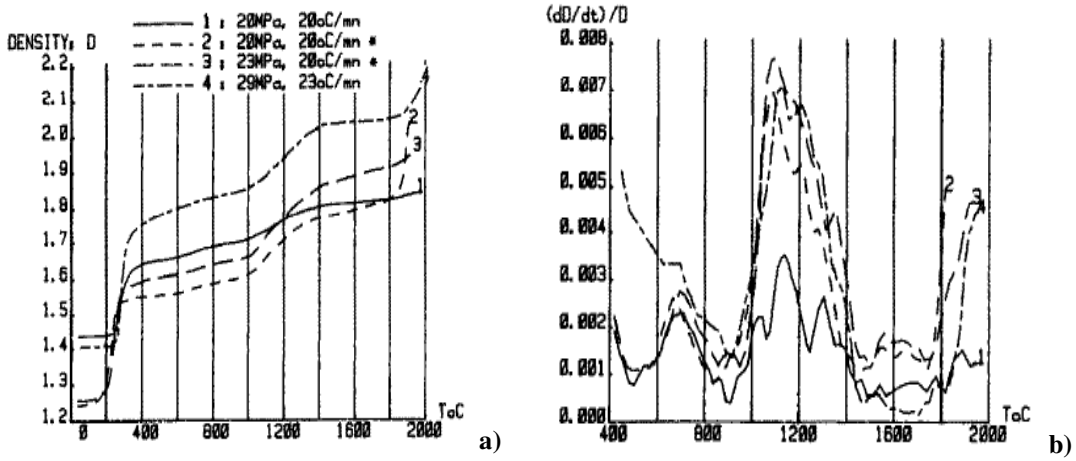

Figure 2.6: Densification during reactive hot pressing: a) absolute density; b) densification rate (* for screened reactive mixtures) [19].

Table 2.5: Absolute densities of hot pressed materials at maximum sintering temperature [19].

Material	Pressure (MPa)	Absolute density
1	20	1.85
2	20	2.05
3	23	1.95
4	29	2.2

2.5.2 Low-pressure high-temperature sintering conditions and properties of resulting ceramic materials

Holcombe and Horne [48] produced boron suboxide (B_7O) by blending zinc oxide powder with boron powder. The blended powders were isostatically pressed at about 140 MPa into pellets and heated in the presence of inert atmosphere to a temperature in the range of 1200-1500^oC to effect the reduction of zinc oxide by the boron. This material was characterised as having an average Vickers hardness value of 38.2 GPa at 100g load (fracture toughness note reported). A density of 2.80 g/cm^3 was measured for this material. Surprisingly, the measured density is higher than the theoretical density of B_6O (2.59 g/cm^3). This is an indication that the zinc oxide did

not react completely with the boron powder and therefore the B_6O powder produced was containing zinc impurities. Since the density of zinc (7.1 g/cm^3) is higher than the theoretical density of B_6O, the density of the resulting sintered compact would be higher than that of B_6O. This material is described as highly refractory, resistant to oxidation and acids and suitable for use on surfaces subject to abrasion, e.g., grinding wheels, drill bits, machine tools and in structures employed in high temperature applications.

Goosey and Anderson **(52)** fabricated boron suboxide by hot pressing at about 2000^{o}C under a pressure of about 40 MPa. The boron suboxide was compacted from a mixture of boron and boron oxide in a metal die lined with graphite and tantalum. The compacted article was coated with a mixture of boron nitride and boric oxide and was subjected to a second pressing step while heating at a temperature sufficient to melt the boron oxide in the compacted mixture. After allowing the metal die to cool, the compacted article was removed and placed in a graphite die also coated with boron nitride and lined with tantalum and then hot pressed. The resulting material was reported as being 'sound' boron suboxide article, free of contaminants. The product possesses outstanding physical properties (Knoop hardness of 30 GPa at 100g load and modulus of elasticity of about 480 GPa) that render it suitable for a variety of applications such as cutting tools, ceramic bearings, and grinding media. The measured density of the material was 2.60 g/cm^3. The fracture toughness for this material was not reported.

Petrak *et al*. **(38)** produced B_6O by reaction hot pressing from a mechanically mixed boron and B_2O_3 (the actual pressing temperature and pressure was not reported). Phases observed in the hot pressed samples were boron suboxide and boron. Nevertheless, a slight amount of B_2O_3 was also observed in some of the samples. Measured densities were more that 99% of theoretical density. The linear expansion coefficient for this material increased with increasing temperature and has an average value of 5.69 x 10^{-6}/^{o}C for the temperature range of 20-900^{o}C, which is greater than

that of B_4C. Knoop hardness of B_6O measured at load of 100g was 30.4 GPa, similar to B_4C (30.2 GPa) prepared and measured under the same conditions. The zero porosity Young's modulus value was about 470 GPa with Poisson's ratio of 0.155 and flexural strength of about 350 MPa with an average grain size of 2 µm.

Bairamashvili *et al*. [53] fabricated boron suboxide (B_6O) by a hot pressing technique in a compaction press and in vacuum at high temperature (exact temperature and pressure not reported). The physicomechanical properties of this material were measured and compared with those of SiB_4 and B_4C which belong to the same family and prepared in the same way as the B_6O. The resulting materials had more than 90% of the theoretical densities and the compositions were approximately stoichiometric. Summary of the measured properties are given in table 2.6. The compression strength measured for B_6O varies from 63 GPa at 20°C to 39 GPa at 1000°C. The microhardness values for B_4C and B_6O were nearly identical and SiB_4 were slightly lower (fracture toughness not reported). The elastic moduli of B_4C, B_6O and SiB_4 were measured in air at room temperature by the dynamic specimen – bending method.

Table 2.6: Physicomechanical properties of B_6O, B_4C and SiB_4 [53].

Sample	Density (g/cm^3)	σ_{comp} (GPa) at RT	Hardness (GPa)	Young's modulus (GPa)	Linear thermal expansion coefficient ($\times 10^{-6} K^{-1}$) [RT-1000 °C]	Thermal conductivity at 100°C, W/mK
B_6O	2.4	63	32	440	5.5	10.2
B_4C	2.4	79	35	480	4.5	14.7
SiB_4	2.35	50.2	27	280	6.0	5.9

Brodhag and Thévenot [19] produced boron suboxide ($B_{12}O_2$) by hot pressing 'sound' pellets either by starting from a mixture of boron and boron anhydride for reactive sintering, or $B_{12}O_2$ powder prepared by the boron reduction of zinc oxide and leached in acid for reducing zinc content. Boron nitride lining was used to prevent carbon

diffusion in the sample during hot pressing in graphite dies. Hot pressing was carried out at temperatures up to 2000°C and pressures between 20 and 29 MPa. The sintering mechanism was explained and discussed in section 2.5.1. The resulting materials were porous and therefore the properties were not reported (see table 2.4).

Badzian [18] produced boron suboxide via high temperature (about 2000°C) sintering under pressures from 100 to 1000 MPa from boron and B_2O_3. The sintered bodies were melted in induction furnace in an argon atmosphere and properties measured. The melted material was found to be black in colour. Chemical analysis was done on the powder and $B_{22}O$ composition was assumed. The melted material has a microhardness measured by Hanemann indentation (80g load) of 60 GPa. This material shows polycrystalline morphology, easily wear a diamond tip parallel to the (001) plane, or scratches a (111) diamond face in any direction.

In 1991, Srikanth *et al.* [31] attempted to determine the nature of the B_xO phases that occurred in the field defined by pressure of 0 to 1.5 GPa, temperature between 1200-1700°C, and the compositional range $2/3 \leq x \leq 24$. Amorphous boron powder and boric acid were the starting reactants. After processing at elevated temperature and pressure, for compositions over the range $2/3 \leq x \leq 6$, B_2O_3 (identical to the hexagonal starting material) and B_6O ($R\bar{3}m$) were the dominant phases present. For the compositions $6 \leq x \leq 24$, B_6O and rhombohedral B were the primary phases identified. Densities obtained ranged from 2.20 to 2.46 g/cm^3. The hardness values obtained were dominated by the occurrence of B_6O. However, there were some suggestions of high values of hardness on a localised scale in specimens near $B_{22}O$ composition. Fragments of processed specimen containing B_6O were observed to scratch Al_2O_3 (easily) and SiC.

Ellison-Hayashi *et al.* [2][20][54][55] produced boron suboxide (B_6O) by hot pressing a stoichiometric mixture of elemental boron and boron oxide powders at temperatures in the range of about 1800-2200°C and at pressure of about 14-40 MPa for a period of

about 5 minutes to 3 hours while encapsulated by hBN. An average Knoop hardness (100g load) of about 38 GPa was reported and for some material about 42 GPa. They claimed that the powder can be crashed into granules and used as abrasive grit, or grit bonded to tools which require highly abrasive surfaces. The high hardness was attributed to the presence of Mg in boron starting powder which aid in densification. The fracture toughness was not reported.

Kayhan and Inal **(5)** fabricated B_6O compact from B_6O powder produced by reacting boron and zinc oxide. Hot pressing was carried out at 1600^oC in vacuum under pressure of 40 MPa for 2 and 4 hours, respectively. An inductively heated graphite die was used. An intermediate barrier layer of boron nitride was used between the green sample and the graphite die and rams to prevent carbon diffusion from the die to the sample. During pressing, the pressure was maintained at 10 MPa up to the sintering temperature and then was increased to 40 MPa. The densities measured were 2.15 and 2.18 g/cm^3, respectively. The samples were then given a high temperature treatment at 1800^oC under vacuum with no pressure applied for full densification (densities measured were 2.31 and 2.39 g/cm^3, respectively). The Vickers microhardness (100g load), fracture toughness and flexural strength values measured for these materials are summarised in table 2.7. The fracture toughness was calculated from three-point bend testing with notch radius of 0.4 mm.

From table 2.7 the properties measured for pure B_6O materials are very surprising and unexpected since the fracture toughness was already high (6.23 MPam$^{1/2}$) for the pure hot pressed material even before infiltrating with aluminium. This is contradictory to what have been reported in literature up to date, that pure B_6O sintered compacts have low fracture toughness values (brittle). Using the fracture toughness (K_{IC}) and reported strength values (σ), the defect size (a) can be estimated as **(56)**:

$$a = Y\left[K_{IC} / \sigma\right]^2 \qquad \textbf{[2.3]}$$

where Y ≈ 1. This gives a very large defects (≈ 0.8 cm) questioning the validity of the data.

Table 2.7: Summary of properties of B_6O hot pressed at 1600°C in vacuum under 40 MPa [5].

Material	Density (g/cm^3)	Hardness (GPa)	Fracture toughness ($MPam^{1/2}$)	Flexural strength (MPa)	Phases
2h hot pressed	2.15	35	5.35	57.18	B_6O, B, B_2O_3
4h hot pressed	2.18	35	5.52	59.07	B_6O, B, B_2O_3
2h hot pressed & heat-treated	2.31	36	5.84	62.43	B_6O, B
4h hot pressed & heat-treated	2.39	37	6.23	66.70	B_6O, B
4h hot pressed, heat-treated & infiltrated	2.53	40	8.12	86.88	B_6O, Al_2O_3, $Al_{1.67}B_{22}$

2.5.3 High-pressure high-temperature conditions and properties of resulting ceramic materials

Itoh *et al*. [3] produced B_6O compact via high-pressure (3-6 GPa) high-temperature (1400-1800°C) techniques from powdered B_6O synthesised from amorphous boron and boron oxide (B_2O_3) for 10 to 20 minutes in inert atmosphere. The specimen chamber was surrounded by an hBN capsule and a graphite heater was used for heating purposes. A single phase sintered compact having Vickers microhardness (200g load) of between 31 and 33 GPa under pressures of 3-5 GPa and 1700°C for 20 minutes can be produced. It was found that the B_6O sintered compact was of intragranular fracture type while the toughness was low. The B_6O sintered compact had superior oxidation resistance in air at high temperatures (up to 1000°C) in comparison with a B_4C sintered compact prepared in the same conditions (5 GPa, 1700°C and 20 minutes). The B_2O_3 layer formed during oxidation functioned as a protective layer and does oxidise mildly until about 1000°C.

The synthesis of B_6O single crystals at high pressure and high temperature was discussed in section 2.4. However, properties of these materials were not mentioned. He *et al*. [9][11] produced B_6O single crystals at high pressure (~ 5.5 GPa) and high temperature (2100^oC) for 60 minutes with grain sizes over 100 µm. This made it possible to measure the Vickers hardness on separate single crystals. The Vickers hardness was measured using a pyramidal diamond indentation method, after the samples had been polished using diamond abrasive disks and slurries. The average Vickers hardness was 45 GPa under a load of 0.98N [9]. The corresponding fracture toughness, measured using Anstis' equation, was 4.5 $MPam^{1/2}$.

2.6 Boron suboxide composites

B_6O sintered compacts have been discussed in section 2.5. Fracture toughness of a single crystal B_6O is 4.5 $MPam^{1/2}$ with a corresponding Vickers hardness of 45 GPa. The Vickers microhardness values obtained for polycrystalline B_6O range from ~31 to ~38 GPa [2][4]. However, fracture toughness for polycrystalline B_6O is less than 1.5 $MPam^{1/2}$ which limits industrial applications. The cause for the low fracture toughness obtained in the sintered compacts is not understood. Efforts have been made to increase the fracture toughness by forming B_6O composites with other ultrahard materials such as diamond, boron carbide (B_4C), and cubic boron nitride (cBN). B_6O composites have also been produced with aluminium and carbon additions. Summary of these investigations is given below.

In 1999, Kayhan and Inal [5] densified B_6O sintered samples which have been infiltrated with aluminium (99.99% purity) at temperatures between 1100-1250^oC to improve their mechanical properties. In filtrations were carried out in a tube furnace in pure argon atmosphere with no external pressure applied. A temperature of 1200^oC was found to be the optimum infiltration temperature. Table 2.7 summarises the properties of this material. Measured density was 2.53 g/cm^3. A Vickers microhardness of 40 GPa (100g load) with a corresponding fracture toughness of 8.1

$MPam^{1/2}$ was obtained. The fracture toughness was calculated from three-point bend testing. This fracture toughness is the highest reported for B_6O composite materials. However, even before infiltrating this material with aluminium, the 'pure' B_6O sintered compact was having a fracture toughness of 6.23 $MPam^{1/2}$ (see table 2.7) which is quite surprising. In sections 2.5.2 and 2.5.3 the properties of 'pure' B_6O sintered compacts were discussed and it was shown that 'pure' B_6O compacts are brittle or have low fracture toughness values.

Itoh *et al*. [(4)] produced B_6O composites in the B_6O-xB_4C (x = 0-40 vol. %) system under high pressure high temperature conditions (3-5 GPa, 1500-1800^oC) from the mixture of in-laboratory synthesised B_6O powder and commercially available B_4C powder. Relationship among the formed phases, microstructures and mechanical properties of the sintered composites was investigated as a function of sintering conditions and added B_4C content. It was found that neither solid solutions nor new compound was formed under the sintering conditions and that the sintered composite consists of the mixed phases of B_6O and B_4C. Under these sintered conditions, strong interparticle bonding between B_6O and B_4C increased the hardness and toughness of the sintered composites. A maximum microhardness of ~46 GPa (200g load) was reported from B_6O-30 vol. % B_4C powder under sintering conditions of 4 GPa, 1700^oC and 20 minutes. Fracture toughness was less than 1 $MPam^{1/2}$.

Itoh *et al*. [(14)] later investigated high-pressure sintering behaviour in the B_6O-cBN system using in-laboratory synthesised B_6O and commercially available cBN powders. The phase relation, microstructure and mechanical properties of the composites were examined by varying the added cBN amount and its average grain size as well as the sintering conditions. No reaction occurred between the two components under high pressure (4-6 GPa) and high temperature (1500-1800^oC) conditions. Well dispersed B_6O-x(cBN) sintered composites of almost full density were prepared in the range of x = 0-50 vol.% by sintering at 6 GPa and 1800^oC for 20 minutes. A maximum Vickers microhardness of 46 GPa (200g load) was attained by

adding 40 vol. % cBN with an average grain size of 0.5 μm. A maximum fracture toughness of about 1.8 $MPam^{1/2}$ (using Niihara's equation) was obtained at 60 vol. % cBN addition. It is believed that crack deflections along the B_6O-cBN grain boundary contributed to the increase in fracture toughness.

Sasai *et al*. [7] prepared sintered composites in the B_6O-*x*diamond (*x* = 0-80 vol.%) system under high pressure and high temperature conditions (3-5 GPa, 1400-1800°C) from a mixture of in-laboratory synthesised B_6O powder and commercially available diamond powder with various grain sizes for 20 minutes. The phases formed, microstructures and mechanical properties of the sintered composites were investigated on varying the added diamond content and sintering conditions. It was concluded that neither solid solution nor new chemical compounds were formed under the sintering conditions. Sintered composites of full density consisted of mixed phases of B_6O and diamond. A maximum microhardness of 57 GPa (200g load) was measured in the B_6O-60 vol. % diamond (grain size < 0.25 μm) sintered composite under the sintering conditions of 5 GPa, 1700°C and 20 minutes. The fracture toughness, however, was less than 1 $MPam^{1/2}$ (measured using Niihara's equation).

Recently, Shabalala [16] produced B_6O composites using Al-B-O and C containing compounds at low-pressure high-temperature (hot pressing) conditions (1600-1900°C, 50 MPa, 20 minutes). The composite powders were prepared by mixing in-laboratory synthesised B_6O powder with commercially available Al_2O_3, and by coating it with Al_2O_3 using a Chemical Vapour Deposition (CVD) process. Relationship among the formed phases, microstructures, and mechanical properties of the sintered composites were investigated. Measured densities were higher than 97% theoretical density. Al_2O_3 addition via mixing and CVD produced B_6O composites with better mechanical properties, especially fracture toughness. Increasing the amount of Al (or Al_2O_3) slightly reduces the hardness but significantly increases the fracture toughness of the B_6O composites. The sample with the lowest amount of Al (2.2 wt% Al) had Vickers hardness of 31.1 GPa (500g load) and fracture toughness of

3.1 $MPam^{1/2}$. The increase in fracture toughness was attributed to the formation of alumina borate, $Al_{18}B_4O_{33}$, as a secondary phase at grain boundary interfaces. In addition, the residual stresses produced by the mismatch in thermal expansion coefficients between B_6O and $Al_{18}B_4O_{33}$ improved the fracture toughness. Composites produced from the addition of C had decreased Vickers hardness in the range of 22.8 - 25.9 GPa (500g load) but increased fracture toughness in the range of 5.25 - 5.48 $MPam^{1/2}$. The increase in fracture toughness was attributed to the formation of B_4C phase as well as some traces of $Al_{18}B_4O_{33}$ from the starting B_6O powders. Summary of B_6O composite materials are given in table 2.8

In conclusion, a careful selection of additives and/or binders in combination with controlled sintering conditions could result in a production of B_6O composites having a unique combination of mechanical properties for industrial applications.

Table 2.8: Summary of the mechanical properties of B_6O composite materials.

Composite materials	Microhardness, (GPa) 100g load	Fracture toughness, K_{IC} ($MPam^{1/2}$)	Elastic modulus (GPa)	Reference
B_6O crystal	45	4.5	-	(9)
B_6O sintered compact	31-38	<1.5	470	(2)(38)
B_6O-30 vol.%B_4C	~46 (200g load)	Very low	-	(4)
B_6O-40 vol.% cBN	~46 (200g load)	<1.8	-	(14)
B_6O-60 vol.% diamond	~57 (200g load)	<1	-	(7)
B_6O infiltrated with Al	41	8.7	-	(5)
B_6O coated with Al_2O_3 (Al = 2.2wt %)	31.1 (500g load)	3.1	514	(16)
B_6O-10 wt% C	22.8 (500g load)	5.5	-	(16)

2.7 Potential industrial applications of boron suboxide-based materials

Diamond, cBN and their sintered composites are widely used as superhard materials in industry for drilling, cutting, milling, and grinding. However, diamond has a major drawback in that it reacts with iron and cannot be used for machining ferrous alloys at high temperatures due to the onset of its transformation to the graphite structure [(1)]. This prompted the synthesis of a second superhard material (cBN); its structure derived from that of diamond. cBN is half as hard as diamond, but does not react as strongly with iron and can be used for machining ferrous alloys. However, as temperature increase cBN weakens due to diffusion wear. Additionally the synthesis is more difficult.

Boron suboxide-based materials produced and discussed in this chapter possess good physical and mechanical properties comparable to diamond and cBN. B_6O has similar thermostability as cBN [(9)]. The oxidation resistance of single phase B_6O and B_4C sintered compact has been compared and found that the oxidation resistance of B_6O in air at high temperatures is far superior to that of B_4C and comparable to cBN which have similar crystal structure and hardness to B_6O [(3)(9)]. The product of the oxidation (B_2O_3) during the initial stages serves as a protective layer and thus oxidises mildly until about 1000^{o}C. For these reasons, B_6O has an advantage over the use of diamond in certain applications. Boron suboxide therefore becomes a potentially good candidate for cutting tools and other industrial applications where abrasive wear resistance is essential [(2)(5)(48)(54)(55)(57)]. The strong covalent bonds and short interatomic bond length contribute to the exceptional physical and chemical properties such as great hardness, low mass density, high thermal conductivity, high chemical inertness and excellent wear resistance [(3)(6)(9)(13)(10)(17)]. B_6O also has potential applications as semiconductors due to estimated band gap of 2 eV based on photoluminescence, theoretical calculations and consistency with red-orange colour [(58)(59)]. Nevertheless, commercial applications have not yet been realised due to its low fracture toughness.

2.8 Improving fracture toughness of boron suboxide via sintering additives

One feature of microstructure that has greatest influence on the mechanical properties of materials, especially fracture toughness, is the composition of the grain boundary phase. The other feature is the grain sizes of the phases in the sintered material. This is discussed in section 2.9.

In ceramic materials, stress applied to a material does not result in limited plastic deformation and therefore stress relaxation does not occur by this mechanism. Instead, the stresses become concentrated at flaws/cracks in the material. The critical stress intensity factor (K_{IC}) for a material is defined to be the stress intensity at a crack tip in the material required to cause further propagation of the crack. Fracture toughness therefore may be defined to be the resistance to fracture of a ceramic material.

In some of the B_6O sintered composites investigated and discussed in section 2.6, the sintering additives acted as liquid phase at sintering temperature which could have an added advantage of lowering the sintering temperature [(5)(16)]. Furthermore, production cost could be reduced and lower densification temperature also means a lower rate of grain growth and hence finer microstructure could be obtained. Additionally, finer grain sizes result in a material with higher hardness, strength and wear resistance.

The presence of secondary phases in the sintered compacts allows the activation of toughening mechanisms such as crack bridging and crack deflection. This is believed to occur because of mismatch in thermal expansion between the secondary phase and the B_6O phases, which places the grain boundary under residual stress [(16)(60)]. Interfacial debonding at the interface between the grain and grain boundary is a second mechanism for promoting intergranular fracture by weakening the grain boundary [(61)(62)]. Both phenomena produce a path along the grain boundaries for the crack to propagate along. The resultant intergranular crack path results in more energy being expended than would be if the crack path were transgranular, since the

intergranular path is effectively longer than the transgranular path. Some of the individual toughening mechanisms in ceramic materials are highlighted below. However, more than one type of toughening mechanism can be active in the fracture of a particular specimen.

2.8.1 Toughening by crack deflection

Crack deflection can take place when there are local areas in a ceramic that have lower resistance to crack propagation than an average plane cutting through at right angles to the tensile stress. Additionally, crack deflection can occur in a bimodal microstructure containing weaker secondary phases at the grain boundaries, which typically require about half the fracture surface energy of a single crystal [(56)]. A crack advancing through a polycrystalline ceramic thus attempts to follow a path along the grain boundaries. This leads to staggered crack paths which subsequently lead to greater energy loss per unit length of a straight line running perpendicular to the applied stress. Thus, the energy required to propagate a crack over a given range will be much higher and therefore the material is said to be tough. Crack deflection can also cause partial bridging by grains or second-phase particles. Cracks deflected or pinned are caused by stress fields associated with thermal expansion mismatch between the second-phase particles and the matrix or by existence of weakened interfaces [(63)(64)]. The sign of the residual stress determines the direction of deflection. Specifically, a secondary phase particle that is embedded in a matrix with a lower thermal expansion coefficient than the matrix will lead to the generation of tangential tensile stress after cooling the material from the processing temperature causing the crack to deflect toward the particle. Alternatively, a second phase with a greater thermal expansion coefficient than the matrix induces a tangential compressive stress near the particle/matrix interface and diverts the crack around the particle [(63)(65)]. These stresses are caused by the greater degree of thermal contraction/expansion of the particle with respect to the thermal expansion/contraction of the matrix. However, toughness measurements suggest that the sign and magnitude of the residual stress have no significant influence on the magnitude of crack interaction toughening [(66)].

The generation of tangential tensile/compressive stresses in the matrix is accompanied by the generation of radial compressive/tensile stresses in the matrix.

When a crack approaches, or intercepts a second phase particle, it will characteristically tilt (deflect) at an angle, θ, out of its original plane as shown schematically in figure 2.7a. The initial tilt angle depends upon the orientation and position of the particle with respect to the advancing crack and the sign of the residual stress developed between the particle and the matrix. Subsequent advance of the crack may result in crack front twist (Figure 2.7b), if for instance the orientations of adjacent particles require the crack to tilt in opposite directions. The increase in fracture toughness imparted by deflection of the crack is evaluated from the local stress intensities at the tilted and twisted portions of the crack front. Faber and Evans [(63)] found out that an increase in toughness by crack deflection only depends on particle shape and volume fraction of the secondary phase but not particle size. The most effective morphology for deflecting propagating cracks is the rod of high aspect ratio which can account for four fold increases in fracture toughness followed by disk and sphere. Toughness increases with increasing volume fraction of deflecting particles up to about 20 vol. % and increases very little with further increase in volume fraction. Crack deflection appears to be the dominant toughening mechanism in platelet-reinforced alumina [(56)].

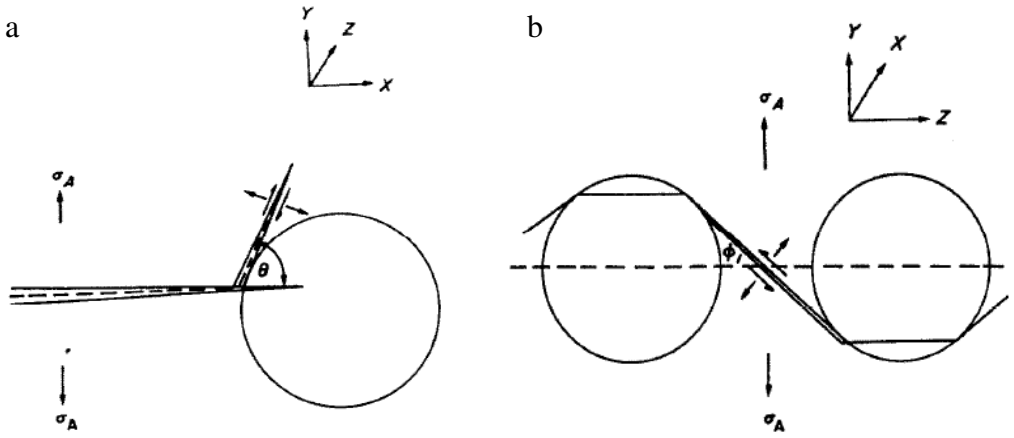

Figure 2.7: Schematic diagrams of typical crack deflection. a) Tilt and b) twist of the crack front [(63)].

2.8.2 Toughening by crack bowing

Crack bowing is the development of a nonlinear crack front for a planar crack. This phenomenon is different from crack deflection, which is the development of out-of-plane portions of the crack [(56)]. Crack bowing originates from resistant second phase particles in the path of propagating crack. This toughening mechanism could be described as a crack advancing in a plane, but pinned by barriers with an average spacing of d and bowing out between the pinning points under the action of a stress. Crack bowing and crack deflection processes (both of which are insensitive to particle size) occur simultaneously [(63)].

2.8.3 Toughening by crack bridging

Crack bridging is a toughening mechanism which develops behind an advancing crack. Crack bridging is the process of physical contact formation between the mating crack surfaces, through fibres, whiskers, platelets, inclusions and surface asperities, which interlock the mating crack surfaces [(67)]. Crack bridging enhances crack energy dissipation due to the presence of ligamentary bridges that span from one crack face to the other. On one hand, the dissipation of energy could be due to the frictional

sliding of the ligaments against the matrix material which generates heat. On the other hand, energy dissipation can occur when the ligamentary grain material has different elastic and yield strength properties to the surrounding matrix [(56)]. Contributions to the toughness caused by reinforcing elements that bridge between crack surfaces are separated into two parts: ductile and brittle. The former refers to metal-toughened ceramics (cermets) and relies on high toughness and ductility to permit metal ligaments to exist and to contribute to toughness through plastic dissipation. When the bridging material is brittle such that its toughness is similar to that of the matrix, the occurrence of bridging is more subtle and requires either microstructural residual stresses or weak interfaces or both [(68)].

2.8.4 Transformation toughening

The stress-induced transformations that can cause significant toughening include martensitic and ferroelastic transformation as well as twinning. This type of toughening mechanism is mostly seen in ceramics containing zirconia in metastable form. It is found that the stresses around a crack tip cause transformation of a volume fraction of tetragonal zirconia particles to monoclinic form out to a distance from the crack tip dependent on the applied stress and a critical value required for the transformation [(56)].

2.8.5 Toughening by microcrack

Microcracks occur within regions of local residual stress caused by thermal expansion mismatch and/or transformation. In case of residual tensile stress, microcracks occur either within the second phase particle or at the interface, whereas microcracks develop within the matrix in case of residual compressive stress in the particle. The microcracks also occur along the lowest fracture energy paths and locally relieve the residual tension. Consequently, a dilatation occurs governed by the volume displaced by the microcrack. A microcrack also reduces the elastic modulus of the microcrack process zone. When the microcracks are activated by the passage of macrocrack,

change in toughness occurs. These microcracks can act as crack arrestors or change the direction of a straight advancing crack [(68)(69)]. However, this contribution is partially counteracted by a degradation of the material ahead of the microcrack. The basic material quantities that allow microcracking (residual stress and low fracture energy interfaces) also lead to grain bridging.

2.9 Improving mechanical properties by reducing grain sizes in sintered materials

One other feature of microstructure which has the greatest influence on the mechanical properties of materials is the grain sizes of the phases in the sintered material. For tooling systems, the most promising way to develop new tool materials with improved properties is to reduce the grain size in the sintered microstructures to nanoscale [(8)(70-72)]. Advantages of reducing the grain size include reduction in sintering temperatures, improved properties (e.g. hardness, wear resistance and strength), and new possibility of designing new structures or composite materials. The unique properties of these materials are derived from their large number of grain boundaries compared to coarse-grained polycrystalline counterparts [(73-75)]. The decrease in grain size strengthens metals as well as ceramics according to Hall-Petch law [(8)(75)]. The relationship is described mathematically by Hall-Petch equation which is

$$\sigma_y = \sigma_o + k_y/\sqrt{d} \qquad [\mathbf{2.4}]$$

where k_y is a material constant, σ_o is a material constant for the starting stress for dislocation movement, d is the mean grain size and σ_y is the yield stress. However, the strength tends to tend to increase with decreasing grain size down to a critical value (20 nm). When the grain size is below 20 nm, strength appears to decrease with further grain refinement [(75)].

Different processing routes have been used to reduce powder sizes. These includes a wide range of vapour (physical and chemical vapour deposition), liquid (sol-gel and wet chemical), and solid state (mechanical milling and mechanochemical synthesis) processing routes [(74)(75)]. However, mechanical milling and spray conversion are commonly used to produce large quantities of nanopowders [(75)]. Depending on the process route taken, different internal structures are produced that affect the properties of the sintered compact. In this thesis, mechanical milling has been chosen for the production of B_6O submicron particles.

The comminution process of milling is widely used in ceramic processing to reduce the average particle size of a material, liberate impurities and reduce porosities of particles, modify the particle size distribution, disperse agglomerates and aggregates, reduce the maximum particle size, increase the content of colloids, and to modify the shape of particles [(76)]. Common mills used for grinding ceramics materials are ball mills, vibratory mills, attrition mills, fluid energy mills and roller mills. In high attrition mill, which has been used for milling experiments in this project, small grinding media and granular material are intensely agitated. Contamination due to wear of the mill lining and media is considerable and is commonly eliminated by chemical leaching, sedimentation, or magnetic separation. Attrition grinding is used for producing submicron powders of hard refractory oxides, carbides, nitrides, titania pigments, and paper-grade kaolin.

2.10 Motivation for the research objectives and structure of the experimental work

The objective of this research was to improve the overall mechanical properties, especially fracture toughness, of boron suboxide-based composites available up to date for industrial applications using hot pressing (HP) technique.

2.10.1 Motivation for the research objectives

As mentioned earlier in this chapter, the hardness of a single crystal boron suboxide (B_6O) is 45 GPa which is comparable to that of cBN (45-50 GPa) [(9)]. Additionally, the fracture toughness of B_6O single crystal was found to be 4.5 $MPam^{1/2}$, which is higher than that of cBN (2.8 $MPam^{1/2}$), and also approaches that of single crystal diamond (5 $MPam^{1/2}$). It has also been shown that boron suboxide has a better thermal stability compared to diamond and can be produced without the need for high pressures. Boron suboxide therefore becomes a potentially good candidate for cutting tools and other industrial applications where abrasive wear resistance is essential.

In spite of the high fracture toughness (4.5 $MPam^{1/2}$) for a single crystal B_6O, the fracture toughness for polycrystalline B_6O is less than 1.5 $MPam^{1/2}$ which limits industrial applications. The Vickers microhardness values obtained for polycrystalline B_6O through high-pressure high-temperature processes range from 31 to 38 GPa. The low fracture toughness obtained in the sintered compacts is not completely clear. Efforts have been made to increase the fracture toughness by forming B_6O composites with other ultrahard materials such as diamond, boron carbide (B_4C), and cBN [(4)(7)(14)]. High hardness values were recorded for the composites ($Hv_{0.2}$ ~ 46 GPa) but fracture toughness values did not exceed 1.8 $MPam^{1/2}$. Recently, Shabalala [(16)] produced B_6O composites with aluminium via hot pressing and obtained high fracture toughness (3.1 $MPam^{1/2}$) with respectable hardness ($Hv_{0.5}$ ~ 31.1 GPa). These results suggest that a careful selection of additives in combination with controlled sintering

conditions could result in a production of B_6O composites having a unique combination of mechanical properties suitable for industrial applications.

2.10.2 Structure of experimental work

Based on the results of Shabalala [16] it was proposed that boron suboxide can be liquid phase sintered using oxide sintering additives. In liquid phase sintering, the sintering additive either melts or reacts with another sintering additive or the major component to form a liquid, usually eutectic. This means that in the case of ceramic systems, in which the eutectic liquid phase formation governs the effectiveness of the densification, phase diagrams are important in choosing the sintering additives, their composition and the sintering conditions (especially temperature) [77]. In the light of this, an estimation of thermodynamic function of boron suboxide at high temperatures was developed. The developed data was entered into the FactSage™ 5.4.1 thermodynamic software and used for the calculations of phase equilibria in different B_6O-oxide/metal containing systems. The aim of these calculations was to determine possible candidates for the densification of boron suboxide materials. Details of the estimation and calculations can be found in Chapter 3.

The objective of this project was to improve the overall mechanical properties of B_6O composites and to investigate the relationship between the microstructure and the mechanical properties obtained via hot pressing. In achieving this objective, Chapter 4 dealt with the milling and sintering of boron suboxide composites. The milling of boron suboxide powders was to drive the particle sizes down to the submicron range. Y_2O_3, Al_2O_3, and SiO_2 were mainly used as the sintering additives. It was found that these oxides can form stable liquid and have quite high stability during sintering conditions. Additionally, Pd, TiB_2 and TiC were also used. Admixed powders were hot pressed at high temperatures ($\geq 1800^oC$) to obtained densed materials.

Characterisation of the hot pressed materials is dealt with in Chapter 5. The microstructure and phase composition of the hot pressed composites were characterised using scanning electron microscopy (SEM), transmission electron microscopy (TEM) and X-ray diffractometry (XRD). Densities of the samples were measured using Achemides principle to determine the extent of densification. Vickers hardness and indentation toughness were used to characterise the mechanical properties of the hot pressed materials. The cracks resulting from the indentation were studied using optical and scanning electron microscopes. In the discussion chapter (Chapter 6) relations between the powder, composition, densification and formed microstructures are explained. The conclusions made from this work and recommendations for future work are presented in Chapter 7.

3 Thermodynamic Properties of Boron Suboxide (B_6O)

3.1 Introduction

Boron suboxide-based compounds are normally densified at high temperatures ($\geq$1700^{o}C) and/or high pressures. B_6O materials produced thus far had shown good hardness values but their fracture toughness values were less than 2 MPam$^{1/2}$. Recently it was shown that the addition of Al or Al_2O_3 results in improved fracture toughness (3.1 MPam$^{1/2}$) with only minor reduction in hardness **(16)**. A detailed understanding of the processes which take place during hot pressing would be helpful in the search of new additives for B_6O materials. A possible way for predicting the phase formation is the use of thermodynamic calculations. However, current knowledge on the thermodynamic properties of boron suboxide (B_6O) is limited to temperatures up to 800K **(78-80)**. The Gibbs energy of B_6O as a function of temperature, composition and possibly pressure is the basis for such predictions. In this chapter the thermodynamic function of B_6O at high temperature has been estimated and used for the calculation of phase equilibria in different B_6O-oxide/metal containing systems.

3.2 Estimation of thermodynamic function of boron suboxide (B_6O)

All thermodynamic properties (volume, entropy, enthalpy, internal energy, heat capacity and chemical potential) are related to the Gibbs energy. However, it is useful to store and apply the data of a pure stoichiometric substance in the form of enthalpy of formation and entropy at standard conditions (T=298.15K and P=1bar) as well as temperature function of the heat capacity. The heat capacity is integrated over temperature to derive the temperature dependence of H and S as follows **(81)**:

$$H = H^{0} + \int_{298.15}^{T} C_p(T)dT \qquad [\mathbf{3.1}]$$

$$S = S^0 + \int_{298.15}^{T} C_p(T)/T dt \qquad [\mathbf{3.2}]$$

Thus knowing H, S, C_p, other thermodynamic data for B_6O could be calculated.

The entropy for B_6O was determined as $\Delta S_{298.15} = 39.91 J/mol/K$ [**3.3**]

and

$$\Delta H_f^{\theta}(B_6O, s, 298.15K) = -527 \pm 32 KJmol^{-1} \quad \textbf{(78)} \qquad [\mathbf{3.4}]$$

The temperature dependence heat capacity was established for the temperature range 298.15K – 800K as

$$C_p = 54.55936 + 17.263\times10^{-2}T - 28.2\times10^{5}T^{-2}(J/mol.K) \quad \textbf{(80)} \qquad [\mathbf{3.5}]$$

The enthalpy of formation quite agrees with other values for similar compounds such as B_6Si, B_6As, and B_6P as shown in figure 3.1 **(78)**. B_6Si has similar structure, composition and chemical bonding as B_6O and therefore would have similar entropy and C_p values. Thermodynamic data for B_6Si were taken from FactSage™ databank **(82)**. Since the Gibbs energy also depends upon $\Delta H_{298.15}, S_{298.15}, \text{and} C_p$, the C_p expression for B_6Si has been used to assist in correcting C_p expression at higher temperatures. The C_p mathematical model for B_6Si for temperature range 298.15K – 2000K is as follows:

$$\Delta C_p^{\theta}(B_6Si) = 141.691 + 0.038501T - 5879400T^{-2}(J/mol.K) \qquad [\mathbf{3.6}]$$

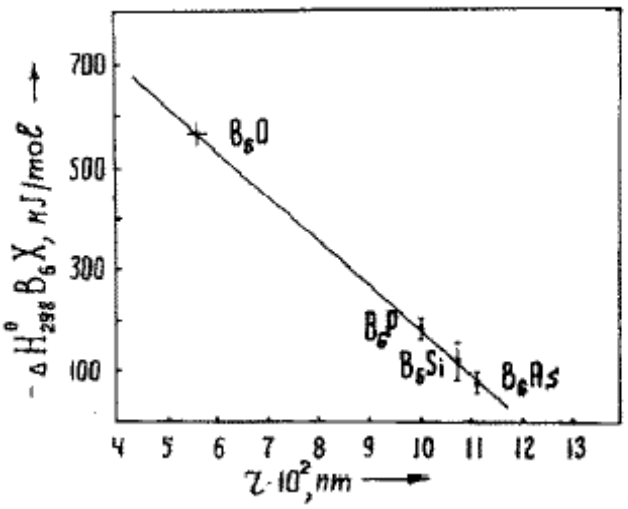

Figure 3.1: The dependence of standard enthalpy of B_6X compounds on the radius of the atom X introduced into the structure of α-rhombohedral boron [(78)].

From equations [**3.5**] and [**3.6**], a graph of C_p versus temperature was plotted (see figure 3.2). The extrapolation of the C_p values of B_6O to higher temperatures gives large differences between the two compounds. Usually the atomic heat capacities of all solid elements are in the range of 3R (= 24.9 J/K) where R is gas constant (rule of Dulong and Pettit). Additionally, the molar heat capacity of a solid chemical compound is approximately equal to the sum of the molar heat capacities of its constituent chemical elements [(81)]. While this is true for many elements around room temperature, (normally at 1- 2 times Θ/T; where Θ is Debye temperature which is materials dependent constant) the actual values approach 0 at 0 K and can exceed 3R at elevated temperatures if the elements melt or evaporate [(81)]. Using this rule the heat capacity of B_6Si can be estimated as 207.2 J/K compared to 217.223 J/K or 204.716 J/K found in literature [(82)] at 2000K. It follows that the maximum heat capacity of B_6O should be equal to the heat capacity of six boron atoms plus one oxygen atom. That is, it has to be in the same region as B_6Si. Therefore 213 J/K mol was chosen as

the value at 2000K and a linear C_p function, above the measured range (781 K), was introduced to correct the deviation between the heat capacities of B_6O and B_6Si in the temperature range of 800K to 2300K (see figure 3.2).

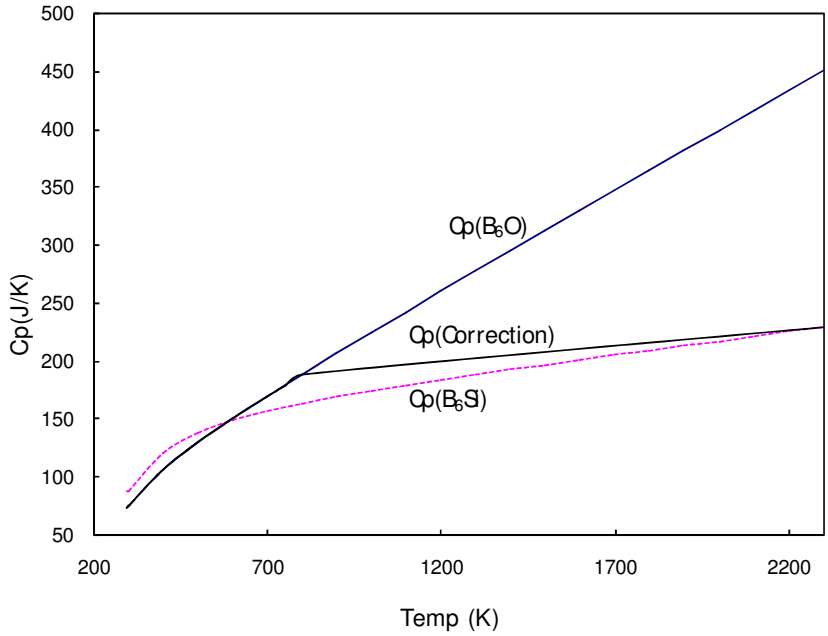

Figure 3.2: Graph of temperature versus heat capacity for B_6Si, B_6O (extrapolated experimental values) and B_6O after correction (the data of B_6Si taken from [82]). The data of B_6O were measured in the range 298.15K to 800K [80].

The used C_p function therefore was:

$$C_p = 54.55936 + 17.263\times10^{-2}T - 28.2\times10^{5}T^{-2}\text{ , J/mol.K} \qquad [\mathbf{3.7}]$$

for T < 800K [79] and

$$C_p = 0.023T + 166.54\text{ , J/mol.K (determined by approximation in this work)} \qquad [\mathbf{3.8}]$$

Therefore,

$$C_{p(correction)} = \int_{298.15}^{800} C_p dT + \int_{800}^{2300} C_p dT \qquad [\mathbf{3.9}]$$

$$C_{p(correction)} = (54.55936 + 17.263\times10^{-2}T - 28.2\times10^{5}T^{-2}) + (166.54 + 0.023T) \; [\mathbf{3.10}]$$

Using the C_p values of B_6Si instead of the approximated B_6O, the ΔG of B_6O would be somewhat lower. E.g. at 2000K it would be -920.48 kJ/mol in comparison to -914.391 kJ/mol for the used dataset. This difference corresponds to an error of less than 1%. This difference can be viewed as the uncertainty of the determined values, even for B_6Si. The data do not take into account the fact that B_6O is normally non-stoichiometric [6]. However, no data concerning the dependence of thermodynamic data on the oxygen content in B_6O are known. Therefore in all calculations we assume the ideal composition of B_6O.

The thermodynamic data ($\Delta H_{298.15}, S_{298.15}$ and $C_{p(correction)}$) obtained were used to calculate the needed phase equilibria using FactSage™ 5.4.1.

3.3 Phase equilibra calculations

Thermodynamic calculations at all times give results that help to offer means of systematising and modelling the behaviour of interacting phases, allowing the phase relations existing in multiphase systems to be described. A combined approach using thermodynamic calculations coupled with experimental measurement is frequently highly effective. In this section, thermodynamic calculations of the phase composition of $B_6O/C/B_4C$, $B_6O/Ti/TiC$, $B_6O/Al/Al_2O_3$ and $B_6O/Al_2O_3/Y_2O_3/SiO_2$ - composite materials have been described. The results have been used in explaining the sintering behaviour of B_6O composite materials.

The determination of the content of B_2O_3 on the surface of the B_6O powder is difficult, because oxygen analysis of the materials does not give conclusive results due to the non-stoichiometry of the B_6O. The washing of the powder in warm alcohol/water reduces but does not remove the B_2O_3 surface layer completely. The calculations were carried out between 1200 to 2000°C using the starting composition of the materials assuming 1 wt% B_2O_3 in the material. In some cases the amount of B_2O_3 was increased or decreased to test how stable the solutions are. Additionally, 0.1 wt% Argon was used except when the overall pressure was increased to 10 atmospheres to test the stability of the formed phases. The calculation was done by minimisation of the Gibbs Energy of the system using the EQUILIB module of the program FactSage 5.5.

3.3.1 B_6O-C-B_4C Systems

The thermodynamic calculations involving B_6O and C showed that at low temperatures (<1500°C), carbon is in equilibrium with B_6O and reacts with B_2O_3 forming B_6O:

$$9\ C(s) + 3\ B_2O_3(l) = B_6O(s) + 9\ CO(g) \qquad [\mathbf{3.11}]$$

This reaction strongly depends on the CO - partial pressure and therefore the stability of the liquid B_2O_3 during sintering strongly depends on transport of CO. Figure 3.3 shows the phase composition of the solid and gas phase for B_6O/C system. At 1544°C, the CO partial pressure reaches 1 atmosphere resulting in strong reduction of B_2O_3 in the system with a fixed pressure of 1 atm.

Carbon can react also with B_6O as follows:

$$2\ B_6O(s) + 5\ C(s) = 3\ B_4C(s) + 2\ CO(g) \qquad [\mathbf{3.12}]$$

The formed CO partial pressure is lower than the equilibrium pressure of reaction [**3.11**] (see figure 3.4a). Therefore the reaction takes place only after decomposition of B_2O_3.

At 1616°C, the CO partial pressure of reaction [**3.12**] reaches 1 atmosphere and carbon strongly reduces B_6O forming B_4C and CO. The added carbon therefore reduces on the one hand B_2O_3 and evaporates as CO and, on the other hand forms B_4C. The CO partial pressures of the two reactions as a function of temperature are shown in figure 3.4a. The areas of the stability of the different phases are shown, which are separated by the lines. Even if the thermodynamic calculations suggest that B_4C would be decomposed at low temperatures (see figures 3.4a and 3.4b), this would be unlikely to happen during cooling or heating due to kinetic reasons. Therefore the use of B_4C in B_6O/B_4C composites will result in more reproducible results of sintering due to reduced interaction. This means that regardless of the starting composition, B_6O and B_4C phases would be present at the sintering temperature (1900°C). However, when the overall pressure in the system is increased, for instance, to 10 atmospheres, C could be stable up to about 1875°C and B_4C forms at about 1880°C (see figure 3.5).

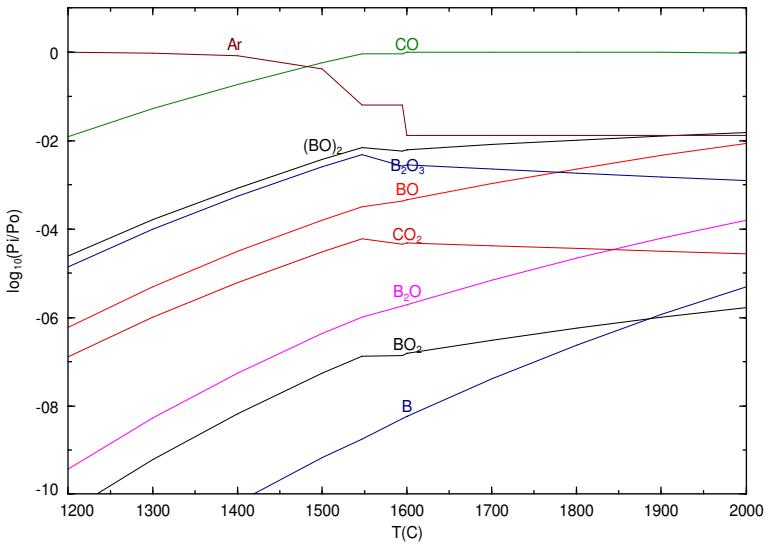

a)

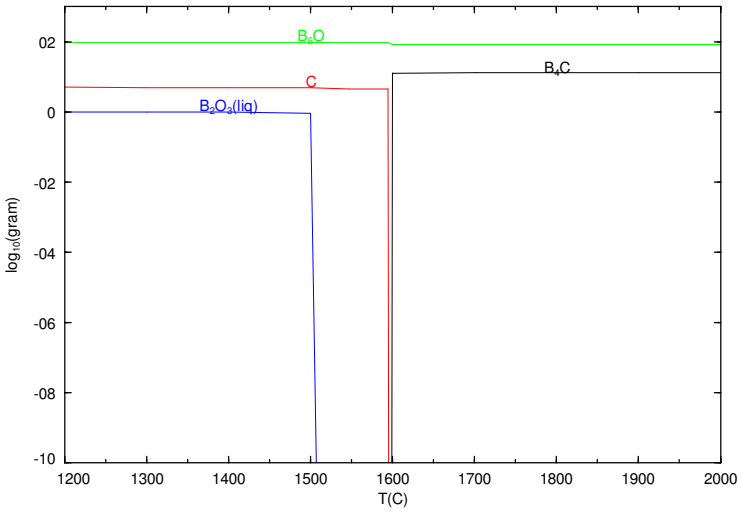

b)

Figure 3.3: Composition of the gas (a) and solid/liquid (b) phases for B_6O-5wt%C system.

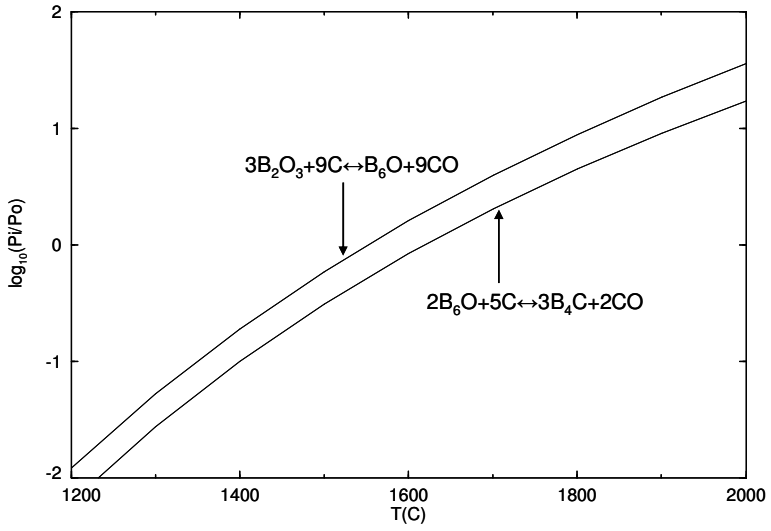

a)

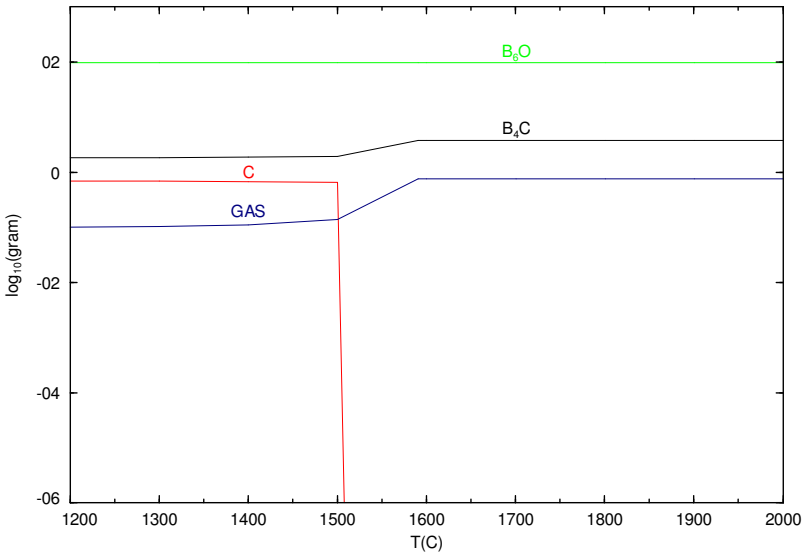

b)

Figure 3.4: (a) Partial pressure of CO for the two solid systems, $B_6O/B_2O_3/C$ and $B_6O/B_4C/C$. (b) Composition of the solid phase for B_6O-5wt%B_4C system.

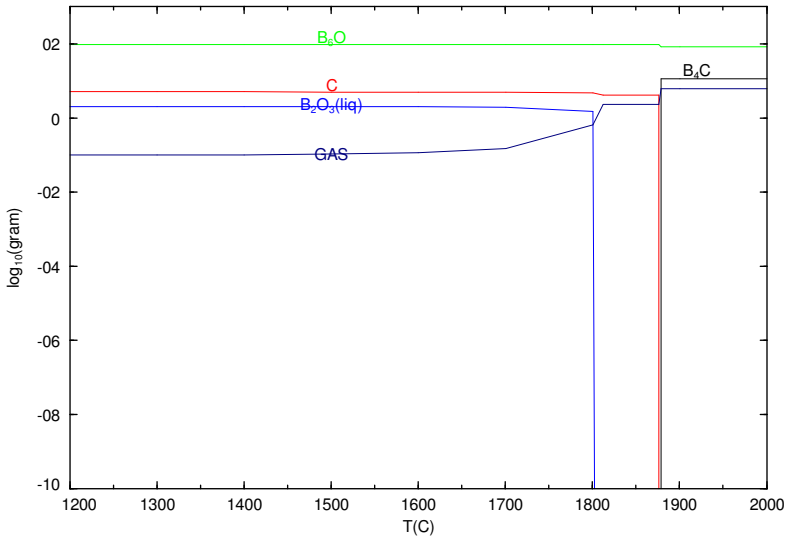

Figure 3.5: Composition of the solid/liquid phases for B_6O-5wt%C system at 10 atms.

3.3.2 B_6O-Ti-TiC-TiB_2 Systems

The thermodynamic calculations involving B_6O and Ti showed that TiB_2 is in equilibrium with B_6O together with liquid phases constituting TiO_2, Ti_2O_3, and B_2O_3 (see figure 3.6b). Removing B_2O_3 from the starting composition gives similar results indicating that the presence/absence of B_2O_3 in the system will not affect the resulting equilibrium compositions. Ti reacts with B_6O forming TiB_2 and B_2O_3 as follows:

$$8\ Ti(s) + 3\ B_6O(s) = 8\ TiB_2(s) + B_2O_3(l) \qquad [\mathbf{3.13}]$$

The formation of B_2O_3 liquid is as a result of reaction [**3.13**] as well as B_2O_3 already present in the system. At about 1900^{o}C, the partial pressure of $(BO)_2$ and B_2O_3 is higher than the Ar pressure which is as a result of complete consumption of B_2O_3 liquid which could be described by the reaction:

$$B_6O(s) + 5B_2O_3(l) = 8(BO)_2(g) \quad [\mathbf{3.14}]$$

$$B_2O_3(l) = B_2O_3(g) \quad [\mathbf{3.15}]$$

This means that Ti metal is not in equilibrium with B_6O and B_2O_3 but rather reacts with B_6O forming TiB_2. Reactions [**3.14**] and **[3.15]** occur even in B_6O-B_2O_3 system.

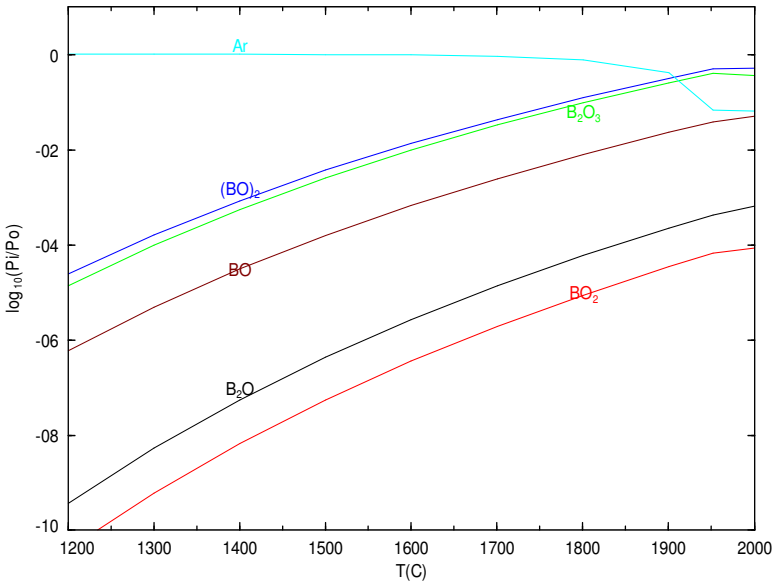

a)

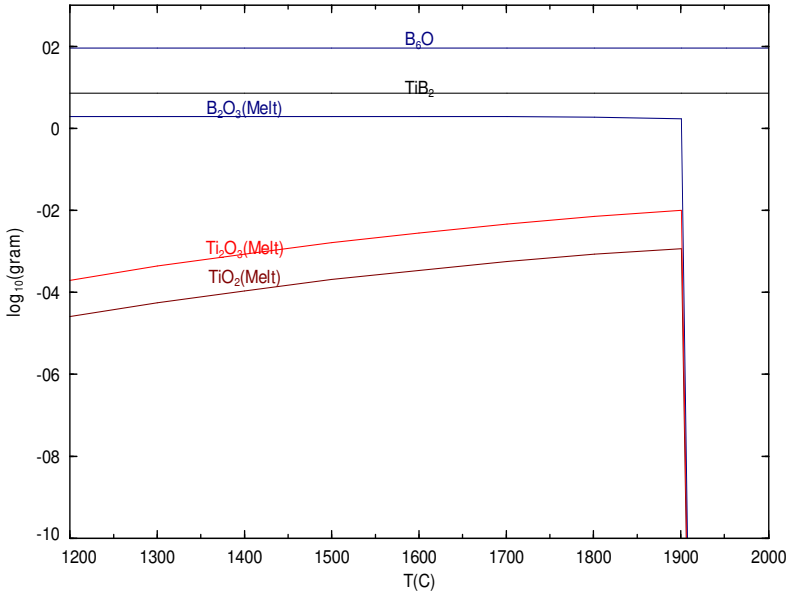

b)

Figure 3.6: Composition of the gas (a) and solid/liquid (b) phases for B_6O-5wt%Ti system.

With the introduction of TiC, the gas composition is similar to that of B_6O-C-B_4C system (compare figures 3.3a and 3.7a) with CO partial pressure much higher than Ar. At low temperatures, TiC is reduced to C, which is the case with B_4C addition. The reaction could be described in two stages as follows:

At low temperatures (<1500^oC)

$$TiC(s) + B_6O(s) = TiB_2(s) + C(s) \quad [\mathbf{3.16}]$$

$$TiC(s) + B_6O(s) = B_2O_3(l) + CO(g) \quad [\mathbf{3.17}]$$

Above 1500^oC, the CO partial pressure becomes much higher than the Ar pressure. Carbon decomposes to form B_4C; behaviour similar to B_4C and C addition. The reaction could be described as follows:

$$7\ C(s) + 2\ B_2O_3(l) = B_4C(s) + 6\ CO(g) \quad [\mathbf{3.18}]$$

In the absence of B_2O_3, similar results are obtained showing that B_2O_3 has no effect on the phases present within this temperature range. This means that at lower temperatures, B_2O_3 will be decomposed by C (reaction [**3.18**]) coming from the decomposition of TiC (reaction [**3.17**]). Reaction [**3.18**] will depend on the CO partial pressure. Additionally, B_2O_3 liquid decomposes into gaseous phase increasing the partial pressures of $(BO)_2$ and B_2O_3.

Therefore for higher amounts of TiC, a stronger decomposition takes place which results in reduced densification. Similar reasoning could be said for Ti addition as discussed earlier in this section. Therefore the addition of TiC and Ti is only recommended in small amounts less than 5 wt%.

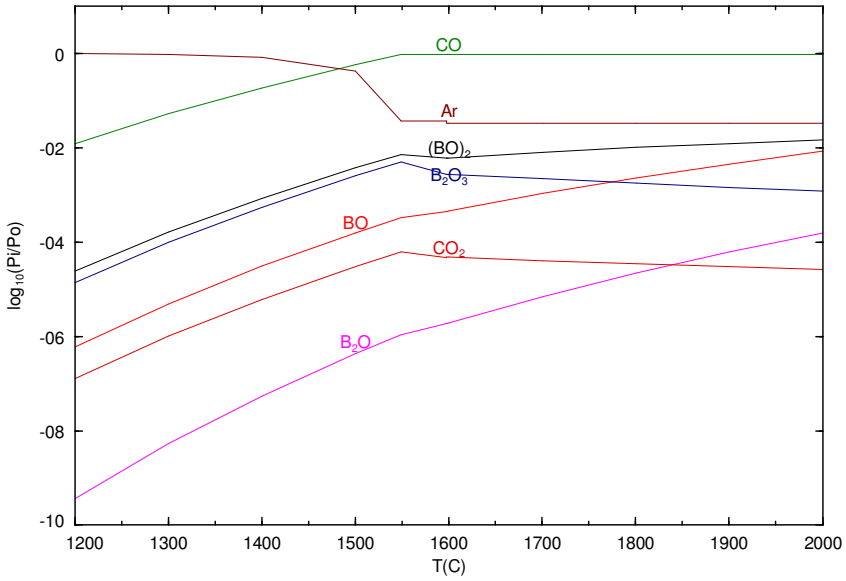

a)

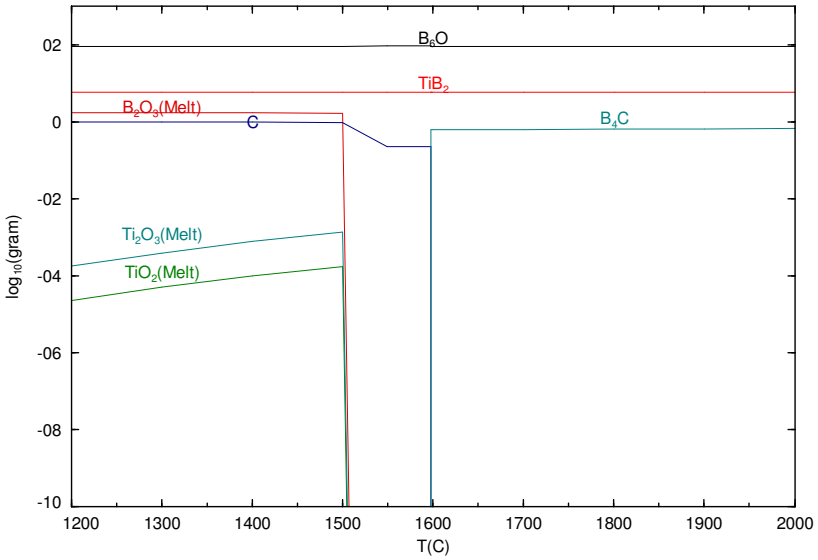

b)

Figure 3.7: Composition of the gas (a) and solid/liquid (b) phases for B_6O-5wt%TiC system.

3.3.3 B_6O-Al-Al_2O_3 System

The results of the thermodynamic calculations for B_6O-Al_2O_3 system indicate an oxide liquid containing Al_2O_3 and B_2O_3 in equilibrium with B_6O and $Al_{18}B_4O_{33}$ (Figure 3.8). The existing B_2O_3 on the surface of the starting powder and the Al_2O_3 added formed aluminium borates, and at high temperatures an oxide liquid. The amount of Al_2O_3 and B_2O_3 in the starting composition will strongly change the amount of liquid phase existing during sintering and hence affect the extent of densification during sintering. This liquid could recrystallise to form Al_2O_3-B_2O_3 compounds during cooling. The type of aluminium borate formed would depend on the ratio of Al_2O_3 to B_2O_3 in the liquid. According to the phase diagram (Figure 3.9), a liquid phase is formed at 1200^{o}C if the Al_2O_3/B_2O_3 mol ratio is between 9:2 and 2:1. All secondary phases are dissolved in the liquid at the incongruent melting point of $Al_{18}B_4O_{33}$.

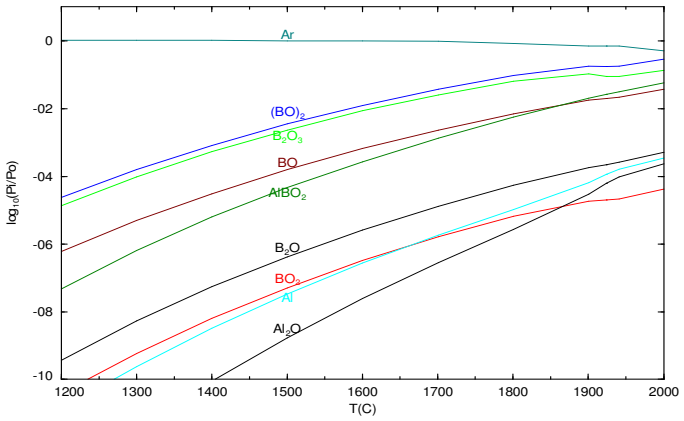

a)

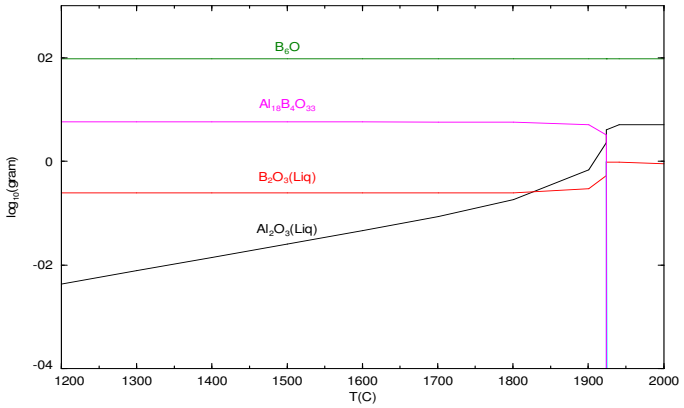

b)

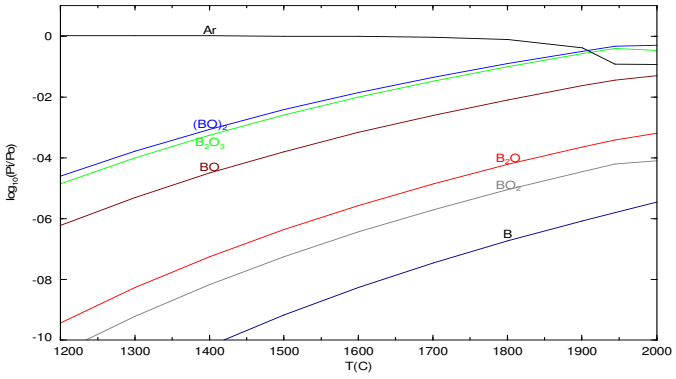

c)

Figure 3.8: Composition of the gas (a) and solid/liquid (b) phases for B_6O-5wt%Al_2O_3 system. (c) Composition of the gas phases for B_6O-1wt%B_2O_3 system.

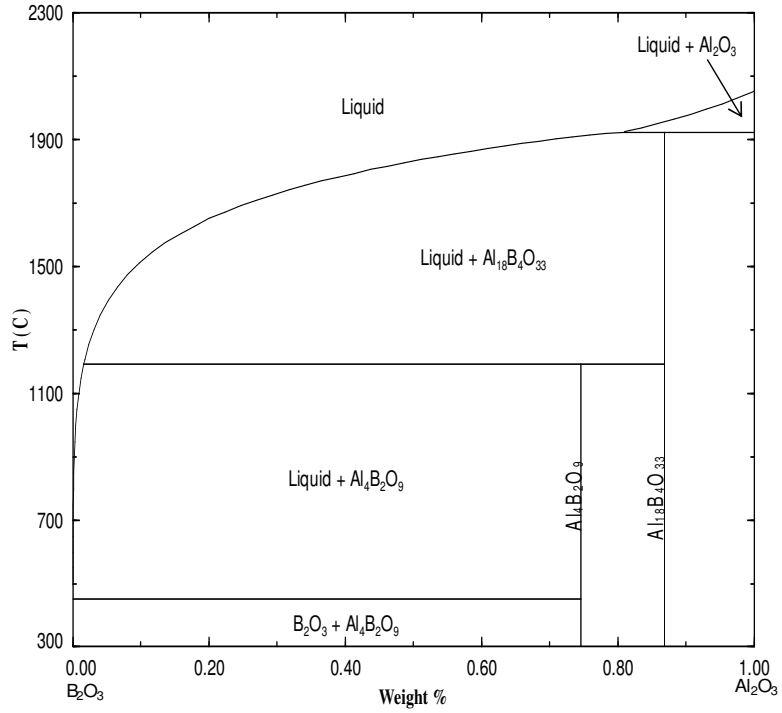

Figure 3.9: Calculated phase diagram of Al_2O_3 – B_2O_3 system. This diagram completely agrees with the diagram given in literature [83].

Comparing the gas compositions of figures 3.8a and 3.8c, it can be concluded that the addition of Al_2O_3 lowers the partial pressure of boron containing compounds by a factor of 2 at 1900°C. This helps to stabilise the liquid phase during sintering. Thus the addition of Al_2O_3 reduces the activity of B_2O_3 in the oxide melt and therefore the partial pressures. In figure 3.8c, $(BO)_2$ and B_2O_3 have the highest partial pressures. The first is formed due to the interaction between B_6O and B_2O_3. The second is caused by the evaporation of B_2O_3 itself.

For B_6O-Al system, the thermodynamic calculations show the formation of Al_2O_3 and AlB_{12} in equilibrium with B_6O (Figure 3.10). The Al reacts with B_6O forming Al_2O_3 and AlB_{12} according to the reactions:

$$3\ B_6O + 2x\ Al = x\ Al_2O_3 + 3\ B_6O_{(1-x)} \quad [\mathbf{3.19}]$$

$$2\ B_6O + Al = AlB_{12} + Al_2O_3 \quad [\mathbf{3.20}]$$

Thus Al reacts with B_6O reducing the oxygen content in the B_6O due to the existence of the non-stoichiometry of B_6O. Additionally, even in the absence of B_2O_3 in the starting composition, these phases are observed at equilibrium. In the presence of B_2O_3, the Al_2O_3 formed in equation **[3.19]** could react with B_2O_3 forming aluminium borates. Thus the addition of Al reduces at least partially the amount of B_2O_3 in the system.

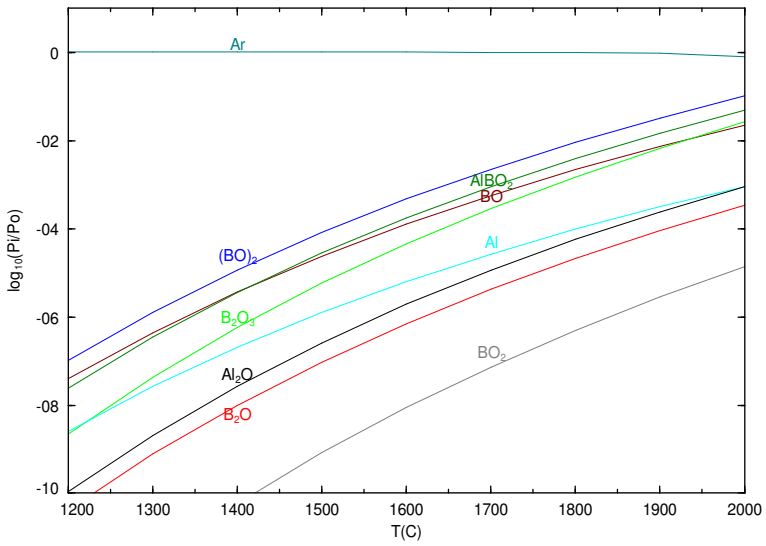

a)

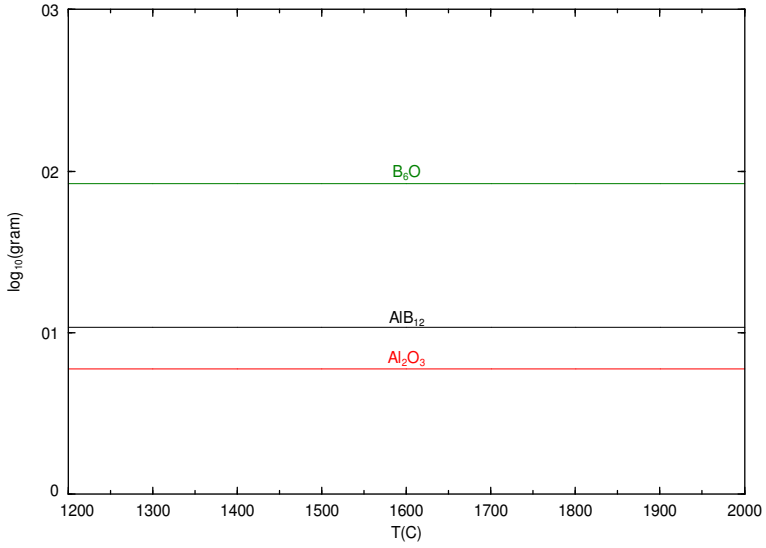

b)

Figure 3.10: Composition of the gas (a) and solid (b) phases for B_6O-5wt%Al system.

3.3.4 B_6O-Al_2O_3-Y_2O_3-SiO_2 system

The results of the thermodynamic calculations for B_6O-Al_2O_3-Y_2O_3 system indicate the formation of B_2O_3 oxide liquid which is in equilibrium with B_6O, $Al_{18}B_4O_{33}$ and $Y_3Al_5O_{12}$ (Figure 3.11). It must be mentioned here that calculations carried out in this system are first estimation due to the fact that no data concerning the solubility of Y_2O_3 in B_2O_3/Al_2O_3 melt exist. Therefore the calculated existence of B_2O_3 oxide liquid in reality means a B_2O_3-containing melt.

For 62 mol % Al_2O_3 (YAG composition), $Al_{18}B_4O_{33}$ disappears at about 1800°C increasing the partial pressure of the gas phase and only appears again after about 1950°C. Additionally, the B_2O_3 liquid is stable until about 1940°C where it disappears into gaseous phase. On the other hand, for Al_2O_3 mol % of 80 (also YAG composition) $Al_{18}B_4O_{33}$ is stable even up to 2000°C. B_2O_3 in this case is stable up to about 1900°C and disappears into gaseous phase increasing the partial pressures of the B-O composition. This means that for higher Al_2O_3 content, there is enough Al_2O_3 to react with B_2O_3 present at the starting composition to form a stable $Al_{18}B_4O_{33}$ according to figure 3.11. If the sintering temperature, for instance, is 1900°C, the liquid B_2O_3 will recrystallise to form boron-rich compounds during cooling. The amount of the liquid phase present will affect the densification of the sintered materials.

With the introduction of SiO_2 into the system (i.e. B_6O-Al_2O_3-Y_2O_3-SiO_2 system) aluminium borate does not form. Instead yttrium silicates will be in equilibrium with B_6O and $Y_3Al_5O_{12}$ (Figure 3.12)

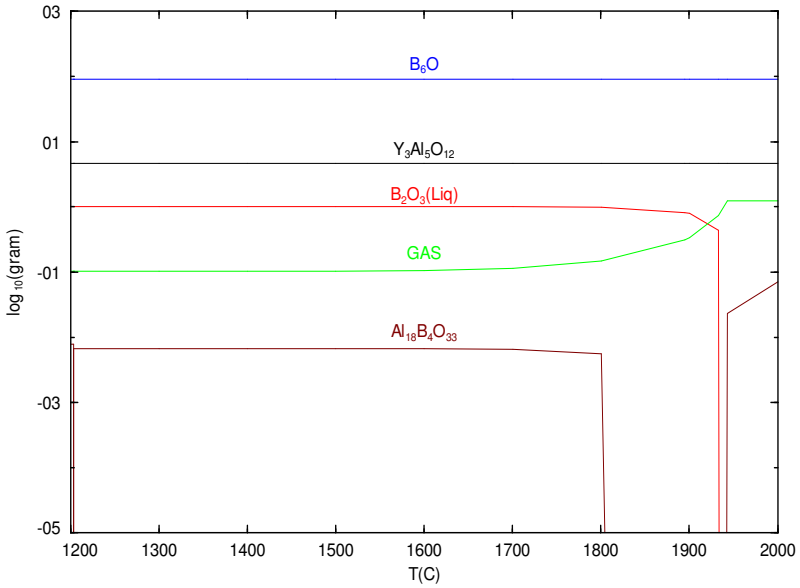

a)

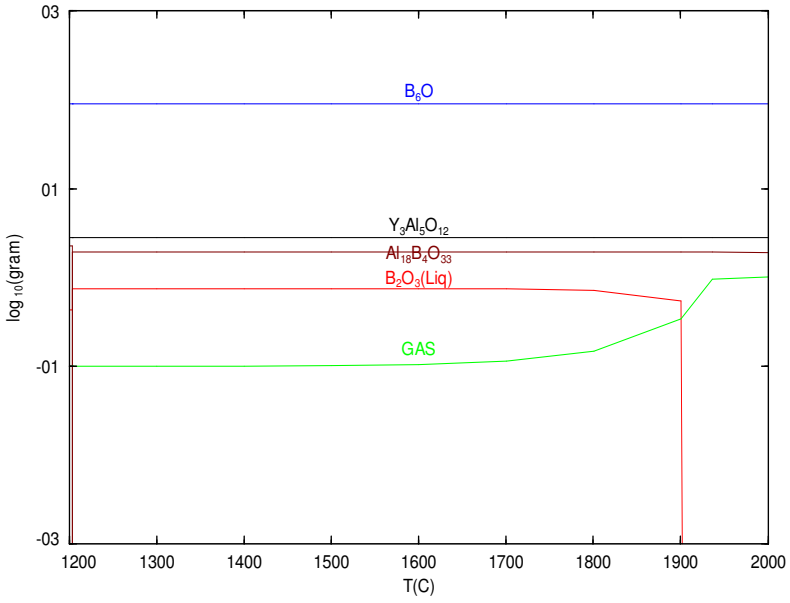

b)

Figure 3.11: Composition of the solid/liquid phases for B_6O-62mol%Al_2O_3-38mol%Y_2O_3 system (a) and B_6O-80mol%Al_2O_3-20mol%Y_2O_3 system (b).

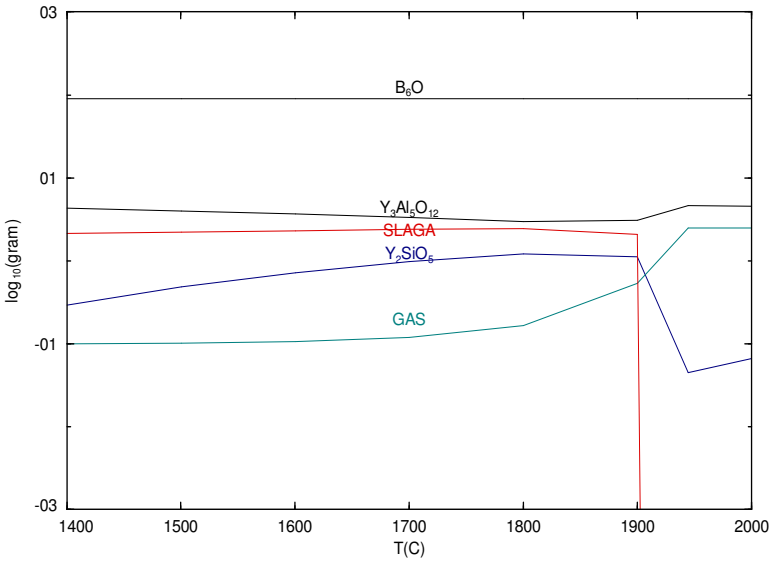

Figure 3.12: Composition of the solid/liquid phases for B_6O-2wt%Al_2O_3-2.65wt%Y_2O_3-1wt%SiO_2 system.

3.4 Conclusions

Thermodynamic properties of B_6O have been estimated up to 2300K. The data has allowed the prediction of the stability of the liquid and crystalline phases in B_6O composites. Therefore this can form the basis for the search of new sintering additives that would allow the sintering of B_6O composites at lower temperatures.

From the above thermodynamic calculations, it has been shown that B_6O can be liquid phase sintered using a wide range of oxide additives. In liquid phase sintering, the sintering additive melts or reacts with another sintering additive or the major component to form a liquid. From the above thermodynamic calculations, Al_2O_3 and Y_2O_3 were selected as the main sintering additives to be used in this research with the introduction of SiO_2 to test the effect it will have on densification process.

4 Experimental Procedure

4.1 Introduction

This chapter describes the materials, methodology, equipments, and relevant formulae used in this project. Results obtained from the experimental work are presented in Chapter 5.

4.2 Materials and chemicals

Amorphous boron (supplied by H.C. Starck, Germany) and boric acid (Saarchem) powders were used as the starting materials for the synthesis of boron suboxide. Additionally, boron suboxide (B_6O) powder produced at IKTS – Dresden was used for the major part of the hot pressing investigations carried out in this project. Al_2O_3, Y_2O_3, SiO_2, TiC, and TiB_2 powders were used as sintering additives. The compositions of these additives are described in detail in section 4.4. $PdCl_2$ was reduced to Pd and also used as sintering additive. A summary of all the materials and chemicals used are tabulated in table 4.1.

4.3 Synthesis and milling of boron suboxide (B_6O) powder

4.3.1 Synthesis of boron suboxide (B_6O) powder

Amorphous boron (B) and boric acid (H_3BO_3) powders were dry mixed in a turbular mixer (WAB T2C) for 3 hours using molar ratio B:H_3BO_3 = 8:1.03. This molar ratio included 3% excess of H_3BO_3 in comparison to the stoichiometric equation [**4.1**] which accounts for the evaporation of B_2O_3 that occur during synthesis:

$$16B + 2H_3BO_3 = 3B_6O + 3H_2O \qquad [\mathbf{4.1}]$$

Alumina balls with diameter of 12 mm were used as milling media during mixing. The turbular mixer was stopped after every 40 minutes and the sample container

manually stirred to remove powders that were stacked on the walls of the plastic container.

Table 4.1: Materials and chemicals used in this project.

Material/Chemical	Particle size, d_{50} (μm)	Purity (%)	Supplier
B	0.8	90	H.C. Starck
H_3BO_3	-	99	Saarchem
B_6O	100	-	IKTS-Dresden
α-Al_2O_3 (AKP 50)	0.15	99.9	Sumitomo
Y_2O_3	0.2	-	H.C. Starck
SiO_2	40	-	Heraeus
TiC	2	99.5	Johnson Matthey
TiB_2	2.5	-	H.C. Starck
$PdCl_2$	-	99.9	Sigma-Aldrich
h-BN rods	-	-	GE Advanced Ceramics
Propan-1-ol	-	99.7	Saarchem
Sodium hexametaphosphate	-	-	Saarchem
Methanol	-	99	Saarchem
Ethanol	-	99	Saarchem
HCl	-	-	Saarchem
Diamond spray	1	-	Struers
Diamond extender	-	-	Struers
Distilled water	-	-	-
Argon	-	UHP	Afrox

The mixture was loaded in an alumina boat and placed in the centre of α-Al_2O_3 tube (hot zone area) which has been inserted into a furnace (TSH 17/75/150 Elite Thermal Systems). The furnace has capabilities of running to a maximum temperature of

1700°C with eurotherm microprocessor that controlled the temperature profile. The furnace temperature was measured by a standard Pt-Rh thermocouple which was connected to the microprocessor.

The powder was heat treated in ultra high purity argon stream from room temperature to 300°C at 5°C/min and dwelled at this temperature for 30 minutes to allow the transformation from boric acid (H_3BO_3) to boron oxide (B_2O_3). The furnace was then heated at the same rate up to 1380°C and dwelled at this temperature for 6 hours to give it enough time for the reaction between boron oxide and boron to form boron suboxide. It was cooled afterwards at 5°C/min to room temperature. The boron suboxide powder produced via this method was washed in alcohol and dried in a rotary evaporator. The heating cycle is shown in figure 4.1. The synthesised powder was characterised using X-ray diffractometry, scanning electron microscopy and particle sizing techniques. Part of the B_6O powder produced was coated with palladium and hot pressed as described in section 4.5. Additionally, pure B_6O was sintered and the properties measured and compared with the coated powder.

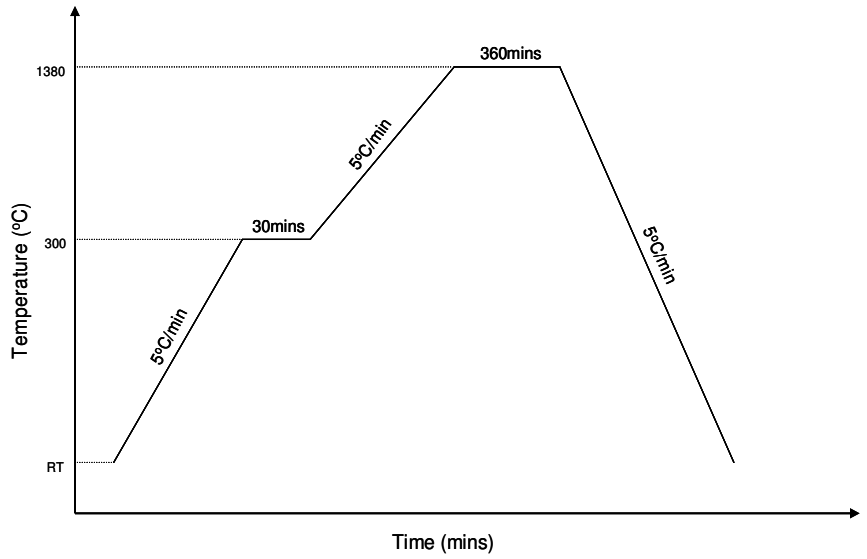

Figure 4.1: Temperature profile for B_6O synthesis. RT = room temperature.

4.3.2 Milling of boron suboxide (B_6O) powder

The purpose for milling B_6O powder was to drive the particle size down to the submicron size range. This could have an added advantage of improving the mechanical properties of B_6O sintered composites compared to their microcrystalline counterparts due to the small size of the grains and large fraction of the atoms located at the grain boundaries.

Synthesised boron suboxide powder with average agglomerate particle size of 100 µm (supplied by IKTS - Dresden) was charged into a stainless steel attrition mill (S/N 200603, Szegvari Attritor System having 750 ml capacity). Steel balls of 2.5 mm and 1 mm diameter were used. The ratio by weight of charge to ball was kept at 1:10. Mill speed was kept constant at 200 rpm at room temperature, except when 1 mm diameter steel balls were used; in this case the speed was increased to 300 rpm. Figure 4.2 shows schematic diagram of an attrition mill.

Propan-1-ol was used as the grinding media. Weight of the balls was measured before and after milling to determine weight loss during milling. The attrition mill was stopped at selected milling times of 5, 20, 30, and 50 hours using 2.5 mm balls. Additionally, 30-hour milled powder was further milled for 5 hours using 1 mm diameter steel balls to investigate the effect of ball size on milling. After every requisite time interval, required amounts of powders were withdrawn for washing and particle sizing, taking due care to avoid sampling errors. This was carried out to understand the milling kinetics. The samples were further characterised using X-ray diffractometry and scanning electron microscopy techniques.

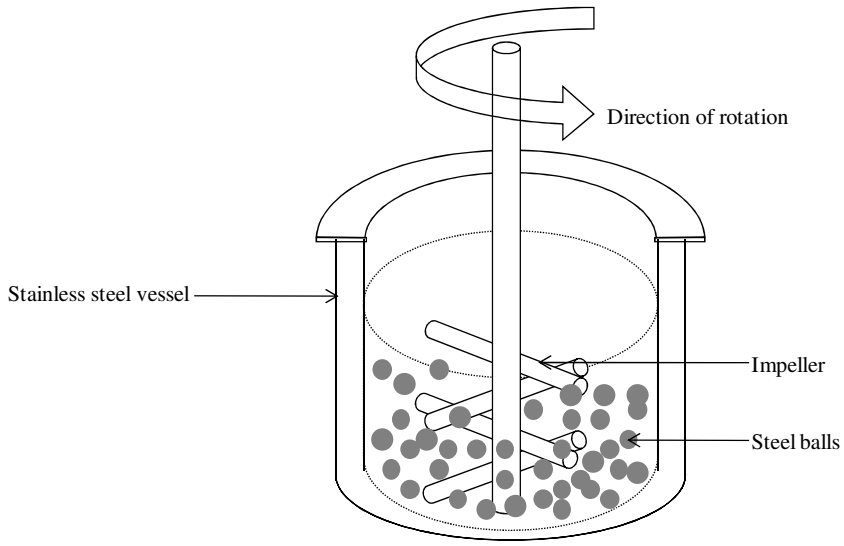

Figure 4.2: Schematic diagram of an attrition mill.

4.3.3 Washing of boron suboxide (B_6O) powder

After establishing the optimum milling conditions (that is 30 hours milling using 2.5mm diameter balls in propan-1-ol), two batches of B_6O were milled for the hot pressing experiments. In order to recover pure B_6O powder for further processing, contaminants (mainly Fe and Cr) introduced during milling were minimised by washing the milled B_6O powders in 1 M HCl followed by washing in ethanol and warm methanol to remove any B_2O_3 remaining in the powder. For every 100g of milled powder, 2.5 litres of 1 M HCl was used for the washing. HCl solution was changed after every 24 hours. The HCl solution was changed five times for the first batch of milled powder (denoted by '***a***' in the naming of the hot pressed materials) and 10 times for the second batch of milled powder (denoted by '***b***' in the naming of the hot pressed materials). In both cases, the washing did not remove the impurities completely. Nevertheless, the levels of impurities were strongly reduced by increasing the time of washing for the second batch of milled powder. After the washing, B_6O powders were dried in a rotary evaporator and kept in desiccators for

further processing. XRD and SEM analyses were carried out on milled powders before and after washing in HCl to determine the phases and amount of Fe and Cr in powders. Additionally, washed and dried B_6O powder samples were taken for ICP-OES analysis to determine the level of impurities left in the powders.

4.3.4 Chemical analysis of milled boron suboxide (B_6O) powder

An inductively coupled plasma optical emission spectrometer, ICP-OES (SPECTRO CIRUS CCD), was used to determine the level of concentrations of Fe and Cr in the washed powders. Samples (0.1g) were digested in a solution containing 3 ml HNO_3 (55%), 2 ml HCl (32%) and 3 ml HF (40%) by microwave digestion technique (Multiwave 3000 SOLV). Digestion was done at 260^{o}C for 30 minutes. The following analytical wavelengths were chosen (nm): 259.941 Fe and 267.716 Cr. These wavelengths showed a good linear response between concentration and intensity and were free from interferences in the range of concentrations used in the present study.

4.4 Admixing boron suboxide (B_6O) powder with additives

To improve the mechanical properties, especially fracture toughness of the 'pure' polycrystalline B_6O hot pressed compacts, different sintering additives were used. These additives were expected to reduce and/or replace the existing B_2O_3 on the surfaces of B_6O particles by reacting with it to form oxide/boride phases. Three compositions (indicated by arrows in figure 4.3) with different amount of Al_2O_3 and Y_2O_3 (based on the Al_2O_3-Y_2O_3 phase diagram) were selected and mixed with B_6O to produce the composites. To obtain B_6O composites with various structures for studies, alumina – yttria mole ratio and sintering additive volume content were varied. The ratio of the different additives are summarised in table 4.2. These variables were chosen with the intention of obtaining separate structures and grain boundary chemistry which could assist in establishing the causes of the different properties obtained and consequently establish a relationship between structure and mechanical properties. The process variables were expected to produce materials with

varying amounts of phases at the grain boundaries. These differences in grain boundary composition were expected to affect properties of the materials. Additionally, SiO_2 was added to Al_2O_3 and Al_2O_3-Y_2O_3 systems to understand the role SiO_2 plays in the densification process and also its effect on the structure and properties of hot pressed composites. Al_2O_3, TiB_2, Pd, and TiC were also used as sintering additives. Coating of B_6O with Pd has been described in section 4.5.

The mixing was carried out in methanol using 2 mm alumina balls for 2 hours in a planetary mill (Fritsch Pulverisette 6). The milling vessel used was alumina having 250 ml capacity. The mill was operated at a speed of 200 rpm to minimise contaminations from the alumina balls. The mixed powders were dried using the rotary evaporator for hot pressing experiments. Admixed powders were characterised using X-ray diffractometry and scanning electron microscopy techniques.

Table 4.2: Compositions of sintering additives used in this project.

Al_2O_3 (wt %)	Y_2O_3 (wt %)	SiO_2 (wt %)	TiB_2 (wt %)	TiC (wt %)	Al_2O_3/Y_2O_3 molar ratio
1.00	1.32	-	-	-	62/38
2.00	2.65	-	-	-	62/38
2.83	3.75	-	-	-	62/38
2.87	1.58	-	-	-	80/20
4.88	1.22	-	-	-	80/20
1.48	3.26	-	-	-	50/50
2.10	4.63	-	-	-	50/50
2.00	2.65	1.00	-	-	62/38
2.70	3.57	1.35	-	-	62/38
2.54	1.40	1.27	-	-	80/20
3.43	1.89	1.72	-	-	80/20
2.00	-	1.00	-	-	-
1.00	-	-	-	-	-
2.00	-	-	-	-	-
3.00	-	-	-	-	-
-	-	-	5.00	-	-
-	-	-	-	5.00	-

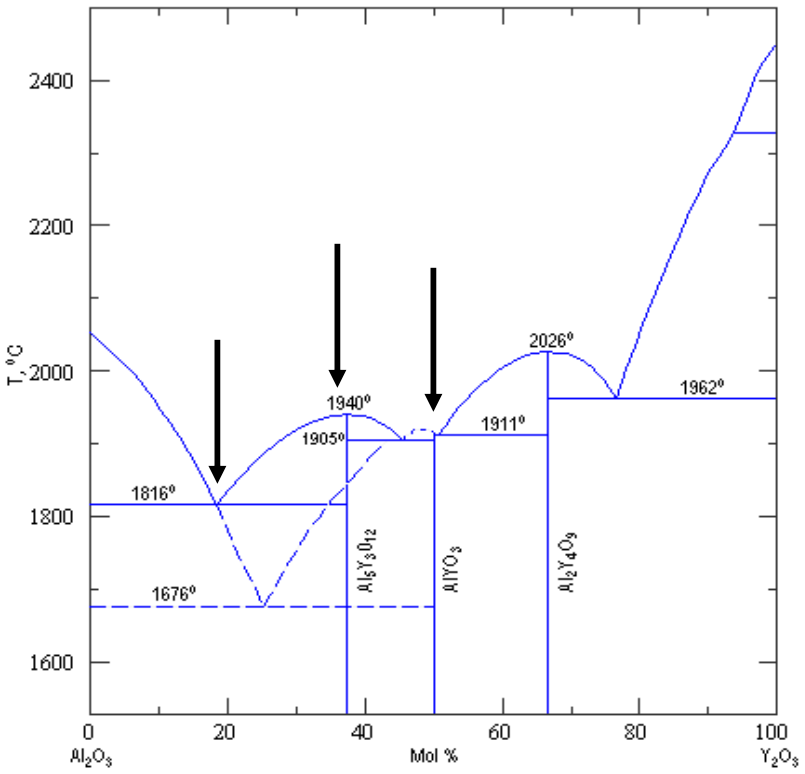

Figure 4.3: Phase diagram of Al_2O_3 -Y_2O_3 system [83].

4.5 Coating of boron suboxide (B_6O) with palladium

Palladium chloride ($PdCl_2$) was used as a source of Pd in coating the B_6O powder. The intention was to form pure metal or palladium boride with B_2O_3 existing on the surfaces of B_6O particles thereby forming a stronger grain boundary. $PdCl_2$ (weight representing 5 vol. % Pd) was dissolved in 1 M HCl and B_6O powder was added. B_6O powder used in this investigation was the one produced at Wits University and discussed under section 4.3.1. The mixture was stirred and dried using rotary evaporator. The dried sample was put in an alumina boat and placed in a hot zone area of the tube furnace as described in section 4.3.1. The furnace was heated up to 400^{o}C and dwelled at this temperature for 60 minutes to remove any chlorine (Cl) left in the powder as a result of mixing in 1 M HCl. The furnace was cooled to room

temperature and the sample removed for characterisation. The temperature profile of the furnace is shown in figure 4.4.

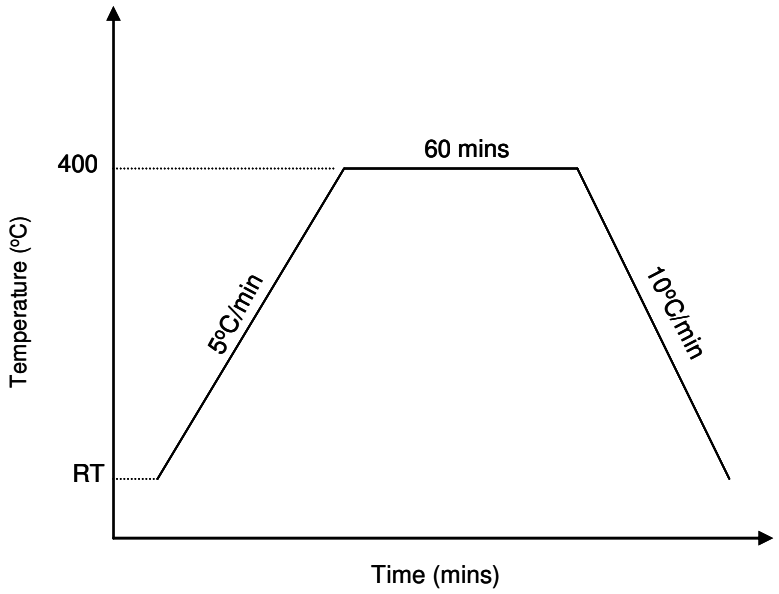

Figure 4.4: Temperature profile used for coating B_6O with Pd. RT = room temperature.

4.6 Hot pressing of boron suboxide (B_6O) based materials

A uniaxial hot press (HP20-2560-FP20 Thermal Technology) was used for all the hot pressing experiments carried out in this research. The furnace, heated by graphite elements, has a maximum operating temperature of 2100^{o}C and is water-cooled. The force is applied through graphite punches uniaxially from the bottom graphite punch. A schematic diagram of the die assembly is shown in figure 4.5. A rotary vacuum pump is attached to the hot press and is capable of vacuum levels of 10 mtorr.

Before hot pressing, all graphite components in the hot-zone of the furnace were coated with h-BN suspension (37g of h-BN and 100 ml of water) which has been stabilised with poly-vinyl pyrolidone (2g). The suspension was stirred using magnetic

stirrer bar until the consistency of the entire suspension was uniform. The suspension was then used to coat the graphite components. The graphite components coated include punches and die insert. h-BN sample cells were used for all hot pressing experiments. The inner and outer diameter of the cell is 18 mm and 25.4 mm, respectively; the height is 18 mm. The furnace was evacuated to a pressure less than 300 mtorr and then back filled with ultra high purity argon. Argon was allowed to flow through the furnace during the entire hot pressing process.

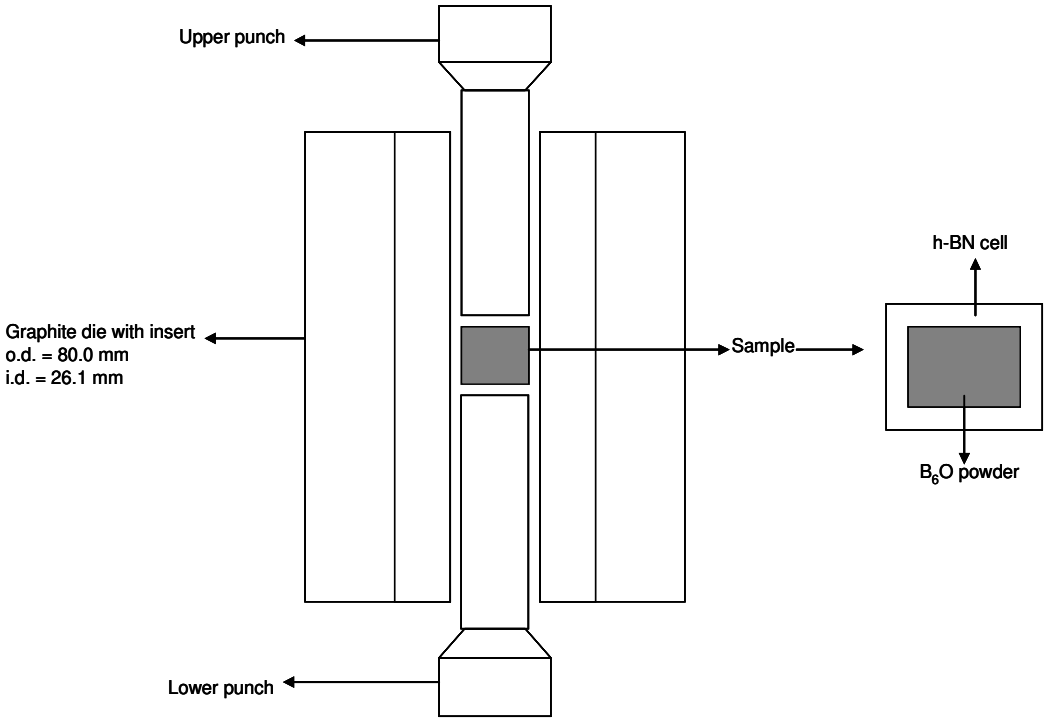

Figure 4.5: The schematic diagram of the uniaxial hot pressing die assembly.

Hot pressing was carried out at high temperatures (≥1600^{o}C) under a pressure of 50 MPa for 20 minutes. For pure B_6O, the applied pressure was increased gradually to 30 MPa when the temperature reached 1700^{o}C (200^{o}C lower than hot pressing temperature) at a heating rate of 15^{o}C/min. At this temperature (1700^{o}C), it was

dwelled for 20 minutes after which the temperature was increased at a rate of 10°C/min to 1900°C. Dwelling time at 1900°C is 20 minutes by which time the applied pressure is kept constant at 50 MPa. After the heat treatment the hot press was cooled at 20°C/min to room temperature. A similar hot pressing cycle was used for all other hot-pressed materials. A typical hot pressing cycle is shown in figure 4.6. The variables used in figure 4.6 have been defined in table 4.3.

During cooling, furnace temperature lagged behind the programmed temperature at temperatures lower than 800°C. At about 600°C, the applied load was removed from the sample. The hot pressed samples were recovered from between the punches and the sample cells for analyses. The hot pressed samples were of 18 mm in diameter and 2 to 4 mm in thickness.

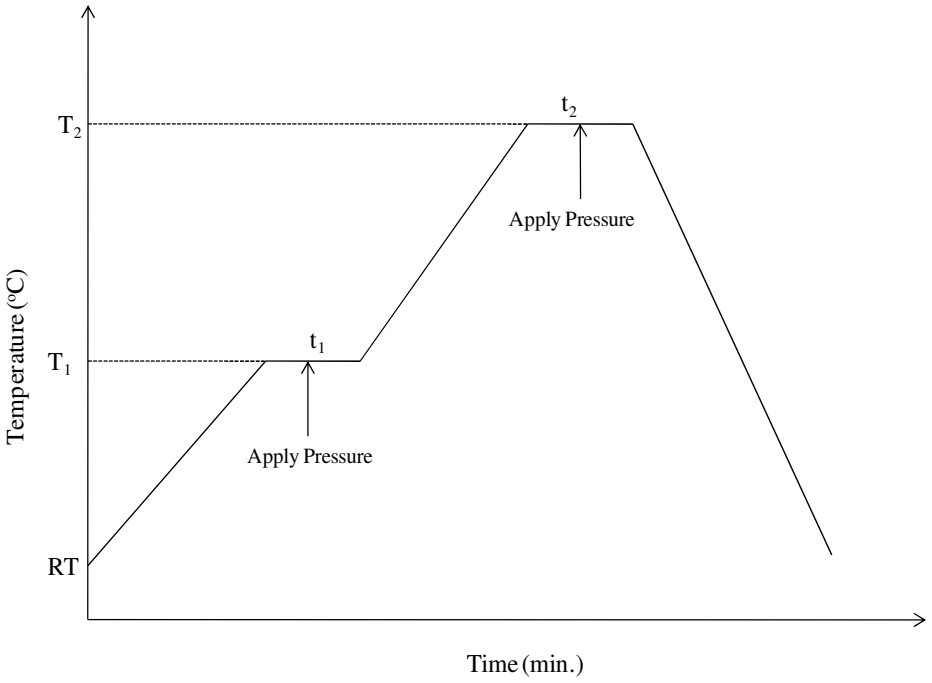

Figure 4.6: A typical hot pressing cycle used in this project. RT = room temperature (see table 4.3 for definition of variables).

Table 4.3: Hot pressing cycles for the various hot pressing experiments carried out in this research showing the definition of the variables used in figure 4.6.

Hot pressing cycle	Heating rate up to T_1 (^oC/min)	T_1(^oC), t_1 (min.)	Heating rate up to T_2 (^oC/min.)	T_2(^oC), t_2 (min.)	Applied Pressure (MPa)	
					t_1	t_2
'Pure' B_6O	15	1700, 20	10	1900, 20	30	50
Pd coated B_6O	15	1400, 20 1700, 20	10	1600, 30 1900, 30	30	50
Composite materials	15 20*	1600, 20 1400, 5*	10 20*	1800, 20	30 50*	50

*This hot pressing cycle was used for the second batch of milled B_6O powder to reduce grain growth and to improve densification

4.6.1 Heat treatment (annealing) of hot-pressed boron suboxide (B_6O) composites

Heat treatments of B_6O composites namely **18**B_6O**1**Al**1.32**Y***b***, **18**B_6O**2**Al**2.65**Y***b***, **18**B_6O**2.87**Al**1.58**Y***b***, and **18**B_6O**2**Al**2.65**Y**1**Si***b*** were carried out to determine the thermal stability of the binder phases formed after hot pressing as well as possible phase transformation of the binder phases. Nomenclature of hot pressed materials is described in section 4.6.2. The heat treatment experiments were carried out in uniaxial hot press in argon atmosphere at 1250^{o}C for 10 hours. The materials were covered with B_6O powder and placed in hBN pots to minimised decomposition and contamination from furnace environment (graphite components). The materials were then characterised based on phase and microstructural transformations, density and weight loss.

4.6.2 Nomenclature of hot pressed materials

B_6O composite materials with different additives and additive contents have been hot pressed from two batches of milled B_6O powders (B_6O powder produced at IKTS) and from B_6O powder produced at Wits. For easy referencing, materials hot pressed in this project have been named according to their hot pressing temperature, composition, batch of milled powder, and heat treatment condition. The first two numbers denote the temperature at which the material was hot pressed, except in cases where materials were hot pressed at 1750^{o}C and 1850^{o}C. In such cases three numbers have been used (i.e. 175 and 185 respectively). This is followed by the composition of the material. All additive contents are in weight % except for Pd where volume % was used. In case of the oxide additives, the oxygen part was not included in the naming. The composition has "***a***" (first batch of milled powder) or "***b***" (second batch of milled powder) attached to it indicating the type of B_6O powder used to produce the hot pressed compact. Composite materials without these notations mean that it has been produced from B_6O powder synthesised at Wits. Repeated runs are differentiated from first run by 1 or 2 at the end of the material name. For the materials that were heat treated, the abbreviation HT has been added at the end. Some examples of the method of naming all hot-pressed materials are given in table 4.4. Full list of all the hot-pressed materials and their properties have been given in Appendix B.

Table 4.4: Summary of material nomenclature and condition of preparation.

Material	Designate
19B_6O***a***	Pure B_6O hot-pressed at 1900°C from first batch of milled B_6O powder
18B_6O**1**Al**1.32**Y***b***	B_6O composite hot-pressed at 1800°C from second batch of milled B_6O powder which contains 1wt%Al_2O_3 and 1.32wt%Y_2O_3
18B_6O**2**Al**2.65**Y***b*****-2**	B_6O composite hot-pressed at 1800°C from second batch of milled B_6O powder which contains 2wt.%Al_2O_3 and 2.65wt%Y_2O_3. Repeated run.
18B_6O**2**Al**2.65**Y***b*****-1HT**	B_6O composite hot-pressed at 1800°C from second batch of milled B_6O powder which contains 2wt%Al_2O_3 and 2.65wt%Y_2O_3. First run and heat treated (annealed).
18B_6O**2**Al**2.65**Y**HTP*b***	B_6O composite hot-pressed at 1800°C from second batch of milled B_6O powder and contains 2wt%Al_2O_3 and 2.65wt%Y_2O_3. Admixed powder was heat treated before hot pressing.
19B_6O**5**TiC***a***	B_6O composite hot-pressed at 1800°C from first batch of milled B_6O powder which contains 5wt%TiC
19B_6O**5**Pd	B_6O composite hot-pressed at 1900°C and contains 5 vol. % Palladium metal. B_6O powder produced at Wits was used.

4.7 Characterisation techniques

Before characterisation, all hot-pressed materials were ground on the surface to remove any h-BN material adhered unto the hot-pressed material. Densities of the materials were measured immediately after hot pressing. Materials were then cut into 2 to 4 pieces using diamond saw for further analyses. Cross-sections of hot-pressed materials were carefully polished after hot mounting in bakelite powder followed by lapping on Struers 80, 120, 220, 600 and 1200 grit. Grinding was carried out to achieve a flat surface and to remove any scratches. Materials were then polished on a

Pan cloth to 1 μm surface finish using diamond spray and diamond extender to remove surface stress raisers and machining damage such as microcracks and to increase the reproducibility of data, especially, crack size. Samples were rinsed with ethanol and dried.

4.7.1 Particle sizing

The size and size distributions of milled boron suboxide particles as well as other powders were determined using Malvern Mastersizer® (Hydro2000MU accessory). This equipment measures the equivalent mean volume of particles and is based on the principle of laser diffraction. The intensity and angle of diffraction of a monochromatic laser beam as it interacts with the particle in a dispersion medium is related to the particle size. In order to obtain average particle size with narrow particle size distribution, tests were conducted using sodium hexametaphosphate (NHMP) as a dispersant. For the best results of highest absolute value of zetapotential (see figure 4.7), B_6O powders were dispersed in 0.05% NHMP solution using external ultrasound for 1 minute. The background measurement was done using NHMP solution with the same concentration (0.05%) exercising extreme care in order to achieve a clean background. About 10 mg of powder was prepared and put in 1L beaker containing about 800 ml of solution for the size distribution tests. Obscuration was less than 16%. Particles added to the NHMP solution in the beaker were homogenised using a stirrer at a pump speed of 2000 rpm. The ultrasonic was adjusted to 75% of its maximum. As the particle sizes were reduced to submicron range, characteristic data of particle as well as dispersant were necessary for analysing the raw data. A refractive index of 3.88 and an absorption value of 1 were used to determine the size distribution of the milled powder. The refractive index for B_6O is not known precisely and was proposed based on measurement at IKTS.

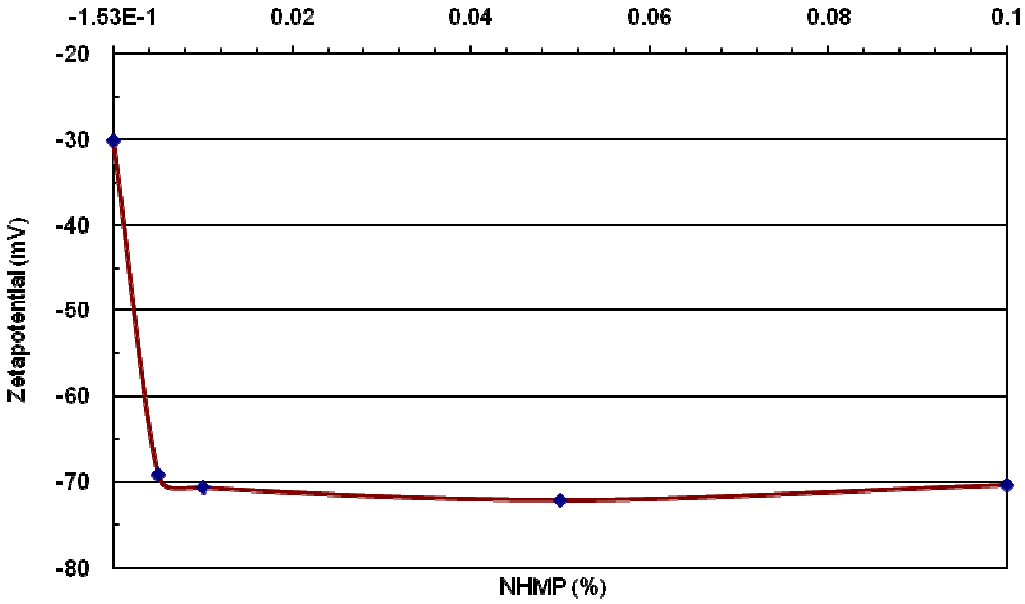

Figure 4.7: Zetapotential versus sodium hexametaphosphate (NHMP) solution (an experiment conducted in the IKTS Dresden, Germany).

4.7.2 X-ray diffraction (XRD)

A Philips (PW1710) X-ray diffractometer fitted with monochromatic Cu Kα radiation set at 40 kV and 20 mA was used to determine the phase composition of powders and hot-pressed materials. Scan width (2θ) was between 10^{o} and 80^{o} with a step size of 0.02. Phase identification was done using Philips Analytical X'Pert HighScore® software with an in-built International Centre for Diffraction Data (ICSD) database. B_6O and other peaks were identified by comparing the acquired d-values to the values obtained from the database as well as from previous investigation.

4.7.3 Scanning electron microscopy (SEM) and optical microscopy

The microstructures, composition, and morphology of powders and hot-pressed materials were analysed by means of scanning electron microscopy (SEM) and optical microscopy (Olympus BX41M). A Philips scanning electron microscope

(ESEM XL30) equipped with energy dispersive X-ray spectrometer (EDX) was used to analyse the various elemental composition found in the materials.

4.7.4 Transmission electron microscopy (TEM)

A Phillips CM20 transmission electron microscope (TEM) equipped with EDX was used to analyse the various elemental composition found in the materials.

4.7.5 Density measurements

Densities of hot-pressed materials were measured right after hot pressing using Archimedes principle. Materials with thickness ranging from 2 to 4 mm were immersed in distilled water and boiled for 5 hours in order to remove air from the pores in the materials. The boiled water containing the material was then allowed to cool to room temperature. The following formulae were used to calculate the densities and the open porosities.

Material dry weight = d

Volume of material = V

Soaked weight after boiling in distilled water = we

Suspended weight in distilled water = w

Density of distilled water = 1 g/cm^3

Bulk density, $\rho = d/V = d\rho_{H_2O}/(we - w)$ **[4.2]**

Open porosity, $P_o = (we - w)/\rho_{H_2O}.V = 100\% \times (we - d)/(we - w)$ **[4.3]**

Each mass was determined five times and the mean values used to calculate the density and open porosity of the materials.

Theoretical densities of the hot pressed materials were calculated based on the rule of mixtures according to the following formula:

$$\rho_{theretical} = \sum m_i \Big/ \sum m_i / \rho_i \qquad [\mathbf{4.4}]$$

where, m_i = weight % of component *i*; $\rho_{B6O0.9}$ = 2.55 g/cm^3; ρ_{B2O3} = 1.85 g/cm^3; ρ_{Al2O3} = 4 g/cm^3; ρ_{Y2O3} = 4.85 g/cm^3; ρ_{SiO2} = 2.3 g/cm^3 were used in the calculations. Errors in these calculations are inevitable since B_6O density changes strongly with oxygen content. Therefore in calculating the theoretical densities, the oxygen content was assumed to be 0.9. This oxygen content can only be achieved at high pressure sintering condition. It has also been assumed that the grain boundaries of the hot pressed materials consist of Al_2O_3, Y_2O_3 and SiO_2. In reality these phases react during hot pressing to form yttrium aluminates and yttrium silicates phases having different densities. Another assumption made in the calculation of theoretical densities is weight percent of B_2O_3 (1 wt%) which is present in the starting powder.

4.7.6 Hardness and fracture toughness measurements

Materials for hardness and fracture toughness measurements were prepared as described in the introductory paragraph of section 4.5. The hardness and fracture toughness of the hot pressed materials were measured by indentation technique using a Vicker's indenter (LECO V-100-A2 Vickers Hardness Tester machine) with a load of 5kg and 1kg. Additionally, microhardness tester (FM-700) with loads of 2kg and 0.5kg were used. The length of the cracks generated by the indentation was measured (see figure 4.8) and the crack lengths were used to calculate the fracture toughness of the materials. The following formulae were used to calculate the Vickers hardness and indentation fracture toughness (Anstis equation) of all hot-pressed samples [(9)(84)].

$$Hv = 1854.4P/(2a)^2 \qquad [\mathbf{4.5}]$$

$$K_{IC} = \xi(E/H_v)^{1/2}(P/c^{3/2}) \qquad [\mathbf{4.6}]$$

where *2a* is the arithmetic mean of the two diagonals in micrometers (μm), P is the applied load in Newton (N), ξ = 0.016 is a calibration constant, E is Young's modulus and *c* is the radial crack length (m) as shown in figure 4.8. The unit of the calculated hardness and fracture toughness are given in GPa and $MPam^{1/2}$, respectively [9]. The hardness reported in Chapter 5 will be reported as Hv_x where v is Vickers and *x* is the load at which the hardness was determined. The fracture toughness has been calculated using an applied load of 5kg. Young's modulus of composites containing Al_2O_3/Y_2O_3 and $Al_2O_3/Y_2O_3/SiO_2$ were determined experimentally as described in section 4.7.7. For composites containing only Al_2O_3, a Young's modulus of 514 GPa, determined experimentally by Shabalala [16] has been used to calculate the fracture toughness. For the rest of the composite materials, a Young's modulus of 470 GPa was assumed which is the value determined by Petrak *et al*. [38] for pure B_6O hot pressed sample with zero porosity.

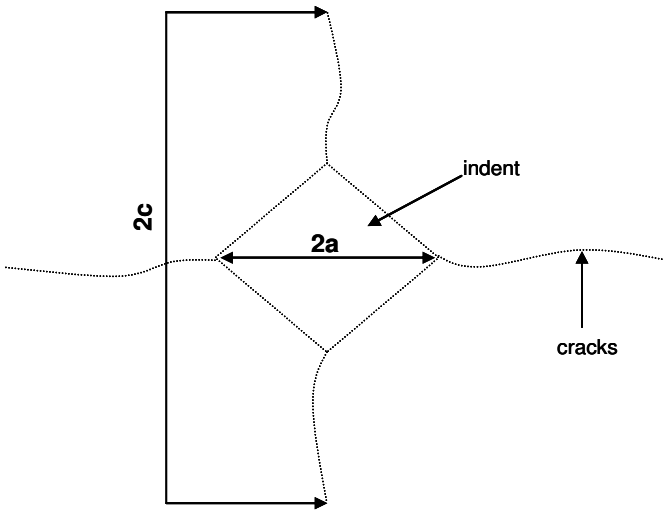

Figure 4.8: Schematic representations of a Vickers indent.

4.7.7 Determination of elastic properties of the hot-pressed composites

The elastic modulus of the hot pressed materials was determined by applying an ultrasound pulses on the cross section of the materials using oil and honey as a transmission media. The velocities of ultrasonic waves were measured by using a piezoelectric transducer and measuring the transit time through the specimen. If v_L is the velocity of longitudinal waves and v_t is the velocity of transverse waves, the shear modulus was calculated from the thickness and density of each material using the following equation:

$$\mu = \rho v_t^{\,2} \qquad [\mathbf{4.7}]$$

Poisson's ratio was calculated from

$$\upsilon = 1 - 2(v_t / v_L)^2 \big/ 2[1 - (v_t / v_L)^2] \qquad [\mathbf{4.8}]$$

and the Young's modulus was obtained from

$$E = 2\mu(1 + \upsilon) \qquad [\mathbf{4.9}]$$

Additionally, the bulk modulus (K) was calculated from the following formula:

$$K = \rho(3v_L^{\,2} - 4v_t^{\,2})/3 \qquad [\mathbf{4.10}]$$

5 Results

5.1 Introduction

This chapter presents the results of the synthesis, milling, admixing and coating of boron suboxide (B_6O) powders, and hot pressing of boron suboxide-based composites. The results also cover heat treatment and elastic properties of selected B_6O composites. Discussion of these results and the relationship between densification-to-microstructure-to-property are presented in Chapter 6.

5.2 Synthesis and milling of boron suboxide (B_6O) powder

5.2.1 Synthesis of boron suboxide (B_6O) powder

SEM micrograph of boron suboxide (B_6O) powder synthesised at Wits as described in section 4.3.1 is shown in figure 5.1a. The synthesised B_6O powder was washed with warm ethanol to dissolve any B_2O_3 formed as a result of using excess boric acid during synthesis. The colour of the synthesized B_6O powder was dark brown. The particle size distribution of B_6O powder, determined using Malvern Mastersizer (described in section 4.7.1), is shown in figure 5.1b. The surface morphology of the powder was predominantly spherical. The shape is a characteristic of B_6O powder samples. Figure 5.1c shows the XRD pattern of the synthesised B_6O powder after washing in ethanol showing only B_6O peaks.

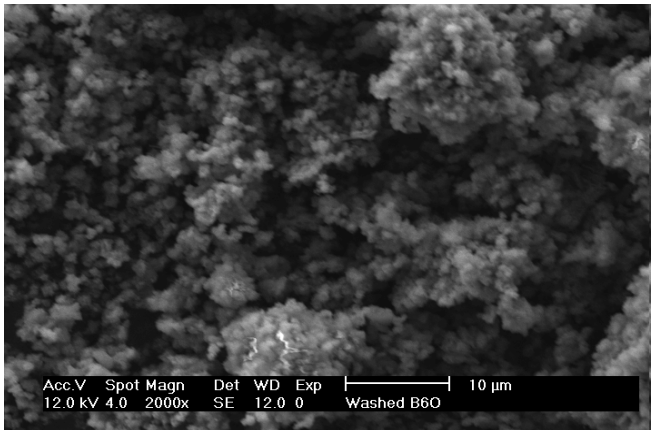

a)

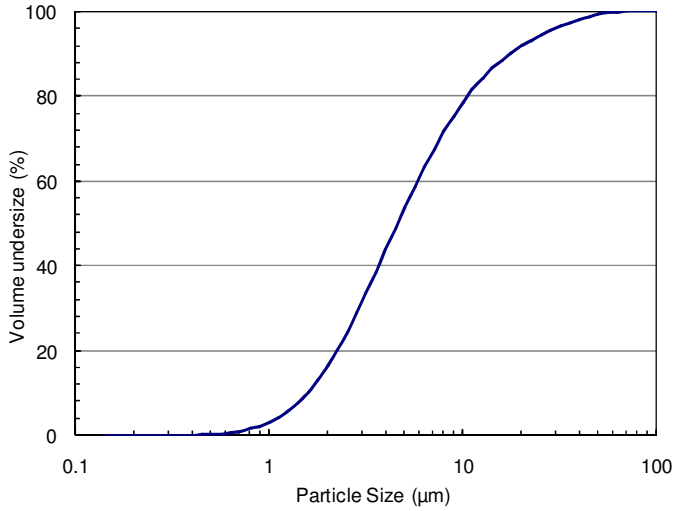

b)

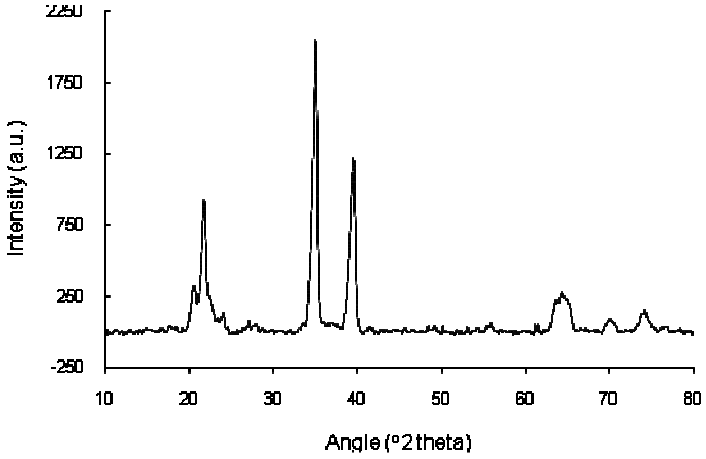

c)

Figure 5.1: As-synthesised boron suboxide powder at Wits. (a) SEM. (b) Size distribution, d_{50} = 4.59 µm (c) XRD pattern after washing in ethanol showing B_6O peaks only.

5.2.2 Milling of boron suboxide (B_6O) powder

For the milling experiments, B_6O powder produced at IKTS – Dresden was used. The milling conditions and the particle sizing techniques are described under sections 4.3.2 and 4.7.1, respectively. Figure 5.2 reveals the dependence of the size distribution of the powders on milling time. As milling time increases the average particle size of B_6O powder decreases and approaches a relatively constant value of ~0.4 µm with 2.5 mm steel balls. A drastic change occurs within the first 20 hours of milling, and subsequently stabilises as the milling time increases. Driving the particles further down with an average particle size (d_{50}) of ~0.2 µm was not attainable, even when 1 mm balls were used at higher mill speed (300 rpm). From these investigations it was concluded that the optimum milling conditions are: 30 hours milling time at 200 rpm using 2.5 mm balls. These conditions were used for the second batch of milling experiments and the result was reproducible (see figure 5.2b). SEM micrographs of the starting powder as well as powders milled for 5, 20 and 30 hours are shown in figure 5.3.

A refractive index of 3.88 and particle absorption value of 1 were used to determine the size distribution of the milled powder (see figure 5.2). However, current experimental work at IKTS to determine the refractive index and particle absorption of the milled B_6O powder gives 2.409 and 0.08, respectively. The size distribution of the milled powders (Figure E1 in Appendix E) is not strongly influenced by the refractive index and particle absorption in comparison to what has been given in figure 5.2. However, coarse particles of more than 10 µm in size were found in the milled powders, although their concentration is very low near the limit of detection.

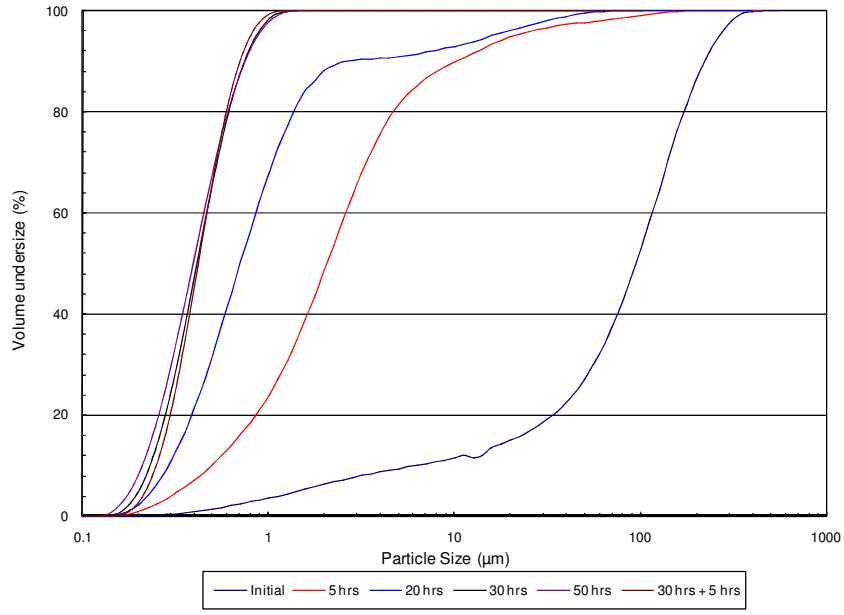

a)

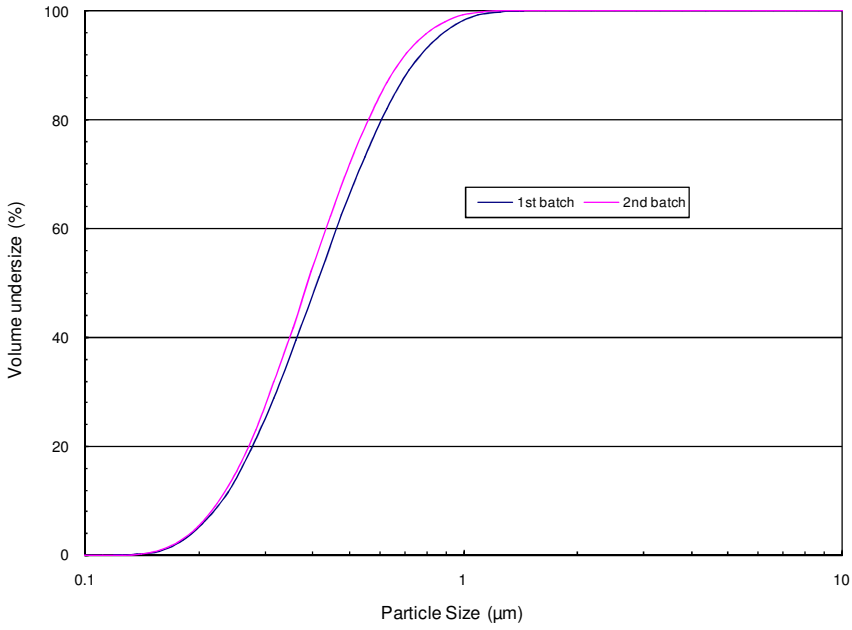

b)

Figure 5.2: Dependence of particle size distribution of B_6O powders on milling time. a) B_6O powder milled for 5, 20, 30 and 50hrs using 2.5 mm balls. Powder milled for 30hrs was further milled for 5hrs using 1 mm balls. b) Comparing size distribution of 1st and 2nd batch of B_6O milled for 30 hrs.

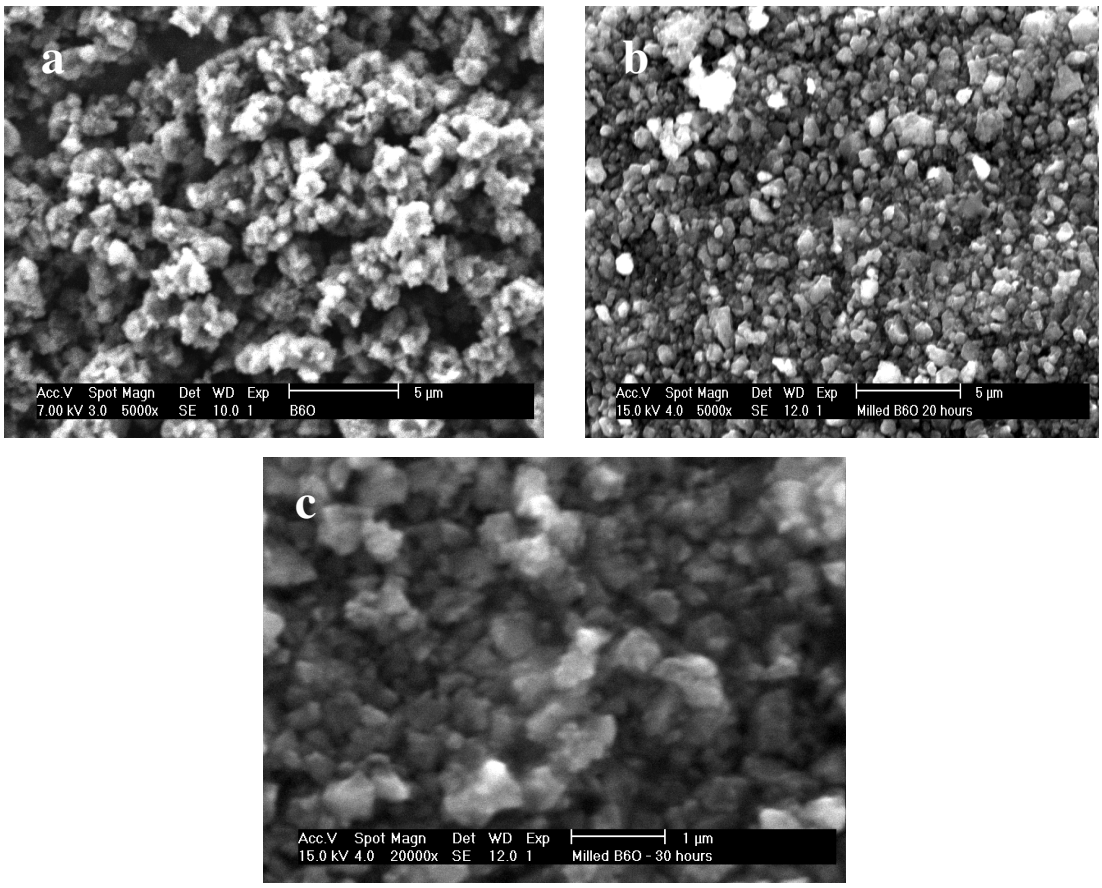

Figure 5.3: SEM images of B_6O powders milled for a) 5hrs. b) 20hrs. c) 30hrs.

5.2.3 Changes in chemical composition of B_6O powder due to milling

Contamination is unavoidable during milling although the extent can be minimised under certain conditions. Milling parameters used in this project are described in section 4.3.2. The profile of contamination of as-milled powder in propan-1-ol is shown in figure 5.4a. It can be seen that as milling time increased the weight loss of balls during milling also increased. This indicates that contamination occurs during milling. Iron (Fe) and chromium (Cr) in the steel balls were the major contaminants in the milled powder. XRD pattern of powder milled for 30 hours is shown in figure 5.4b. Continuous washing of milled powder in 1 M HCl reduced Fe and Cr concentrations strongly (see figure 5.4c). Washing of milled B_6O powder has been

described in section 4.3.3. Chemical analysis (ICP-OES) carried out on washed powders, as described in section 4.3.4, showed some level of contaminations (Table 5.1). Nevertheless, the second washing of B_6O milled for 30 hours (2nd batch) reduced these impurities strongly (see figure 5.5 and table 5.1).

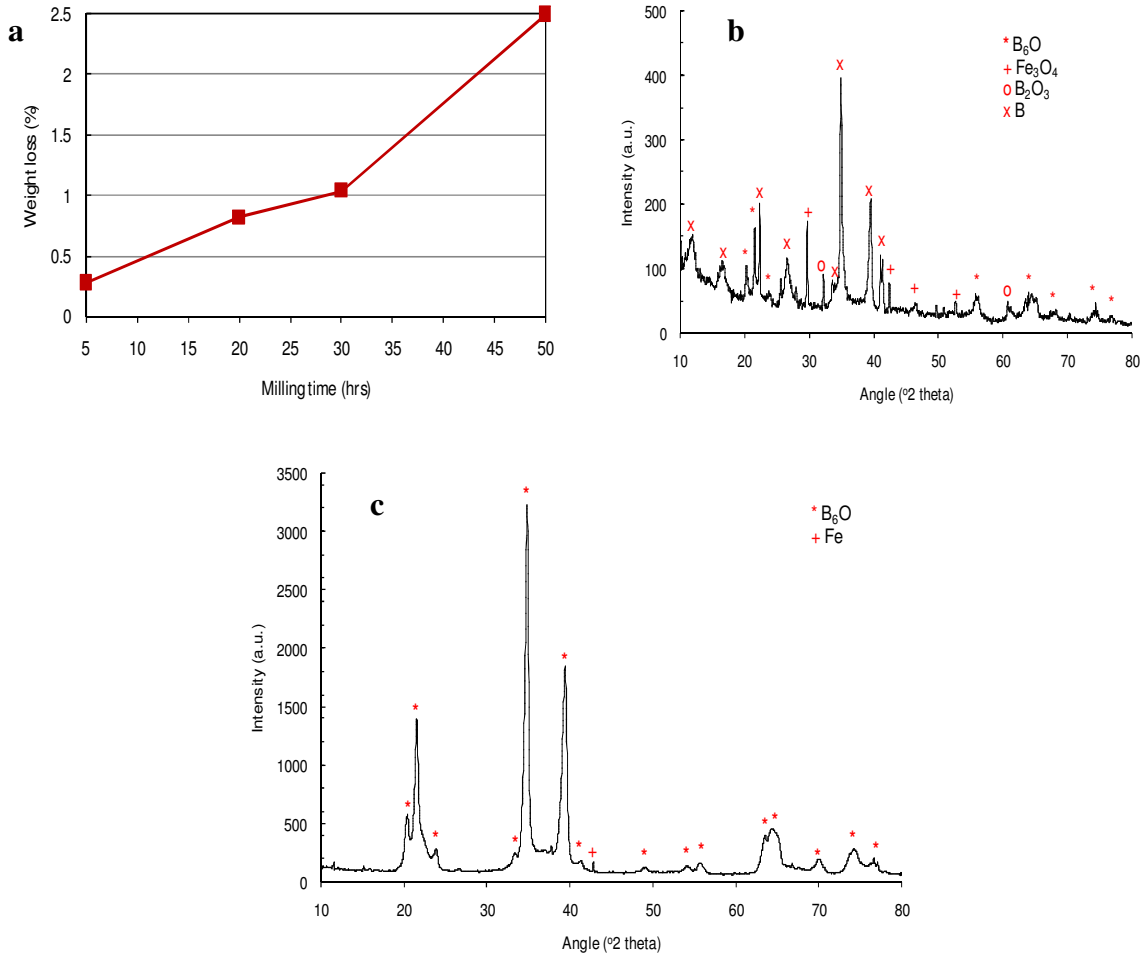

Figure 5.4: a) Graph of weight percent loss of steel balls as a function of time. b) XRD pattern of B_6O milled for 30 hours. c) XRD of B_6O milled for 30 hours and washed in 1 M HCl for 5 days followed by washing in methanol.

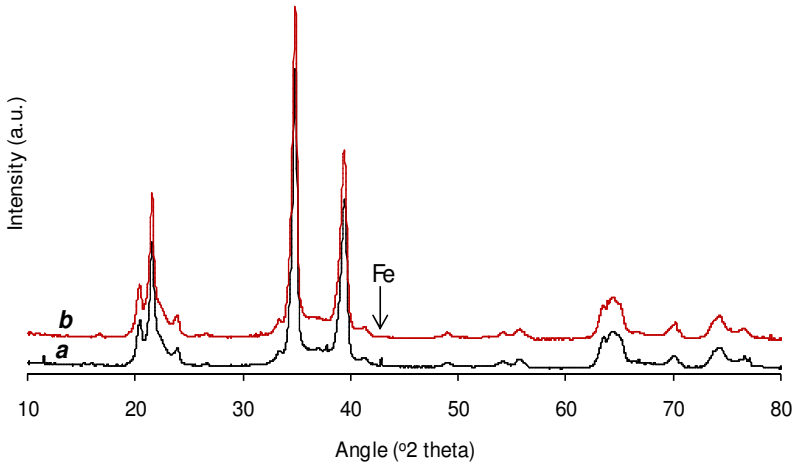

Figure 5.5: XRD pattern of B_6O powder milled for 30 hours showing B_6O peaks. a) First batch. b) Second batch.

Table 5.1: Chemical analysis (ICP-OES) of B_6O milled for 30 and 50 hours and washed in 1 M HCl.

Milling time (hrs)	Fe (wt%)	Cr (wt%)
50	0.86	0.35
30 (First batch)	0.096	0.086
30 (second batch)	0.016	0.018

5.3 Admixing of boron suboxide (B_6O) powder

In section 4.4, admixing of boron suboxide (B_6O) with various additives was described. SEM images of Al_2O_3 (AKP50), Y_2O_3 (grade C from H.C. Starck) and SiO_2 (from Heraeus) powders are shown in figure 5.6. The Al_2O_3 powder was fine and white. The yttria had a fine whisker white appearance whilst the SiO_2 powder showed bimodal distribution. Different weight percent of additives were used in order to

understand the densification mechanisms. The admixed B_6O powders were analysed using XRD and SEM to check the homogeneity of the second phase in the B_6O matrix. A typical XRD pattern of B_6O admixed with Al_2O_3 and Y_2O_3 is shown in figure 5.7. SiO_2 used in this investigation was amorphous. The XRD patterns of B_6O admixed with Al_2O_3, TiC and TiB_2 respectively are also shown in Appendix C.

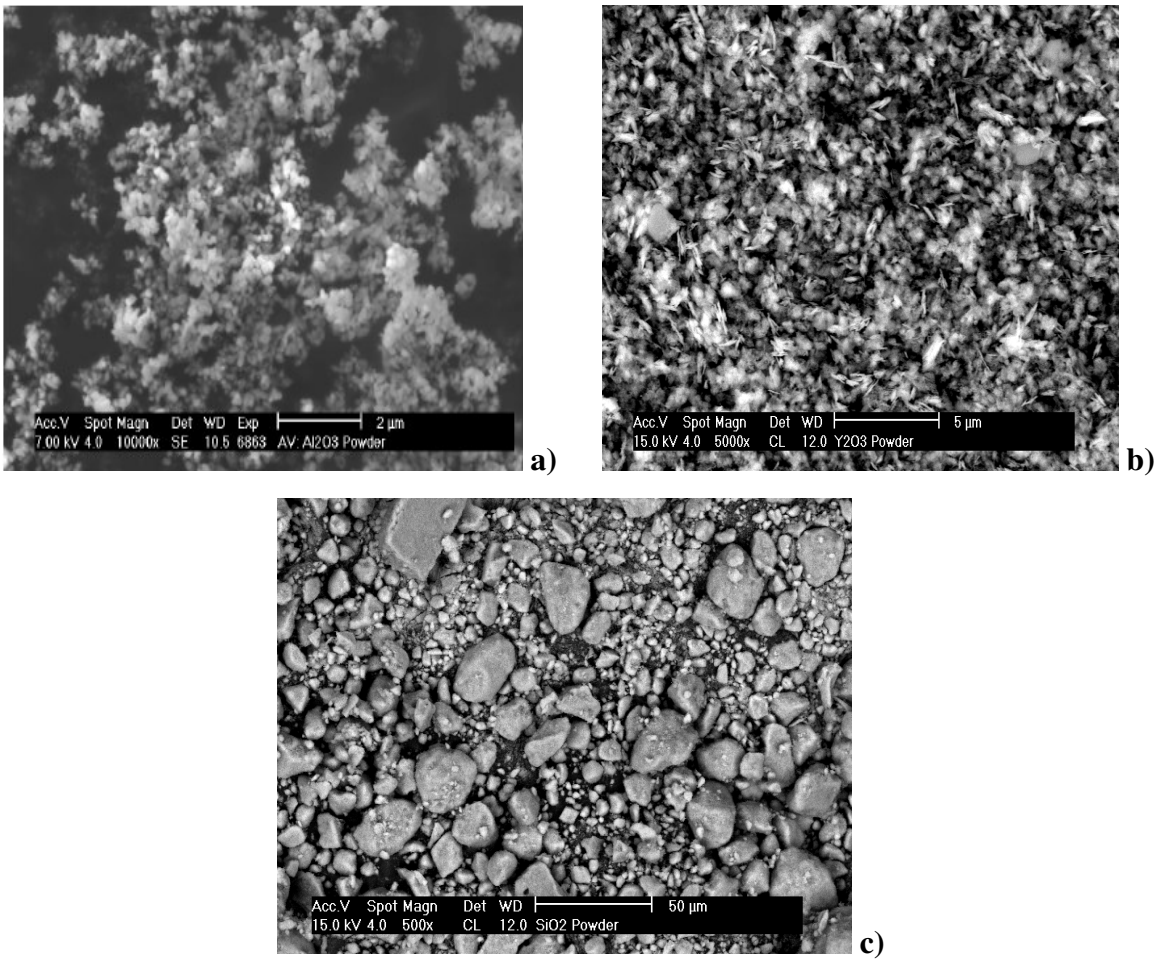

Figure 5.6: SEM of images of (a) Al_2O_3 (AKP50) (b) Y_2O_3 (from H.C. Starck) (c) SiO_2 (from Heraeus) powders.

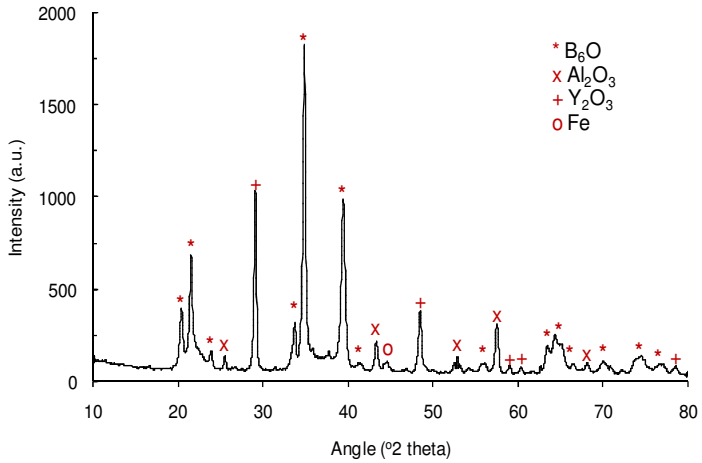

Figure 5.7: XRD pattern of B_6O powder admixed with 2wt % Al_2O_3, 2.65wt % Y_2O_3.

The homogeneity of the admixed powders was investigated by using SEM X-ray mapping which determines the distribution of elements within the admixed powders. EDX mapping of B_6O admixed with 2 wt% Al_2O_3 and 2.65 wt% Y_2O_3 is shown in figure 5.8 showing good homogenous distribution of additives.

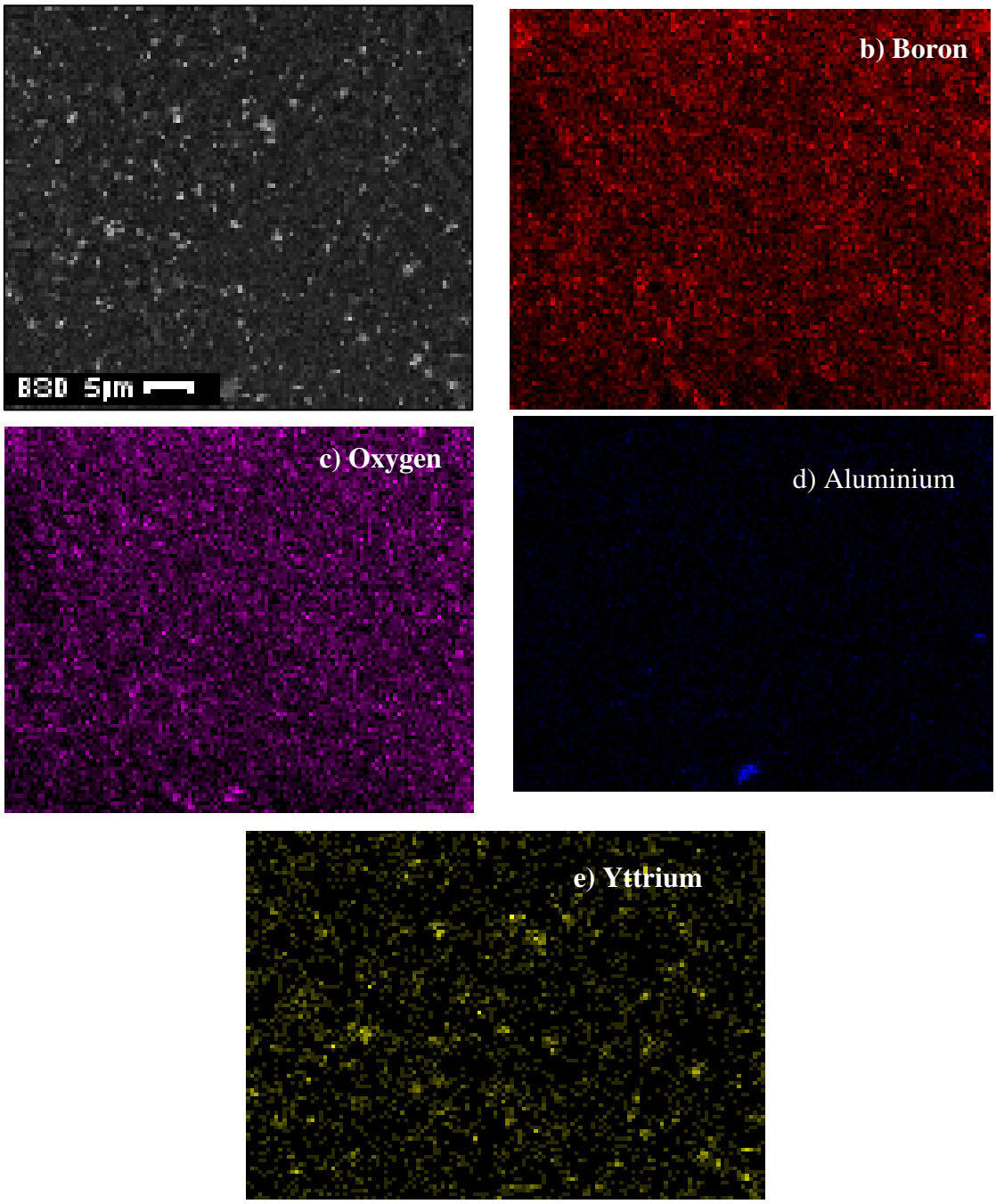

Figure 5.8: EDX mapping images of B_6O admixed with 2wt% Al_2O_3 and 2.65wt% Y_2O_3 showing good homogeneity of admixed powder.

5.4 Doping of boron suboxide powder with palladium

In section 4.5 the doping of B_6O with palladium (Pd) was described. $PdCl_2$ was reduced to Pd during coating. Weight of $PdCl_2$ representing 5 vol. % of Pd was used. Figure 5.9 shows the SEM image and XRD pattern of the doped powder. It is evident that doping of B_6O using this technique produced good distribution of Pd in B_6O powder.

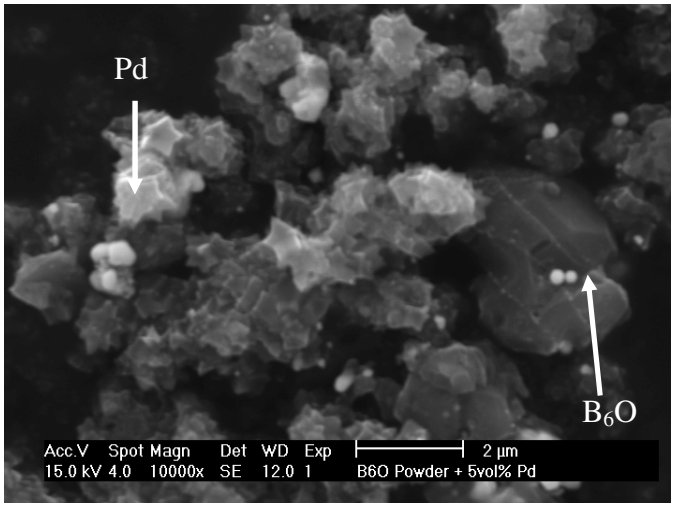

a)

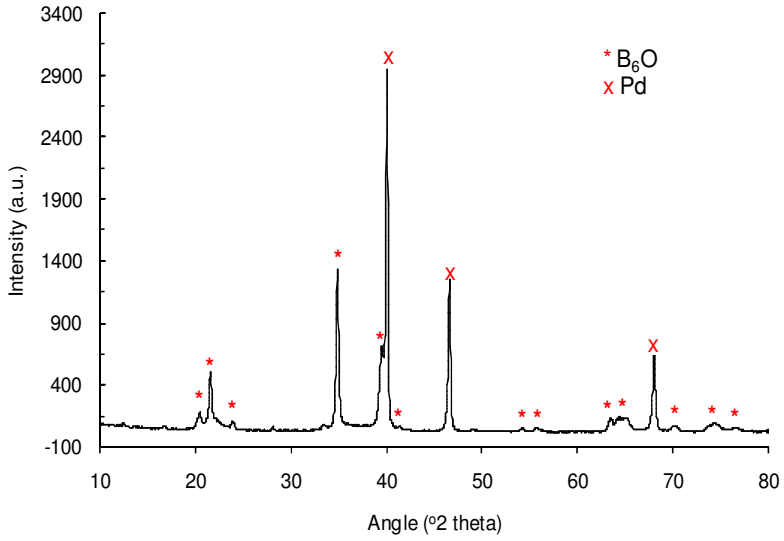

b)

Figure 5.9: Pd-doped B_6O powder (a) SEM (b) XRD pattern.

5.5 Hot pressing of boron suboxide-based materials

5.5.1 Hot pressed 'pure' B_6O materials

B_6O powders (first and second batch milled for 30 hours) were hot pressed at 1900°C for 20 minutes under a pressure of 50 MPa using a uniaxial hot press as described in section 4.6. Additionally, B_6O powder produced at Wits was hot pressed under the same hot pressing conditions. Table 5.2 summarises the properties of the hot-pressed materials. It was found that hot pressed B_6O material produced from first batch of milled B_6O powder (**19**B_6O***a***) had good fracture toughness (3.3 $MPam^{1/2}$) compared to the other two 'pure' B_6O materials which were found to be brittle. The increase in fracture toughness of **19**B_6O***a*** material can be attributed to the relatively high levels of Fe and Cr impurities (table 5.1) in the starting powder. These impurities formed Fe-Cr-B phases at the grain boundaries which resulted in the improved fracture toughness. The measured densities, however, were similar for the milled powders but higher for the **19**B_6O material. 1kg and 0.5kg loads were used to determine the Vickers hardness for **19**B_6O***b*** and **19**B_6O materials since higher loads caused chipping of the B_6O grains. Hence, the facture toughness was not measured for these materials. At these loads, the Vickers hardness of **19**B_6O material was lower than **19**B_6O***a*** and **19**B_6O***b*** materials. The higher hardness values obtained for **19**B_6O***a*** and **19**B_6O***b*** is connected with the smaller grain sizes of the sintered compact. The low fracture toughness observed for **19**B_6O***b*** and **19**B_6O materials agrees with other sintered 'pure' B_6O materials produced thus far which have been found to be brittle. Details of the structure-properties relationship will be dealt with in Chapter 6.

Table 5.2: Properties of 'pure' B_6O material hot pressed at 1900°C under a pressure of 50 MPa for 20 minutes.

Material	Density (g/cm^3)	% Theoretical density	Open porosity (%)	Vickers hardness, Hv (GPa)			K_{IC} ($MPam^{1/2}$)
				5kg	1kg	0.5kg	
19B_6O***a***	2.48	97.3	3.6	30.1±0.8	-	34.7±1.1	3.3±0.1
19B_6O***b***	2.48	97.3	1.1	-	35.7±1.6	35.6±1.5	Brittle
19B_6O*	2.52	98.8	1.9	-	29.4±0.5	32.3±1.4	Brittle

*Produced from B_6O synthesised at Wits University

Figure 5.10 shows the XRD pattern of the hot pressed 'pure' B_6O materials. XRD patterns have similar peaks with two additional peaks for the milled B_6O powders at $2\theta = 45.10^o$ and 45.96^o belonging to Fe-Cr-B phases. These additional peaks are more pronounced in **19**B_6O***a*** material than in **19**B_6O***b*** material because of the high content of these impurities in the former material. The Fe-Cr-B peak is not visible in the XRD spectra for **19**B_6O material (figure 5.10c). Figure 5.11 shows the SEM images of the hot pressed materials. EDX carried out on **19**B_6O***a*** material showed that the secondary phases constitute mainly Fe, Cr and Mg. On the contrary, EDX carried out on **19**B_6O***b*** and **19**B_6O materials showed mainly Mg as the secondary phase. Mg found comes from the boron powder used to produce B_6O. The grain size of the hot pressed compacts could not be determined from the SEM images. This is partly due to lack of good etchant for this material. Additional SEM images of the hot pressed materials are given in Appendix D (Figure D1).

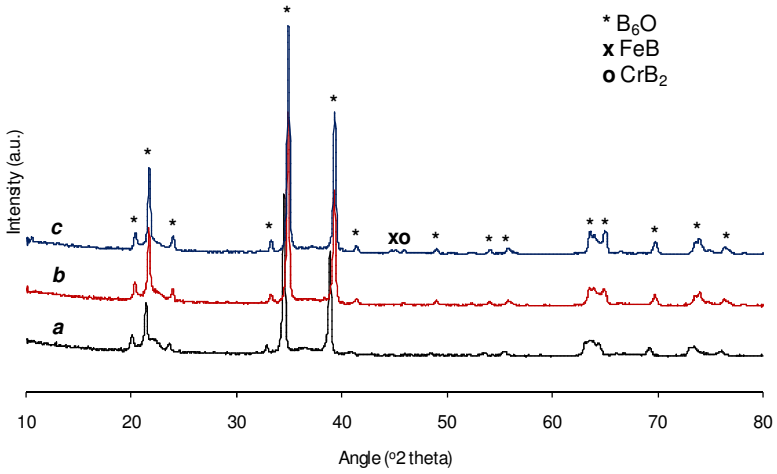

Figure 5.10: XRD pattern for 'pure' B_6O hot pressed material. (a) **19**B_6O. (b) **19**B_6O***b***. (b) **19**B_6O***a***.

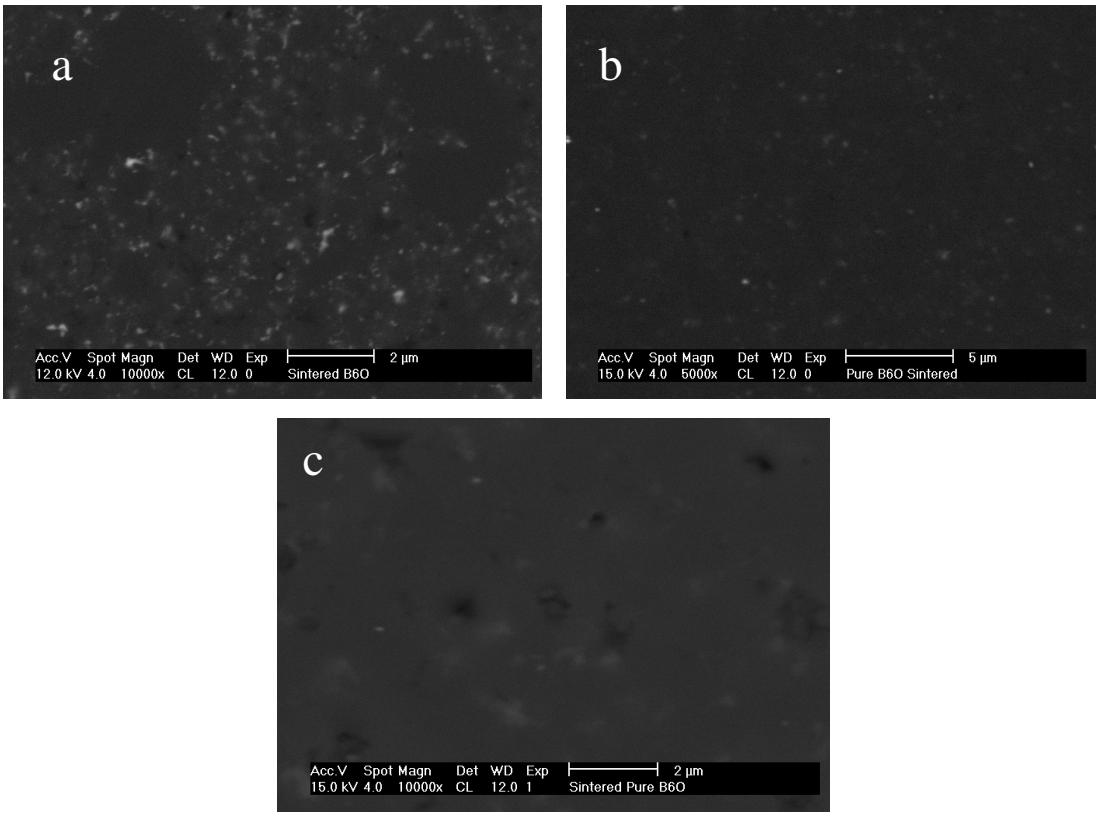

Figure 5.11: SEM micrograph of hot-pressed 'pure' B_6O material. (a) **19**B_6O***a*** (b) **19**B_6O***b*** (c) **19**B_6O.

5.5.2 Hot pressed B_6O-Al_2O_3-Y_2O_3 composites

For this composite, three different Al_2O_3/Y_2O_3 mol % additive ratios were investigated, namely 80:20, 62:83, and 50:50 respectively. Additionally, for each of the three mol % ratios, the amount of Al_2O_3 and Y_2O_3 were varied. The reason was to obtain B_6O composites with various structures and grain boundary chemistry which could assist in establishing relationship between structure and mechanical properties. These process variables were expected to produce materials with varying amounts of phases at the grain boundaries which will subsequently affect the measured properties. The ratios of the different additives have been given in table 4.2 (Chapter 4). Admixing of the powders has also been described in section 4.4. Two different hot pressing profiles were used as described in Chapter 4 (Section 4.6). The first hot pressing profile was used to produce composites from the first batch of milled powder (denoted by '***a***') whilst the second hot pressing profile was used for the second batch of milled powder (denoted by '***b***'). The second hot pressing profile was used to improve densification and also to minimise grain growth. Materials were hot pressed at 1800^{o}C instead of 1900^{o}C as given in section 4.6 under a pressure of 50 MPa for 20 minutes. Mechanical properties and densities measured on the hot pressed materials are given in table 5.3. Naming of the hot pressed materials has been described under section 4.6.2.

Table 5.3: Densities and mechanical properties of B_6O-Al_2O_3-Y_2O_3 composites hot pressed at 1800°C under a pressure of 50 MPa for 20 minutes.

Material	Density (g/cm^3)	% Theoretical density	Open porosity (%)	Vickers hardness (GPa)			K_{IC} ($MPam^{1/2}$)
				Hv_5	Hv_2	$Hv_{0.5}$	
18B_6O**1**Al**1.32**Y***a***	2.41	93.8	3.2	30.4±1.8	29.8±1.7	31.4±1.9	5.4±0.3
18B_6O**1**Al**1.32**Y***b*****-1**	2.51	97.7	3.0	28.8±0.8	-	-	4.7±0.6
18B_6O**1**Al**1.32**Y***b*****-2**	2.54	98.8	0.9	29.7±0.6	32.4±0.9	34.0±1.9	4.1±0.3
18B_6O**2**Al**2.65**Y***a***	2.53	97.7	1.6	29.7±2.8	29.6±0.7	30.7±1.0	6.2±1.0
18B_6O**2**Al**2.65**Y***b*****-1**	2.55	98.5	1.9	29.1±0.4	-	-	4.6±0.4
18B_6O**2**Al**2.65**Y***b*****-2**	2.56	98.8	1.2	29.2±0.7	31.4±1.2	33.0±1.8	4.4±0.1
18B_6O**2.83**Al**3.75**Y***b*****-1**	2.57	98.5	0.8	28.1±0.7	-	-	5.1±0.8
18B_6O**2.83**Al**3.75**Y***b*****-2**	2.57	98.5	1.2	28.2±0.8	29.5±1.4	30.5±0.6	4.1±0.6
18B_6O**2.87**Al**1.58**Y***b***	2.53	98.7	0.8	28.3±0.9	29.4±0.9	31.4±0.9	3.8±0.9
18B_6O**4.06**Al**2.24**Y***b***	2.57	98.5	0.5	29.2±0.7	28.4±0.8	30.7±1.1	4.3±0.8
18B_6O**1.48**Al**3.26**Y***b***	2.57	99.2	1.2	27.9±0.4	27.4±1.0	28.6±0.8	3.8±0.6
18B_6O**2.1**Al**4.63**Y***b***	2.56	97.7	1.4	27.8±1.3	28.0±1.5	29.0±1.2	3.3±0.3
19B_6O***b***	2.48	97.6	1.1	**-**	-	35.6±1.5	Brittle

a) First batch of milled B_6O powder. b) Second batch of milled B_6O powder. 1) First run. 2) Repeated run.

It can be observed that densities obtained for the second batch of milled powder ('***b***') were higher than those obtained for the first batch of milled powder ('***a***'). This is due to the different hot pressing profiles used for these two composites, as discussed in Chapter 4 (Section 4.6). That is for the first batch of milled powder, a longer hot pressing cycle was used in comparison to the one used for the second batch. Additionally, application of pressure was carried out at much lower temperature (1400^{o}C) in comparison to that of the first batch of milled powder (1600^{o}C). Nevertheless, when the same hot pressing profile was used, the densities as well as the mechanical properties measured on the hot pressed composites were reproducible. Additionally, the open porosities obtained for the composites prepared from the first batch of milled powder were higher than for the composites prepared from the second batch of milled powder. This is also connected with the different hot pressing profiles used.

The Vickers hardness values measured for these composites were slightly lower than that of 'pure' B_6O but their fracture toughness values improved significantly. For instance, B_6O composite material containing 1wt% Al_2O_3, 1.32wt% Y_2O_3 (**18**B_6O**1**Al**1.32**Y***b***-**2**) and 2wt% Al_2O_3, 2.65wt% Y_2O_3 (**18**B_6O**2**Al**2.65**Y***b***-**2**) has $Hv_{0.5}$ of 34.0 GPa and 33.0 GPa respectively, compared to $Hv_{0.5}$ of 35.6 GPa for 'pure' B_6O (**19**B_6O***b***). Their corresponding fracture toughness values are 4.1 MPam$^{1/2}$ and 4.4 MPam$^{1/2}$, respectively. For small weight % of the binder added the fracture toughness of the composite increased significantly compare to 'pure' B_6O which was found to be brittle.

Figure 5.12 shows a typical XRD pattern for the three Al_2O_3/Y_2O_3 mol % ratios investigated. Only B_6O crystalline phases were observed except those with 80 mol % Al_2O_3 in the additives. For 80 mol % Al_2O_3, $Al_{18}B_4O_{33}$ crystalline grain boundary phases were formed besides B_6O. Varying the amount of Al_2O_3 and Y_2O_3 (for the same Al_2O_3/Y_2O_3 mol % ratio) did not influence the phases present in the hot pressed materials. The XRD patterns for the other hot pressed composites are given in

Appendix C. Comparing the admixed powder to the hot pressed composites (Figures 5.5 and 5.12), it is evident that Al_2O_3 and Y_2O_3 reacted completely by the disappearing of these phases. However, the grain boundary phases were amorphous and could not be determined by XRD technique.

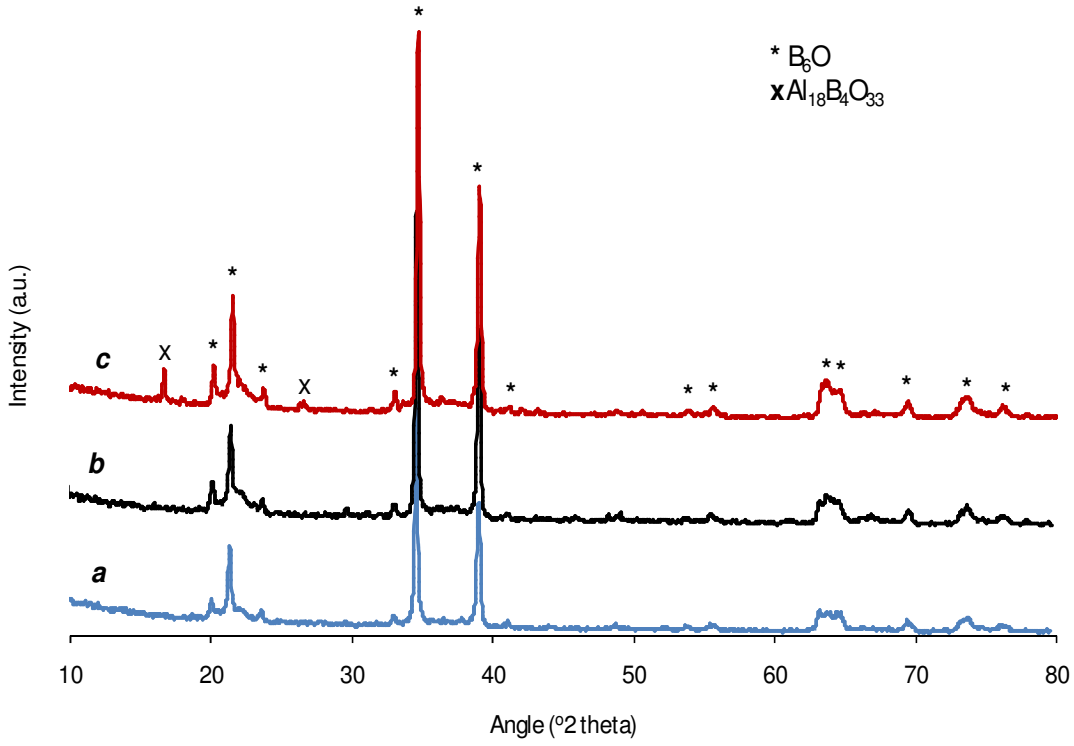

Figure 5.12: XRD pattern of hot pressed B_6O-Al_2O_3-Y_2O_3 composites. a) **18**B_6O**4.06**Al**2.24**Y (80:20 mol %). b) **18**B_6O**1.48**Al**3.26**Y (50:50 mol %). c) **18**B_6O**2**Al**2.65**Y (62:38 mol %).

Figure 5.13 shows backscattered images of hot pressed composite materials produced from first and second batches of milled powders respectively. It can be seen from the SEM images that the porosities in the B_6O composite materials produced from the first batch of milled powder are higher than those produced from the second batch of milled powder. As mentioned, this is connected to the different hot pressing profiles used.

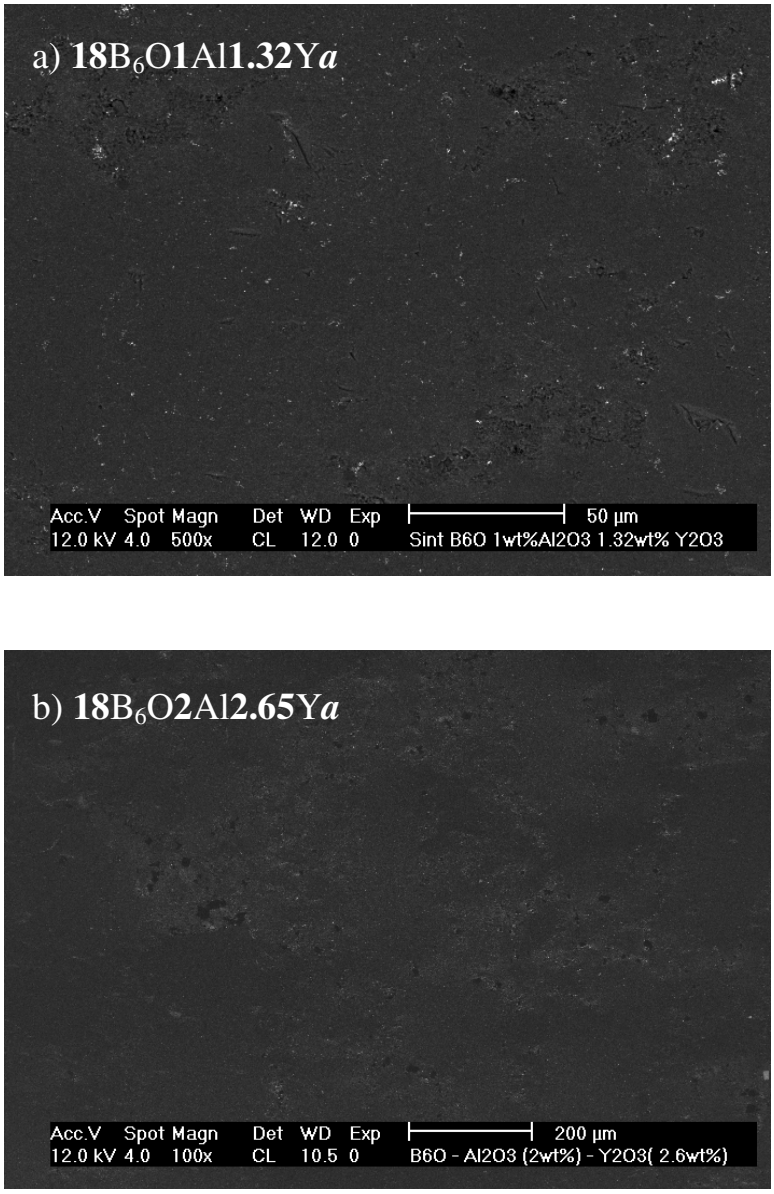

Figure 5.13: Backscattered (SEM) images of Al-Y-doped B_6O hot pressed composite materials.

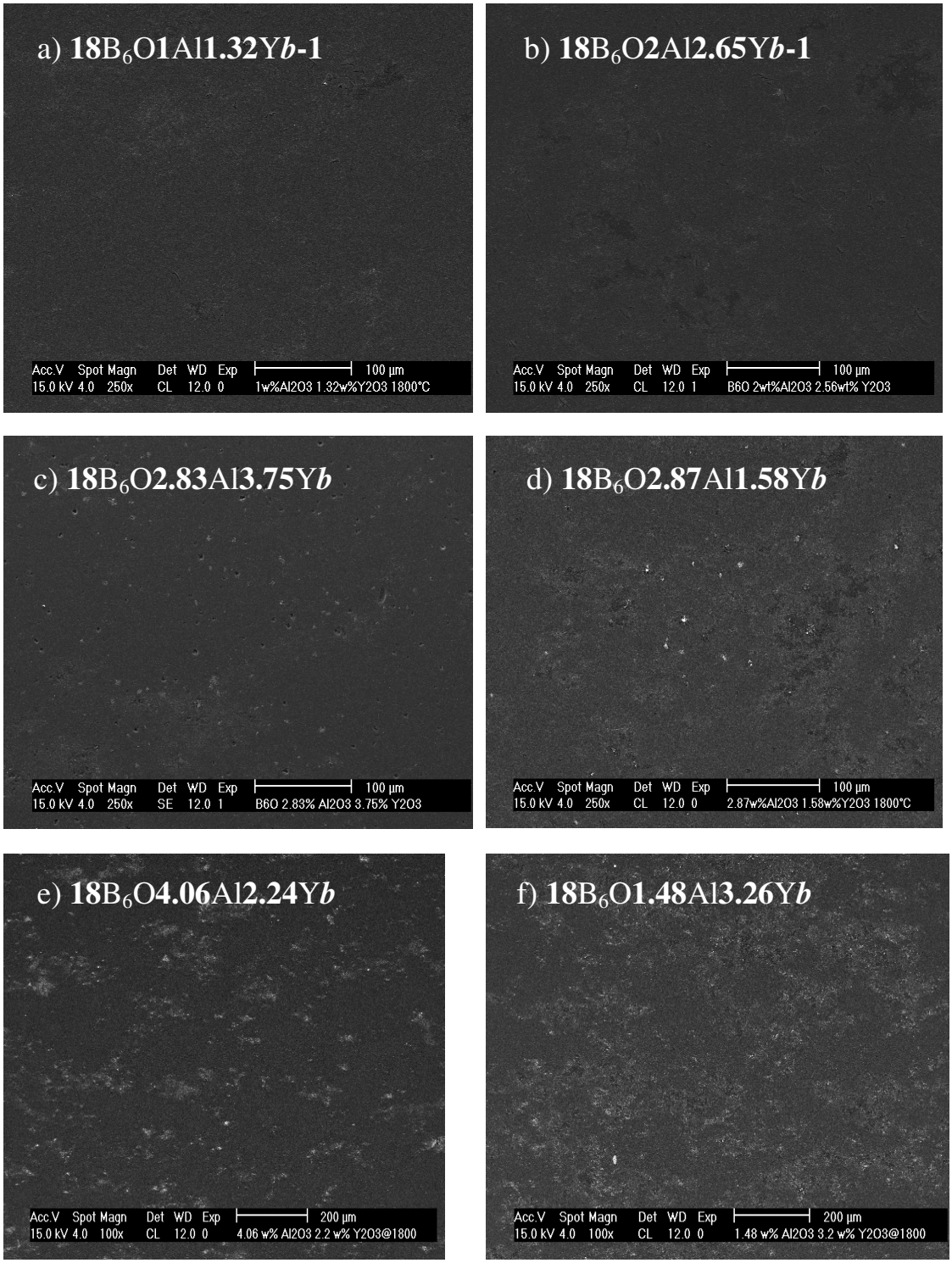

Figure 5.13: Continuation of backscattered (SEM) images of Al-Y-doped B_6O hot pressed composite materials. Additional images are given in Appendix D.

It could also be seen from the micrographs that as the amount of Al_2O_3/Y_2O_3 increased, there is segregation (pockets) of liquid phases in the microstructure due to bad wetting behaviour of Y_2O_3. Porosities also increased at the grain boundaries as the amount of additive increased. Energy dispersive X-ray (EDX) analyses show that these pockets of liquid phase has higher amount of yttrium than aluminium. Materials containing fewer amount of additives (**18**B_6O**1**Al**1.32**Y***b*****-1** and **18**B_6O**2**Al**2.65**Y***b*****-1**) had good homogeneity of the binder phase in the hot pressed composites. It can also be observed from the SEM images that all the hot pressed materials were nearly complete dense, especially for the composites produced from the second batch of milled powder. There is also some pullout of the binder phase due to long polishing of the materials. It must be mentioned here that B_6O is an ultrahard material. In order to obtain scratch free surface after grinding, long polishing times were required. However, the grain boundary phase is not as hard as B_6O. This caused pullout of the binder phases which looks like pores in the materials. At higher magnifications, one could observe little or no grain growth in the hot pressed compacts produced from the second batch of milled powder (see Appendix D). This is partly due to the high ramp rate (20^oC/min) as well as lower hot pressing temperature (1800^oC) used.

TEM analysis was carried out on Al-Y-doped B_6O composite sintered using spark plasma sintering (SPS) technique at IKTS to understand the structure and composition of the grain boundary as well as to assist relating structure to the properties for this composite. This material was sintered at 1800^oC under 50 MPa for 5 minutes. The composition was similar to **18**B_6O**2**Al**2.65**Y material prepared in this work and therefore can be compared with it. Figure 5.14a shows that the individual B_6O grains are not well faceted and the material has isolated pockets of glassy phases. The grain sizes of B_6O in this material are homogenous and in the submicron range; same as the starting powder indicating no grain growth. There were also some dislocations and stacking faults within the B_6O grains as a result of the hot pressing processes. Multiple twin boundaries in B_6O grains were observed. Glass phases observed (Figure 5.14b) decomposed when exposed to incident electron beam which

indicates that the glass phase is electron beam sensitive. EDX analysis reveals the incorporation of B, Al, Y, Mg and O into the glassy phase. Mg in this case comes from boron starting powder. Figure 5.14c shows a typical HRTEM image of grain boundaries observed in the Al-Y-doped B_6O material. No evidence of grain boundary wetting was observed and was therefore concluded that these grain boundaries have clean interfaces. Hence the sintering process could not be fully described as a typical liquid phase sintering.

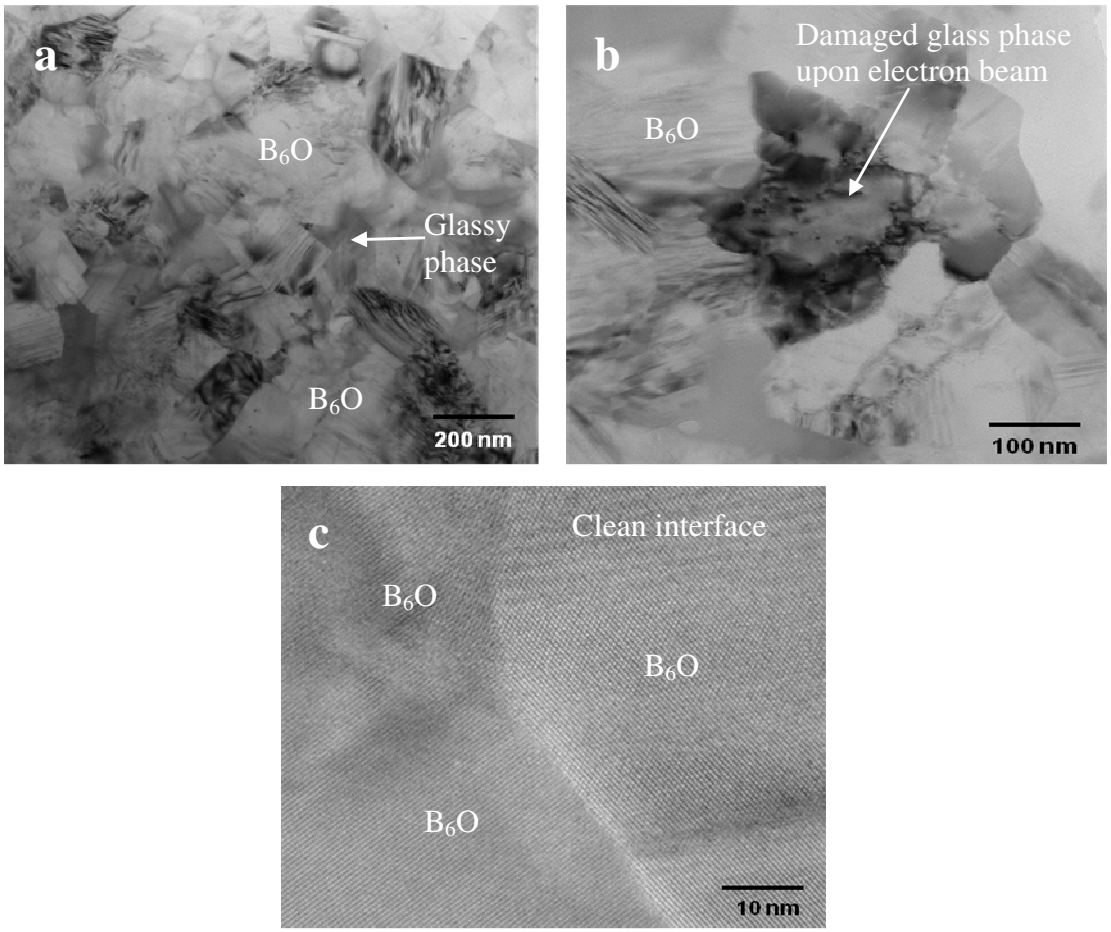

Figure 5.14: TEM micrograph of (a) overall microstructure of the Al-Y-doped B_6O composite material sintered via SPS showing no grain growth and isolated pockets of glassy phase. (b) damaged glassy phase upon electron beam radiation for about 1 minute indicating the sensitivity of the glassy phase. (c) a triple grain junction in the Al-Y-doped B_6O material which does not contain any residual glass phase (clean interface).

The fractured pieces of selected Al-Y-doped B_6O hot pressed materials were examined to understand the fracture mode that occurred in this composite using SEM. Figure 5.15 shows the images obtained. There was pullout in **18**B_6O**2**Al**2.65**Y***b*****-2** material (Figure 5.15b). From these micrographs it was observed that fracture was mainly transgranular. Higher resolution was difficult to obtain. Nevertheless, it is thought that fracture may also occur along the twin boundaries and stacking faults as indicated by TEM results.

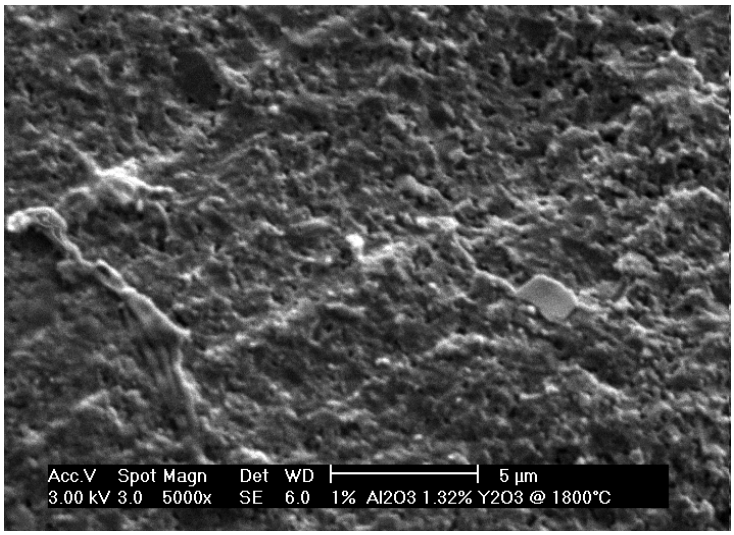

a)

b)

Figure 5.15: SEM images of fractured surfaces of Al-Y-doped B_6O hot pressed materials. a) **18**B_6O**1**Al**1.32**Y***b*****-1**. b) **18**B_6O**2**Al**2.65**Y***b*****-2**.

The hot pressing temperature for the composites was optimised using B_6O composite containing 2 wt% Al_2O_3 and 2.65 wt% Y_2O_3. The admixed powder was hot pressed at 1750°C and 1850°C under a pressure of 50 MPa for 20 minutes and the properties measured and compared to composite material hot pressed at 1800°C. Table 5.4 shows the densities and mechanical properties measured for the materials produced.

Table 5.4: Mechanical properties of B_6O composite material containing 2 wt% Al_2O_3 and 2.65 wt% Y_2O_3 hot pressed at different temperatures.

Material	Density (g/cm^3)	% Theoretical density	Open porosity (%)	Hv_5 (GPa)	$Hv_{0.5}$ (GPa)	K_{IC} ($MPam^{1/2}$)
175B_6O**2**Al**2.65**Y***a***	2.27	87.6	5.9	16.6±2.1	-	7.2±0.6
185B_6O**2**Al**2.65**Y***a***	2.58	99.6	1.2	27.8±2.1	30.7±1.4	3.4±0.1
18B_6O**2**Al**2.65**Y***a***	2.53	97.7	1.6	29.7±2.8	30.7±1.0	6.3±1.0

Material hot pressed at 1750°C (**175**B_6O**2**Al**2.65**Y***a***) had the least density whilst material hot pressed at 1850°C (**185**B_6O**2**Al**2.65**Y***a***) had the highest density. Material hot pressed at 1800°C (**18**B_6O**2**Al**2.65**Y***a***) had intermediate density. Nevertheless, hardness value obtained for **185**B_6O**2**Al**2.65**Y***a*** using 5kg load was slightly lower than that obtained for **18**B_6O**2**Al**2.65**Y***a*** material under the same load. However, the microhardness values for both samples are similar. This is an indication that at higher temperature (1850°C) grain growth occurs as well as decomposition of boron oxide rich phases. **175**B_6O**2**Al**2.65**Y***a*** material had the highest fracture toughness. This is connected with the high open porosity (5.9%) in the hot pressed material which inhibits crack propagation. The fracture toughness of material hot pressed at 1800°C was better than material hot pressed at 1850°C. The lower fracture toughness could be connected with the segregation of grain boundary phase in the microstructure (see figure 5.17c). Based on these properties, the optimum hot pressing temperature for these composites was established to be 1800°C.

Figure 5.16 shows the XRD pattern for these composites while figure 5.17 shows the backscattered (SEM) images of the composites. Additional SEM images of these composite materials are given in Appendix D (Figure D4). Phases identified using XRD were similar for all hot pressed materials showing only B_6O crystalline phases. It was observed that the XRD peaks become sharper with increasing temperature. Thus, as the hot pressing temperature increased the crystallinity of B_6O changes, changing the oxygen occupancy in the B_6O structure. A possible way of relative estimation of the amount of oxygen would be to calculate the intensity ratio of the different peaks. The theoretical calculations using the crystal structure data (ICSD 73624) indicate that the ratio of the (101) and (104) peaks are very sensitive to the oxygen content [(85)]. Figure 5.18 shows the sensitivity of oxygen content on the ratio (101)/(104) peaks. When the ratios at 1750, 1800, and 1850^{o}C were calculated, 4.5, 8.5 and 10.6% respectively, were obtained. This means that the oxygen occupation factor decreases with increasing sintering temperature. This could be connected with decomposition at higher temperature. EDX on the binder phases showed mainly Al, Y and O. The SEM images show that at hot pressing temperature of 1850^{o}C, the binder phase was not homogenously distributed. There is segregation of the grain boundary phases in the microstructure. The reason for the large segregations in the microstructure is probably connected with the bad wetting behaviour of yttria as shown in the TEM results.

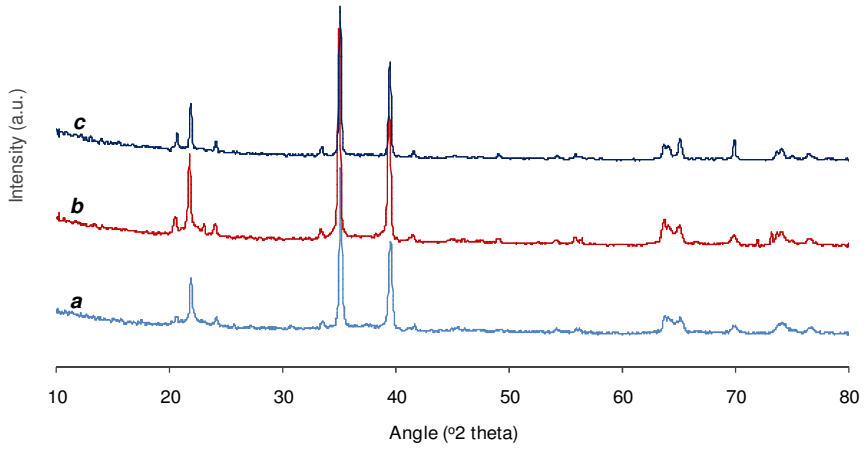

Figure 5.16 : XRD pattern of B_6O composite materials hot pressed at different temperatures showing only B_6O peaks. a) 1750°C (b) 1800°C (c) 1850°C.

It has been reported that B_2O_3 present on the surfaces of B_6O particles affect the mechanical properties of the hot pressed compacts. To test how the presence of B_2O_3 will affect the properties of this composite, B_6O admixed with 2 wt% Al_2O_3 and 2.65 wt% Y_2O_3 was repeatedly washed in warm water followed by washing in warm methanol to strongly reduce B_2O_3 content in the powder. Part of this admixed powder was hot pressed immediately after washing at 1800°C under a pressure of 50 MPa for 20 minutes. The other part of the admixed powder was heated at 250°C for 90 minutes to partially oxidise B_6O to B_2O_3. Weight of the admixed powder was measured before and after the heat treatment. Weight gain was 0.6% which was used as a measure of the amount of B_2O_3 that has been introduced into the admixed powder. The calculated B_2O_3 introduced is about 1 wt%. This heat treated powder was also hot pressed under the same hot pressing conditions as the powder that was not heat treated (hot pressing conditions: 1800°C, 50 MPa, 20 minutes). Table 5.5 summarises the properties measured for these composite materials.

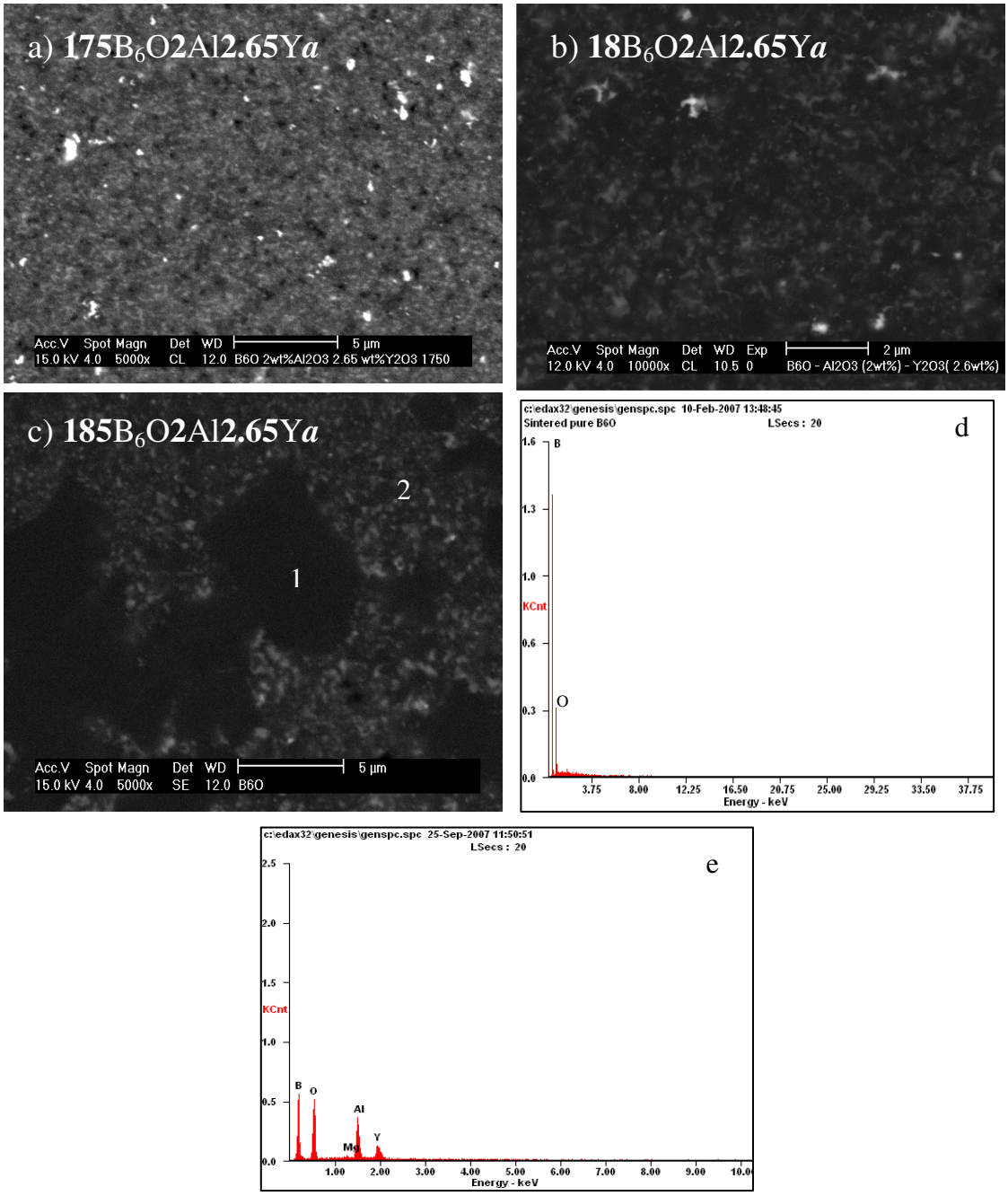

Figure 5.17: Backscattered (SEM) images of B_6O composite materials hot pressed at a) 1750°C b) 1800°C c) 1850°C d) EDX at spot 1. e) EDX at spot 2. The segregation of grain boundary in 'c' could be due to changes in wetting behaviour or grain growth as temperature increases. More detailed analyses are needed to understand this.

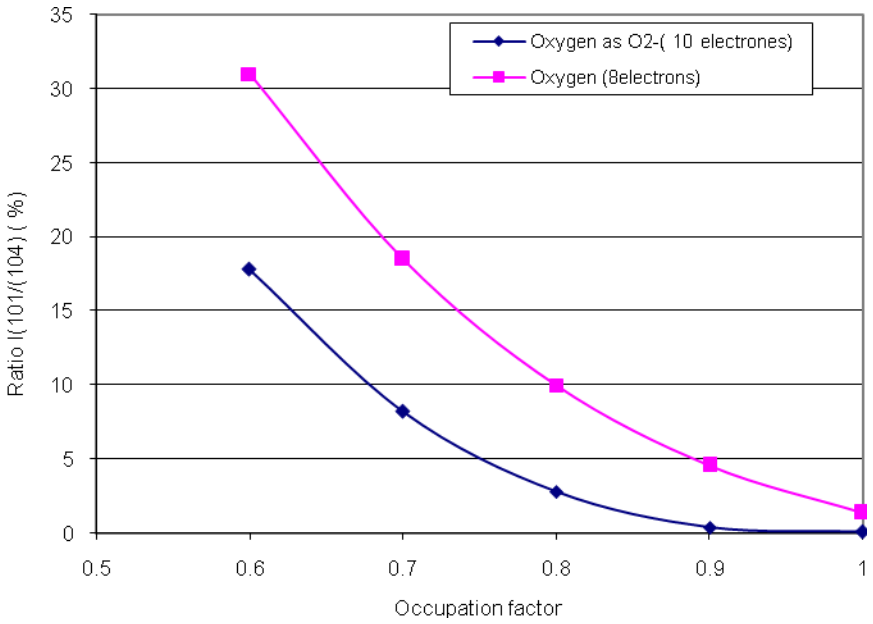

Figure 5.18: Ratio of the intensity of (101)/ (104) peaks as a function of the occupation factor of the oxygen position (an investigation carried out at IKTS) [85].

Table 5.5: Densities and mechanical properties of B_6O composites containing 2 wt% Al_2O_3 and 2.65 wt% Y_2O_3 produced from untreated and heat treated powders.

Material	Density (g/cm^3)	% Theoretical density	Open porosity (%)	Hv_5 (GPa)	K_{IC} ($MPam^{1/2}$)
18B_6O**2**Al**2.65**Y***b*****-1**	2.55	98.5	1.9	29.1±0.4	4.6±0.4
18B_6O**2**Al**2.65**Y**HTP*b***	2.54	98.4	1.7	26.4±0.5	4.3±0.3

It was observed that introducing B_2O_3 before hot pressing decreased the hardness value by 9.6%. The measured densities and fracture toughness were somewhat similar. This is an indication that the presence of B_2O_3 strongly affects the hardness

of hot pressed compacts. This means that the level of B_2O_3 in the starting B_6O powder must be kept very low in order to have very good mechanical properties of the sintered compact. Figure 5.19 compares the SEM images of the two materials. The presence of liquid B_2O_3 during hot pressing resulted in large segregation of the grain boundary phase. Cracks in the microstructure were caused by pullout of B_2O_3 at the grain boundaries during polishing of the material. Additional images of material produced from heat treated powder are given in Appendix D (Figure D5).

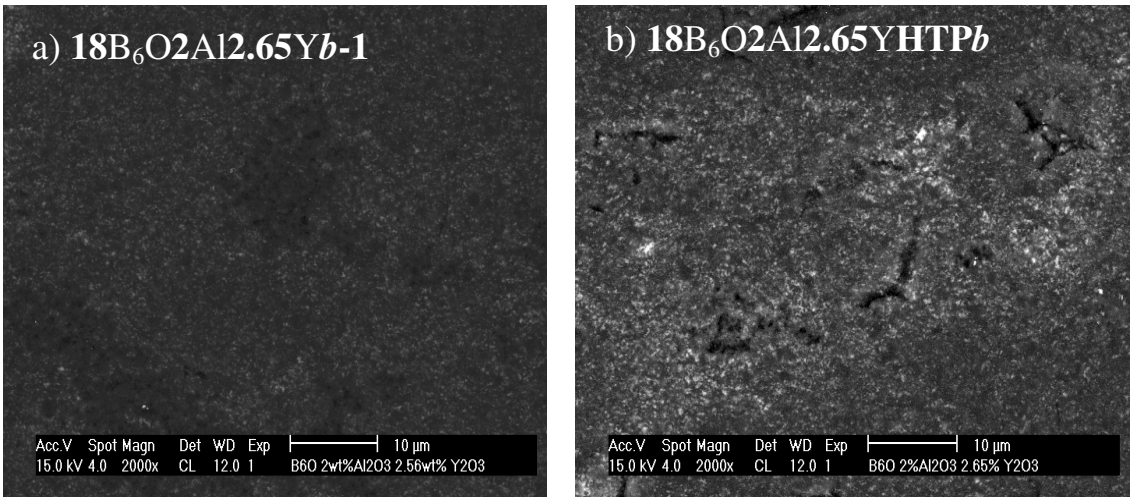

Figure 5.19: Backscattered (SEM) images of B_6O composite containing 2 wt% Al_2O_3 and 2.65 wt% Y_2O_3 produced from a) untreated and b) heat treated of admixed powders.

5.5.3 Hot pressed B_6O-Al_2O_3-Y_2O_3-SiO_2 composites

Having produced and obtained a good combination of properties for B_6O composites containing Al_2O_3 and Y_2O_3 additives, SiO_2 was introduced to the B_6O-Al_2O_3-Y_2O_3 system to test the effect of SiO_2 addition on densification of these composite materials. SiO_2 was also added to test any structure to property changes that will occur in the composites. SiO_2 used in this work was amorphous. Details of the composition of the different composites are given in table 4.2. XRD pattern of $B_6O/Al_2O_3/Y_2O_3/SiO_2$ admixed powder is similar to the one shown in figure 5.7 since

SiO_2 is amorphous and cannot be determined by XRD technique. A typical XRD pattern of B_6O admixed with Al_2O_3, Y_2O_3, and SiO_2 is given in Appendix C (figure C4). Composites were produced by hot pressing at 1800°C under a pressure of 50 MPa for 20 minutes. The densities and mechanical properties measured are given in table 5.6.

Table 5.6: Densities and mechanical properties of B_6O composites containing Al_2O_3, Y_2O_3 and SiO_2 as additives.

Material	Density (g/cm^3)	% Theoretical density	Open porosity (%)	Vickers hardness, (GPa)		K_{IC} ($MPam^{1/2}$)
				Hv_5	$Hv_{0.5}$	
18B_6O**2**Al**2.65**Y**1**Si***a*	2.46	95.0	4.4	30.0±1.6	30.9±0.9	4.9±1.0
18B_6O**2**Al**2.65**Y**1**Si***b*	2.55	98.5	1.2	27.6±0.6	30.9±1.1	3.2±0.5
18B_6O**2.7**Al**3.57**Y**1.35**Si***b*	2.58	98.9	0.1	27.4±1.0	31.4±1.9	3.7±0.4
18B_6O**2.54**Al**1.4**Y**1.27**Si***b*	2.56	99.2	1.1	27.4±0.9	27.6±0.4	3.9±0.9
18B_6O**3.43**Al**1.89**Y**1.72**Si***b*	2.59	100.0	0.5	28.3±0.4	29.8±0.8	4.6±0.8
18B_6O**2**Al**2.65**Y***b***-1**	2.55	98.5	1.9	29.1±0.4	33.0±1.8	4.6±0.4
19B_6O***b***	2.48	97.6	1.1	-	35.6±1.5	Brittle

Densities obtained for the composites produced from the second batch of milled powder were once again higher than that produced from the first batch of milled powder. As mentioned, the reason is connected to the different hot pressing profiles used. Densities obtained were more than 98% of the theoretical densities. For comparison, the results of B_6O composite without SiO_2 addition hot pressed under the

same conditions (**18**B_6O**2**Al**2.65**Y***b*****-1**) and 'pure' B_6O (**19**B_6O***b***) are also given in table 5.6.

Vickers hardness values obtained for composites with SiO_2 additions were lower compared to those without SiO_2 additions. Vickers hardness obtained for composite produced from the first batch of milled powder (**18**B_6O**2**Al**2.65**Y**1**Si***a*) was very high even at 5kg load. This composite (**18**B_6O**2**Al**2.65**Y**1**Si***a*) also had the highest porosity with the lowest density.

XRD analyses on the hot pressed composites are shown in figure 5.20. The XRD pattern of the composite without SiO_2 has been added for comparison. Only B_6O crystalline phases were identified for compositions containing 62 mol % Al_2O_3 in the additives. For 80 mol % Al_2O_3 in the additives, small crystalline phase at $2\theta = 16.64^o$ belonging to $Al_{18}B_4O_{33}$ was observed. XRD patterns with high SiO_2 content produced better crystalline phases. Si-containing crystalline phase was not observed in the XRD spectra. SEM images of these composites are shown in figure 5.21. Additional images are given in Appendix D (Figure D6). It is obvious from the micrographs that exaggerated grain growth occurred under the hot pressing conditions when the amount of SiO_2 was increased, say from 1 wt% to 1.35 wt%. EDX analysis on the secondary phases shows the presence of Si. This Si could form some amorphous phases such as mullite or yttrium silicates as predicted based on thermodynamic considerations (see Chapter 3). Details of the structure to property relationship are dealt with in Chapter 6.

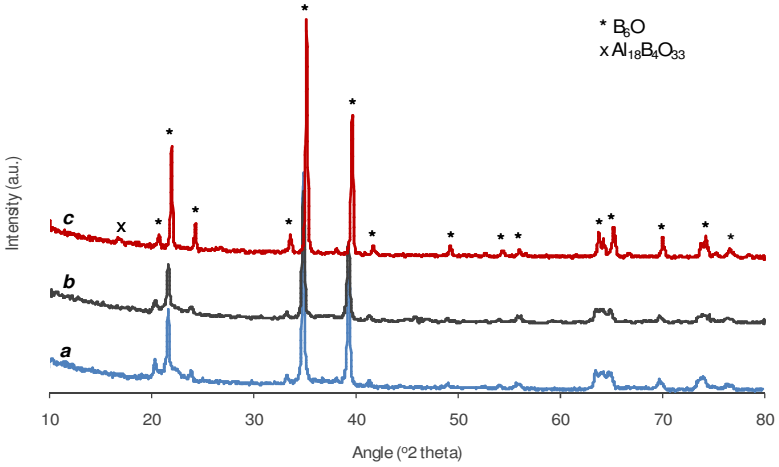

Figure 5.20: XRD pattern of B_6O composites a) **18**B_6O**2**Al**2.65**Y***b*** b) **18**B_6O**2**Al**2.65**Y**1**Si***b*** and c) **18**B_6O**3.43**Al**1.89**Y**1.72**Si***b***.

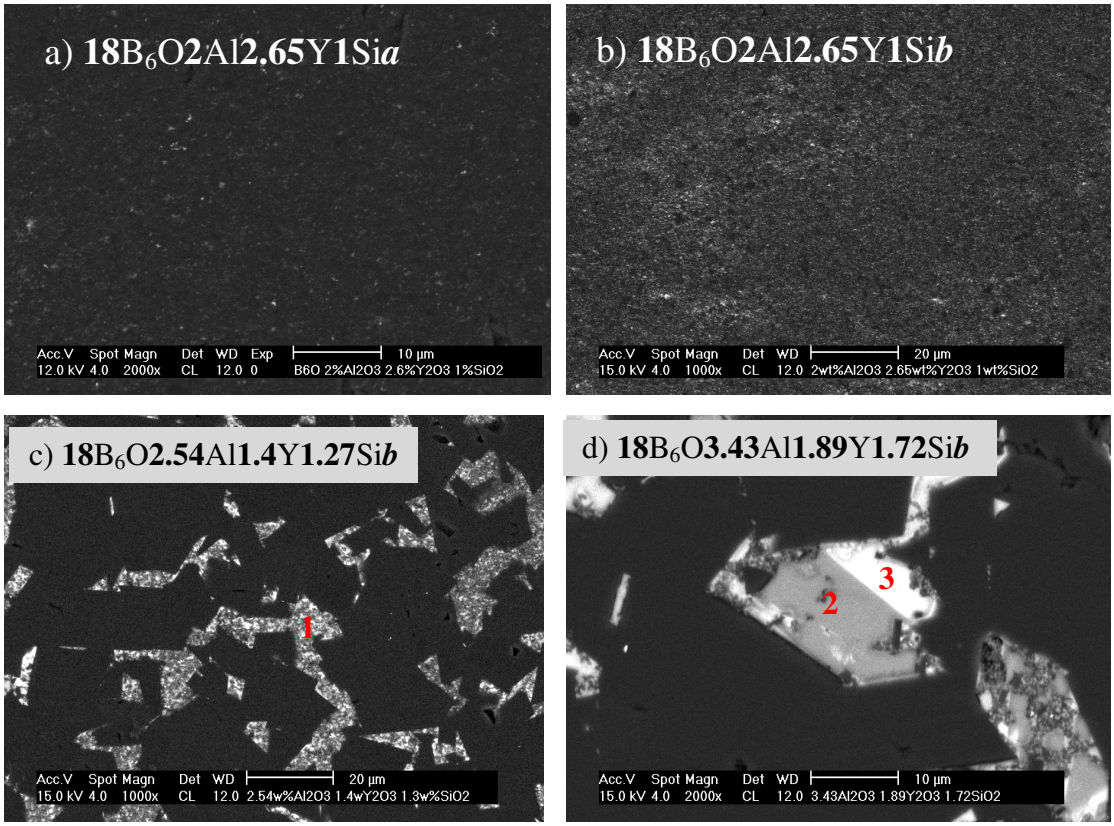

Figure 5.21: Backscattered (SEM) images of Al-Y-Si-doped B_6O hot pressed composites showing grain growth in higher SiO_2 content.

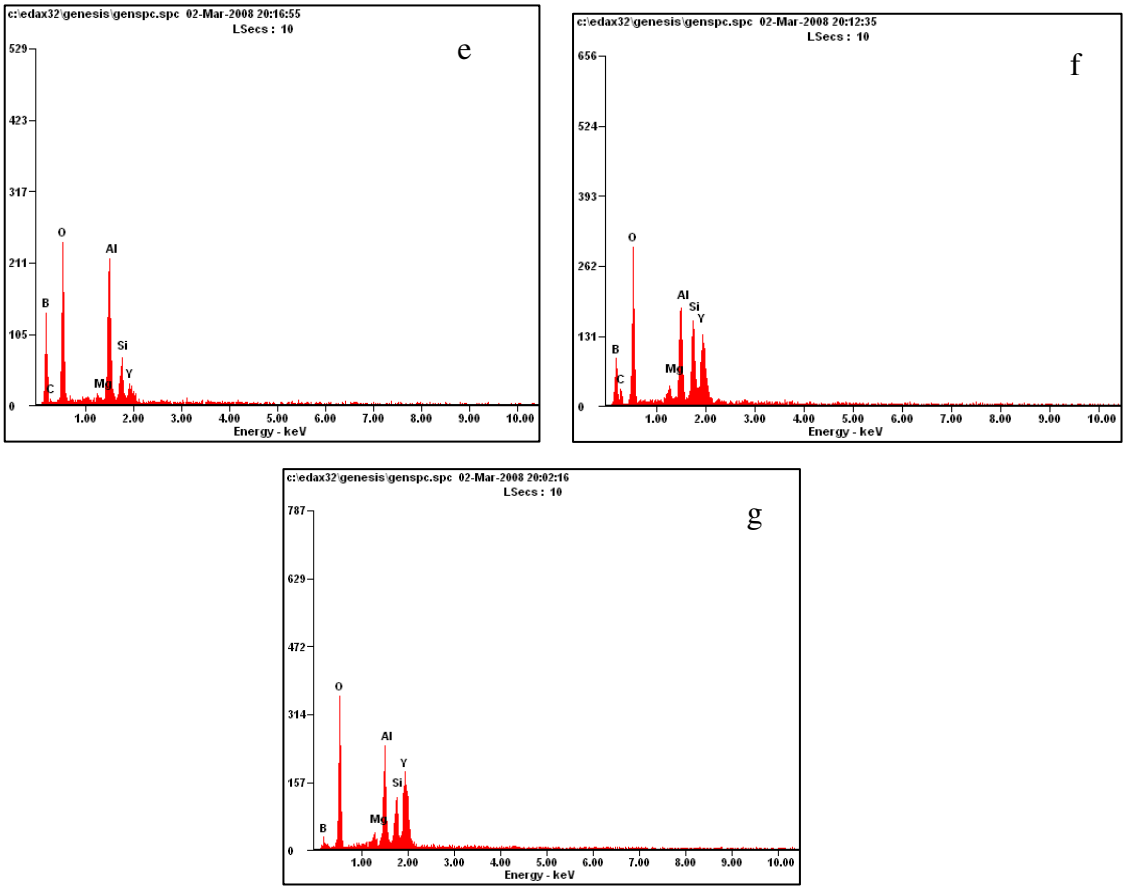

Figure 5.21: Continuation – EDX at spot e) 1. f) 2. g) 3.

TEM investigation was carried out on **18**B_6O**2**Al**2.65**Y**1**Si***a*** material to understand the grain boundary structure, composition and also to compare the structure to the Al-Y-doped B_6O materials. Figure 5.22 shows the TEM micrographs of **18**B_6O**2**Al**2.65**Y**1**Si***a*** hot pressed material. Similar structure was observed in comparison to Al-Y-doped B_6O hot pressed material (**18**B_6O**2**Al**2.65**Y***a***). The individual B_6O grains are not well faceted and have isolated pockets of glassy phases (Figure 5.22a). The grain sizes of B_6O are also homogenous and in the submicron range. There were also some dislocations and stacking faults with multiple twinning within the B_6O grains (Figure 5.22b). Glass phase (Figure 5.22c) decomposed upon

exposure to incident electron beam which indicates that the glass phase is electron beam sensitive. EDX analysis reveals incorporation of B, Al, Y, Si, Mg and O into the glass phase. Mg in this case comes from boron starting powder. Figure 5.22d shows a typical HRTEM image of grain boundaries showing no evidence of grain boundary wetting as in the case of Al-Y-doped B_6O material. Therefore it was concluded that these grain boundaries have clean interfaces.

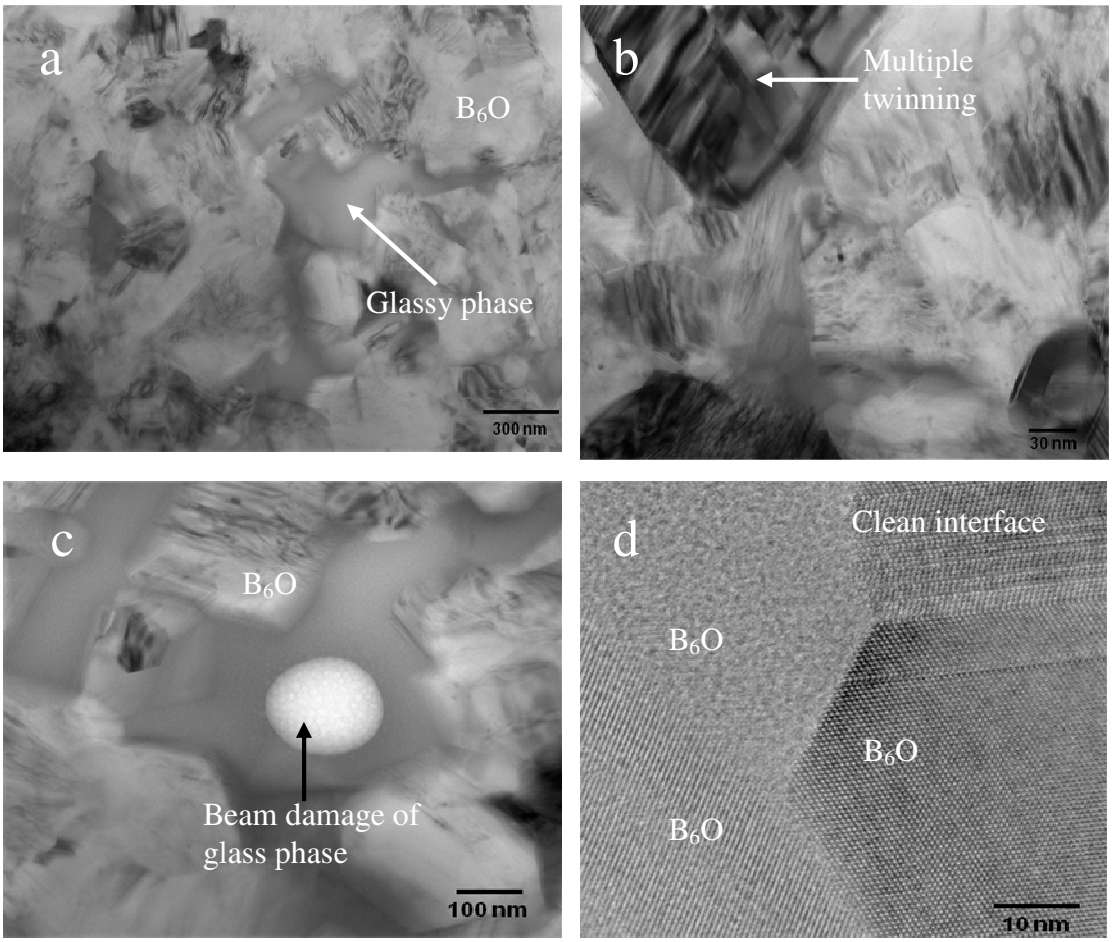

Figure 5.22: TEM micrograph of (a) overall microstructure of **18**B_6O**2**Al**2.65**Y**1**Si***a***-1** hot pressed material showing no grain growth and isolated pockets of glassy phase. (b) B_6O grain showing multiple micro-twinning. (c) glass phase damage upon electron beam radiation indicating the sensitivity of this glass phase. (d) a triple grain junction in the Al-Y-Si-doped B_6O material which does not contain any glass phase (clean interface).

The fractured surface of **18**B_6O**2**Al**2.65**Y**1**Si***b* was examined under SEM to understand the fracture mode. Figure 5.23 shows the SEM images of the fractured surface. It could be observed from this micrograph that transgranular fractured occurred in this composite. Higher resolution was difficult to obtain. It is believed that fracture occurred along the twin boundaries and stacking faults as found in TEM results although no conclusive evidence for this fracture mechanism was found in this work.

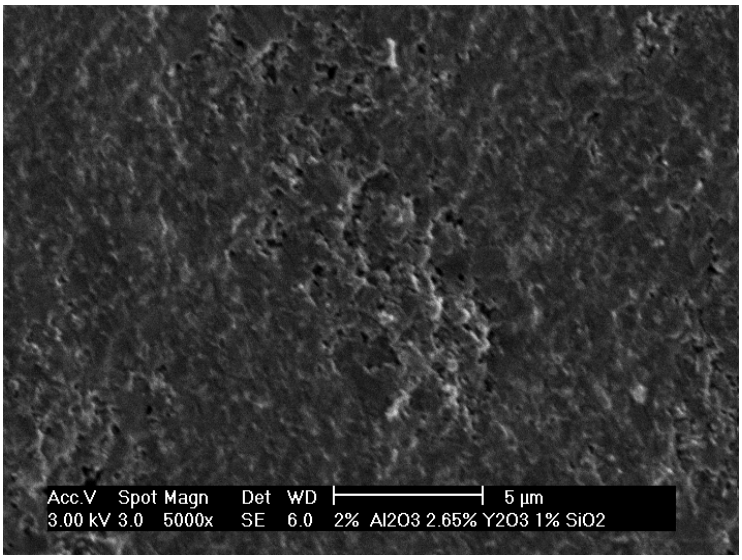

Figure 5.23: SEM image of fractured surface of **18**B_6O**2**Al**2.65**Y**1**Si***b* material.

5.5.4 Hot pressed B_6O-Al_2O_3 composites

B_6O composite materials containing 1 wt%, 2 wt% and 3 wt% Al_2O_3 respectively, were additionally produced at a hot pressing temperature of 1900^oC under a pressure of 50 MPa for 20 minutes. XRD pattern of B_6O admixed with 1 wt% Al_2O_3 is given in Appendix C (figure C1). It was assumed that the B_2O_3 present on the surfaces of B_6O particles would react with Al_2O_3 forming aluminium borates which could

improve the fracture toughness of these composites. Table 5.7 shows the densities and mechanical properties measured for these composites.

Table 5.7: Densities and mechanical properties of B_6O composites containing Al_2O_3.

Material	Density (g/cm^3)	% Theoretical density	Open porosity (%)	Vickers hardness, (GPa)		K_{IC} ($MPam^{1/2}$)
				Hv_5	$Hv_{0.5}$	
19B_6O**1**Al***a***	2.51	98.4	3.0	30.2±1.8	30.9±0.6	5.8±0.5
19B_6O**2**Al***a***	2.54	99.2	1.8	29.5±1.5	30.6±1.1	5.5±0.6
19B_6O**3**Al***a***	2.55	99.2	2.1	27.0±0.7	28.9±0.5	4.5±0.5
18B_6O**2**Al**1**Si***a***	2.42	94.5	4.1	28.0±1.5	28.4±0.6	5.2±0.7
19B_6O***a***	2.48	97.6	3.6	30.1±0.8	34.7±1.1	3.3±0.1

Densities higher than 97% of their theoretical densities were achieved. The high densities achieved are connected with the higher hot pressing temperature used which resulted in high amount of liquid phase present to accelerate mass transport via liquid phase sintering. Higher fracture toughness values were obtained for these composites with very good hardness values. 1 wt% SiO_2 was added to 2 wt% Al_2O_3 and hot pressed at lower temperature (1800^oC) to determine the effect of SiO_2 on densification of this composite. The properties obtained for this composite have been included in table 5.7 for comparison. Even though the hardness and fracture toughness values obtained were similar to composites without SiO_2 addition, the density was low. Porosity of 4.1% was measured for this material. The high porosity in **18**B_6O**2**Al**1**Si***a*** composite is connected with the lower hot pressing temperature used which resulted in less densification. Details of the densification mechanism are presented in Chapter 6. Figure 5.24 shows XRD pattern of the hot pressed composites (**19**B_6O**2**Al***a*** and **18**B_6O**2**Al**1**Si***a***). Similar XRD pattern were obtained for

19B_6O**1**Al***a*** and **19**B_6O**3**Al***a*** materials. The XRD pattern identified aluminium borate ($Al_{18}B_4O_{33}$) as the crystalline grain boundary phase. No Si-containing peak was identified in **18**B_6O**2**Al**1**Si***a*** material. Figure 5.25 shows the SEM images showing some defects in the microstructures as well as some in-homogeneities. EDX analysis on **18**B_6O**2**Al**1**Si***a*** material showed the presence of Si in the hot pressed composite. Cracks in microstructure are pull-outs of the grain boundary phases due to bad polishing and also presence of B_2O_3 in the hot pressed material.

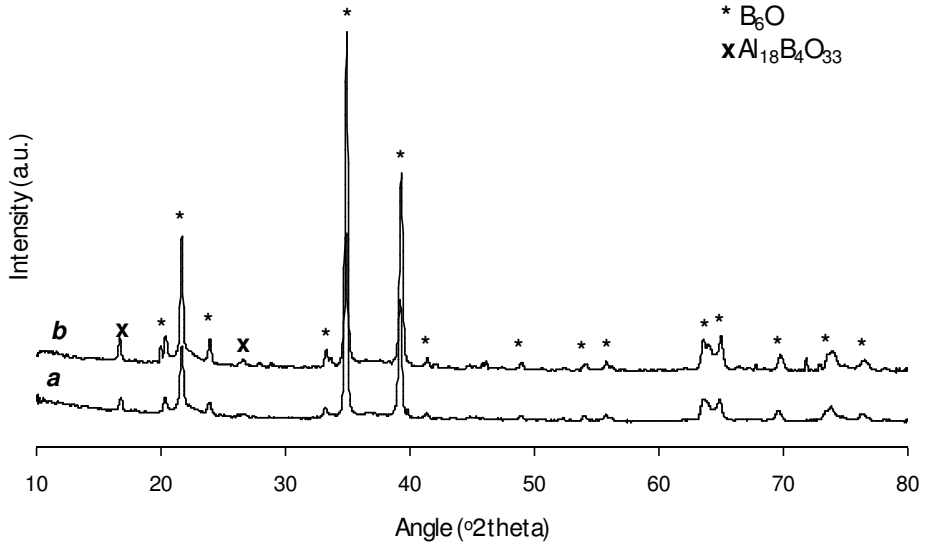

Figure 5.24: XRD pattern of B_6O composites containing Al_2O_3 and SiO_2. (a) **19**B_6O**2**Al***a***. (b) **18**B_6O**2**Al**1**Si***a***.

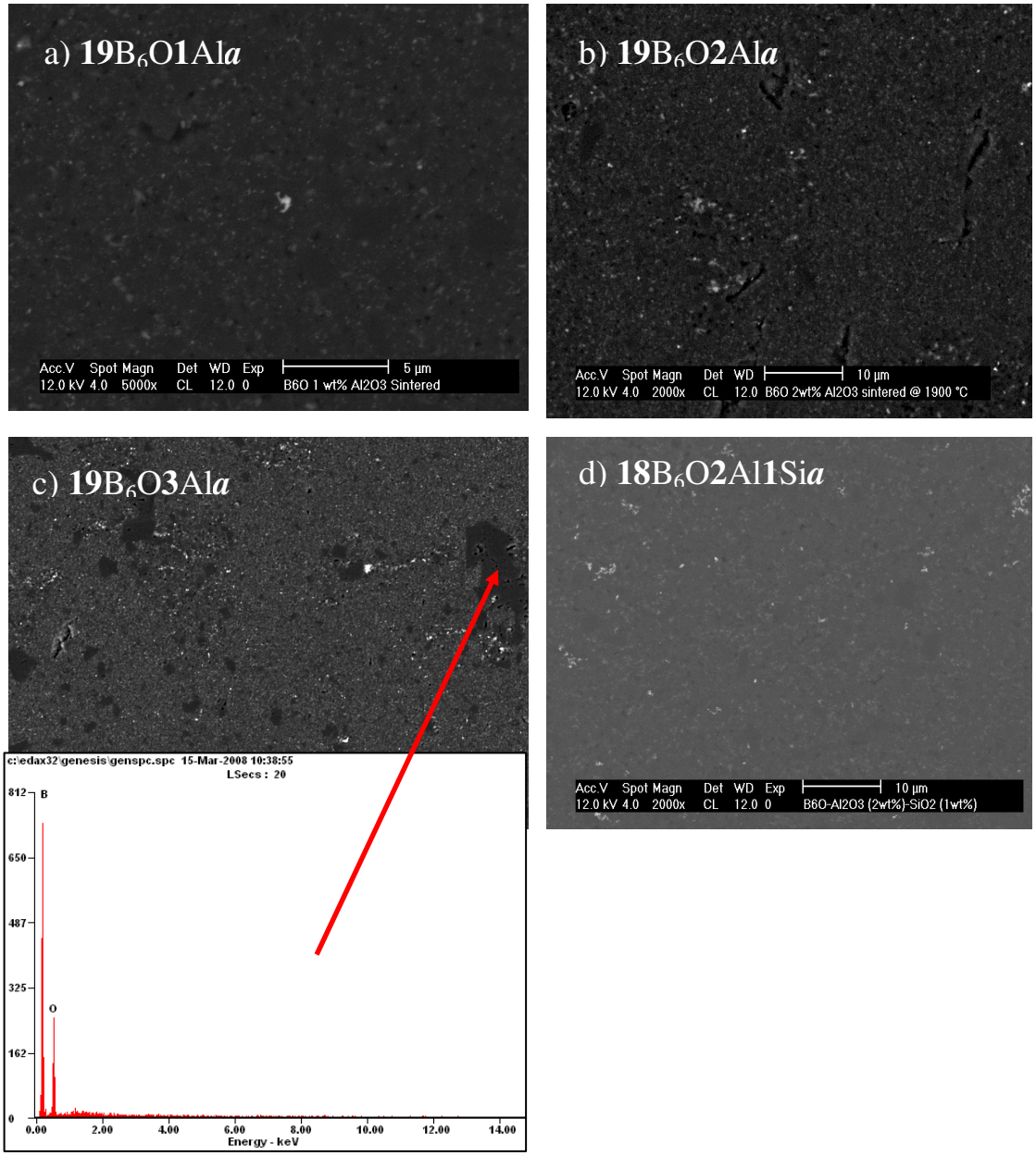

Figure 5.25: Backscattered (SEM) images of Al-doped B_6O hot pressed composites. (a) **19**B_6O**1**Al***a*** (b) **19**B_6O**2**Al***a*** (c) **19**B_6O**3**Al***a*** (d) **18**B_6O**2**Al**1**Si***a***.

5.5.5 Hot pressed B_6O composites with Ti compounds

B_6O composites were additionally produced by adding TiC and TiB_2 to try and improve the fracture toughness. XRD patterns of B_6O powder admixed with 5 wt% TiC and 5 wt% TiB_2 are given in Appendix C (figure C1). The admixed powders were hot pressed at 1900°C under a pressure of 50 MPa for 20 minutes. First batch of milled B_6O powder was used to produce these composites. The measured densities and mechanical properties are given in table 5.8.

Table 5.8: Densities and mechanical properties of B_6O composites with Ti compounds.

Material	Density (g/cm^3)	% Theoretical density	Open porosity (%)	Vickers hardness, (GPa)		K_{IC} ($MPam^{1/2}$)
				Hv_5	$Hv_{0.5}$	
19B_6O**5**TiC***a***	2.49	95.8	2.4	26.7±0.6	28.2±1.3	4.3±0.3
19B_6O**5**TiB_2***a***	2.62	100.8*	0.8	26.5±1.5	27.8±0.8	6.7±0.9
19B_6O***a***	2.48	97.6	3.6	30.1±0.8	34.7±1.1	3.3±0.1

*% Theoretical density can be more than 100 since calculations were based on rule of mixtures.

Density obtained for B_6O-TiB_2 composite was higher than B_6O-TiC composite. The hardness values were however similar. Compared to 'pure' B_6O (**19**B_6O***a***) the hardness of the Ti-based composites decreased strongly. Vickers hardness ($Hv_{0.5}$) of 28.2 GPa and 27.8 GPa were obtained for **19**B_6O**5**TiC***a*** and **19**B_6O**5**TiC***a*** composites respectively. A higher fracture toughness value was obtained for B_6O-TiB_2 composite. XRD patterns of the hot pressed composites are shown in figure 5.26. TiB_2 was present in both hot pressed materials besides B_6O. Additionally, small amounts of $Al_{18}B_4O_{33}$ were present in the hot pressed composites. The presence of Al in the composites is as a result of contaminations introduced during the mixing of B_6O with these additives. Evidence of this Al impurity is shown in the EDX spectra

in figure 5.27. Al_2O_3 balls and vessel were used for the mixing. Backscattered SEM images are also shown in figure 5.27. The white phase is TiB_2 and the grey phase is Al-B-Mg-O compounds.

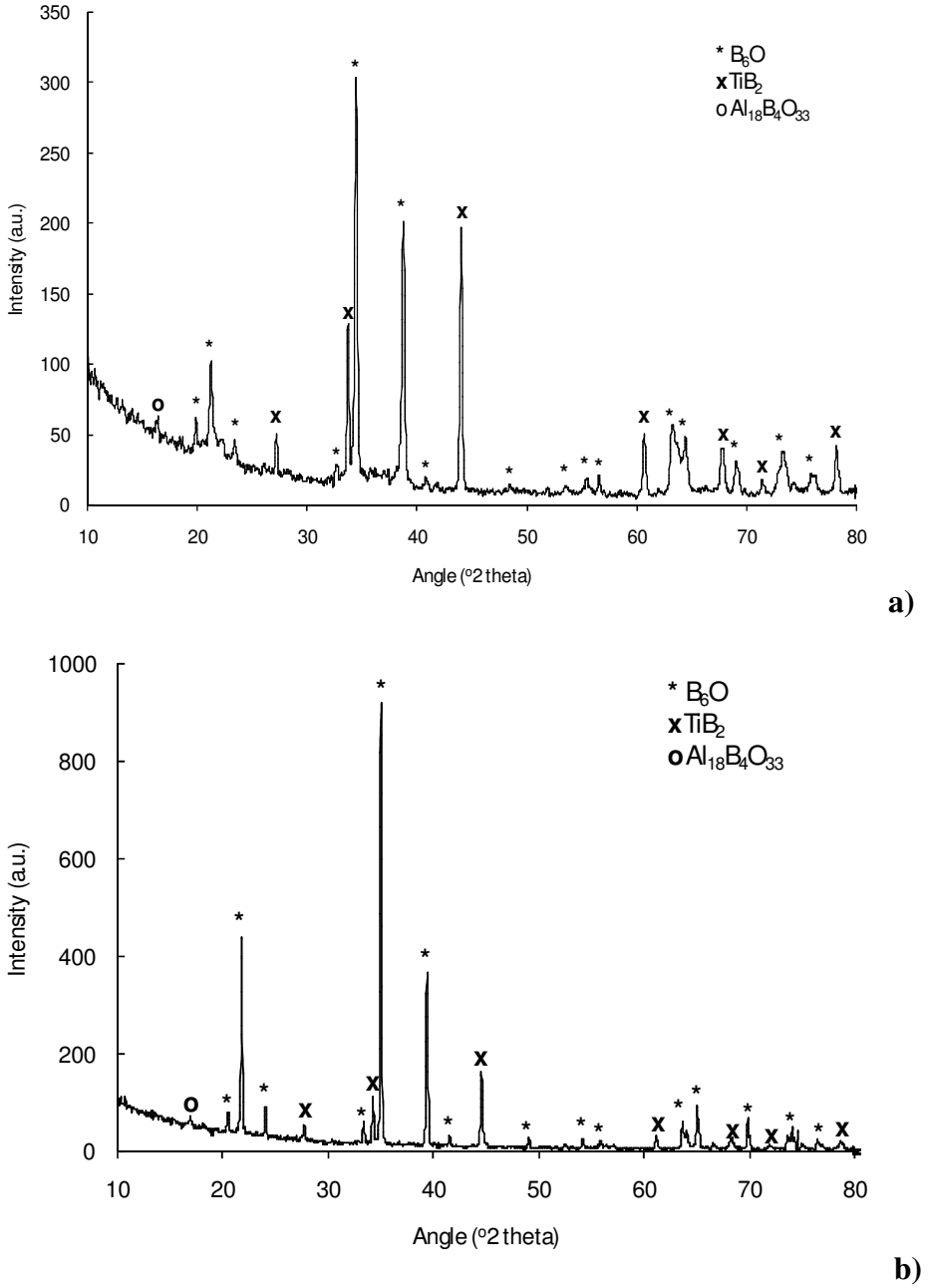

Figure 5.26: XRD pattern of hot pressed B_6O composites. a) **19**B_6O**5**TiC***a***. b) **19**B_6O**5**TiB_2***a***.

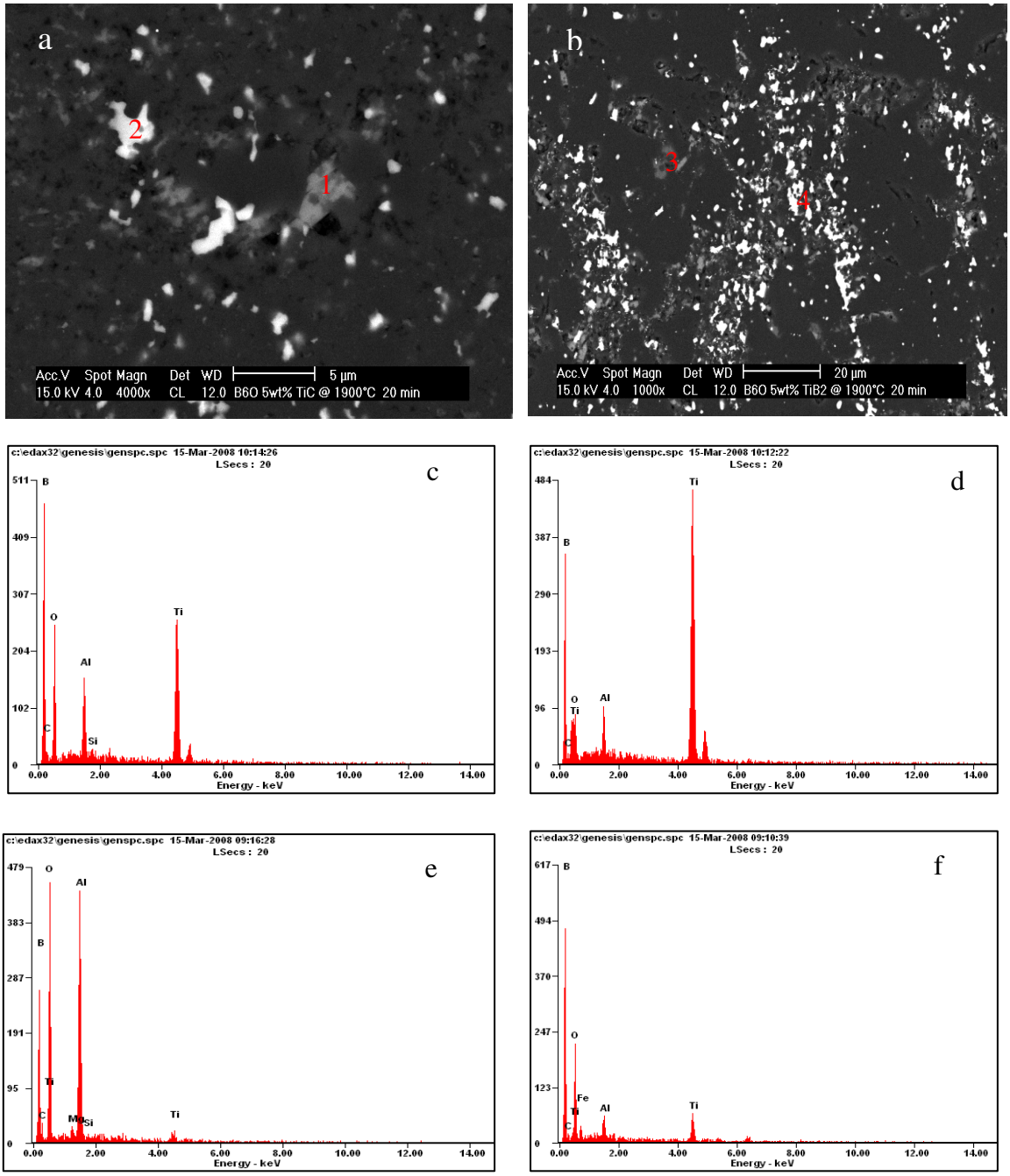

Figure 5.27: Backscattered (SEM) images of B_6O composites. a) **19**B_6O**5**TiC***a***. b) **19**B_6O**5**TiB_2***a***. c) EDX at spot 1. d) EDX at spot 2. e) EDX at spot 3. f) EDX at spot 4.

5.6 Heat treatment (annealing) of B_6O composites

Heat treatments of selected hot pressed B_6O composites were carried out at 1250°C for 10 hours in Ar atmosphere to determine the stability of the formed oxide phases and to test any transformation of the oxide phases formed during hot pressing. Materials heat treated included **18**B_6O**1**Al**1.32**Y***b*****-2**, **18**B_6O**2**Al**2.65**Y***b*****-2**, **18**B_6O**2.87**Al**1.58**Y***b***, and **18**B_6O**2**Al**2.65**Y**1**Si***b***. Summary of properties measured before and after heat treatments have been given in table 5.9. **18**B_6O**1**Al**1.32**Y***b*****-2** material was stable under the heat treatment conditions with the densities before and after heat treatment being the same. Only slight decomposition was observed for the other composites. There were slight reductions in densities for **18**B_6O**2**Al**2.65**Y***b*****-2HT** and **18**B_6O**2.87**Al**1.58**Y***b***HT** materials. However, the differences are too small and could be within the error limit. Hardness values of all heat treated materials increased slightly whereas their fracture toughness values remained almost the same with an exception of **18**B_6O**2**Al**2.65**Y**b-2HT** material where the fracture toughness decreased. There were no phase changes after heat treatment. XRD analysis of the heat treated materials is shown in figure 5.28. Comparison of XRD patterns before and after heat treatment has been shown in figure 5.29. No crystallisation was observed after the heat treatment. Figure 5.30 shows the optical images of the heat treated materials. These images reveal that no decomposition occurred during heat treatment. Dark spots in microstructure are as a result of bad polishing. SEM images of the heat treated materials are shown in figure 5.31. From the micrographs it is clear that the materials were stable under the heat treatment conditions.

Table 5.9: Properties before and after heat treatment of selected materials.

Material	Weight loss (wt %)	Density (g/cm^3)	Open porosity (%)	Hv_5 (GPa)	K_{IC} ($MPam^{1/2}$)
18B_6**O1**Al**1.32**Y***b***-2**	-	2.54	0.9	29.7±0.6	4.1±0.3
18B_6**O1**Al**1.32**Y***b***-2HT**	0	2.54	0.8	30.0±0.8	3.5±0.4
18B_6**O2**Al**2.65**Y***b***-2**	-	2.56	1.2	29.2±0.7	4.4±0.1
18B_6**O2**Al**2.65**Y***b***-2HT**	0.4	2.52	1.6	31.5±1.2	3.6±0.6
18B_6**O2.87**Al**1.58**Y***b***	-	2.53	0.8	28.3±0.9	3.8±0.9
18B_6**O2.87**Al**1.58**Y***b***HT**	0.2	2.50	1.1	30.2±0.5	3.6±0.6
18B_6**O2**Al**2.65**Y**1**Si***b***	-	2.55	1.2	27.6±0.6	3.2±0.5
18B_6**O2**Al**2.65**Y**1**Si***b***HT**	0.3	2.56	2.3	28.5±1.0	3.7±0.3

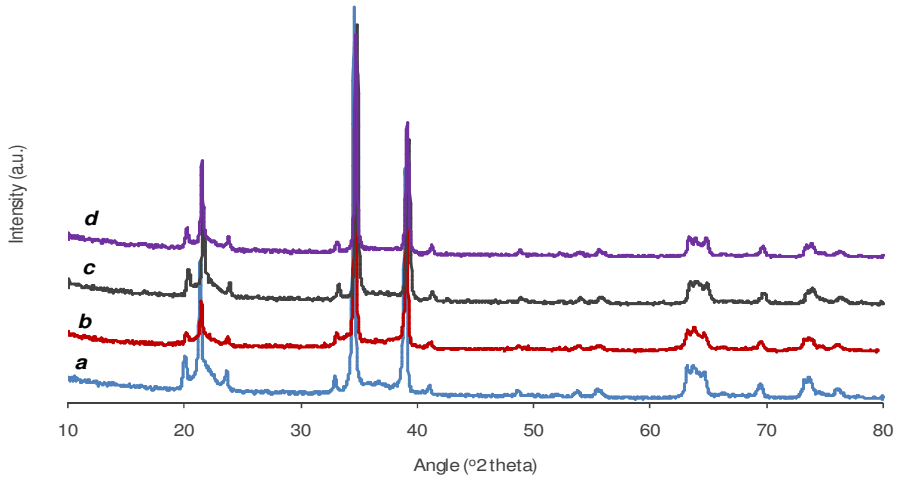

Figure 5.28: XRD pattern of heat treated materials showing only B_6O peaks. a) **18**B_6**O1**Al**1.32**Y***b***-2** b) **18**B_6**O2**Al**2.65**Y***b***-2** c) **18**B_6**O2.87**Al**1.58**Y***b*** d) **18**B_6**O2**Al**2.65**Y**1**Si***b***.**

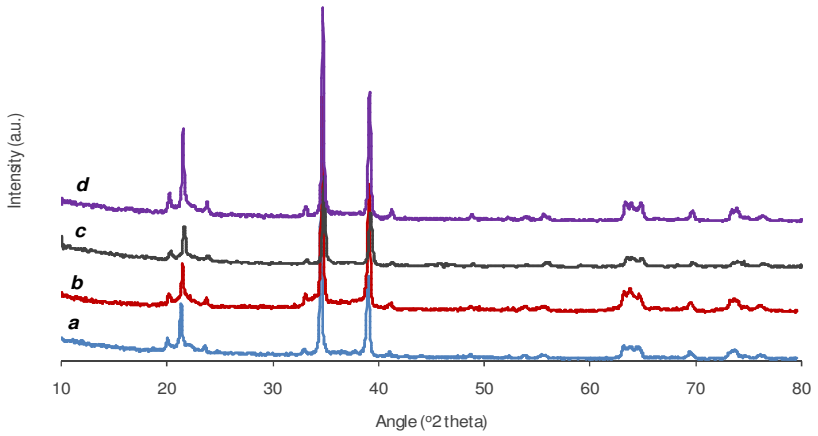

Figure 5.29: XRD pattern before and after heat treatment showing only B_6O peaks. a) **18**B_6O**2**Al**2.65**Y***b*****-2** b) **18**B_6O**2**Al**2.65**Y***b*****-2HT** c) **18**B_6O**2**Al**2.65**Y**1**Si***b*** d) **18**B_6O**2**Al**2.65**Y**1**Si***b***HT**.

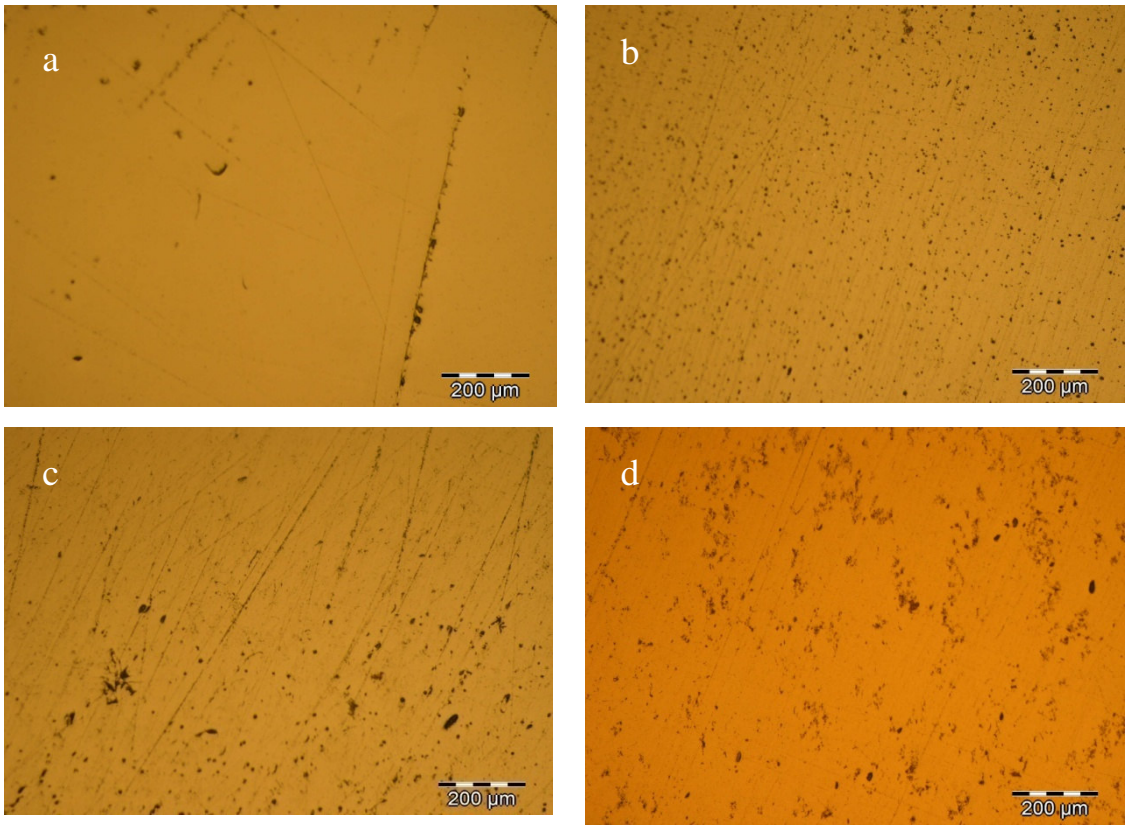

Figure 5.30: Optical images of heat treated materials. a) **18**B_6O**1**Al**1.32**Y***b*****-2HT** b) **18**B_6O**2**Al**2.65**Y***b*****-2HT** c) **18**B_6O**2.87**Al**1.58**Y***b***HT** d) **18**B_6O**2**Al**2.65**Y**1**Si***b***HT**.

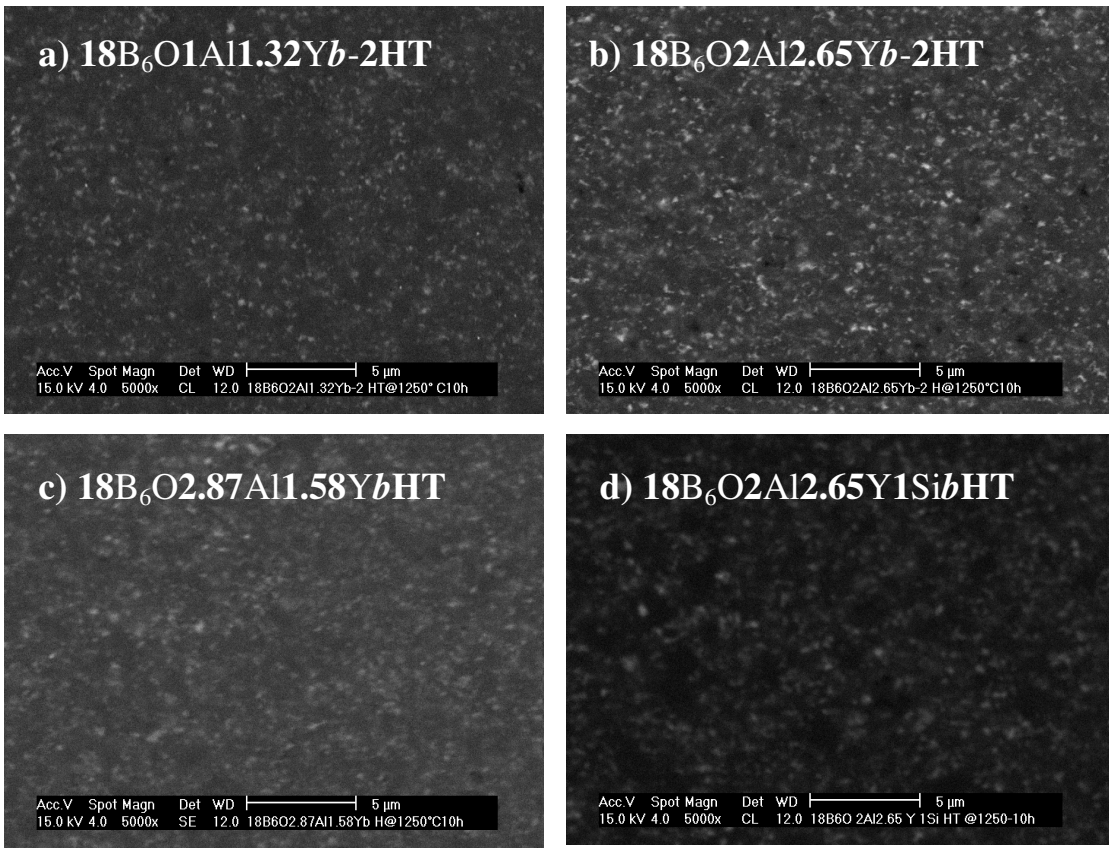

Figure 5.31: Backscattered (SEM) images of heat treated materials.

5.7 Elastic properties of hot pressed B_6O composites

The elastic properties of selected B_6O composites were determined using ultrasound as described in section 4.7.7. The elastic moduli data determined were used to calculate the indentation fracture toughness values for the B_6O composites containing Al_2O_3, Y_2O_3 and SiO_2 additives. Table 5.10 shows the elastic properties of **18**B_6O**1**Al**1.32**Y***b***, **18**B_6O**2**Al**2.65**Y***b***, **18**B_6O**2.87**Al**1.58**Y***b***, and **18**B_6O**2**Al**2.65**Y**1**Si***b*** materials. As the amount of additive (i.e. Al_2O_3 content in additives) increased the elastic modulus decreased. **18**B_6O**2.87**Al**1.58**Y***b*** material had the least elastic constants. Details of the relationship between the microstructure and elastic properties have been described in Chapter 6.

Table 5.10: Elastic constants of selected hot pressed composites.

Material	Density (g/cm^3)	Elastic modulus, E (GPa)	Shear modulus, μ (GPa)	Bulk modulus, K (GPa)	Poison ratio, *v*
18B_6O**1**Al**1.32**Y***b***	2.54	462±3	194±1	249±3	0.191±0.008
18B_6O**2**Al**2.65**Yb	2.57	451±2	196±4	213±2	0.148±0.005
18B_6O**2.87**Al**1.58**Y***b***	2.57	429±4	183±1	207±2	0.158±0.002
18B_6O**2**Al**2.65**Y**1**Si***b***	2.58	459±1	200±2	217±3	0.147±0.004

5.8 Pd-doped B_6O composite

B_6O was doped with 5 vol. % Pd and hot pressed at 1600°C and 1900°C under a pressure of 50 MPa for 30 minutes. B_6O powder produced at Wits was used to produce the composite. The intention was to form pure metal or palladium boride with B_2O_3 existing on the surfaces of B_6O particles thereby forming a stronger grain boundary. The hot pressing cycle used to produce the composite is given in table 4.3. Details of the doping process are presented in Chapter 4 (Section 4.5). XRD and SEM of the doped powder have been shown in figure 5.11. Table 5.11 summarises the properties of the composite. For comparison, the properties of hot pressed 'pure' B_6O (**19**B_6O) produced from B_6O powder synthesised at Wits have been included in the table. **19**B_6O was hot pressed at 1900°C under pressure of 50 MPa for 20 minutes. Additionally, the properties of **18**B_6O**2**Pd composite hot pressed at 1800°C under 50 MPa for 20 minutes had been included in table 5.11. This material was produced in a separate work (by a 4th year BSc student) under my supervision.

Table 5.11: Properties of Pd-doped B_6O composite.

Material	Density (g/cm^3)	% Theoretical density	Open porosity (%)	Hv_5, (GPa)	K_{IC} ($MPam^{1/2}$)
16B_6O**5**Pd	1.75	58.7	26.7	-	-
19B_6O**5**Pd	2.82	94.6	4.4	22.5±0.9	13.5±3.2
18B_6O**2**Pd	2.61		1.6	28.0±1.2	5.1±0.8
19B_6O*	2.52	99.2	1.9	29.4±0.5 (1kg load)	Brittle

* 'Pure' B_6O hot pressed from B_6O powder synthesised at Wits.

Material hot pressed at 1600°C (**16**B_6O**5**Pd) did not densify and therefore properties were not measured. Porosity of 26.7% was measured for this material. A density of 2.82 g/cm^3 was obtained for the material hot pressed at 1900°C (**19**B_6O**5**Pd) which is about 95% of the theoretical density. This material had very good fracture toughness but the hardness decreased strongly compared to the 'pure' B_6O (**19**B_6O). **18**B_6O**2**Pd material had very good combination of properties. The higher hardness recorded in comparison to **19**B_6O**5**Pd material is due to the low volume % of Pd used. Additionally, less open porosity was measured for **18**B_6O**2**Pd material in comparison to **19**B_6O**5**Pd. XRD pattern of **19**B_6O**5**Pd material is shown in figure 5.32. Pd_2B crystalline grain boundary phase was identified beside B_6O. Similar XRD pattern was obtained for **18**B_6O**2**Pd material. SEM images of the hot pressed materials are shown in figure 5.33. SEM images show inhomogeneous distribution of Pd_2B in the hot pressed compact. Figure 5.33b was taken at the centre of the hot pressed material. The non homogeneity of the secondary phase is somewhat connected with the high hot pressing temperature (1900°C) as well as the long dwelling time (30 minutes) used. There is also some residual porosity in the hot pressed material.

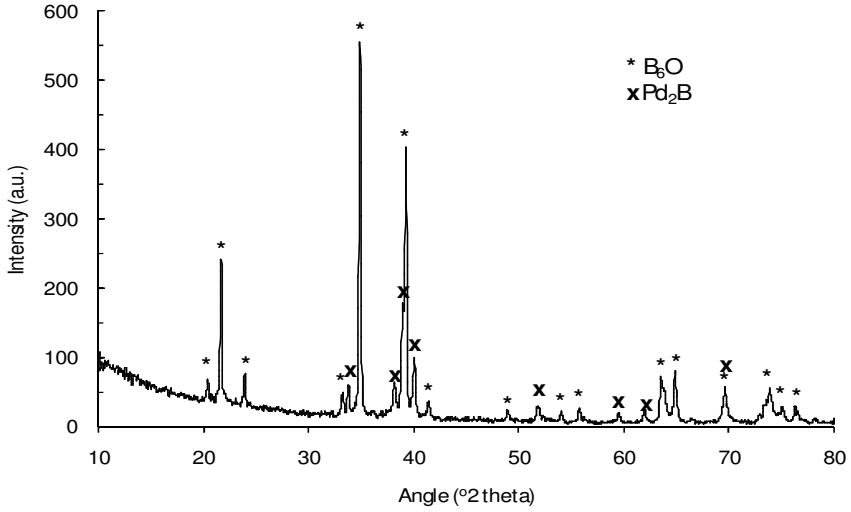

Figure 5.32: XRD pattern of Pd-doped B_6O composite hot pressed at 1900°C for 30 minutes (**19**B_6O**5**Pd).

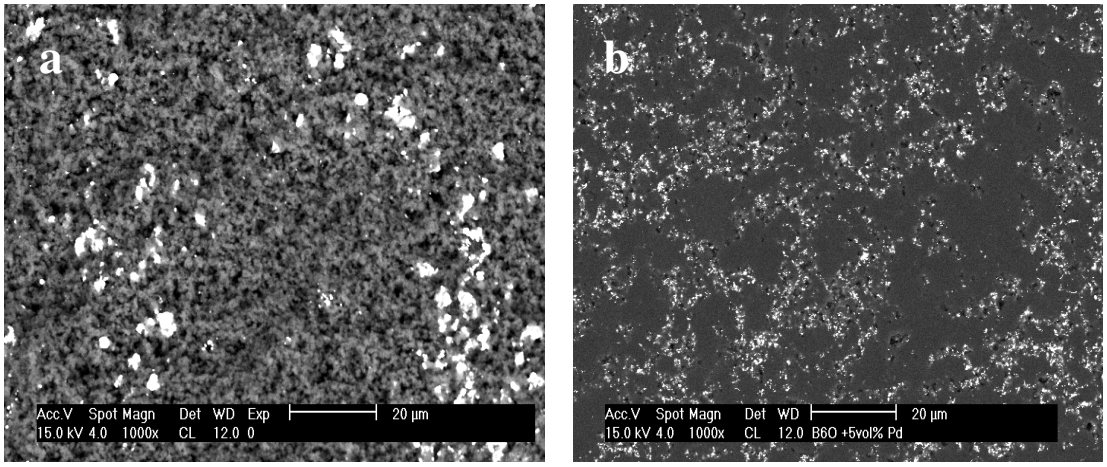

Figure 5.33: Backscattered (SEM) images of Pd-doped B_6O hot pressed materials. a) **16**B_6O**5**Pd b) **19**B_6O**5**Pd.

There was also some decomposition and in-homogeneity (segregation of Pd and boron) at the edges of **19**B_6O**5**Pd material. Figure 5.34 shows the SEM images taken at the edges of the material. It was observed that one edge of the material was boron-rich whilst the other edge of the same material was Pd-rich. This could be connected

with temperature gradient in the furnace. A detailed densification mechanism is presented in Chapter 6.

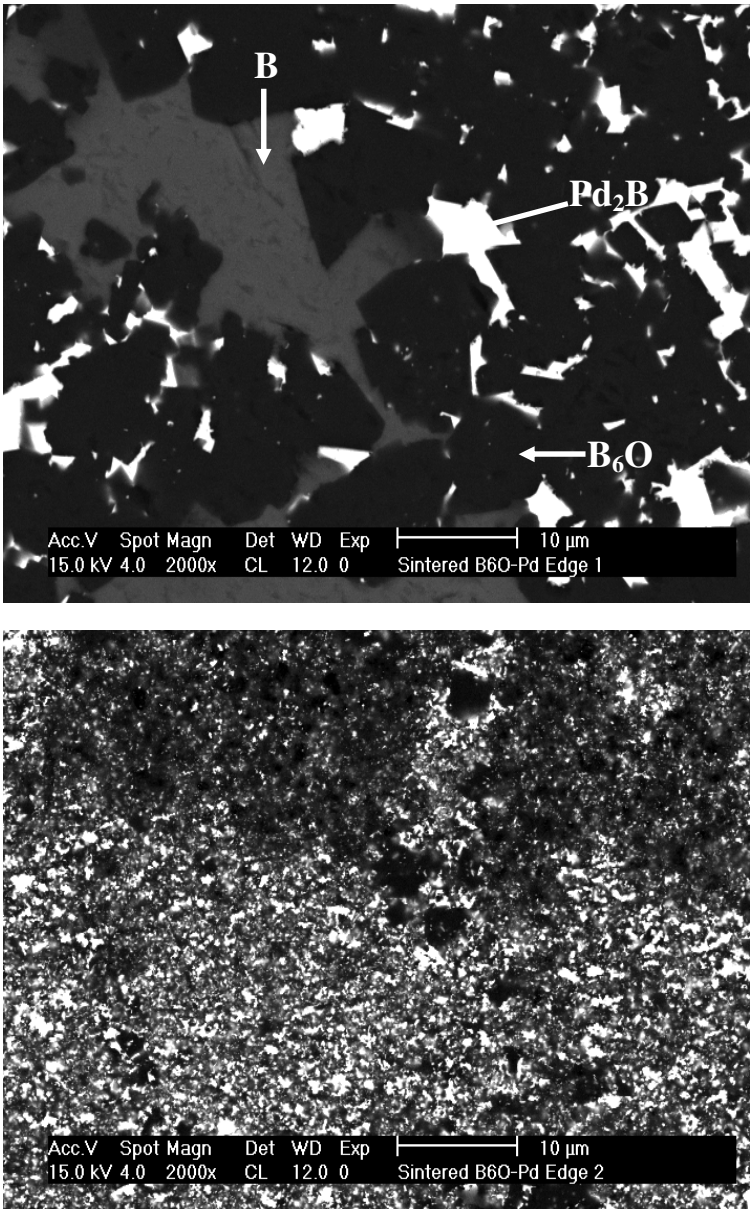

Figure 5.34: Backscattered (SEM) images of **19**B_6**O5**Pd material which has been hot pressed at 1900°C under a pressure of 50 MPa for 30 minutes. (a) Edge 1. (b) Edge 2.

6 Discussion

6.1 Introduction

This chapter discusses the results presented in chapter 5 in terms of the relationship between densification, microstructure, and properties of the hot pressed materials as well as the heat treated materials.

6.2 Relationship between densification and microstructure

B_6O and B_6O composites were hot pressed at temperatures between 1600^oC and 1900^oC in argon atmosphere under a pressure of 50 MPa. Summary of the densities obtained for the various hot pressed materials are given in table B1 (Appendix B). The theoretical densities have also been calculated and given in the same table. Assumptions made in the calculation of the theoretical densities have been presented in Chapter 4.

The densities of 'pure' B_6O hot pressed materials are very near theoretical density which varies from 2.47 and 2.59 g/cm^3 depending on the oxygen and B_2O_3 content in the sample. Figure 6.1 shows the dependency of the theoretical density on x in B_6O_x. As the oxygen content increases the theoretical density increases. The presence of B_2O_3 lowers the theoretical density as indicated in figure 6.1 [(85)]. The theoretical density as a function of x for B_6O composite containing 1wt% B_2O_3, 2 wt% Al_2O_3 and 2.65 wt% Y_2O_3 has also be included in the graph for comparison. Figure 6.1 agrees quite well with the estimation of oxygen occupancy calculated using intensity ratio of different peaks shown in figure 5.18. That is, the density increases with oxygen occupation in the crystal lattice.

Densities obtained for both **19**B_6O***a*** and **19**B_6O***b*** was 2.48 g/cm^3 whereas density obtained for **19**B_6O material was 2.52 g/cm^3. When fitted into figure 6.1, the measured densities would have rough estimated x values ranging from 0.76 to 0.85.

This low oxygen content is expected as these materials were sintered at low pressures. The estimation of the oxygen content does not take into account the presence of B_2O_3 and interactions occurring at sintering temperatures. Nevertheless, it was concluded that the materials are nearly completely densified upon hot pressing. Density obtained for B_6O hot pressed material produced from the powder synthesised at Wits (**19**B_6O) was higher than those produced from the milled powders (**19**B_6O***a*** and **19**B_6O***b***). This could be connected with the higher amount of B_2O_3 that might have been present in the starting B_6O powder. More B_2O_3 in the starting B_6O powder will increase the amount of liquid present at hot pressing temperature (1900^oC). The presence of this liquid enhanced mass transport in the liquid phase and under an applied load, nearly densed material was achieved. The presence of B_2O_3 coupled with the large particle sizes of starting powder resulted in the lower hardness value recorded for this material in comparison to the other 'pure' B_6O hot pressed materials. The different concentrations of Fe and Cr contaminations in the B_6O starting powder did not have any influence on the densification of **19**B_6O***a*** and **19**B_6O***b*** materials. Both materials had same density (2.48 g/cm^3). Nevertheless, the effect of these impurities on fracture toughness was significant (see section 6.4).

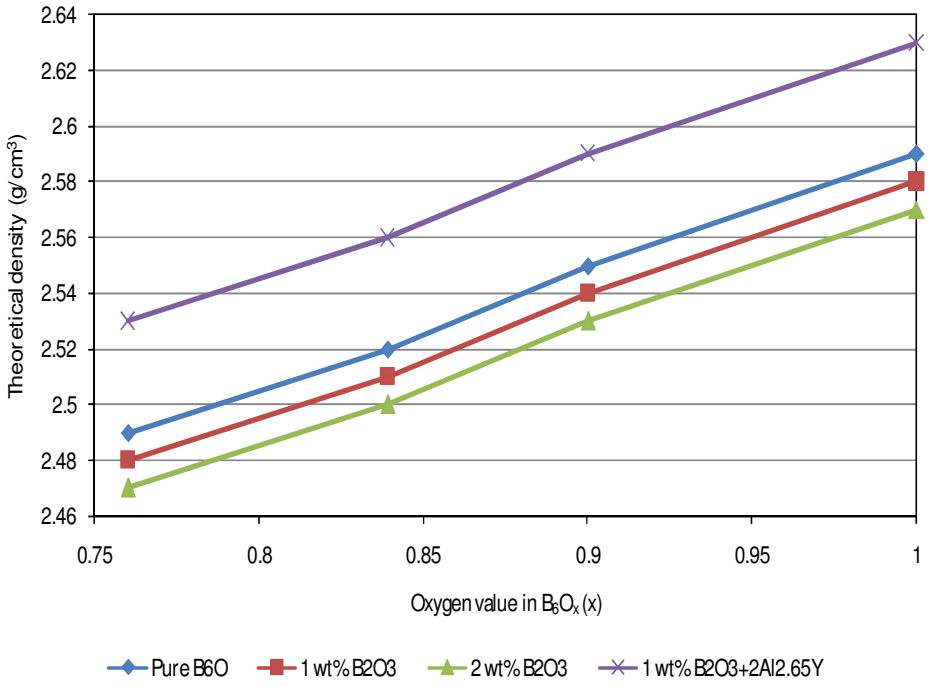

Figure 6.1: Dependency of the theoretical density on x in B_6O_x. Theoretical densities have been taken from ICSD data cards 50-1505, 81-2192, and 87-2288.

The effect of B_2O_3 on hot pressed B_6O-based materials was investigated and presented in Chapter 5. It was found that more B_2O_3 in the starting powder results in lower hardness even though nearly dense material was obtained. The low hardness is connected with liquid B_2O_3 present at hot pressing temperature which resulted in grain growth. Porosities measured and observed in figure 5.19 are partly connected with the decomposition of boron oxide rich phases at 1900°C.

Densities of 'pure' B_6O obtained in this work are encouraging. B_6O is typically unsinterable under ambient pressure conditions. Fully densified compact of B_6O is difficult to obtain in the literature even by high pressure sintering techniques such as hot pressing or hot isostatic pressing [19] and no appropriate sintering aid has been found. This is because B_6O is easily oxidized to form B_2O_3 with the mechanical

strength of the resultant sintered compact degraded [7]. The degradation of mechanical properties by B_2O_3 has been corroborated by the findings in this work.

Most of the hot pressed B_6O composites produced in this work contain Al_2O_3 and Y_2O_3 as sintering additives. Therefore composites containing these additives were used to investigate densification behaviour as a function of sintering temperature. B_6O materials containing 2 wt% Al_2O_3 and 2.65 wt% Y_2O_3 were hot pressed at 1750°C, 1800°C, and 1850°C respectively. Figure 6.2 shows the relationship between hot pressing temperature and density. It was observed that the density of the hot pressed materials increased sharply from 1750°C to 1800°C. Above 1800°C the density only slightly increases. To understand and properly explain the densification process of this composite, one needs to consider the phase diagram of Al_2O_3-Y_2O_3 system which is shown in figure 6.3. The composition under consideration has been indicated with an arrow in that figure. According to the phase diagram, at 1850°C there will not be any liquid present in the composite at sintering temperature. Nevertheless, there is some level of solubility of B_2O_3 in Al_2O_3-Y_2O_3 system (at least from the TEM investigations). The presence of B_2O_3 lowers the melting point in this system, creating enough liquid for densification to occur via liquid phase sintering. Additionally, under applied load near full densification of the composite would be achieved compared to materials hot pressed at lower temperatures. The presence of B_2O_3 is evident in the stability of the glassy phase formed in the composites, which prevents the formation of crystalline grain boundary phases [86].

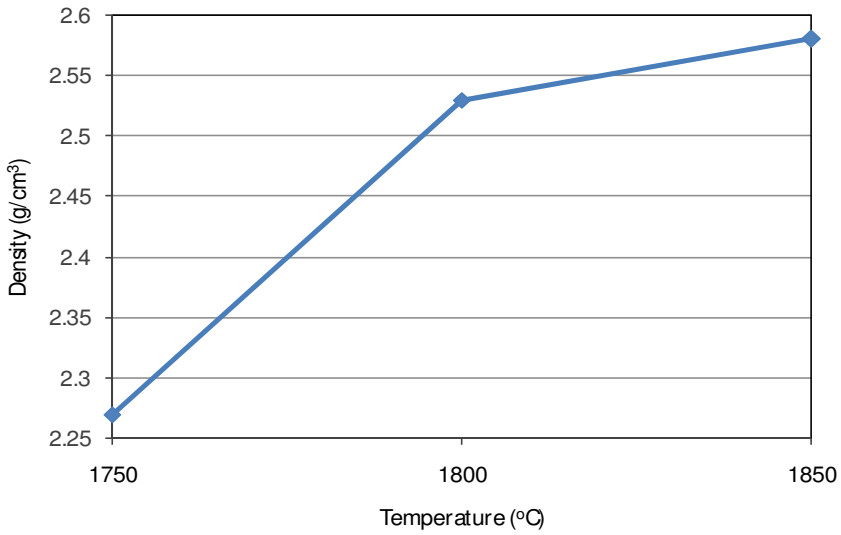

Figure 6.2: Densities of the hot pressed composites containing 2 wt% Al_2O_3 and 2.65 wt% Y_2O_3 as a function of hot pressing temperature.

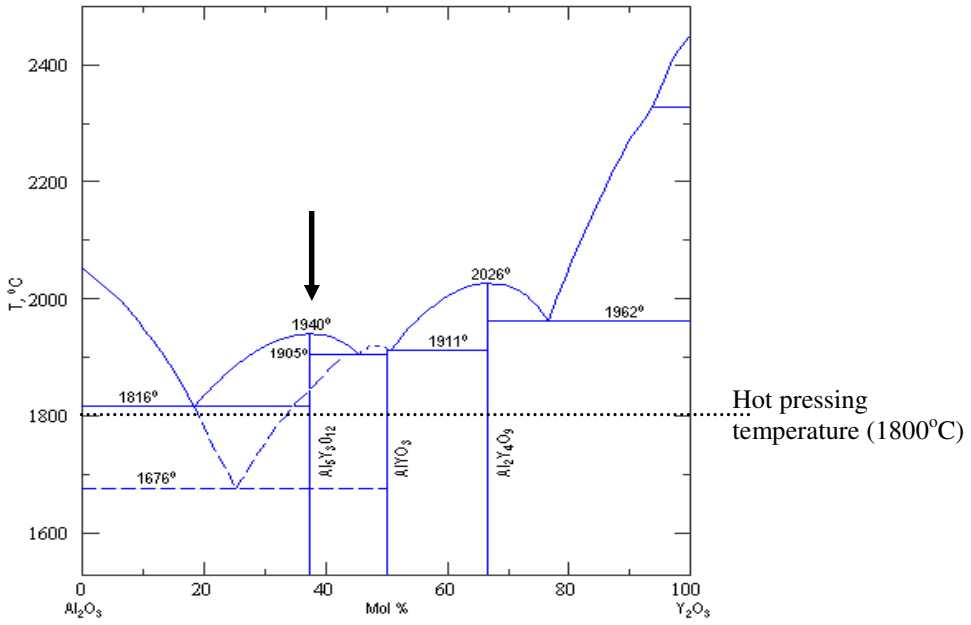

Figure 6.3: Phase diagram of Al_2O_3-Y_2O_3 system [83]. The arrow represents the composite under consideration (62 % mol Al_2O_3:38 % mol Y_2O_3).

Even though high density was obtained for the material hot pressed at 1850°C (**185**B_6O**2**Al**2.65**Y***a***) the macrohardness value obtained was slightly lower (~2 GPa) compared to the material hot pressed at 1800°C (**18**B_6O**2**Al**2.65**Y***a***). The reduction in hardness is connected with the high amount of liquid phase present at hot pressing temperature which resulted in grain growth of the material (see figure 5.17c). This also explains why the microhardness values were similar for materials hot pressed at 1800 and 1850°C although there were slight differences in their macrohardness values. The reduced hardness for **185**B_6O**2**Al**2.65**Y***a*** material could also be connected to the decomposition of boron oxide rich phases at this temperature. The trend of the densities obtained and the observed microstructures are an indication that these composites are somewhat densified via liquid phase sintering. Nevertheless, the sintering mechanism cannot be fully described as the traditional liquid phase sintering since there were no evidence of grain boundary wetting and these boundaries had clean interfaces (Figure 5.14c). Based on the above findings, all the other B_6O composites containing Al_2O_3, Y_2O_3, and SiO_2 additives were hot pressed at 1800°C.

The influence of the amount and ratio of Al_2O_3, Y_2O_3, and SiO_2 additives on densification was studied. The densities obtained for the various composites are given in table B1 (Appendix B). As mentioned earlier, two different hot pressing profiles were used. For the first hot pressing profile, the furnace was heated to 1600°C at 15°C/min and dwelled at this temperature for 20 minutes to apply a maximum pressure of 30 MPa. It was then heated up to 1800°C at 10°C/min for 20 minutes at which time the pressure was increased to 50 MPa. The furnace was cooled afterwards at 20°C/min to room temperature (see figure 4.6 and table 4.3). For the second hot pressing profile the furnace was heated to 1800°C at 20°C/min for 20 minutes. During heating, the temperature was held at 1400°C for 5 minutes to apply the pressure (50 MPa). This means that the second hot pressing profile had less time (about 2.5 hrs) to sinter compared to first hot pressing profile due to the faster heating rate and therefore grain growth is reduced. Additionally, hot pressed materials were under pressure for longer time for the second hot pressing profile compared to the first.

With these differences in the two hot pressing profiles in mind, it was observed that materials produced using the first hot pressing profile resulted in less dense materials. This is an indication of a strong dependence of densification on pressure. For instance, a density of 2.41 g/cm^3 was measured for **18**B_6O**1**Al**1.32**Y***a*** material using the first hot pressing profile whilst 2.54 g/cm^3 was measured for **18**B_6O**1**Al**1.32**Y***b*****-2** material using the second hot pressing profile. Porosities measured using the first hot pressing profile were also higher and the microstructures also looked less densed (see figure 5.13). Similar densification results were obtained for all the other hot pressed materials.

Figure 6.4 shows the densities of B_6O composites sintered at 1800^{o}C as a function of the volume content of oxide additives. Materials produced using the second hot pressing profiles are considered in this case. The sharpest increase in density takes place by adding the smallest amount of additives. Thereafter, increasing the volume fraction of additive only slightly changes the densification behaviour. The differences between the measured density and the theoretical densities in figure 6.4 are within the uncertainty limits (i.e. changes in decomposition and composition of the grain boundaries since the rule of mixtures was used to calculate the theoretical densities). The densification behaviour was similar for the other two mol ratios of Al_2O_3:Y_2O_3. Figure 6.5 shows the relationship between theoretical densities and mol fraction of Al_2O_3 for different volumes of additives in the composites. For smaller volume content of additives (2.72 volume % content), densification decreased slightly with increasing mol fraction of Al_2O_3 in the additives. For 3.87 volume % content of additives, densification increased up to 62 mol % of Al_2O_3 in the additives and then remains constant. According to the phase diagram shown in figure 6.3 the formation of liquid phase is strongly dependant on the B_2O_3 content. In Al_2O_3 rich composition, $Al_{18}B_4O_{33}$ is formed besides the glassy phase.

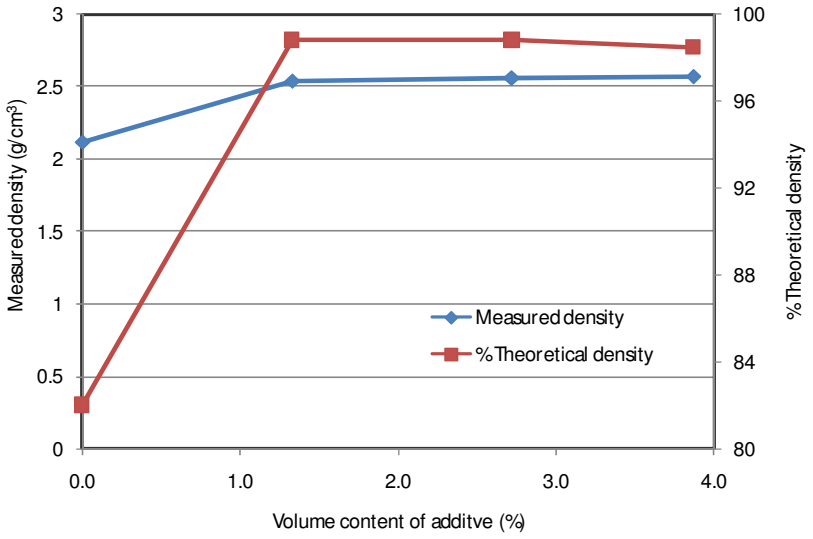

Figure 6.4: Density of B_6O composites hot pressed at 1800°C as a function of volume content of additives (62 mol % Al_2O_3:38 mol % Y_2O_3). Density of pure B_6O sintered at 1800°C was taken from the work of Shabalala [16].

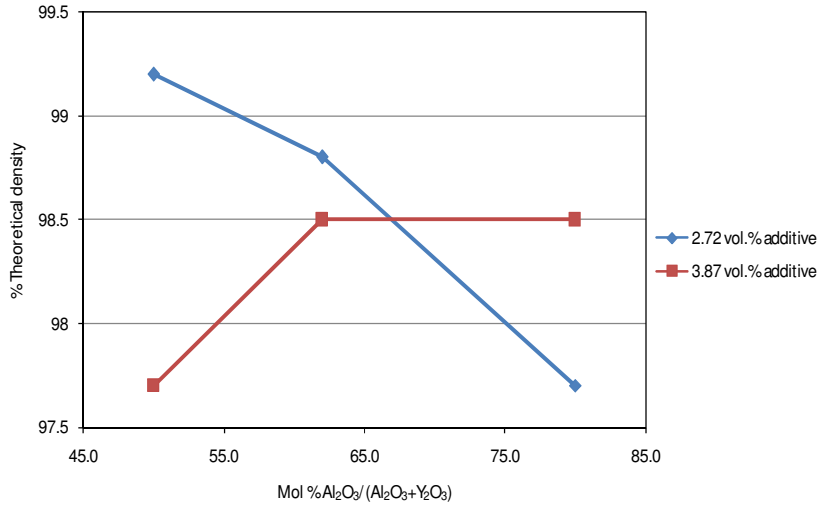

Figure 6.5: Graph of mol % of $Al_2O_3/(Al_2O_3+Y_2O_3)$ versus theoretical density for different volume content of additives.

There was more segregation of Y_2O_3 in the Al_2O_3-rich materials than there was in composites containing less Al_2O_3 and Y_2O_3 (see figure 5.13). The pockets of glassy phases in these microstructures were analysed more closely using energy dispersive

X-ray analysis (EDX) and were found to contain higher content of Y_2O_3. Backscattered SEM image of B_6O composite containing 2.87 wt% Al_2O_3 and 3.75 wt% Y_2O_3 (**18**B_6O**2.87**Al**3.75**Y***b*****-1**) showing segregation of grain boundary phase is shown in figure 6.6a. EDX spectrum of this glassy pocket is also shown in figure 6.6b.

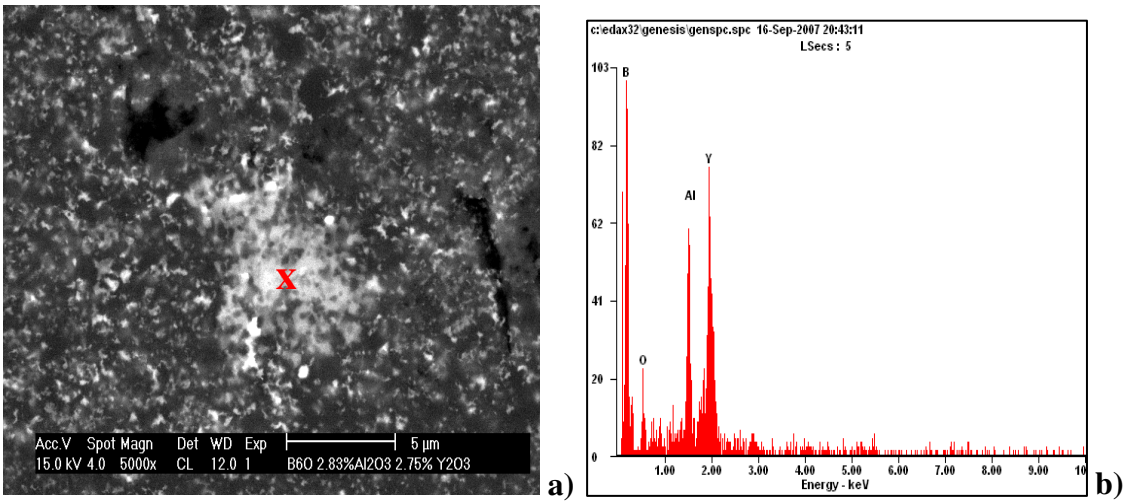

Figure 6.6: (a) Backscattered (SEM) image of **18**B_6O**2.83**Al**3.75**Y***b*****-1**. (b) EDX analysis of spot 'x' in segregated region in **18**B_6O**2.83**Al**3.75**Y***b*****-1** material showing that segregation of grain boundary phase.

XRD patterns of the composites containing Al_2O_3/Y_2O_3 with mol ratios 62/38 and 50/50 did not show any crystalline grain boundary phases. In materials with high Al_2O_3 content, aluminium borates ($Al_{18}B_4O_{33}$) were formed. The formation of $Al_{18}B_4O_{33}$ agrees with the thermodynamic equilibrium calculations presented in Chapter 3 (Section 3.3.4). In the presence of B_2O_3, Al_2O_3 reacts with B_2O_3 forming aluminium borates according to the calculated Al_2O_3-B_2O_3 phase diagram shown in figure 3.9. The type of aluminium borate formed will depend on the amount of Al_2O_3 and/or B_2O_3 available for the reaction to take place.

For B_6O composites containing Al_2O_3, Y_2O_3, and SiO_2, it is important to consider the phase diagram for these three additives in order to explain the densification behaviour. The phase diagram for this system is shown in figure 6.7.

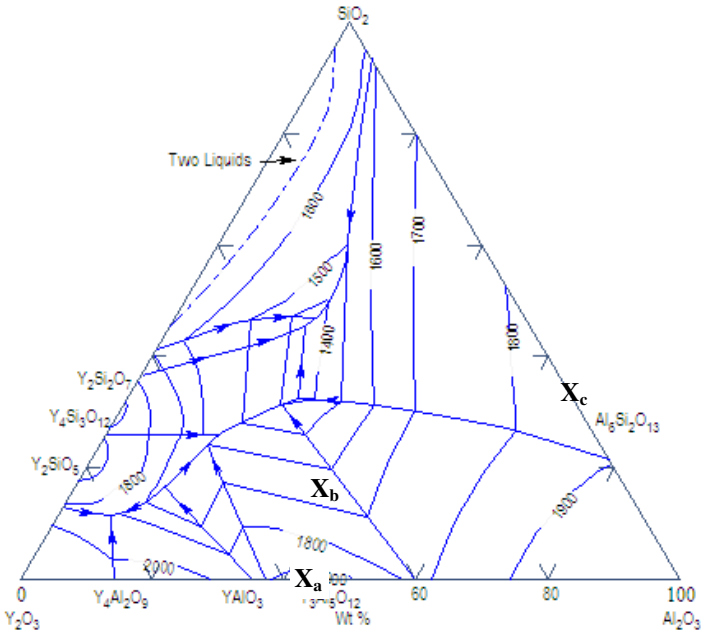

Figure 6.7: Y_2O_3-Al_2O_3-SiO_2 phase diagram [83]. Compositions indicated are X_a 2 wt% Al_2O_3, 2.65 wt% Y_2O_3; X_b 2 wt% Al_2O_3, 2.65 wt% Y_2O_3, 1 wt% SiO_2; X_c 2 wt% Al_2O_3, 1 wt% SiO_2.

The phase diagram shows that when 1 wt% SiO_2 is added to a system containing 2 wt% Al_2O_3 and 2.65 wt% Y_2O_3, for instance, the melting point of the sintering additive is lowered from 1940°C (2wt%Al_2O_3-2.65wt%Y_2O_3 composition) to between 1600 and 1700°C (2wt%Al_2O_3-2.65wt%Y_2O_3-1wt%SiO_2 composition). This means that when the composite is sintered at 1800°C there is enough liquid phase present to accelerate mass transport which improved densification. Of course the presence of B_2O_3 in this system will further lower the melting point strongly since the

melting point of B_2O_3 is much lower. Hence, nearly full densification was achieved for Al-Y-Si-doped B_6O composites. TEM results showed that there is incorporation of boron into the glassy phase. As mentioned earlier, the presence of boron stabilises the glassy phase and prevents the formation of crystalline phases. The high amount of liquid phase during sintering explains why XRD peaks for these composites were sharper (crystalline) compared to the composites containing only Al_2O_3 and Y_2O_3 as sintering additives. The formation of high amount of liquid phase during sintering also resulted in exaggerated grain growth for higher SiO_2 content (see figure 5.21) and therefore lower hardness values were obtained for these materials in comparison to materials without SiO_2 addition. B_6O composite containing Al_2O_3 and SiO_2 (**18**B_6O**2**Al**1**Si***a***) was hot pressed at 1800^oC under a pressure of 50 MPa for 20 minutes. From the phase diagram, the addition of 1 wt% SiO_2 to 2 wt% Al_2O_3 lowers the melting point from 2040^oC (2 wt% Al_2O_3 addition) to between 1800 and 1900^oC (with 1 wt% SiO_2 addition). The presence of B_2O_3 will still lower the melting point of this system. Surprisingly, low density was measured for this composite material suggesting very little B_2O_3 present in the starting powder.

In the post heat treatment of selected materials (**18**B_6O**1**Al**1.32**Y***b*****-2**, **18**B_6O**2**Al**2.65**Y***b*****-2**, **18**B_6O**2.87**Al**1.58**Y***b***, and **18**B_6O**2**Al**2.65**Y**1**Si***b***), the extent of decomposition was measured by means of weight loss measurement. Materials were heat treated at 1250^oC for 10 hours in argon atmosphere. For **18**B_6O**1**Al**1.32**Y***b*****-2**, no decomposition was observed and the measured density did not change after heat treatment. Only slight decomposition was observed for the other materials. The densities however remained almost the same. This means that decomposition is high for high Al_2O_3 content and therefore decomposition of Al_2O_3 and silicates are the main reason for the slight weight losses observed. XRD analyses before and after heat treatments showed no phase change and no crystalline phase was formed after the heat treatment.

B_6O composites containing Al_2O_3 were densified to nearly theoretical densities by hot pressing at 1900°C under a pressure of 50 MPa for 20 minutes. This is 100°C higher than for Al-Y-Si-doped B_6O composites. Al_2O_3 was expected to react with the existing B_2O_3 on the surfaces of B_6O particles during sintering. Densities more than 97% of theoretical densities were achieved. Sharp increase in densification was observed up to 1.2 volume fraction of additive content (Figure 6.8). Thereafter, increasing the amount of additive did not have strong influence of the densification behaviour. It was found out that an increase in the amount of Al_2O_3 could result in scattering of the measured densities [16]. This is due to decomposition of Al_2O_3 at high temperatures.

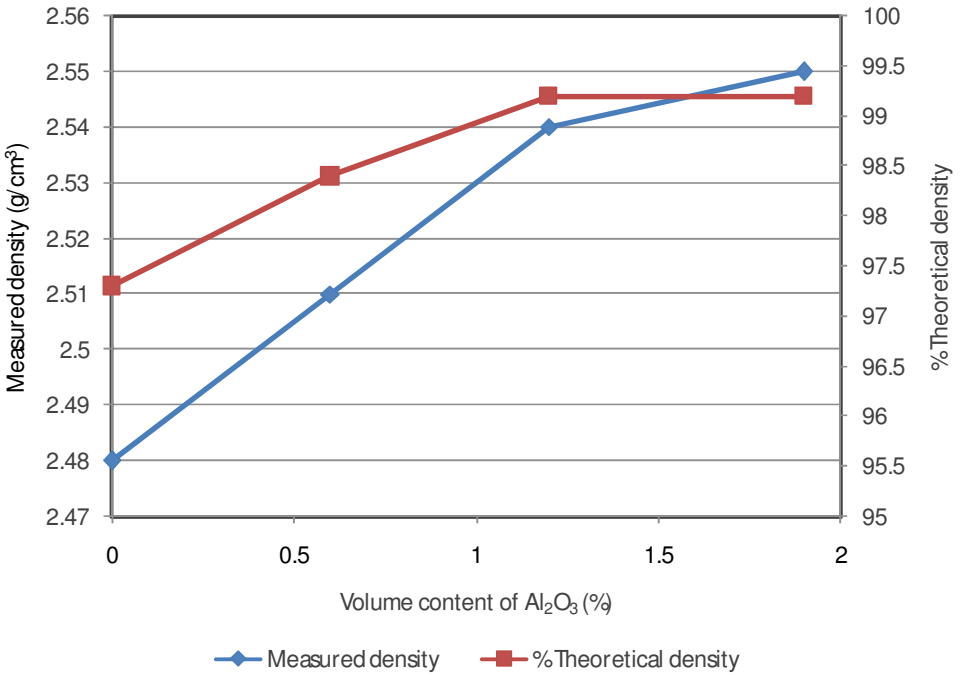

Figure 6.8: Density of B_6O composites hot pressed at 1900°C as a function of volume content of Al_2O_3 additive.

Densification of B_6O composites containing Al_2O_3 could also be explained with the help of Al_2O_3-B_2O_3 phase diagram shown in figure 6.9. Thermodynamic equilibrium calculations for B_6O-Al_2O_3 system indicate that an oxide liquid containing Al_2O_3 and B_2O_3 is in equilibrium with B_6O and $Al_{18}B_4O_{33}$ (Figure 3.8). The existing B_2O_3 on the surface of the starting B_6O powder and the Al_2O_3 added formed aluminium borates, and at high temperatures an oxide liquid. This liquid could recrystallise to form Al_2O_3-B_2O_3 compounds during cooling. The type of aluminium borate formed would depend on the ratio of Al_2O_3 to B_2O_3 in the liquid. According to the phase diagram (Figure 6.9), a liquid phase is formed at about 1200^{o}C if the Al_2O_3/B_2O_3 mol ratio is between 9:2 ($Al_{18}B_4O_{33}$) and 2:1 ($Al_4B_2O_9$). All secondary phases are dissolved in the liquid at the incongruent melting point of $Al_{18}B_4O_{33}$. Thermodynamic calculations presented in Chapter 3 indicate that the addition of Al_2O_3 lowers the partial pressure of boron containing compounds by a factor of 2 at 1900^{o}C. This helps to stabilise the liquid phase during sintering. This follows that the amount of B_2O_3 present will strongly affect densification of B_6O composites as mentioned earlier in this section. Phase analyses (XRD) carried out on the hot pressed materials indicated the formation of $Al_{18}B_4O_{33}$ and this borate phase has been confirm by TEM results by Kleebe *et al*. **(87)**.

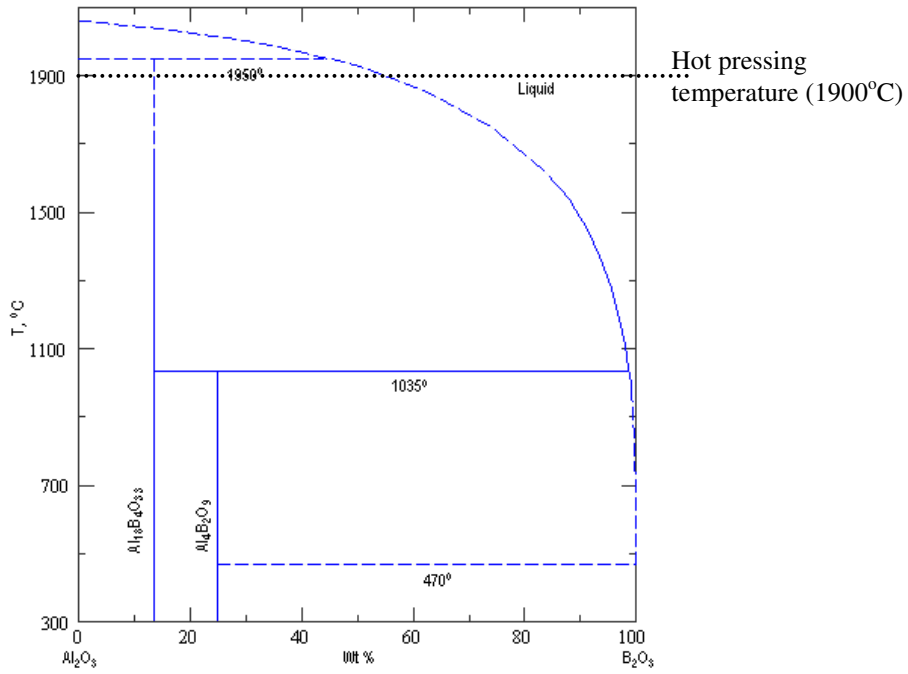

Figure 6.9: Al_2O_3-B_2O_3 phase diagram [83].

The B_6O composite produced by the addition of TiC was not as dense as Al-Y-Si-doped and Al-doped B_6O composites. A material with a density 96% of theoretical was obtained. This material was hot pressed at 1900°C under a pressure of 50 MPa for 20 minutes (100°C higher than Al-Y-Si-doped composites). On the contrary, the addition of TiB_2 resulted in nearly full densification with about 100% of the theoretical density achieved. The reason for the reduced densification in TiC-B_6O composite is due to the strong decomposition of TiC at high temperatures leading to the formation of TiB_2. Details of the reactions involving TiC, B_6O and B_2O_3 are presented in Chapter 3. For higher amounts of TiC, a stronger decomposition takes place which results in reduced densification. Therefore the addition of TiC is only recommended in small amounts less than 5 wt%. At high temperatures (> 1500°C)

TiB_2 is the most thermodynamically stable phase which is the reason for the high density obtained for this material.

B_6O composite was also produced using Pd as additive. This material (**19**B_6O**5**Pd) was hot pressed at 1600 and 1900^oC under a pressure of 50 MPa for 30 minutes. Melting of Pd and B_2O_3 present on the surfaces of B_6O particles takes place below 1200^oC (Figure 6.10). This improved densification due to liquid phase sintering. The formed liquid recrystallises during cooling forming Pd_2B at the grain boundaries. The type of Pd boride formed will depend on the amount of boron dissolved in Pd. SEM investigations revealed that one end of the sample was boron-rich whilst the other end was Pd-rich. The reason for the precipitation of boron in the sample is not completely clear. It could be connected with inhomogeneous temperature distribution in the furnace. A good combination of properties has been achieved by lowering the volume content of Pd (2 vol. %) and sintering temperature (1800^oC). The properties of this material are given in table 5.9.

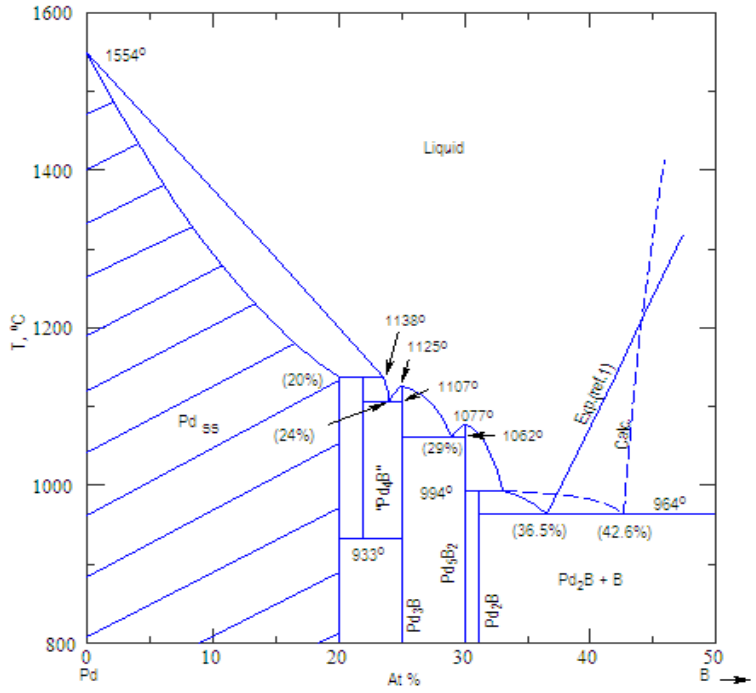

Figure 6.10: Phase diagram for Pd-B system [83].

6.3 Relationship between microstructure and hardness

Mechanical properties for 'pure' B_6O hot pressed materials are given in table 5.2. The grain size of the hot pressed compacts could not be determined using SEM. Nevertheless, the starting mean particle size of B_6O powders produced at Wits (d_{50} = 4.59 µm) was higher than those milled for 30 hours (d_{50} = 0.4 µm). Assuming that there is little B_2O_3 on the surfaces of B_6O particles and therefore no grain growth during hot pressing, the results obtained in this work indicate that the hardness of the hot pressed 'pure' B_6O depends on the grain sizes (Figure 6.11). This is in accordance with what has been predicted by the Hall-Petch relationship which depicts a decrease in hardness with increase in grain size in sintered compact.

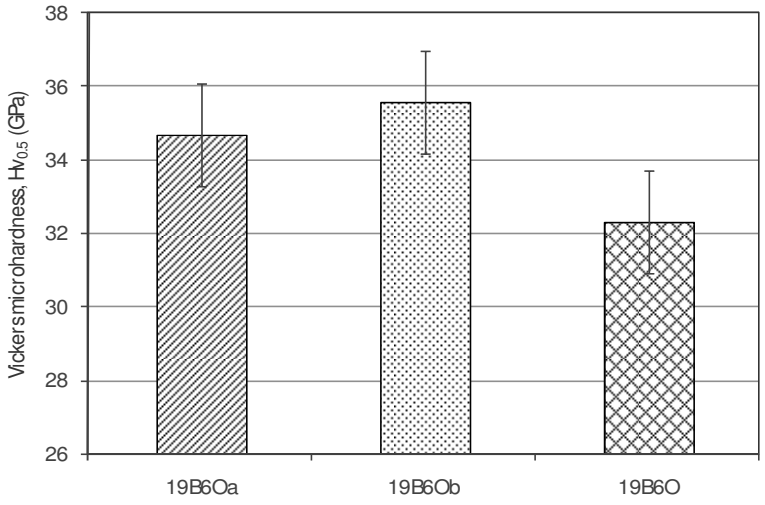

Figure 6.11: Vickers microhardness ($Hv_{0.5}$) of 'pure' B_6O hot pressed materials.

Figure 6.12 shows the differences in hardness of Al-Y-Si-doped B_6O hot pressed composites measured using 5kg load. For comparison, materials produced from the second batch of milled powder have been used. In general, the hardness of 'pure' B_6O material decreased from 35.6 GPa to 27.6 GPa with increasing amount of additive content due to the lower intrinsic hardness of the secondary phases formed. The hardness values of the Al-Y-doped B_6O hot pressed composites were similar. The hardness values for Al-Y-Si-doped B_6O composites were also found to be similar. Nevertheless, the macro-hardness values of the Al-Y-doped B_6O composites were slightly higher than the Al-Y-Si-doped composited even though the measured densities were similar. This is due to the differences in composition of the grain boundaries as well as grain sizes of these composites. Grains sizes of sintered Al-Y-Si-doped composites were higher than that of Al-Y-doped composites.

Figure 6.13 shows the relationship between hardness and volume content of oxide additives for the different Al_2O_3:Y_2O_3 mol ratios. Generally, as the volume content of additive was increased, the hardness decreased for all Al_2O_3:Y_2O_3 mol ratios. This is due to the intrinsic low hardness values of the secondary phases formed.

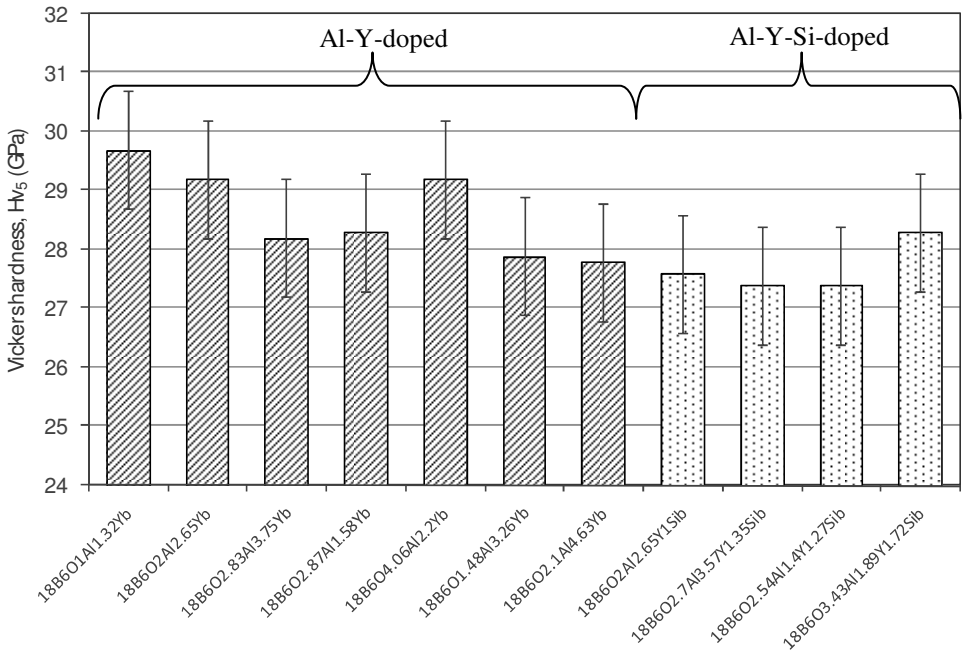

Figure 6.12: Vickers hardness of Al-Y-Si-doped B_6O composites measured using 5kg load.

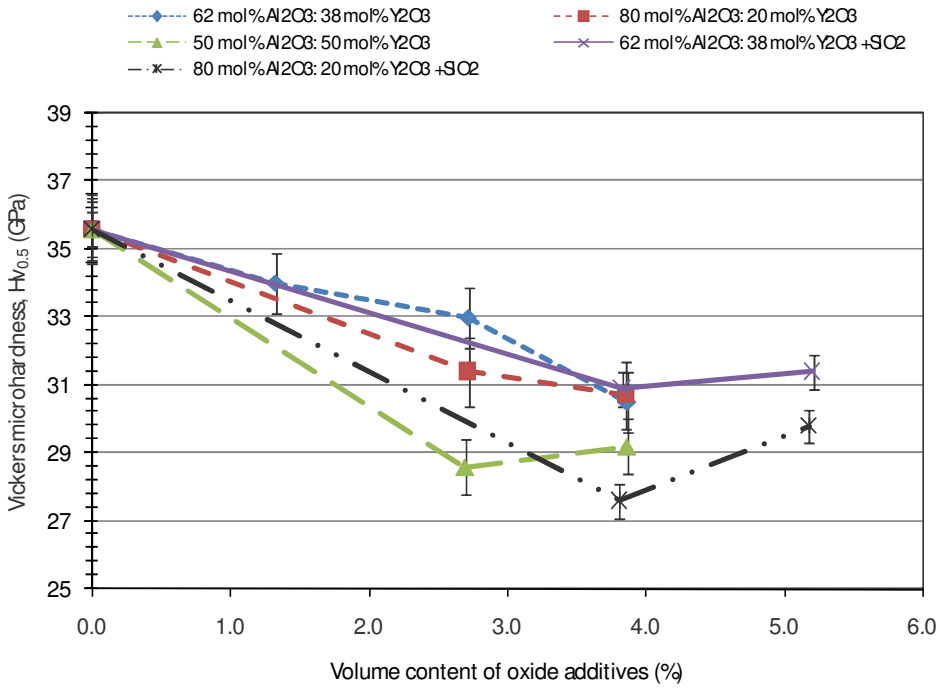

Figure 6.13: Vickers microhardness ($Hv_{0.5}$) as a function of volume content of additives for the various Al_2O_3:Y_2O_3 mol ratios.

The hardness decreased strongly for 50% mol fraction of Al_2O_3 in the additives followed by 80% mol fraction of Al_2O_3 in the additives with SiO_2 addition. Composite containing 62% mol Al_2O_3 in the additives did not show strong reduction in hardness as the volume content was increased. Hardness also increased for higher volume content for composites containing SiO_2 due to changes in the composition of the grain boundaries as compared to composites without SiO_2 addition. The strong reduction in hardness for 50% mol fraction of Al_2O_3 in the additives could be connected with incomplete densification; and for 80% mol fraction, could be connected with decomposition of the oxide additive at sintering temperatures.

Figure 6.14 shows the differences in hardness between the selected hot pressed B_6O composites and their heat treated counterparts. It is clear that the hardness after heat treatment increased. The increase in hardness cannot only be attributed to the decrease in the amount of the grain boundary phase due to decomposition since the densities after heat treatment remained almost the same. The increase in hardness in this work is believed to be connected with the change in composition of the grain boundary phases during heat treatment. The grain boundary composition could change from being Al_2O_3-rich to Y_2O_3-rich. These phases have difference crystal structures and therefore will have different hardness values. The exact hardness values of these phases could not be determined in this work.

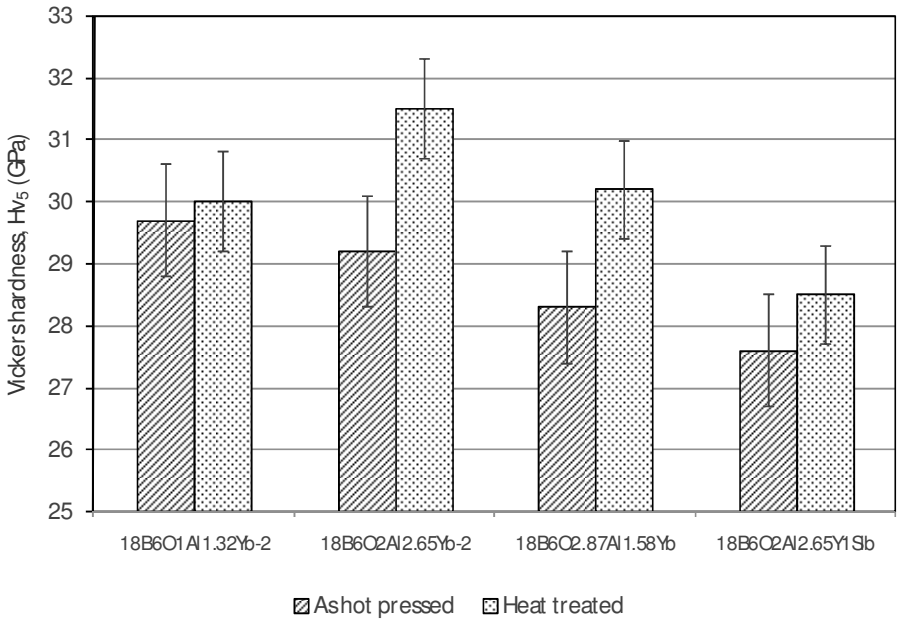

Figure 6.14: Graph comparing the hardness of as hot-pressed B_6O composites with those which were heat treated at 1250°C for 10 hours in argon atmosphere. Hardness values were measured using 5kg load.

For B_6O composites containing Al_2O_3, it was observed that the hardness decreased (Figure 6.15) when the amount of Al_2O_3 was increased. The decline in hardness is due to the increasing amounts of secondary phases at the grain boundaries which are less hard compared to B_6O. Kleebe *et al.* [87] also found out that the decrease in hardness could also be connected with the residual porosities near the aluminium borate phase as a result of stresses created due to the differences in thermal expansion coefficient at the $B_6O/Al_{18}B_4O_{33}$ grain interface or by low chemical stability of the boron-rich phases. The hardness of **19**B_6O**5**TiC***a*** and **19**B_6O**5**TiB_2***a*** materials decreased strongly compared to **19**B_6O***a***. The strong reduction in hardness produced in this work could be connected with the Al impurities introduced during mixing of the powders which formed $Al_{18}B_4O_{33}$ besides TiB_2 and B_6O. The low hardness values are still strange since high hardness ($Hv_{0.4}$ = 37.4 GPa) was recorded for a B_6O composite material containing 2 wt% Al_2O_3, 2 wt% Y_2O_3 and 10 wt% TiB_2 produced

at IKTS [85]. More detailed investigations are necessary to understand the densification behaviour of these materials. The reduced hardness of **19**B_6O**5**Pd is due to the high amount of binder phase introduced. A higher hardness was achieved when the volume content of Pd was reduced (see table 5.11).

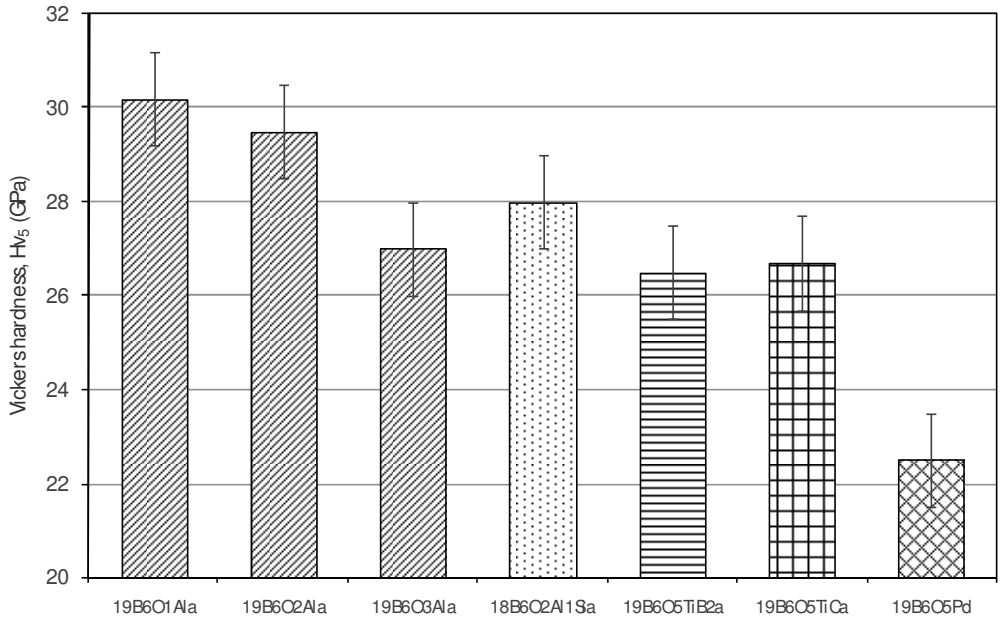

Figure 6.15: Vickers hardness of other B_6O composites measured using 5kg load.

The hardness values obtained for the materials produced in this work are very good considering the fact that is was measured using a load of 500g. For a single crystal B_6O produced by He *et al*. [9], a microhardness of 45 GPa was measured using a load of 100g. It must be mentioned here that the hardness of a single crystal is higher than that of a sintered compact due to the presence of weaker grain boundaries. It can be observed from figure 6.16 that the hardness values of hot pressed 'pure' B_6O produced in this work were higher than that produced by Itoh *et al*. [3] who used high pressure techniques. Hardness values obtained in this work could also be compared with hardness values obtained by Kayhan and Inal [5]. The hardness value obtained by Shabalala [16] is slightly lower than that measured for **19**B_6O***b*** material. This is

connected with the reduced grain sizes of B_6O powder used in this work. The grain size of the sintered compact produced by Shabalala was between 2 and 10 µm whereas the grain size of **19**B_6O***b*** material is less than 1 µm. The Vickers hardness of **19**B_6O***b*** material was also higher than that produced by Goosey and Anderson [52] ($KH_{0.1}$ = 30 GPa), Petrak *et al.* [38] ($KH_{0.1}$ = 30.4 GPa), and Bairamashvili *et al.* [53] ($KH_{0.1}$ = 32 GPa). The wide variation of hardness values reported for B_6O is due to the different ways of producing the sintered compacts. The most obvious reasons for the variation in hardness values are differences in sintering temperature, pressure, impurities introduced during sintering, and sintering time. These could affect the densification of the resulting sintered materials. The process route for synthesising B_6O can also affect its stoichiometry which will subsequently affect the hardness of the sintered compacts.

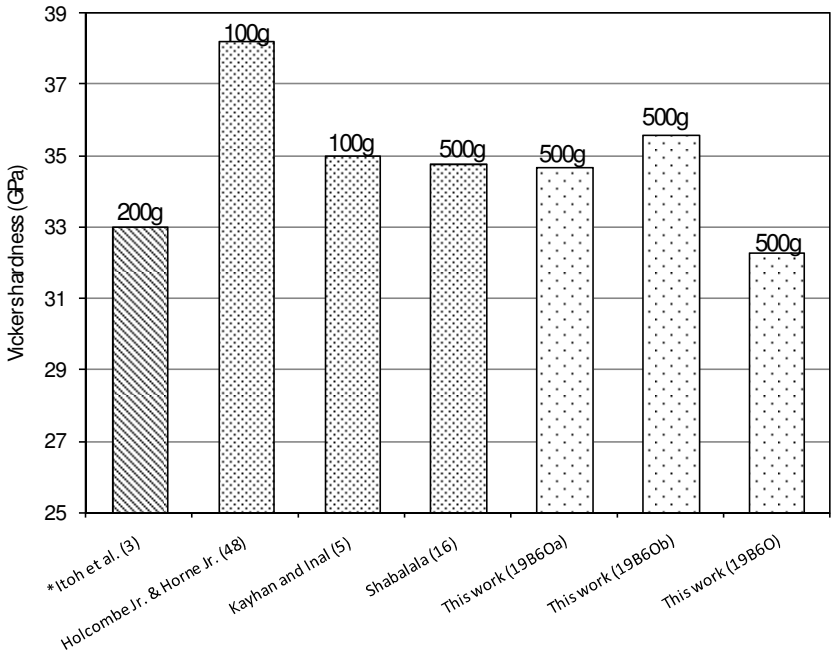

Figure 6.16: Comparing Vickers hardness values of 'pure' B_6O sintered compacts obtained in this work and those obtained by other researchers. Loads used are shown on top of the bars. * High pressure techniques.

It is also important to note that hardness measurement could be done on B_6O composites produced in this work using 5kg load. Measurement values reported for B_6O composites have been carried out using a maximum of 200g load, except for Shabalala who reported hardness values using 0.5 and 5kg loads. Figure 6.17 compares some of the hardness values reported for B_6O composites produced by other researchers. The composition of the doped materials has been given in brackets.

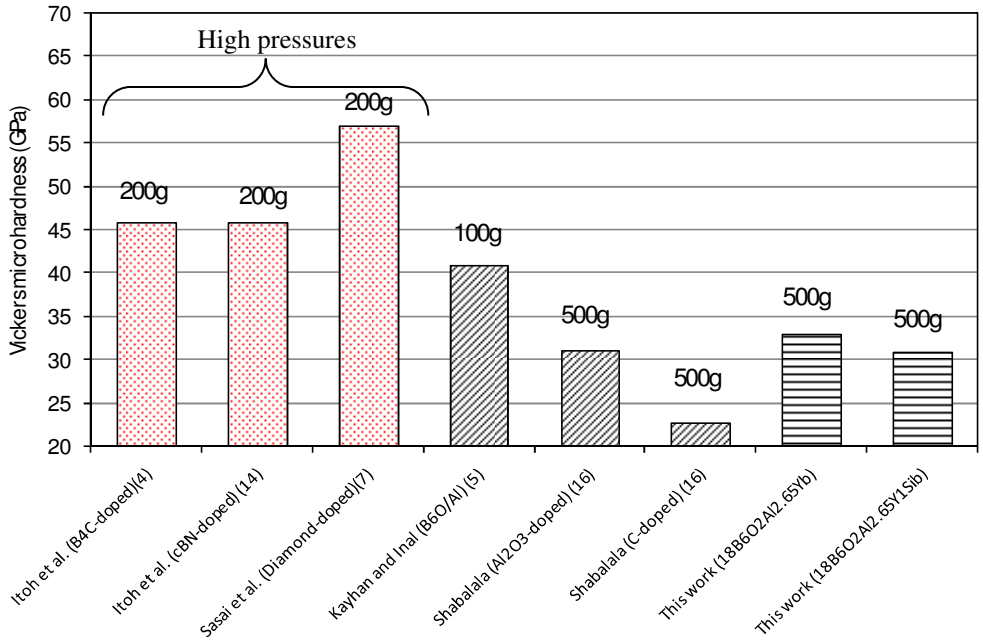

Figure 6.17: Microhardness of **18**B_6O**2**Al**2.65**Y***b*****-2** composite material compared to microhardness obtained by other researchers. Loads used are shown on the graph.

It is clear from figure 6.17 that the hardness value obtained in this work is encouraging. The high microhardness obtained by Itoh *et al*. and Sasai *et al*. was because of the relatively hard secondary phases in the composites. Both found that neither solid solutions nor new compound was formed under the sintering conditions and that the sintered composite consists of the mixed phases of B_6O and B_4C, cBN, and diamond respectively. B_4C, cBN and diamond are all ultrahard materials

compared to aluminium borates formed in composites produced in this work as well as the work of Kayhan and Inal and Shabalala. Even though very high hardness values were recorded for composites produced by Itoh *et al*. and Sasai *et al*., their corresponding toughness values were very low.

6.4 Relationship between microstructure and fracture toughness

Fracture toughness of a single crystal B_6O was found to be 4.5 $MPam^{1/2}$ [9]. 'Pure' B_6O sintered compact is however known to be brittle. The reason for the very low toughness is not understood. Fracture toughness values reported in this work were measured using 5kg load. SEM image showing indentation made with 5kg load on Al-Y-doped B_6O composite is shown in Appendix D (Figure D7). **19**B_6O and **19**B_6O***b*** materials hot pressed in this work were measured using 1 and 0.5kg load. Increasing the load above 1kg caused chipping of the B_6O crystals. Therefore fracture toughness was not measured for these materials. Nevertheless, toughness measurement was carried out on **19**B_6O***a*** material using a load of 5kg and was found to be 3.3 $MPam^{1/2}$. Toughness measurement was possible because of the relatively high concentrations of Fe and Cr impurities in this material which formed boride secondary phases in the hot pressed compact. It must be mentioned here that the material showed a high scattering in the properties measured with partial chipping during indentation. Figure 6.18a shows the indentation crack path in **19**B_6O***a*** material using 5kg load. Fracture was mainly transgranular. Phase analysis using XRD technique identified the secondary phases to be FeB and CrB_2.

Fracture toughness values obtained for B_6O composites produced from the first batch of milled powder were higher than those produced from the second batch of milled powder due to the high concentrations of Fe and Cr in the former. This makes sense because before even adding sintering additives, the fracture toughness of 'pure' B_6O hot pressed from the first batch of milled powder (**19**B_6O***a***) was 3.3 $MPam^{1/2}$. Therefore the addition of small amount of transition metal boride additives would

result in fracture toughness values higher than 3.3 MPam$^{1/2}$ but with minor effect on hardness. Figure 6.19 compares the effect of Fe and Cr contaminations (as a result of milling) on the fracture toughness of the composites produced from the different B_6O powders. It is clear from this figure that Fe and Cr contaminations increased the toughness of composites prepared from the first batch of milled powder in comparison to the second batch of milled powder.

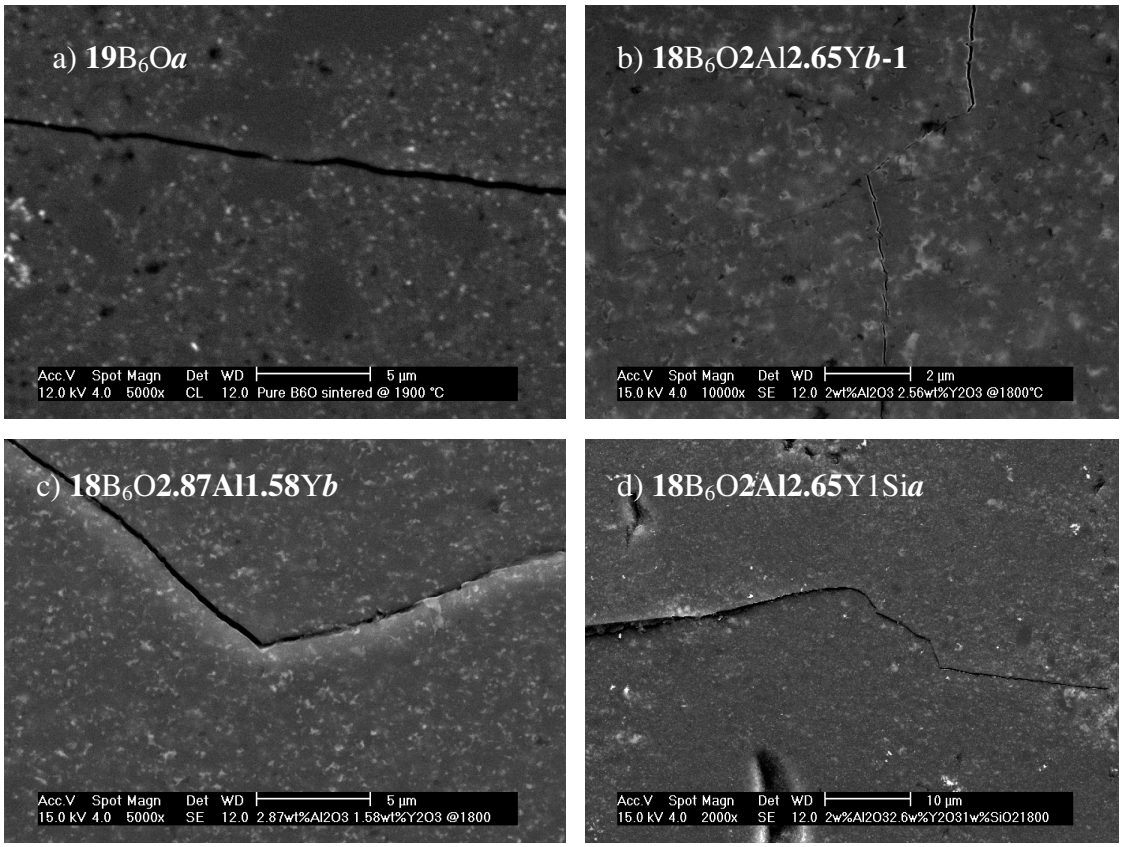

Figure 6.18: Indentation crack path on a polished 'pure'B_6O and B_6O composites using 5kg load.

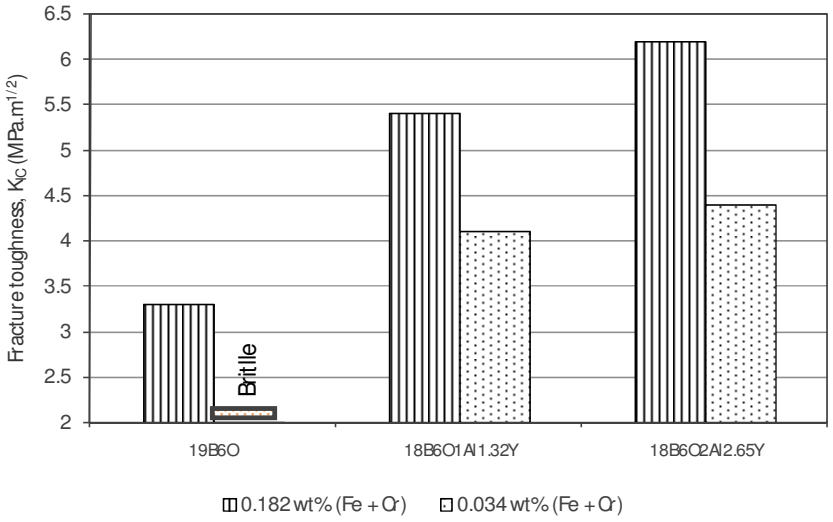

Figure 6.19: Effect of Fe and Cr concentrations in starting B_6O powders (due to milling) on fracture toughness values obtained for sintered composites. Measurements were done using 5kg load. Fracture toughness of **19**B_6O containing 0.034 wt% contamination was not measured due to chipping of the B_6O crystals upon application of load.

Beside the differences arising from the different concentrations of Fe and Cr impurities in B_6O powder as a result of milling, fracture toughness of the different Al-Y-doped B_6O hot pressed composites were similar. Figure 6.20 shows the fracture toughness of the different Al-Y-doped B_6O composites whilst figure 6.21 compares the fracture toughness of these composites with changes in the volume content of oxide additives. Fracture toughness increased sharply for small addition of oxide additives after which no increase in toughness was observed when additive content was increased. This is due to the similarity in grain sizes and grain boundary structure in the different hot pressed materials. Nevertheless, there is significant increase in fracture toughness compared to the 'pure' B_6O hot pressed material (**19**B_6O***b***) which was brittle. The grain boundary phases were found to be amorphous and similar in all hot pressed materials with segregations of yttria in higher additive content. Segregations of yttria could also be the reason why the fracture toughness did not increase for higher volume content of additives.

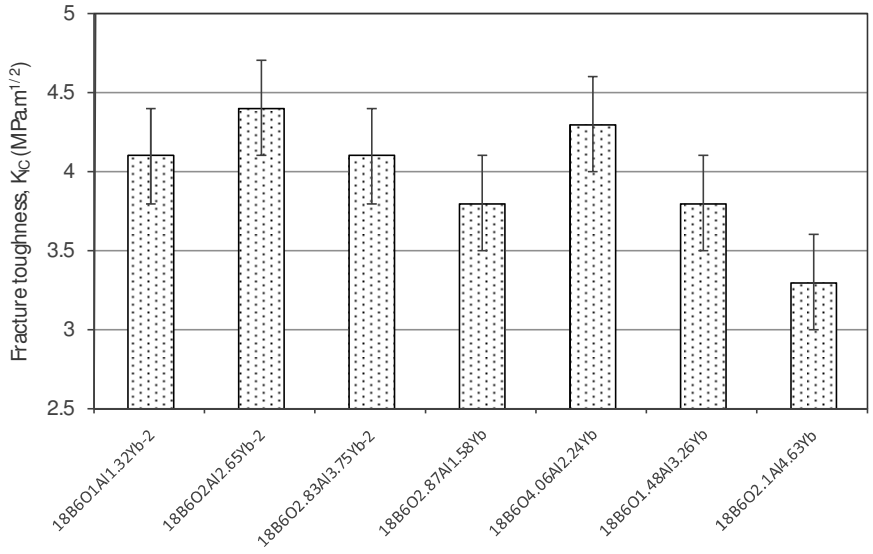

Figure 6.20: Fracture toughness values of Al-Y-doped B_6O hot pressed composites. Measurements were done using 5kg load.

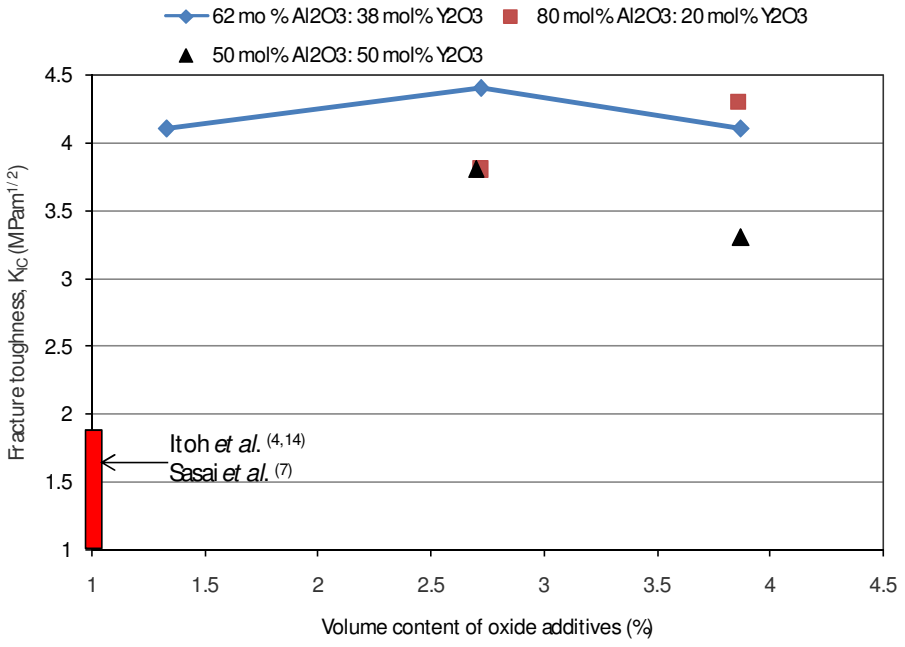

Figure 6.21: Dependence of fracture toughness on the volume content of Al-Y oxide additives (the mole ratios in the additives are given).

The fracture toughness values of Al-Y-Si-doped B_6O composites were also similar (Figure 6.22). Figure 6.23 compares the variation in fracture toughness as the volume content of additive is increased for 62 and 80 % mol fractions of Al_2O_3 in the additives. The fracture toughness increased with increasing volume content of additives. The 80% mol fraction of Al_2O_3 in the additives had higher fracture toughness than the 62% mol fraction of Al_2O_3 in the additives. No segregation of the grain boundary was observed in high additive content compared to Al-Y-doped B_6O composites. Nevertheless, grain growth was observed, at least for higher SiO_2 content. The grain boundary phases therefore indirectly influence the fracture toughness of these composite.

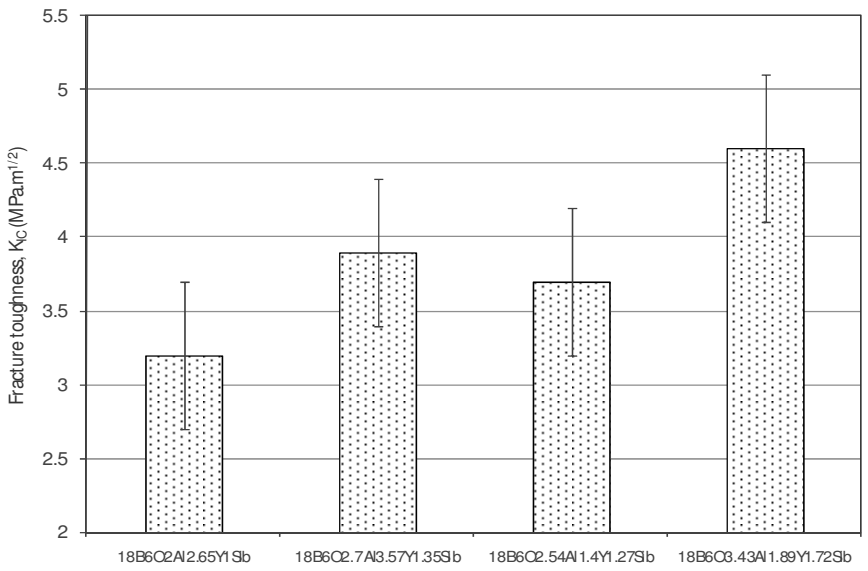

Figure 6.22: Fracture toughness values Al-Y-Si-doped B_6O hot pressed composites. Measurements were done using 5kg load.

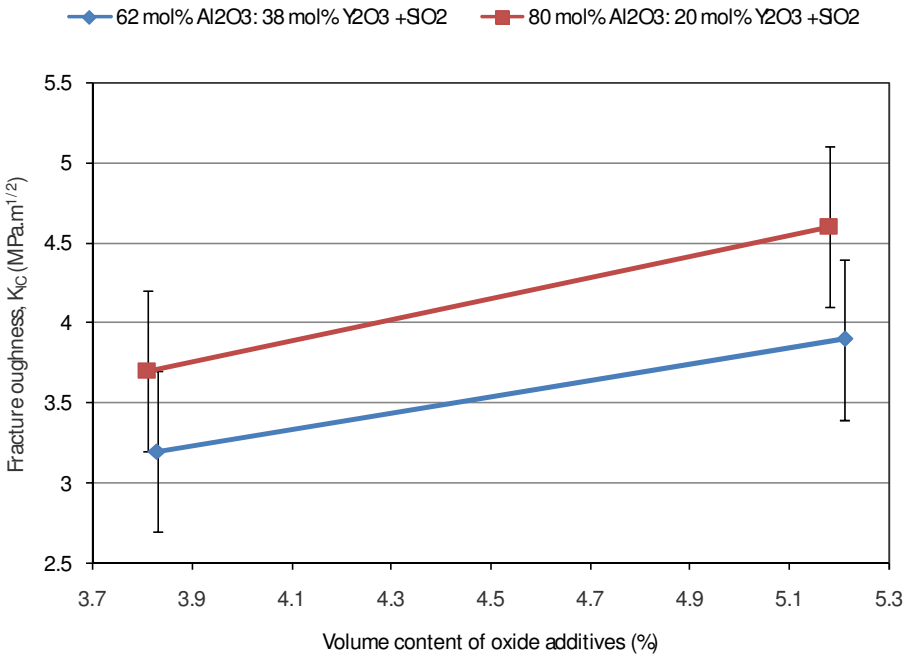

Figure 6.23: Dependence of fracture toughness on the volume content of Al-Y-Si oxide additives (the mole ratios in the additives are given).

SEM images of the crack paths of polished Al-Y-doped and Al-Y-Si-doped B_6O composites are shown in figure 6.18. Additional images are given in Appendix D (Figure D8-9). It was observed that the improvement of fracture toughness is caused by crack deflection and bowing of the propagating cracks. It must be mentioned here that not all cracks were deflected. Crack deflections observed do not follow along grain boundaries and therefore cannot be considered as intergranular fracture. Fracture was predominantly transgranular.

Facture toughness values obtained for B_6O composites containing Al_2O_3 were very good. These composites were produced from the first batch of milled powder. Figure 6.24 compares the fracture toughness values obtained for Al-doped B_6O composites. As the amount of Al_2O_3 increased the fracture toughness decreased. This is surprising since one expects the toughness to increase with increasing Al_2O_3 content since

aluminium borates formed is less hard compared to B_6O. The corresponding hardness decreased with increasing amount of Al_2O_3 addition (Figure 6.15). The only reason for the reduced toughness is due to the strong decomposition reaction at the sintering temperature (1900°C). This decomposition reaction increases with increasing amount of Al_2O_3 in the form of Al_2O as shown in Chapter 3. The decomposition reaction is also affected by the amount of B_2O_3 present in the starting powder. Nevertheless, the fracture toughness values recorded were still high.

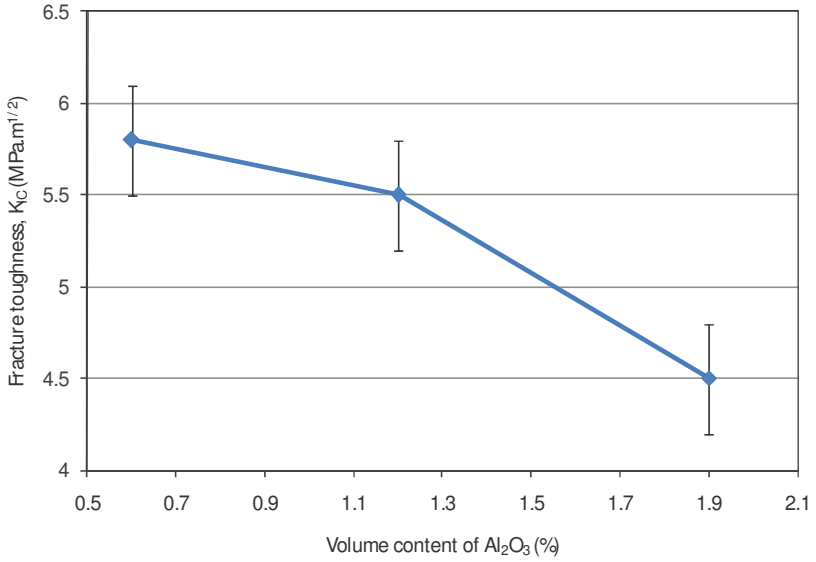

Figure 6.24: Fracture toughness of Al-doped B_6O composites showing a decrease in toughness as the volume content of Al_2O_3 is increased.

The fracture toughness of B_6O composites containing TiC and TiB_2 were very good. A toughness of 4.3 MPam$^{1/2}$ was recorded for B_6O-TiC composite whilst 6.7 MPam$^{1/2}$ was recorded for B_6O-TiB_2 composite. The increase in toughness may be attributed to the composition of the grain boundary phase which comprises of Fe, Cr, Ti, and B. Fracture toughness obtained for Pd-doped B_6O composite was very high (13.5 MPam$^{1/2}$), probably the highest recorded so far for B_6O-based composites. Nevertheless, the hardness dropped to 22 GPa due to the high amount of Pd used. Good combination of hardness (28 GPa) and fracture toughness (5.1 MPam$^{1/2}$) was

obtained when 2 vol. % of Pd was used. Pd_2B was formed at the grain boundaries. It is believed that the grain boundary composition increased the toughness of this composite.

6.4.1 Toughening mechanisms

Observations made in section 6.4 reveal that fracture toughness was increased by addition of small amount of additive content after which any increase in volume content does not result in further improvement of the toughness values. Different fracture mechanisms such as crack deflection due to bimetallic stresses, or due to crack arrest in the secondary phase (e.g. pore), or due to the changes in the grain boundaries between B_6O grains can be proposed for the different B_6O composites produced. Figure 6.25 shows schematic diagrams of the different toughening mechanisms. Fracture toughness enhancement observed in the materials studied in this work could be due to a combination of these different mechanisms.

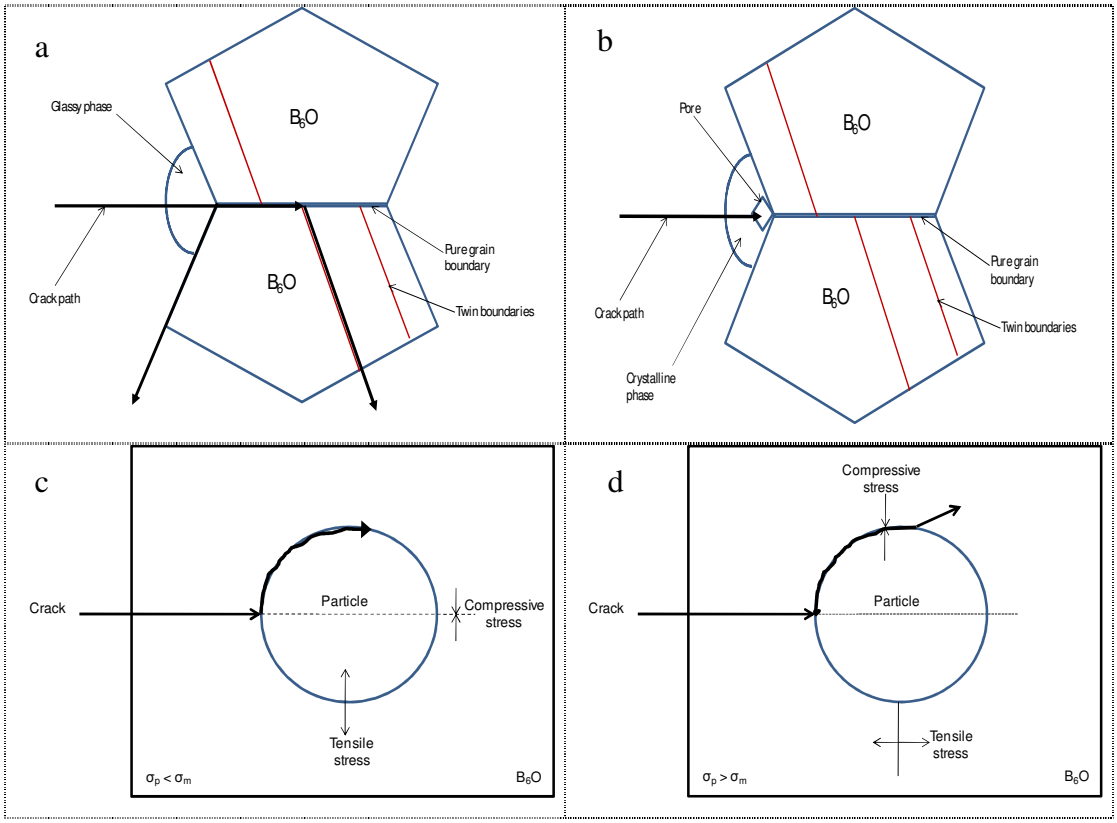

Figure 6.25: Schematic diagram of different fracture mechanisms that can be proposed for B_6O composites produced in this work. (a) Crack deflects either along the grain boundaries or along the twin boundaries in B_6O grains. (b) Crack arrested by pore near the grain boundary. (c) Crack deflection towards the particle due to mismatch in thermal expansion coefficients ($\alpha_p < \alpha_m$) between the particle and B_6O matrix. (d) Crack deflection around the particle due to mismatch in thermal expansion coefficients ($\alpha_p > \alpha_m$) between the particle and B_6O matrix.

Crack deflections and bowing could be observed in figures 6.18 and D9. Such phenomena can be explained by stresses that exist in the composites. The B_6O matrix has different thermal expansion coefficient (CTE) with the secondary phases. Taking B_6O and TiB_2 for example, the CTE values are 5.56 x 10^{-6} and 8.1 x 10^{-6}/°C, respectively **(53)(88)**. Large internal stresses would form when the composite is cooled down from sintering temperature. The internal stresses could be calculated using equation 6.1 **(89)**.

$$\sigma_{rad} = -2\sigma_{\tan}\left(\frac{(\alpha_m - \alpha_s)\Delta T}{[(1-2\nu_s)/E_s + (1+\nu_m)/2E_m]}\right) \quad [\mathbf{6.1}]$$

where $\alpha_{m,s}$ = thermal expansion coefficients of matrix (B_6O) and the secondary phase (TiB_2).

ΔT = change in temperature at which sufficient softening occurs to alleviate the stresses (~1000^oC)

$\nu_{m,s}$ = Poison ratios of matrix (B_6O ~ 0.197) and secondary phase (TiB_2 ~ 0.1-0.15)

$E_{m,s}$ = Elastic moduli of matrix (B_6O ~ 540 GPa) and secondary phase (TiB_2 ~ 366.9 GPa) **(90)**

This gives a stress of between 770 – 840 MPa. Properties of B_6O were taken from Shabalala **(16)**. This reveals high compressive stress to B_6O matrix. Transgranular fracture was observed in the sintered composites and in some cases cracks were deflected. This is an indication that the binding forces between grain boundaries were so strong that cracks tend to advance transgranularly and this can consume more energy. Bowing of propagating crack could also be observed when the B_6O grain undergoes compressive stresses. Additionally, the presence of twin boundaries in B_6O crystals, which is a characteristic of boron compounds, can make major cracks deflect and branch, and also make the development of main cracks consume more energy as shown in schematic diagram (Figure 6.25a). Consequently, these materials showed high toughness.

The high toughness in Al-doped composites is due to the formation of $Al_{18}B_4O_{33}$. Tensile stresses of between 1380 – 1700 MPa would exist between $B_6O/Al_{18}B_4O_{33}$ interface (assuming the following $Al_{18}B_4O_{33}$ properties: E = 400 GPa; CTE = 1.9 x $10^{-6}/^oC$; and ν = 0.2 - 0.3) **(91)**. This stresses could deflect propagating crack towards the particle as shown in figure 6.25c. However, crack deflection is not likely because

around $Al_{18}B_4O_{33}$, pores are formed due to shrinkage during crystallisation [87]. These small pores act as crack-arrest sites (see figure 6.25b) and therefore improve fracture toughness. Additionally, TEM investigations did not show any internal stresses in Al-doped materials. As analysed above, it is believed that fracture enhancement is due to a combination of these mechanisms.

A good combination of fracture toughness and hardness were obtained in this work. Figure 6.26 compares the fracture toughness and hardness values of selected composites obtained in this work to those obtained by other researchers. Fracture toughness has been enhancement by the introduction of secondary phases to the B_6O matrix with small reduction in hardness. The reason for the increase in fracture toughness could be due to many reasons such as crack deflection due to bimetallic stresses, or due to crack arrest in the secondary phase, or due to the solidification of the secondary phases between B_6O particles being present as films or by many other mechanisms. The additives used had the potential of removing the B_2O_3 present at the surfaces of B_6O particles thereby forming other phases that cause bimetallic strain toughening at the grain boundaries.

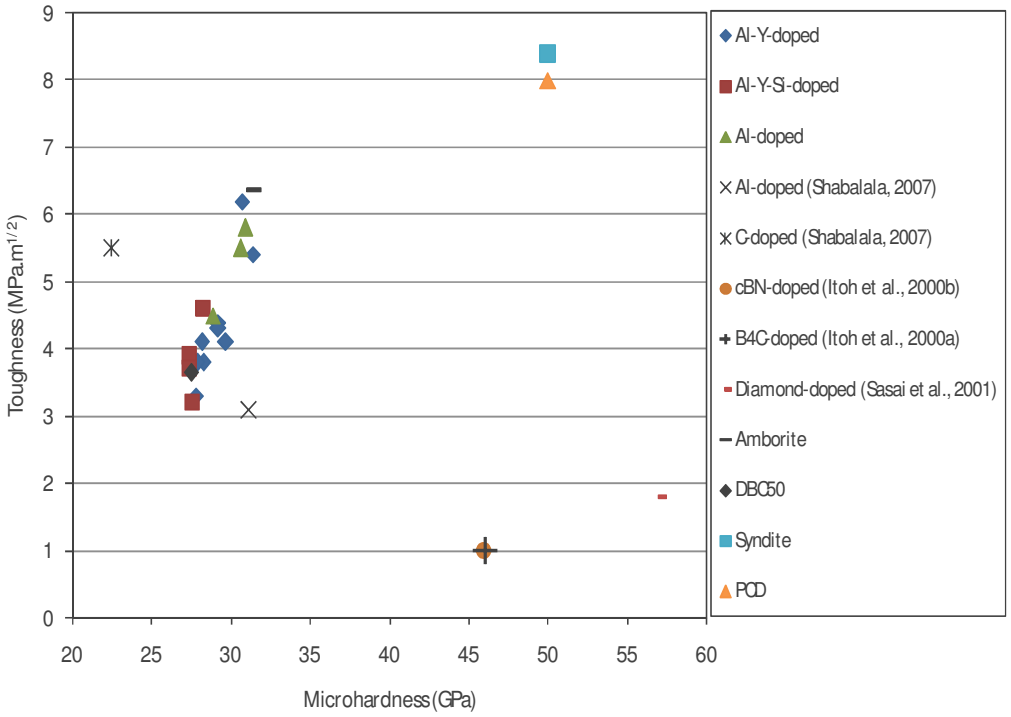

Figure 6.26: Comparison of fracture toughness and hardness values of doped B_6O composites produced in this work and those produced by other researchers. Mechanical properties of other ultrahard materials have also been included for comparison [92]. The data of Kayhan and Inal [5] were not used because they are doubtful (see pages 24-25).

6.5 Relationship between microstructure and elastic properties

The elastic properties of hot pressed B_6O composites namely, **18**B_6O**1**Al**1.32**Y***b***, **18**B_6O**2**Al**2.65**Y***b***, **18**B_6O**2.87**Al**1.58**Y***b***, and **18**B_6O**2**Al**2.65**Y**1**Si***b*** were measured and the results were presented in section 5.7. The elastic moduli of the hot pressed materials are between 429 and 462 GPa. Similarly, the shear moduli are between 183 and 200 GPa whilst the bulk moduli are between 207 and 249 GPa (Table 5.10). As the additive content (Al_2O_3) increased, the elastic properties of the hot pressed composites decreased. Hot pressed composite containing 2.87 wt% Al_2O_3 and 1.58 wt% Y_2O_3 (**18**B_6O**2.87**Al**1.58**Y***b***) recorded the least of the elastic constants.

By first approximation, the elastic modulus of a composite is given by the rule of mixtures as described in equation 6.2 [64]:

$$E = E_1V_1 + E_2V_2 + ... + E_iV_i \qquad [\mathbf{6.2}]$$

Thus each phase contributes according to its volume fraction, V_i. Figure 6.27 and 6.28 shows the relationship between the volume content of oxide additives and the measured elastic constants. It is evident that the elastic constants decreased with increasing volume content of additives. A strong reduction in elastic constants was observed for **18**B_6O**2.87**Al**1.58**Y***b*** material. Microstructural observations showed some segregated grain boundary phases in this material (see figure 5.13). This could be the reason why lower elastic constants were measured for this material.

SiO_2 addition increased the elastic properties slightly (compare **18**B_6O**2**Al**2.65**Y***b*** and **18**B_6O**2**Al**2.65**Y**1**Si***b***) due to changes in the grain boundary composition. The densities obtained for these materials were similar with no clear trend. It is expected that even small amount of SiO_2 addition could form silicates which could affect the elastic constants of the hot pressed composites.

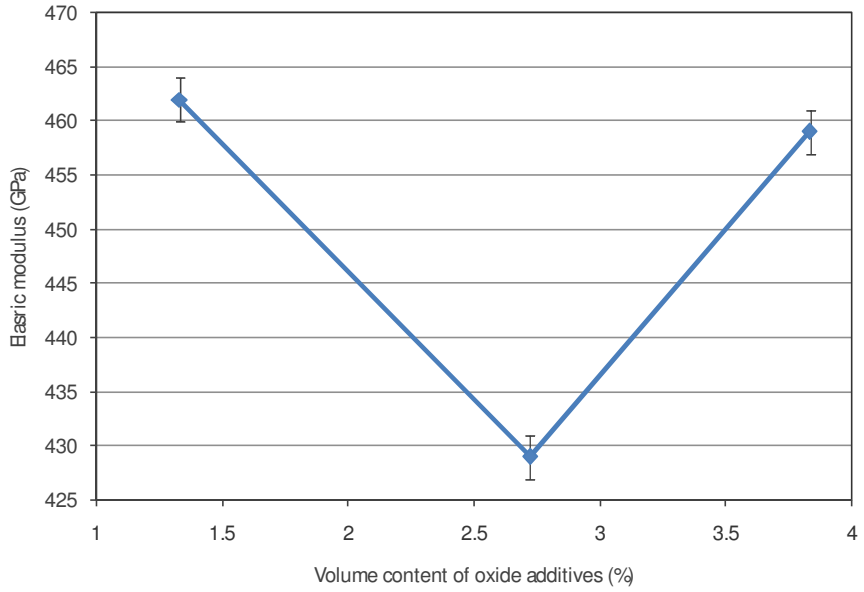

Figure 6.27: Relationship between elastic modulus and volume content of oxide additives for Al-Y-Si-doped composites.

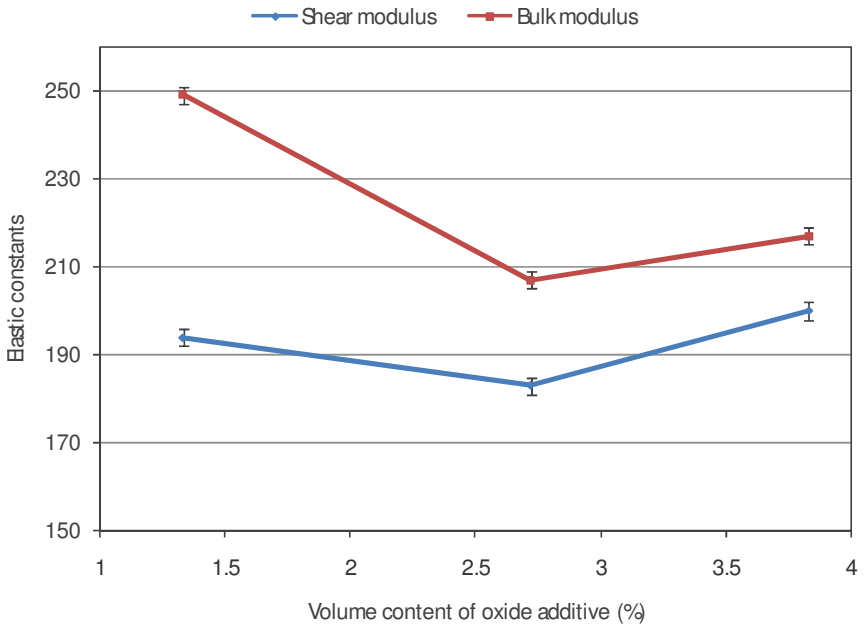

Figure 6.28: Relationship between shear and bulk moduli and volume content of oxide additives for Al-Y-Si-doped composites.

The elastic modulus measured for hot press 'pure' B_6O material produced by Shabalala [16] was 540 GPa. This value decreased linearly with increasing Al content. For instance, the elastic modulus decreased from 540 GPa for 'pure' B_6O to 514 GPa upon adding 2.2 wt% Al. Similar trends were observed for the shear and bulk moduli data. The elastic modulus obtained by Shabalala with 2.2 wt% Al (514 GPa) is higher than values obtained in this work but similar to that obtained for the composite with 3.7 wt% Al (467 GPa). The secondary phase which was mainly $Al_{18}B_4O_{33}$ has elastic modulus of 400 GPa. In the case of Al-Y-doped B_6O, amorphous phase was formed. Nevertheless, the structure could be close to YAG [93] with elastic modulus in the range of 290 - 308 GPa [94][95]. Thus, by using the rule of mixtures (equation 6.2) the high elastic modulus recorded by Shabalala can be expected.

The elastic modulus of hot pressed B_6O obtained by Goosey and Anderson [52] was 483 GPa slightly higher than what has been determined in this work. This material had a measured density of 2.6 g/cm^3. Petrak *et al.* [38] and Bairamashvile *et al.* [53] reported elastic modulus of 470 and 440 GPa respectively, similar to the values recorded in this work. Thus compared to the values recorded for pure B_6O, the elastic properties recorded for B_6O composites produced in this work are encouraging. The wide difference in elastic modulus for pure B_6O could be attributed to the different densities and defects in the microstructures. These defects could be porosities, impurities in the starting powder, and composition of the grain boundary which is mainly B_2O_3. Porosities are considered as secondary phase with zero modulus. B_2O_3 has elastic modulus of 20 GPa [96] and can significantly decrease the elastic modulus if its content is high. Since the content of B_2O_3 is difficult to quantify, it can result in differences in elastic properties, even if B_6O is sintered under the same conditions. A number of studies have shown that the shape of the pores also affects the elastic constants.

There are several observations which attempt to establish correlation between hardness and one single elastic property such as bulk modulus [97] or shear modulus

[98]. After comparing the measured values of hardness in a set of hard materials with their corresponding shear moduli, Teter discovered that hardness increases approximately with increasing shear moduli [99]. Haines *et al*. [100] also established a direct relationship between bulk modulus and hardness for non-metallic materials. A graph of microhardness as a function of elastic constants for the selected materials is shown in figures 6.29 and 6.30. From these figures, the relationships between hardness and at least elastic and bulk moduli agree reasonably well with what has been proposed by Haines *et al*.

It can be concluded that for fully densed microstructure, the elastic properties were found to be related to the grain boundary phase composition. Segregation in the microstructure resulted in lower elastic properties. The elastic moduli data determined were used to calculate the indentation fracture toughness values of the composites.

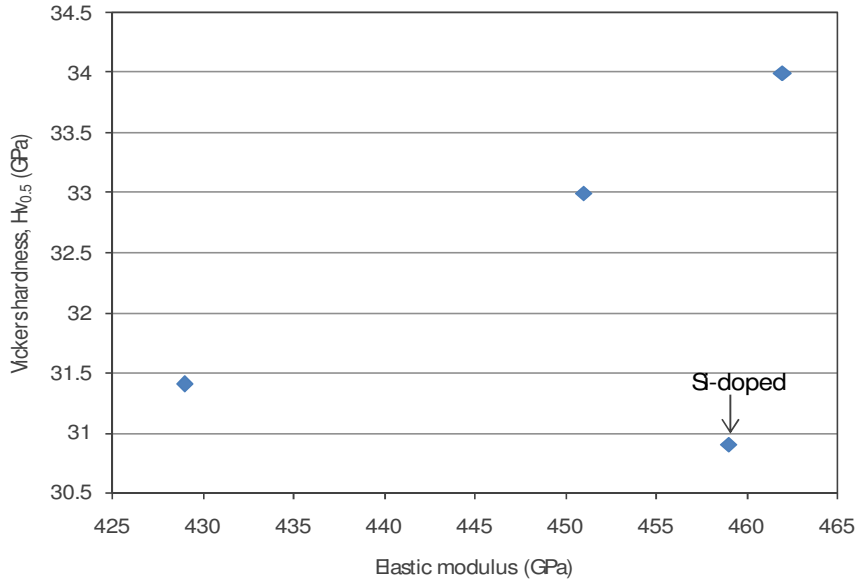

Figure 6. 29: Relationship between microhardness and elastic modulus for the selected composites (**18**B_6O**1**Al**1.32**Y***b***, **18**B_6O**2**Al**2.65**Y***b***, **18**B_6O**2.87**Al**1.58**Y***b***, and **18**B_6O**2**Al**2.65**Y**1**Si***b***).

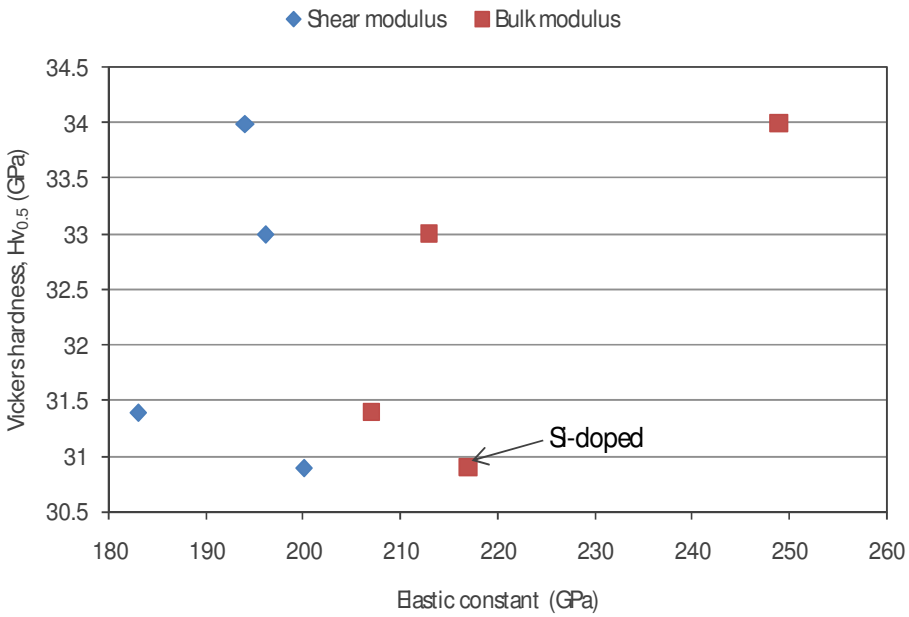

Figure 6.30: Relationship between microhardness and shear/bulk moduli for the selected composites (**18**B_6O**1**Al**1.32**Y***b***, **18**B_6O**2**Al**2.65**Y***b***, **18**B_6O**2.87**Al**1.58**Y***b***, and **18**B_6O**2**Al**2.56**Y**1**Si***b***).

7 Conclusions and Recommendations

Thermodynamic properties of boron suboxide (B_6O) have been estimated up to 2300 K and used to calculate the equilibrium phase composition of B_6O in different systems. The data has allowed predicting the stability of the liquid and crystalline phases formed during sintering. Therefore, this can form the basis for the search of new sintering additives that would allow the sintering of B_6O composites at lower temperatures. From the thermodynamic calculations carried out in this work (Chapter 3), it has been shown that B_6O can be liquid phase sintered using a wide range of oxide sintering additives.

Before hot pressing experiments, B_6O powders were milled in an attrition mill to reduce to particle sizes down to submicron range. Optimum milling conditions were 30 hours milling time in propan-1-ol using 2.5 mm diameter steel balls. The average particle size obtained was 0.4 μm. Impurities introduced during milling were acid washed in HCl and the remained impurities were quantified using chemical analysis (ICP-OES). The reduction in the particle sizes of B_6O before hot pressing improved the mechanical properties especially, hardness of the 'pure' hot pressed B_6O compacts.

Boron suboxide (B_6O) composites were hot pressed using various additives. Most systems studied contain Al_2O_3-Y_2O_3-SiO_2 additives. The Al_2O_3:Y_2O_3 mol ratios (80:20, 62:38, and 50:50) were weighted for different overall additive content. In addition to the above systems, TiC, TiB_2, and Pd were also used as additives. These different compositions were hot pressed at temperatures ranging from 1600 – 1900^{o}C, under 50 MPa, in argon atmosphere for 20 minutes.

The following conclusions were made from this work:

1. Dense (> 97% of theoretical) 'pure' B_6O hot pressed compacts were achieved with an average hardness of 35.6 GPa using 500g load. The hardness value is higher than that produced by Itoh *et al*. [3] who used high pressure techniques. This value can also be compared with hardness values obtained by Kayhan and Inal [5]. The hardness value obtained by Shabalala [16] is slightly lower than what was obtained in this work due to the reduced grain sizes (Hall-Petch effect). The hardness recorded in this work is also higher than that produced by Goosey and Anderson [52] ($KH_{0.1}$ = 30 GPa), Petrak *et al*. [38] ($KH_{0.1}$ = 30.4 GPa), and Bairamashvili *et al*. [53] ($KH_{0.1}$ = 32 GPa). The wide variation of hardness values reported for B_6O is due to the different processing routes taken. The most obvious reasons for the variation in hardness values are differences in sintering temperature, pressure, impurities introduced during sintering, and sintering time. The fracture toughness was however low and agrees with what has been reported by other researchers [4][7][14][16].
2. More than 98% of theoretical densities were achieved for B_6O composites hot pressed at 1800^oC; a temperature lower than the one used to produce densed 'pure' B_6O compacts (1900^oC). Densifications at lower temperatures were possible due to the presence of liquid phase in equilibrium with B_6O during hot pressing. The liquid phase accelerates mass transport thus effecting liquid phase sintering.
3. Good combinations of properties were achieved for all B_6O composites produced in this work (see figure 6.18). Vickers hardness ranging from 27 – 34 GPa and fracture toughness ranging from 3 – 7 $MPam^{1/2}$ were obtained. Fracture toughness of B_6O has been improved by addition of additives such as Al_2O_3, Y_2O_3, SiO_2, TiB_2, TiC, and Pd. The fracture toughness recorded in this work is the highest recorded for all B_6O composites produced so far except values recorded by Kayhan and Inal [5]. They reported a fracture toughness of 8.5 $MPam^{1/2}$ for Al-doped B_6O composite using a load of 100g. It must be mentioned here that even before infiltrating B_6O with Al, the fracture toughness measured by Kayhan and Inal was very high (5.5 $MPam^{1/2}$) and does not corroborate with the measured strength values. Additionally, they used a load of 100g whereas 5kg load was used in this work to measure fracture toughness.

The fracture toughness was also calculated from three-point bend testing with notch radius of 0.4 mm, making the results very doubtful.

4. The fracture toughness of composites containing Al-Y and Al-Y-Si-doped systems appears not to be sensitive to the composition of the grain boundary phase changes compared to the hardness values. Transgranular fracture occurred in Al-Y-doped and Al-Y-Si-doped B_6O composites. Fracture toughness has been enhanced by the introduction of secondary phases to the B_6O matrix with small reduction in hardness. Fracture toughness increase could be due to different mechanisms such as crack deflection due to bimetallic stresses, or due to crack arrest in the secondary phase, or due to the changes in the grain boundaries between B_6O grains. The additives used had the potential of removing the B_2O_3 present at the surfaces of B_6O particles thereby forming other phases that causes bimetallic strain toughening at the grain boundaries.
5. The observed microstructures indicate that with higher volume content in the material, there were segregations of the grain boundary phase. This also led to increased porosities and pull-outs in the microstructures.
6. Post hot pressing heat treatment of selected composites resulted in slight increase in hardness and the corresponding fracture toughness being approximately the same. There were no marked changes in densities. Further work is necessary to understand the mechanism.
7. The presence of B_2O_3 in the starting powders strongly affects the mechanical properties of the resulting hot pressed compacts due to the weaker grain boundary phase formed. Therefore the amount of B_2O_3 should be kept as low as possible.
8. B_6O was successfully doped with Pd and hot pressed. However, there were large pockets of liquid phase due to the very high hot pressing temperature used (1900^oC) and long dwelling time. A fracture toughness as high as 13 $MPam^{1/2}$ was obtained for this composite with a corresponding hardness of 22.5 GPa using 5kg load. Fracture mechanism is not completely clear. Further work is necessary to understand the toughening mechanism. Good combination of hardness (28 GPa) and fracture

toughness (5.1 $MPam^{1/2}$) has been achieved with 2 vol. % Pd addition hot pressed at 1800°C.

9. Composites produced from TiC and TiB_2 showed similar hardness values (Hv_5 for **19**B_6O**5**TiC is 26.7 GPa and Hv_5 for **19**B_6O**5**TiB_2 is 26.5 GPa). However, the fracture toughness of the latter material (4.3 $MPam^{1/2}$) is lower than that of the former (6.7 $MPam^{1/2}$). Further investigations are necessary to understand the densification behaviour.

In conclusion, the materials developed in this work are promising candidates for a new class of liquid phase sintered ultrahard materials produced without ultrahigh pressure. Doping with even small amount oxide additive resulted in a pronounced improvement in fracture toughness values. Properties obtained in this work are comparable to other hard materials used for cutting applications (e.g. amborite, DBC50 and Al_2O_3-TiC composite). Further optimization of the additive content, composition, and mechanical properties are needed to better understand the microstructure formation and toughness mechanisms existing in the materials. This will allow fabrication of B_6O composite material for industrial applications such as cutting tool, drill bits, grinding wheels and abrasives.

References

1. Zerr, A. and Rieldel, R. "Introduction: Novel ultrahard materials", In *Handbook of ceramic hard materials*", [ed.] R. Rieldel, 2000, Vol. 1.

2. Ellison-Hayashi, C., Zandi, M., Shetty, D.K., Kuo, P., Yeckley, R. and Csillag, F. "*Boron suboxide material and method for its preparation*", *5,330,937*, 1994, US Patent.

3. Itoh, H., Maekawa, I. and Iwahara, H. "*High pressure sintering of B_6O powder and properties of the sintered compact*", J. Soc. Mat. Sci., Vol. 47, 1998, pp. 1000-1005.

4. Itoh, H., Maekawa, I. and Iwahara, H. "*Microstructure and mechanical properties of B_6O-B_4C sintered composites prepared under high pressure*", J. Mat. Sci., Vol. 35, 2000, pp. 693-698.

5. Kayhan, I.O. and Inal, O.T. "*Synthesis of aluminium infiltrated boron suboxide drag cutters and drill bits*", J. Mater. Sci., Vol. 34, 1999, pp. 4105-4120.

6. Olofsson, M. and Lundström, T. "*Synthesis and structure of non-stoichiometric B_6O*", J. Alloys and Compds., Vol. 257, 1997, pp. 91-95.

7. Sasai, R., Fukatsu, H., Kojima, T. and Itoh, H. "*High pressure consolidation of B_6O-diamond mixtures*", J. Mater. Sci., Vol. 36, 2001, pp. 5339-5343.

8. Veprek, S. "Nanostructured superhard materials", In *Handbook of ceramic hard materials*, [ed.] R. Rieldel, Weinheim, New York, Wiley, 2000, Vol. 2.

9. He, D., Zhao, Y., Daemen, L., Qian, J., Shen, T.D. and Zerda, T.W. "*Boron suboxide: As hard as cubic boron nitride*", Appl. Phys. Lett., Vol. 81, 2002, pp. 643-645.

10. Garvie, L.A.J., Hubert, H., Petuskey, W.T., McMillan, P.F. and Buseck, P.R. "*High-pressure, high-temperature synthesis in the B-C-N-O system, II. Electron energy-loss spectroscopy (EELS)*", J. Solid State Chem., Vol. 133, 1997, pp. 365-371.

11. He, D., Akaishi, M., Scott, B.I. and Zhao, Y. "*Growth of boron suboxide crystals in the B-B_2O_3 system at high pressure and high temperature*", J. Mater. Res., Vol. 17, 2002, pp. 284-290.

12. Hubert, H., Devouard, B., Garvie, L.A.J., O'Keeffe, M., Buseck, P.R., Putuskey, W.T. and McMillan, P.F. "*Icosahedral packing of B_{12} icosahedra in boron suboxide (B_6O)*", Nature, Vol. 391, 1998, pp. 376-378.

13. Yu, S., Wang, G., Yin, S., Zhang, Y. and Liu, Z. "*Nanostructured films of boron suboxide by pulse laser deposition*", Phys. Lett. A., Vol. 268, 2000, pp. 442-447.

14. Itoh, H., Yamamoto, R. and Iwahara, H. "*B_6O-c-BN composite prepared by high pressure sintering*", J. Amer. Ceram. Soc., Vol. 83, 2000, pp. 501-506.

15. McMillan, P.F., Hubert, H., Chizmeshya, A., Petuskey, W.T., Garvie, L.A.J. and Devouard, B. "*Nucleation and growth of icosahedral boron suboxide clusters at high pressure*", J. Solid State Chem., Vol. 147, 1999, pp. 281-290.

16. Shabalala, T.C. "*The preparation and characterisation of boron suboxide based composites*", University of the Witwatersrand, 2007, PhD Thesis.

17. Hubert, H., Garvie, L.A.J., Devouard, B., Buseck, P.R., Petuskey, W.T. and McMillan, P.F. "*High-pressure, high-temperature synthesis and characterisation of boron suboxide (B_6O)*", Chem. Mater., Vol. 10, 1998, pp. 1530-1537.

18. Badzian, A.R. "*Superhard material comparable in hardness to diamond*", Appl. Phys. Lett., Vol. 53, 1988, pp. 2495-2497.

19. Brodhag, C. and Thévenot, F. "*Hot pressing of boron suboxide $B_{12}O_2$*", J. Less Comm. Met., Vol. 110, 1986, pp. 1-6.

20. Ellison-Hayashi, C., Zandi, M., Murray, Csillag, F.J. and Kuo, S. "*Boron suboxide material and method for its preparation*", *5,135,895*, 1992, US Patent.

21. Hall, H.T. and Compton, L.A. "*Group IV analogs and high pressure, high temperature synthesis of B_2O*", Inorg. Chem., Vol. 4, 1965, pp. 1213-1216.

22. Kharlamov, A.I., Kirillova, N.V., Loichenko, S.V. and Kostyuk, B.D. "*Properties of boron suboxide $B_{13}O_2$*", Powder Metall. Metal Ceram., Vol. 41, 2002, pp. 97-106.

23. Harris, T.K., Brookes, E.J. and Taylor, C.J. "*The effect of temperature on the hardness of polycrystalline cubic boron nitride cutting tool materials*", Inter. J. Refract. Met. and Hard Met., Vol. 22, 2004, pp. 105-110.

24. Lundström, T. and Adreev, Y.G. "*Superhard boron-rich borides and studies of the B-C-N system*", Mater. Sci. and Eng. A, Vol. 209, 1996, pp. 16-22.

25. Cook, B.A., Harringa, J.L., Lewis, T.L. and Russell, A.M. "*A new class of ultrahard materials based on $AlMgB_{14}$*", Scripta Mater., Vol. 42, 2000, pp. 597-602.

26. Takeda, M., Fukuda, T., Domingo, F. and Miura, T. "*Thermoelectric properties of some metal borides*", J. Solid State Chem., Vol. 177, 2004, pp. 471-475.

27. Mota, J.M., Martinez, M.A., Velasco, F. and Criado, A.J. "*Preparation of aluminium boride by powder technology*", Ceram. Inter., Vol. 30, 2004, pp. 301-306.

28. Singh, B.P. "*Characterisation of cubic boron nitride compacts*", Mater. Res. Bull., Vol. 21, 1986, p. 85.

29. Lundström, T. "*Structure and bulk modulus of high-strength boron compounds*", J. Solid State Chem., Vol. 133, 1997, pp. 88-92.

30. Endo, T., Sato, T. and Shimada, M. "*High-pressure synthesis of B_2O with diamond-like structure*", J. Mater. Sci. Lett., Vol. 6, 1987, pp. 683-685.

31. Srikanth, V., Roy, R., Graham, E.K. and Voigt, D.E. "*B_xO: Phases present at high pressure and temperature*", J. Amer. Ceram. Soc., Vol. 74, 1991, pp. 3145-3147.

32. Gao, F., Qin, X., Wang, L., He, Y., Sun, G., Hou, L. and Wang, W. "*Prediction of new superhard boron-rich compounds*", J. Phys. Chem. B, Vol. 109, 2005, pp. 14892-14895.

33. Shirai, K., Masago, A. and Katayama-Yoshida, H. "*High-pressure properties and phase diagram of boron*", Phys. Stat. Sol. (B), Vol. 244, 2007, pp. 303-308.

34. Brodhag, C. and Thévenot, F. "*Hot pressing of various boron phases*", 8th Inter. Symposium on Boron, Borides, Carbides, Nitrides and Related Compounds, 1984, pp. 175-180.

35. Masago, A., Sharai, K. and Katayama-Yoshida, H. "*Crystal stability of α- and β-boron*", Phys. Rev. B, Vol. 73, 2006, p. 104102.

36. Rizzo, H.F., Simmons, W.C. and Bielstein, H.O. "*The existence and formation of the solid B_6O*", J. Electro. Soc., Vol. 109, 1962, pp. 1079-1082.

37. Hoard, J.L., Sullenger, D.B., Kennard, G.H.L. and Hughes, R.E. "*The structure analysis of β-rhombohedral boron*", J. Solid State Chem., Vol. 1, 1970, pp. 268-277.

38. Petrak, D.R., Ruh, R. and Atkins, G.R. "*Mechanical properties of hot-pressed boron suboxide and boron*", Ceram. Bull., Vol. 53, 1974, pp. 569-574.

39. Kobayashi, M., Higashi, I., Brodhag, C. and Thévenot, F. "*Structure of B_6O boron suboxide by Rietveld refinement*", J. Mater. Sci., Vol. 28, 1993, p. 2129.

40. Lundström, T. and Bolmgren, H. "*11th Inter. Symp. on Boron, Borides and Related Compounds*", [eds.] Uno, R. and Higashi, I., Vol. 10, 1994. p. 1.

41. Becher, H.J. and Thévenot, F. "*Infrarotspektroskopische Untersuchung des Borcarbids und seiner isotypen Derivate $B_{12}O_2$, $B_{12}P_2$ und $B_{12}As_2$*", Z. Anorg. Allg. Chem., Vol. 410, 1974, pp. 274-286.

42. Gao, F., Hou, L. and He, Y. "*Origin of superhardness in icosahedral B_{12} materials*", J. Phys. Chem. B, Vol. 108, 2004, pp. 13069-13073.

43. Nieto-Sanz, D., Loubeyre, P., Crichton, W. and Mezouar, M. "*X-ray study of the synthesis of boron oxides at high pressure: Phase diagram and equation of state*", Phys. Rev. B, Vol. 70, 2004, pp. 214108-6.

44. Wartik, T. and Apple, E.F., *J. Am. Ceram. Soc*., Vol. 77, 23, 1955, p. 6400.

45. Kanda, F.A., King, A.J., Russell, V.A. and Katz, W., *ibid*, Vol. 78, 7, 1909, p. 1509.

46. Weintraub, E., *Trans. Am. Electrochem Soc*., Vol. 16, 1926, p. 165.

47. Pasternak, R.A. "*Crystallographic evidence for the existence of B_7O*", Acta Cryst., Vol. 12, 1959, pp. 612-613.

48. Holcombe, Jr. C.E. and Horne, Jr. J.O. "*Method for preparing boron suboxide*", *3,660,031*, 1972, US Patent.

49. Liu, X., Zhao, X., Hou, W. and Su, W. "*A new route for the synthesis of boron suboxide (B_7O)*", J. Alloys and Compds., Vol. 223, 1995, pp. L7-L9.

50. Gladkaya, I.S., Dyuzheva, T.I., Ekimov, E.A., Nikolaev, N.A. and Bendeliani, N.A. "*Crystal growth at high pressure and the problem of characterisation of the interstitial phases in the B-C-O system*", J. Alloys and Compds., Vol. 329, 2001, pp. 153-156.

51. Hubert, H., Garvie, L.A.J., Leinenweber, K., Buseck, P.R., Petuskey, W.T. and McMillan, P.F. "*High-pressure, high-temperature synthesis of superhard boron suboixde*", Mater. Res. Soc., Vol. 410, 1996, pp. 191-196.

52. Goosey, B.F. and Anderson, S.C. "*Method of fabricating boron suboxide articles*", *3,816,586*, 1974, US Patent.

53. Bairamashvili, I.A., Kalandadze, G.I., Eristavi, A.M., Jobava, J.S., Chotulidi, V.V. and Saloev, Y.L. "*An investigation of the physicomechanical properties of B_6O and SiB_4*", J. Less Comm. Met., Vol. 67, 1979, pp. 455-561.

54. Ellison-Hayashi, C., Emond, G.T. and Kuo, S.Y. "*Abrasives material and method of removing material from surfaceI*", *0 0621 327 Al*, 1994, EU Patent.

55 Ellison-Hayashi, C., Emond, G.T. and Kuo, S.Y. "*Method of abrading with boron suboxide (B_xO) and the boron suboxide (B_xO) articles and composition used*", *5,456,735*, 1995, US Patent.

56. Wachtman, J.B. "*Mechanical properties of ceramics*", New York, John Wiley and Sons, 1996.

57. Kurisuchiyan, E., Jiyooji, T.E. and Shii, R.K. "*Grinding by using composition containing boron suboxide*", *7,034,063*, 1995, Japan Patent.

58. Barry, I. "Synthesis of superhard icosahedral boron-rich solids", *Research experience for undergraduate*, 1999, http:/mrsec.la.asu.edu/outreach/reu/reu1999.

59. Lee, S., Kim, S.W., Bylander, D.M. and Kleiman, I. "*Crystal structure, formation enthalpy, and energy bands of B_6O*", Phys. Rev. B, Vol. 44, 1991, pp. 3550-3554.

60. Peterson, I.M. and Tien, T.Y. "*Effect of grain boundary thermal expansion coefficient on the fracture touhgness in silicon nitride*", J. Am. Ceram. Soc., Vol. 78, 1995, pp. 2345-2352.

61. Padture, N.P. "*In situ-toughened silicon carbide*", J. Am. Ceram. Soc., Vol. 7, 1994, pp. 519-523.

62. Sun, E.Y., Becher, P.F., Plucknett, R.P., Hsueh, C.H., Alexander, K.B., Waters, S.B., Hirao, K. and Brito, M.E. "*Microstructural design of silicon nitride with improved fracture toughness: II. Effects of yttria and alumina additives*", J. Am. Ceram. Soc., Vol. 81, 1998, pp. 2831-2840.

63. Faber, K.T. and Evans, A.G. "*Crack deflection processes - I. Theory*", Acta Metall, Vol. 31, 1983, pp. 565-576.

64. Morell, R. "*Handbook of properties of technical and engineering ceramics. Part 1: An introduction for the engineer and designer*", National Physical Laboratory, 1985.

65. Faber, K.T. and Evans, A.G. "*Crack deflection processes - II. Experiment*", Acta Metall, Vol. 31, 1983, pp. 577-584.

66. Faber, K.T., Evans, A.G. and Drory, M.D. "*Fracture mechanics of ceramics*", [eds.] Bradt, R.C., Evans, A.G., Hasselman, D.P.H. and Lange, F.F., Plenum Press, 1982, Vols. 5-6.

67. Swanson, P.L., Fairbanks, C.J., Lawn, B.R., Mai, Y.W., and Hockey, B.J. "*Crack-interface grain bridging as a fracture resistance mechanism in ceramics: I. Experimental study on alumina*", J. Am. Ceram. Soc., Vol. 70, 1987, pp. 279-289.

68. Evans, A.G. "*Perspective on the development of high-toughness ceramics*", J. Am. Ceram. Soc., Vol. 73, 1990, pp. 187-206.

69. Rodel, J. "*Interaction between crack deflection and crackk bridging*", J. Euro. Ceram. Soc., Vol. 10, 1992, pp. 143-150.

70. Boustan, I., Quandt, A., Hernandez, E. and Rubio, A. "*New boron based nanostructured materials*", J. Chem. Phys., Vol. 110, 1999, pp. 3175-3185.

71. Herrmann, M., Schulz, I. and Zalite, I. "*Materials based on nanosize β-Si_3N_4 composite powders*", J. Euro. Ceram. Soc., Vol. 24, 2004, pp. 3327-3335.

72. Siegel, W.R. "Synthesis, structure, and properties of nanostructured materials", In *Fundamental properties of nanostructured materials*, [eds.] Fiorani, D. and Sberveglierr, G., Rimini, 2003, pp. 3-20.

73. Mayo, M.J. "*Processing of nanocrystalline ceramics from ultrafine particles*", Int. Mat. Rev., Vol. 41, 1996, pp. 85-115.

74. Suryanarayana, C. "*Nanocrystalline materials*", Int. Mater. Rev., Vol. 40, 1995, pp. 41-64.

75. Tjong, S.C. and Chen, H. "*Nanocrystalline materials and coatings*", Mater. Sci. and Eng. Reports, Vol. 45, 2004, pp. 1-88.

76. Reed, J.S. "*Principles of ceramic processing*", Vol. 2, New York, Wiley Interscience, 1995, pp. 313-337.

77. Rahaman, M.N. "*Ceramic processing and sintering*", Vol. 2, New York-Basel, Marcel Dekker Inc., 2005, pp. 620-684.

78. Makarov, V.S. and Ugai, Y.A. "*Thermodynamic study of boron suboxide (B_6O)*", J. Less. Comm. Met., Vol. 117, 1986, pp. 277-281.

79. Naumov, V.N., Tagaev, A.B., Tsagareishivili, D.S., Tsagareishvili, G.V. and Tushishvili, M.C. "*Thermodynamic properties of boron suboxide in the temperature range 11.44-311.84 K*", Inst. Metall., Vol. 138, 1990, pp. 321-324.

80. Tsagareishvili, G.V., Tsagareishvili, D.S., Tushishvili, M.C., Omiadze, I.S., Naumov, V.N. and Tagaev, A.B. "*Enthalpy and heat capacity of boron suboxide in the temperature range of 298.15-781.8 K*", Inst. Metall., Vol. 231, 1991, pp. 384-391.

81. Gaskell, D.R. "*Introduction to the thermodynamics of materials*", New York, McGraw-Hill Book Company, 1981, p. 110.

82. SGPS-SGTE pure substance database, *Scientific Group Thermodata Europe*, 2000.

83. ACerS-NIST Phase Equilibrium Diagrams, *NIST Standard Reference Database*, Vol. 31, Version 3.1.

84. Anstis, G.R., Chantikul, P., Lawn, B.R. and Marshall, D.B., *J. Am. Ceram. Soc*., Vol. 64, 1981, p. 533.

85. Herrmann, M. "*Private communication*", 2008.

86. Applewhite, A.L. and Day, D.E. "*Proc. XVth intern. congr. on glass*", Vol. 2b, Leningrad, 1989, p. 337.

87. Kleebe, H.-J., Lauterbach, S., Shabalala, T.C., Herrmann, M. and Sigalas, I. "*B_6O: A correlation between mechanical properties and microstructural evolution upon Al_2O_3 addition during hot pressing*", J. Am. Ceram. Soc., Vol. 91, 2008, pp. 569-575.

88. Li, A., Zhen, Y., Yin, Q., Ma, L. and Yin, Y. "*Microstructure and properties of (SiC,TiB_2)/B_4C composites by reaction hot pressing*", Ceram. Inter., Vol. 32, 2006, pp. 849-856.

89. Liversage, J.H. "*An enhancement of the mechanical properties in functionally graded liquid-phase SiC-TiC ceramic composites*", University of the Witwatersrand. 2005, PhD Thesis.

90. CRC, "Properties of TiB_2", In *Material Science and Engineering Handbook*, p. 507.

91. Uzgur, A.E., Gonenli, I.E. and Tas, A.C. "*Synthesis of aluminium borate whiskers for metal matrix composites*", III ceramic congress, proceedings book, Vol. 2, 1996, Intanbul, pp. 85-91.

92. Ozbayraktar, S. and Rieldel, R. In "*Handbook of ceramic hard materials*", [ed.] R. Rieldel, Weinheim, Wiley, 2000, Vol. 2.

93. Patankar, S.N., Zhang, D., Adam, G. and Sam, F.H. "*Processing of yttrium-aluminium garnets under non-equilibrium conditions*", J. Alloy Compds., Vol. 353, 2003, pp. 307-309.

94. Mulder, C.A.M. and de With, G. "*Translucent $Y_3Al_5O_{12}$ ceramic: Electron microscopy characterisation*", Solid State Ionics, Vol. 16, 1985, pp. 81-86.

95. Yagi, H., Yanagitani, T., Numazawa, T. and Ueda, K. "*The physical properties of transparent $Y_3Al_5O_{12}$: Elastic modulus at high temperature and thermal conductivity at low temperature*", Ceram. Inter., Vol. 33, 2007, pp. 711-714.

96. Pan, Y., Qin, J.H., Morita, M., Tan, S. and Jiang, D. "*The mechanical properties and microstructure of SiC-AlN particulate composite*", J. Mater. Sci., Vol. 33, 1998, pp. 1233-1237.

97. Liu, A.Y. and Cohen, M.L. "*Prediction of new low compressibility solids*", Science, Vol. 245, 1989, pp. 841-842.

98. Leger, J.M., Djemia, P., Ganot, F., Haines, J., Pereira, A.S. and da Jornada, J.A.H. "*Hardness and elasticity in cubic ruthenium dioxide*", Appl. Phys. Lett., Vol. 79, 2001, p. 2169.

99. Teter, D.M. *MRS Bull.*, Vol. 23, 1998, p. 22.

100. Haines, J., Leger, J.M. and Bocquillon, G. "*Synthesis and design of superhard materials*", Ann. Rev. Mater. Res., Vol. 31, 2001, pp. 1-23.

Appendices

Appendix A: Thermodynamic data for B_6O

Table A1: New thermodynamic date for B_6O after corrections. Standard state: pure solid, liquid and ideal gas at 1 atm.

T(K)	Cp(J/K)	H(J)	G(J)	S(J/K)
298.15	74.305	-527000.0	-538601.0	38.910
300.00	75.015	-526861.9	-538673.4	39.372
400.00	105.986	-517713.9	-543904.5	65.476
500.00	129.594	-505899.6	-551770.3	91.741
600.00	150.304	-491889.0	-562226.1	117.228
700.00	169.645	-475883.6	-575187.5	141.863
800.00	184.940	-457984.0	-590573.3	165.737
900.00	187.240	-439375.0	-608262.0	187.652
1000.00	189.540	-420536.0	-628034.9	207.499
1100.00	191.840	-401467.0	-649706.1	225.672
1200.00	194.140	-382168.0	-673123.3	242.463
1300.00	196.440	-362639.0	-698160.0	258.093
1400.00	198.740	-342880.0	-724709.0	272.735
1500.00	201.040	-322891.0	-752678.7	286.525
1600.00	203.340	-302672.0	-781989.4	299.573
1700.00	205.640	-282223.0	-812571.6	311.970
1800.00	207.940	-261544.0	-844364.1	323.789
1900.00	210.240	-240635.0	-877312.3	335.093
2000.00	212.540	-219496.0	-911367.4	345.936

Appendix B: Summary of properties of all hot pressed materials

Table B1: Summary of properties of all hot pressed composites.

Material	Al_2O_3:Y_2O_3 mol ratio	Density (g/cm^3)	Theoretical density (g/cm^3)	% Theoretical density	Open porosity (%)	Crystalline grain boundary phases	Hv_5 (GPa)	Hv_2 (GPa)	$Hv_{0.5}$ (GPa)	K_{IC} ($MPa.m^{0.5}$)
19B_6O***a***	-	2.48	2.55	97.3	3.6	-	30.1±0.8	31.4±1.1	34.7±1.1	3.3±0.1
19B_6O***b***	-	2.48	2.55	97.3	1.1	-	35.7±1.6 (**1kg**)	-	35.6±1.5	Brittle
19B_6O	-	2.52	2.55	98.8	1.9	-	29.4±0.5 (**1kg**)	-	32.3±1.4	Britlle
18B_6O**1**Al**1.32**Y***a***	62:38	2.41	2.57	93.8	3.2	-	30.4±1.8	29.8±1.7	31.4±1.9	5.4±0.3
18B_6O**1**Al**1.32**Y***b*****-1**	62:38	2.51	2.57	97.7	3.0	-	28.8±0.8	-	-	4.7±0.6
18B_6O**1**Al**1.32**Y***b*****-2**		2.54	2.57	98.8	0.9		29.7±0.6	32.4±0.9	34.0±1.9	4.1±0.3
175B_6O**2**Al**2.65**Y***a***	62:38	2.27	2.59	87.6	5.9	-	16.6±2.1	-	-	7.2±0.6
18B_6O**2**Al**2.65**Y***a***	62:38	2.53	2.59	97.7	1.6	-	29.7±1.4	29.6±0.7	30.7±1.0	6.2±1.0
185B_6O**2**Al**2.65**Y***a***	62:38	2.58	2.59	99.6	1.2	-	27.8±2.1	-	30.7±1.4	3.4±0.1
18B_6O**2**Al**2.65**Y***b*****-1**	62:38	2.55	2.59	98.5	1.9	-	29.1±0.4	31.4±1.2	33.0±1.8	4.6±0.4
18B_6O**2**Al**2.65**Y***b*****-2**		2.56	2.59	98.8	1.2		29.2±0.7	-	-	4.4±0.1
18B_6O**2**Al**2.65**Y**HTP*b***	62:38	2.54	2.58	98.4	1.7	-	26.4±0.5	-	-	4.3±0.3
18B_6O**2.83**Al**3.75**Y***b*****-1**	62:38	2.57	2.61	98.5	0.8	-	28.1±0.7	29.5±1.4	30.5±0.6	5.1±0.8
18B_6O**2.83**Al**3.75**Y***b*****-2**		2.57	2.61	98.5	1.2		28.2±0.8	-	-	4.1±0.6
18B_6O**2.87**Al**1.58**Y***b***	80:20	2.53	2.59	97.7	0.8	$Al_{18}B_4O_{33}$	28.3±0.9	29.4±0.9	31.4±0.9	3.8±0.9
18B_6O**4.06**Al**2.24**Y***b***	80:20	2.57	2.61	98.5	0.5	$Al_{18}B_4O_{33}$	29.2±0.7	28.4±0.8	30.7±1.1	4.3±0.8
18B_6O**1.48**Al**3.26**Y***b***	50:50	2.57	2.59	99.2	1.2	-	27.9±0.4	27.4±1.0	28.6±0.8	3.8±0.6
18B_6O**2.1**Al**4.63**Y***b***	50:50	2.56	2.62	97.7	1.4	-	27.8±1.3	28.0±1.5	29.0±1.2	3.3±0.3

Material	Al_2O_3:Y_2O_3 mol ratio	Density (g/cm^3)	Theoretical density (g/cm^3)	% Theoretical density	Open porosity (%)	Crystalline grain boundary phases	Hv_5 (GPa)	Hv_2 (GPa)	$Hv_{0.5}$ (GPa)	K_{IC} ($MPa.m^{0.5}$)
18B_6O**2**Al**2.65**Y**1**Si***a*	62:38	2.46	2.59	95.0	4.4	-	30.0±1.6	-	30.9±0.9	4.9±1.0
18B_6O**2**Al**2.65**Y**1**Si***b*	62:38	2.55	2.59	98.5	1.2	-	27.6±0.6	-	30.9±1.1	3.2±0.5
18B_6O**2.54**Al**1.4**Y**1.27**Si***b*	62:38	2.56	2.58	99.2	1.1	-	27.4±0.9	-	27.6±0.4	3.9±0.9
18B_6O**2.7**Al**3.57**Y**1.35**Si***b*	80:20	2.58	2.61	98.9	0.1	$Al_{18}B_4O_{33}$	27.4±1.0	-	31.4±1.9	3.7±0.4
18B_6O**3.43**Al**1.89**Y**1.72**Si ***b***	80:20	2.59	2.59	100.0	0.5	$Al_{18}B_4O_{33}$	28.3±0.4	-	29.8±0.8	4.6±0.8
18B_6O**2**Al**1**Si***a*	-	2.42	2.56	94.5	4.1	$Al_{18}B_4O_{33}$	28.0±1.5	-	28.4±0.6	5.2±0.7
19B_6O**1**Al***a***	-	2.51	2.55	98.4	3.0	$Al_{18}B_4O_{33}$	30.2±1.8	-	30.9±0.6	5.8±0.5
19B_6O**2**Al***a***	-	2.54	2.56	99.2	1.8	$Al_{18}B_4O_{33}$	29.5±1.5	-	30.6±1.1	5.5±0.6
19B_6O**3**Al***a***	-	2.55	2.57	99.2	2.1	$Al_{18}B_4O_{33}$	27.0±0.7	-	28.9±0.5	4.5±0.5
19B_6O**5**TiC***a***	-	2.49	2.60	95.8	2.4	TiB_2, $Al_{18}B_4O_{33}$	26.7±0.6	-	28.2±1.3	4.3±0.3
19B_6O**5**TiB_2***a***	-	2.62	2.60	100.8	0.8	TiB_2, $Al_{18}B_4O_{33}$	26.5±1.5	-	27.8±0.8	6.7±0.9
16B_6O**5**Pd	-	1.75	2.98	58.7	26.7	Pd_2B	-	-	-	-
19B_6O**5**Pd	-	2.82	2.98	94.6	4.4	Pd_2B	22.5±0.9	-	-	13.5±3.2

Appendix C: XRD patterns of admixed powders and hot pressed composites

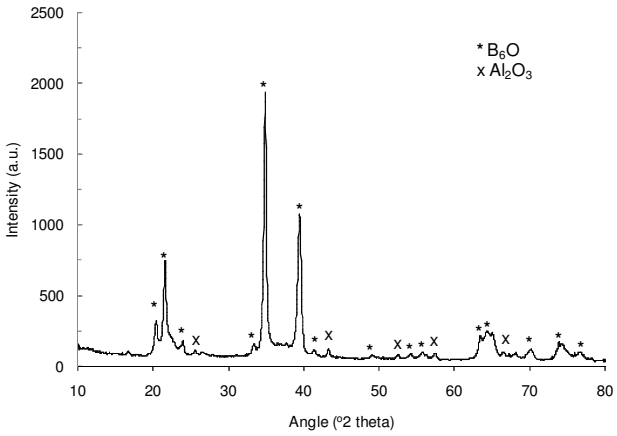

a)

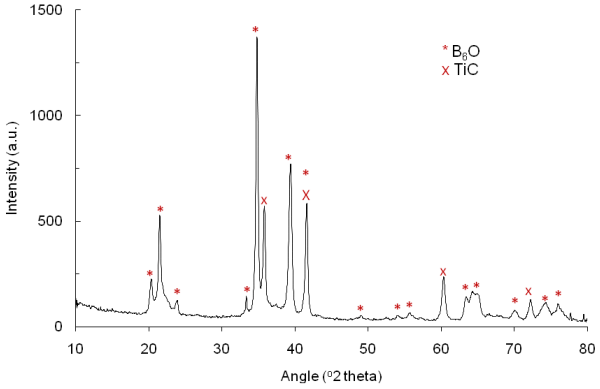

b)

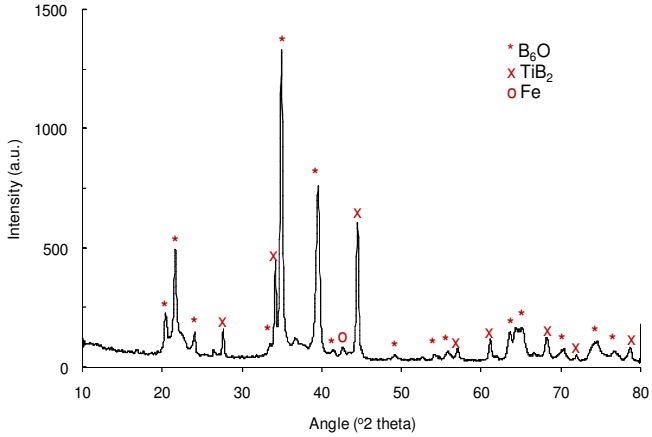

c)

Figure C1: XRD pattern of B_6O powder admixed with a) 1 wt% Al_2O_3 b) 5 wt% TiC. (b) 5 wt% TiB_2.

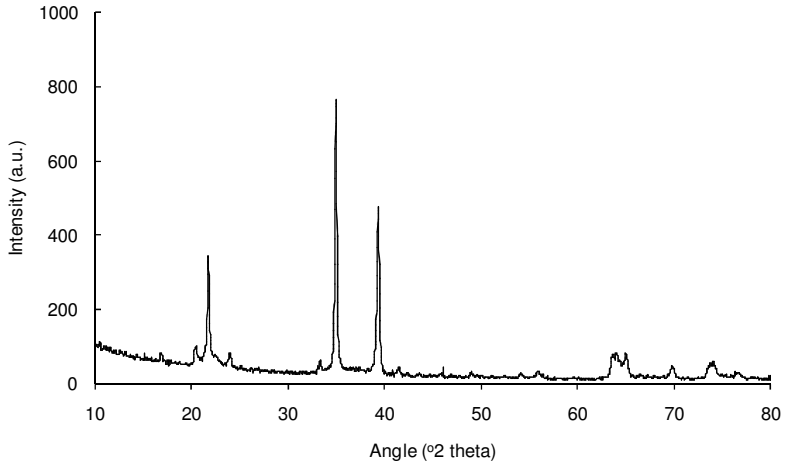

a)

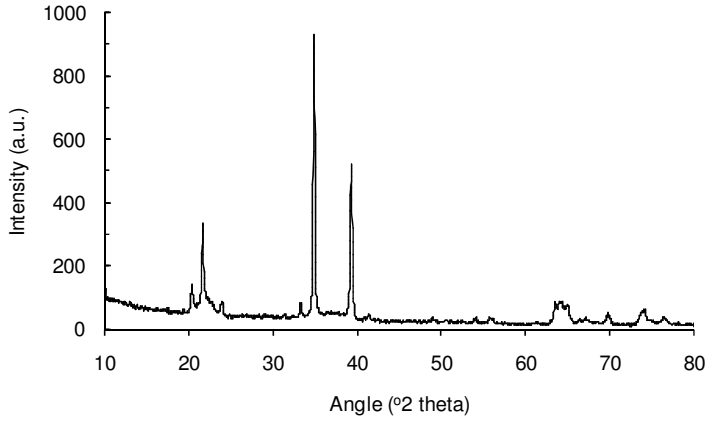

b)

Figure C2: Typical XRD patterns of Al-Y-doped B_6O hot pressed composites showing only B_6O peaks. (a) **18**B_6O**1**Al**1.32**Y (b) **18**B_6O**2.83**Al**3.75**Y

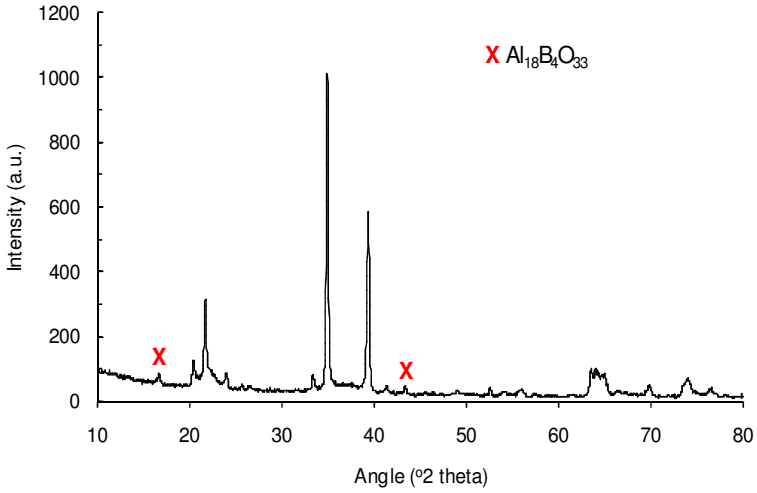

Figure C3: XRD pattern of Al-Y-doped B_6O hot pressed composite (80 mol % Al_2O_3) showing aluminium borate phase. Remaining peaks belongs to B_6O.

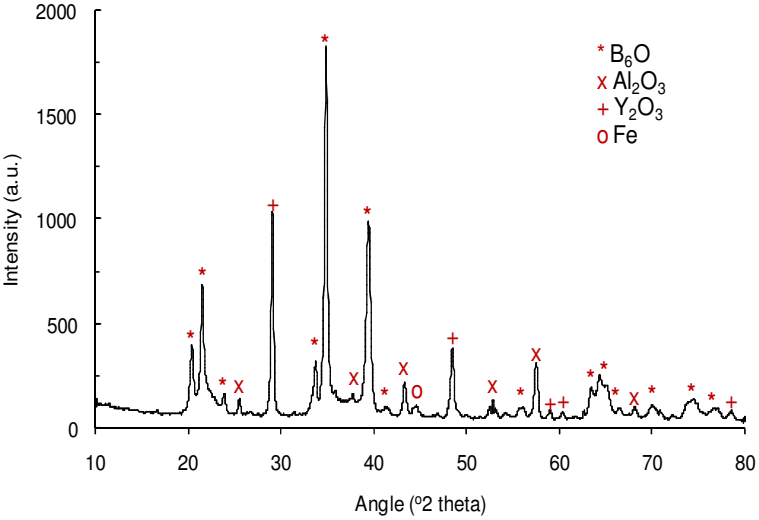

Figure C4: XRD pattern of B_6O admixed with 2 wt% Al_2O_3, 2.65 wt% Y_2O_3, and 1 wt% SiO_2. SiO_2 is amorphous.

Appendix D: SEM micrographs of hot pressed composite materials

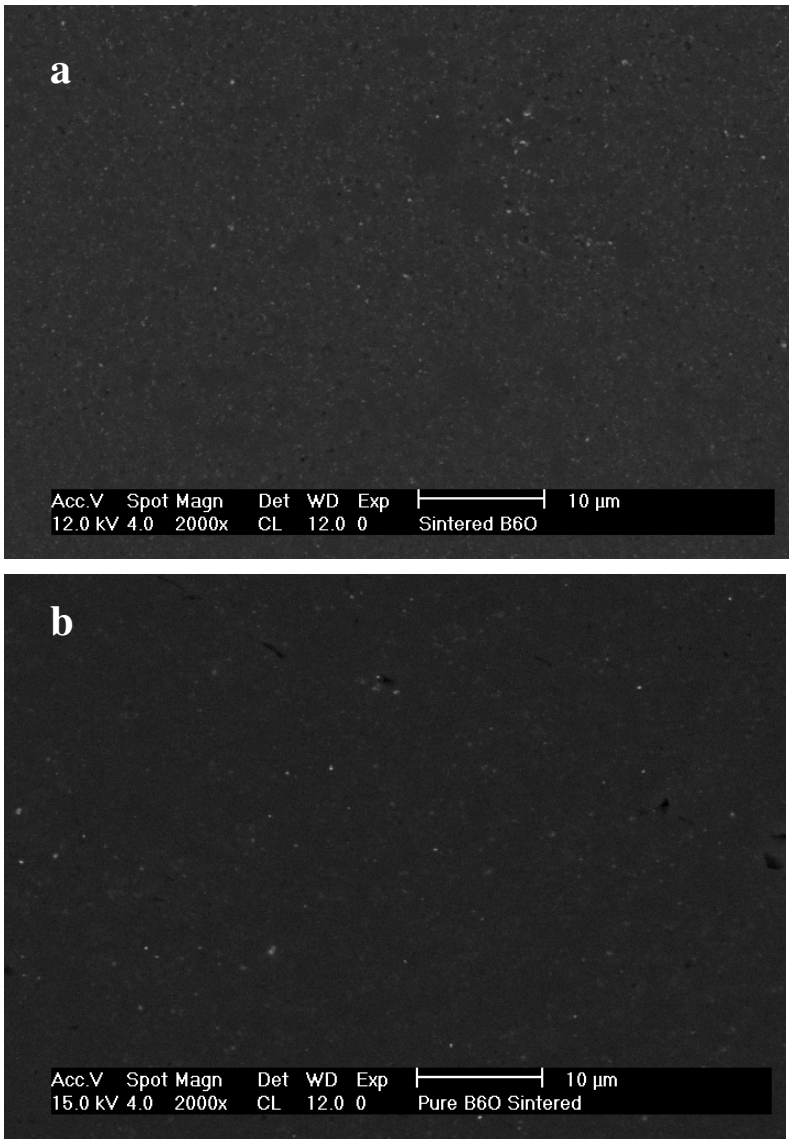

Figure D1: SEM images of pure hot pressed B_6O showing secondary phase. (a) **19**B_6O***a*** (b) **19**B_6O***b***.

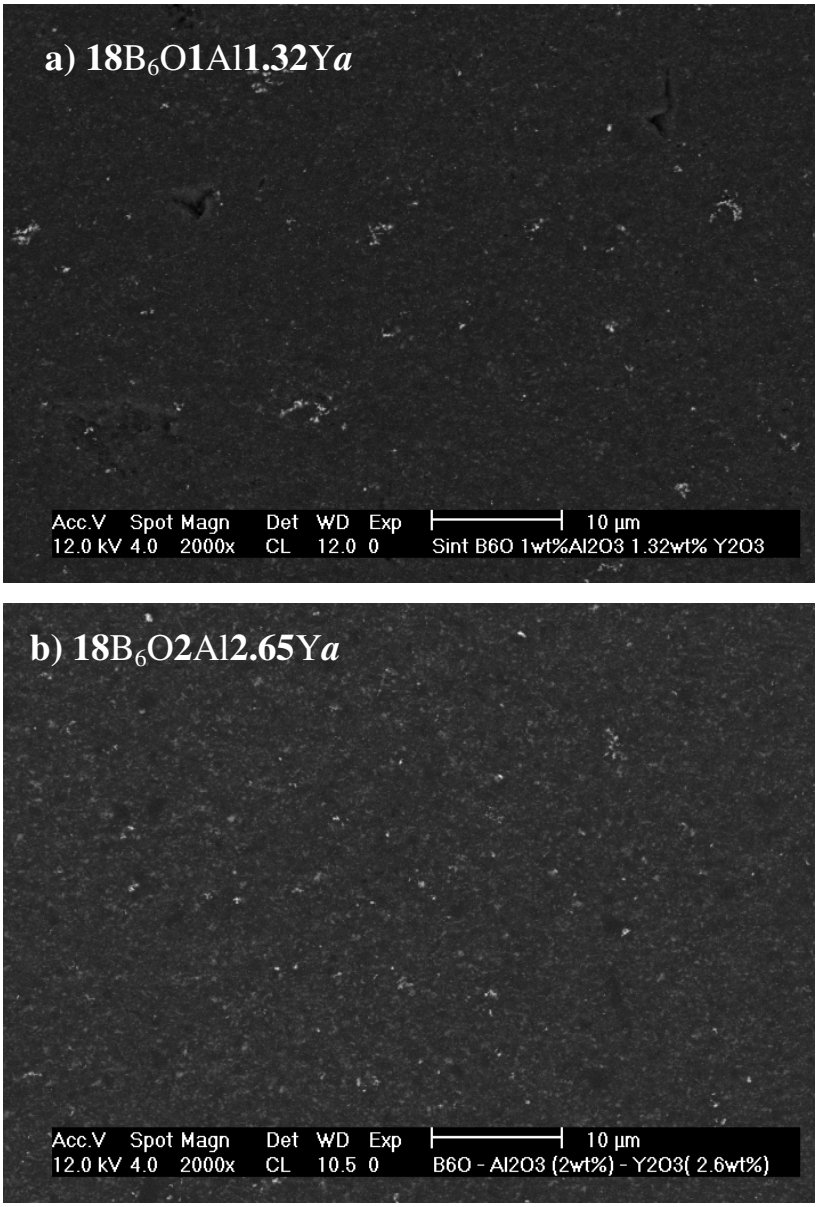

Figure D2: SEM micrographs of Al-Y-doped B_6O hot pressed composite prepared from first batch of milled powder showing homogenous distribution of binder phase. White isolated spots are Fe and Cr contaminations from milling.

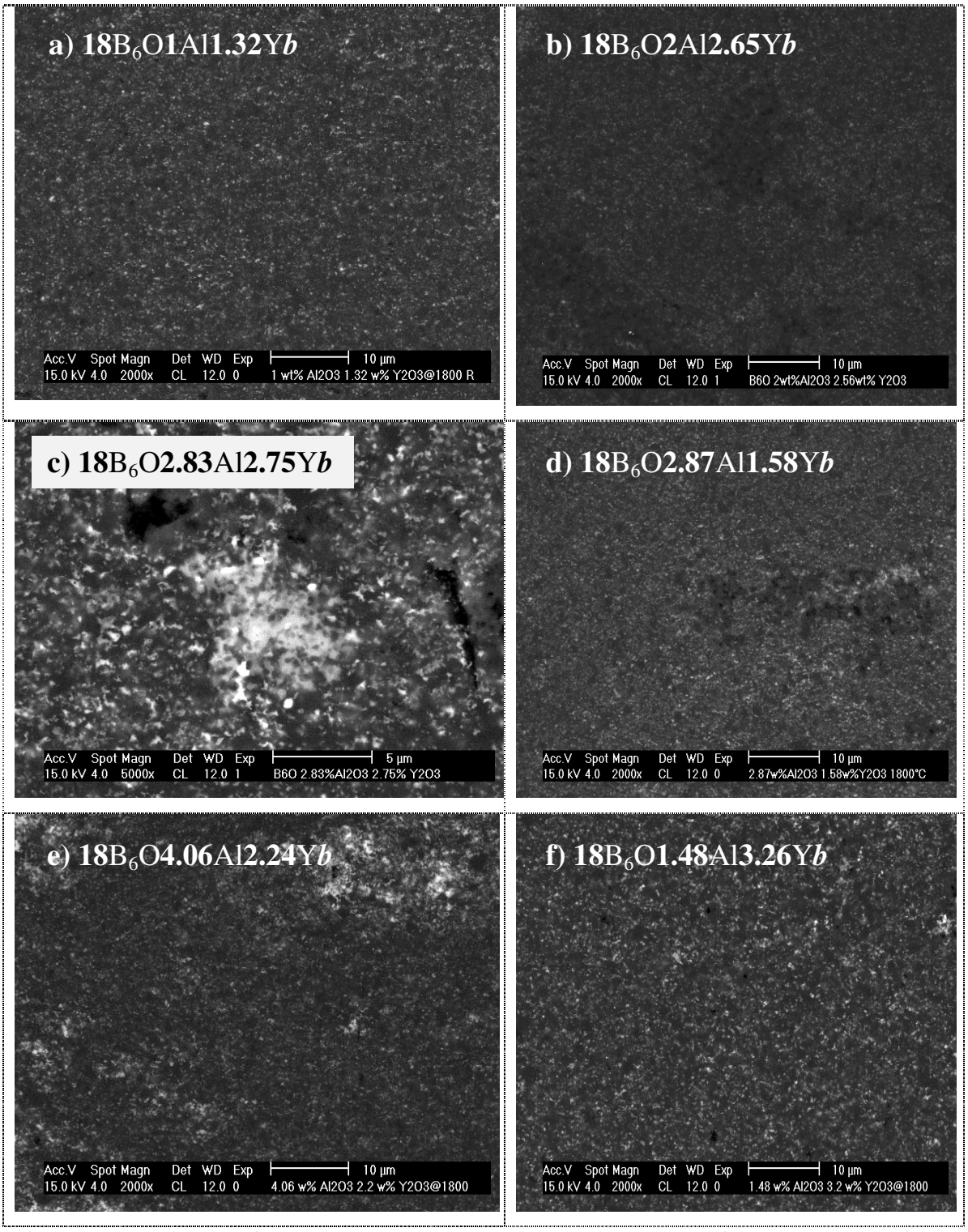

Figure D3: SEM images of Al-Y-doped B_6O hot pressed composites prepared from second batch of milled powder showing segregation of yttria in higher additive content.

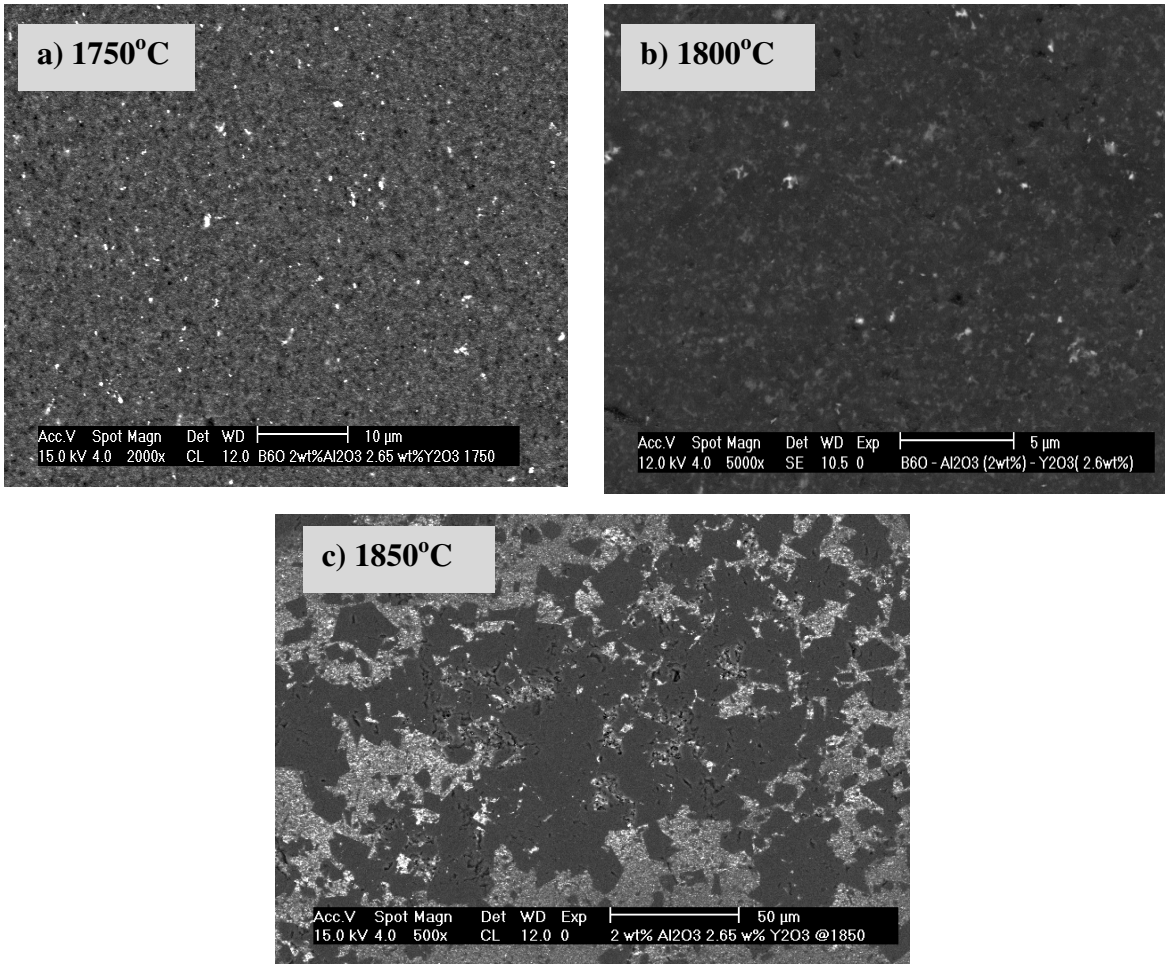

Figure D4: SEM images of Al-Y-doped B_6O hot pressed composites at different temperatures.

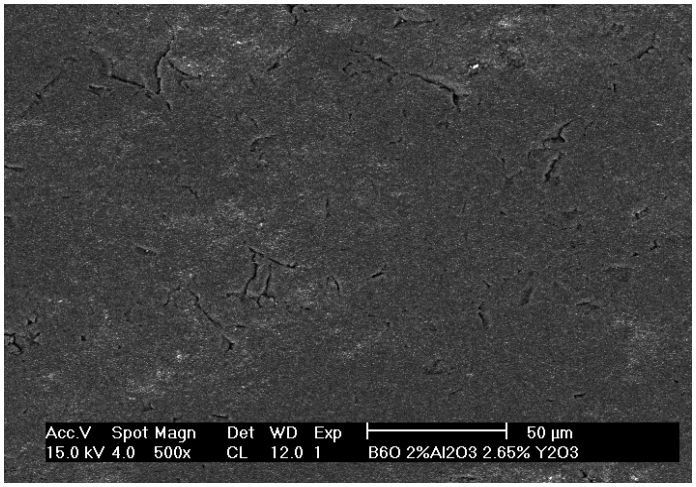

Figure D5: Low magnification image (SEM) of Al-Y-doped B_6O hot pressed composite produced from heat treated powder showing segregation and cracks in microstructure.

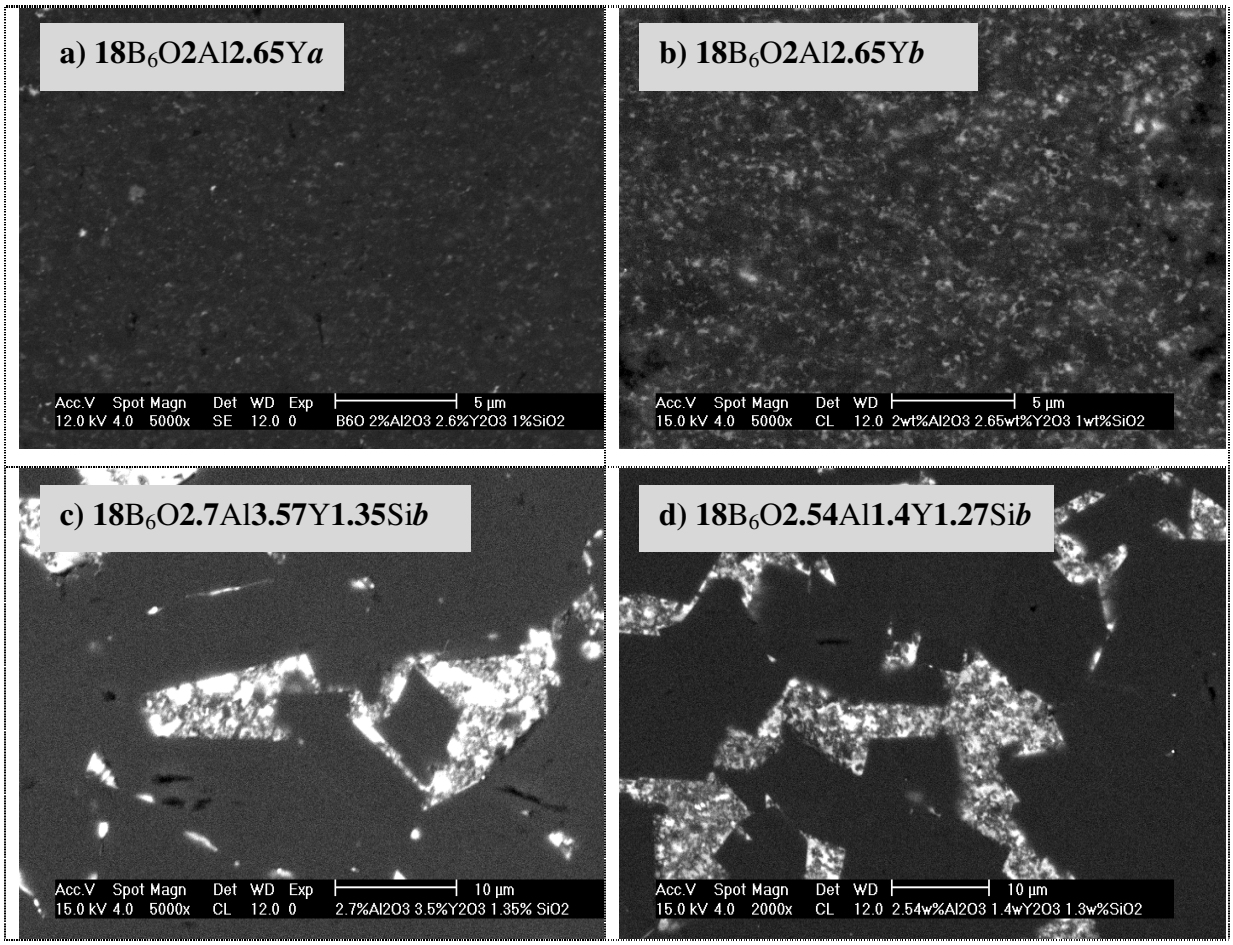

Figure D6: SEM images of Al-Y-Si-doped B_6O hot pressed composites showing grain growth in higher SiO_2 content.

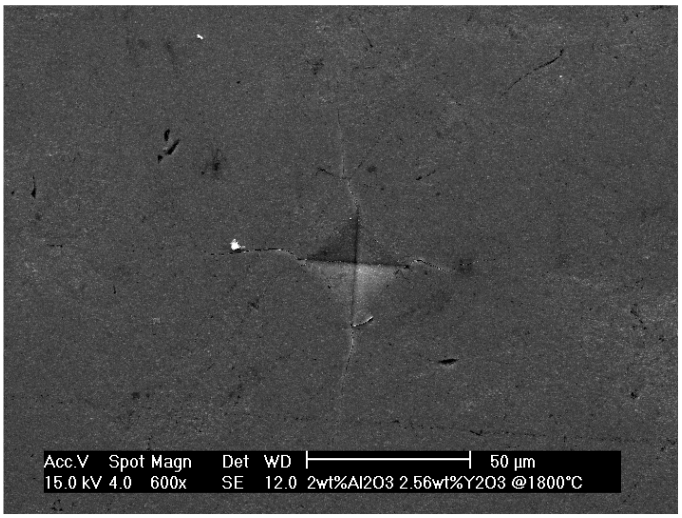

Figure D7: SEM image of polished **18**B_6O**2**Al**2.65**Y***b*** material showing indentation made with 5kg load.

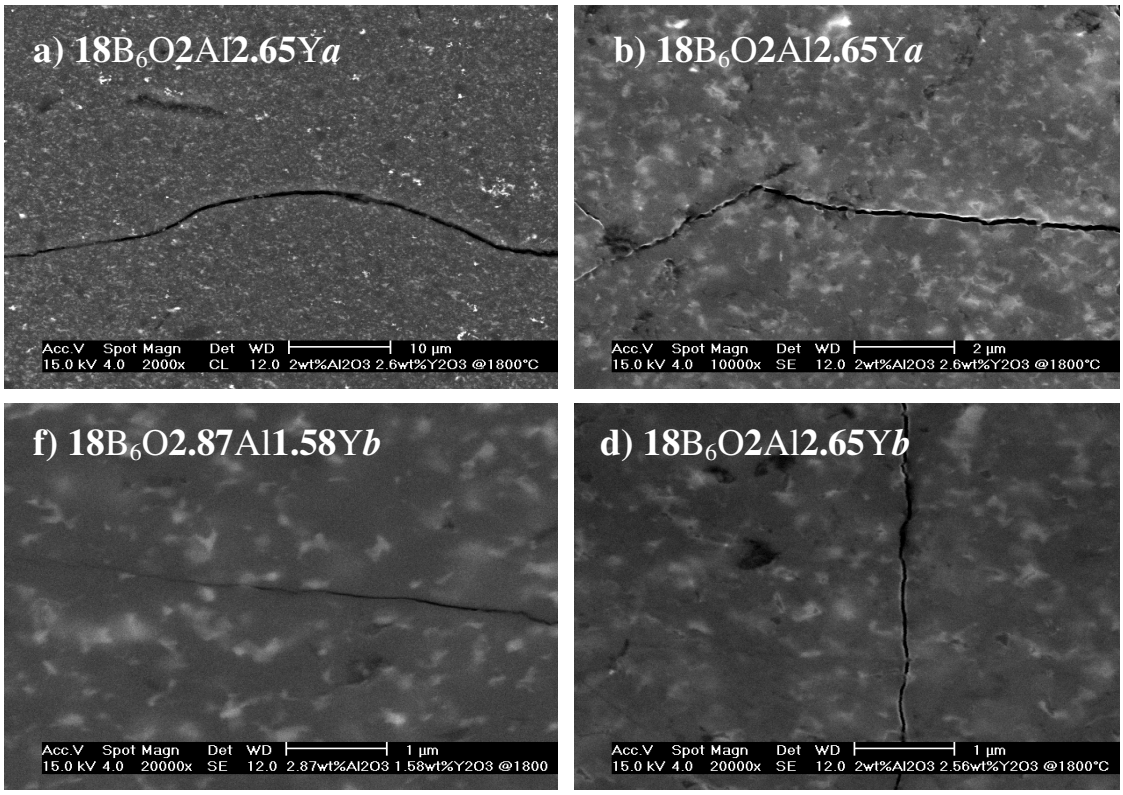

Figure D8: Crack path in polished Al-Y-doped B_6O hot pressed composites indicating some crack deflections. Transgranular fracture occurred in these composites.

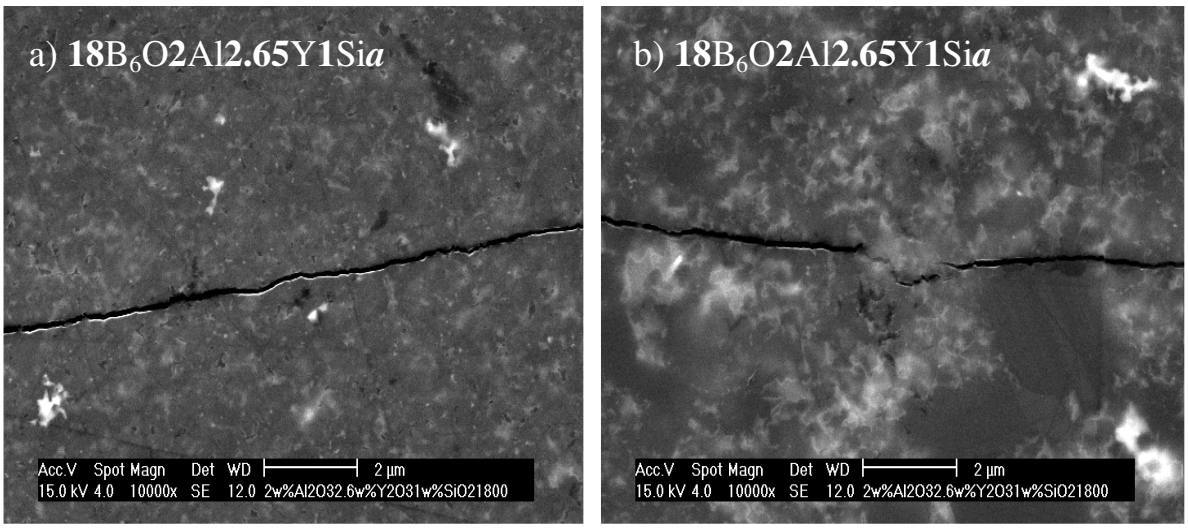

Figure D9: Crack path in polished Al-Y-Si-doped B_6O hot pressed composites indicating some crack deflections. Transgranular fracture occurred in these composites.

Appendix E: Particle size distribution of milled powders using the Mie-theory with refractive index of 2.409 and absorption of 0.08.

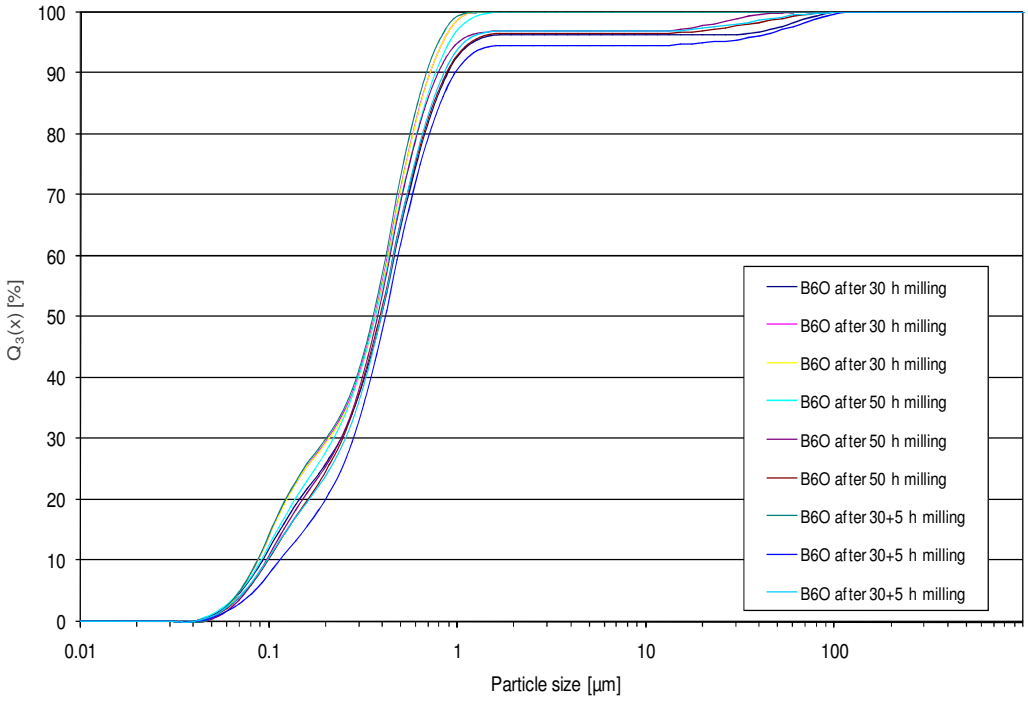

Figure E1: Dependency of particle size distribution of B_6O powders on milling time.